Master thesis

Expected accuracy of Mars rotation and orientation estimation from TGO orbit determination

Alfonso Maria Caldiero

Technische Universiteit Delft - Royal Observatory of Belgium

TU Delft

Master thesis

Expected accuracy of Mars rotation and orientation estimation from TGO orbit determination

by

Alfonso Maria Caldiero

to obtain the degree of Master of Science
at the Delft University of Technology,
to be defended publicly on Monday November 4, 2019 at 1:00 PM.

Student number:	4729226	
Project duration:	March 20, 2019 – November 4, 2019	
Thesis committee:	Dr. ir. D. Dirkx,	TU Delft, supervisor
	Dr. ir. W. van der Wal,	TU Delft
	Dr. J. Guo,	TU Delft
	Dr. S. Le Maistre,	Royal Observatory of Belgium

TU Delft

Preface

This report is a summary of the work performed over the past 9 months at the Royal Observatory of Belgium (ROB), partly in my old office, and partly in my new office. I could write about my personal feelings about this time at ROB, but this is not what you are here for. So I would go straight to the traditional *airing of grievances*[1].

First and foremost, I would like to express my gratitude towards two people who will *have* to read through this: Sébastien, to whom I owe most of the ideas presented in this report (read as: *don't blame me!*), for the countless hours he spent selflessly sharing his knowledge with me; and Dominic, my long-distance supervisor always minutes away when I needed his help, for the patience with which he has kept me on the right track towards a timely completion of the thesis. Then I would like to thank my family, for the moral and financial support, that allowed me to choose my internship (and then thesis project) without having to look at the salary, a luxury which many far more brilliant students can't afford.

As all the time wasted on *TV Tropes* has taught me, the true results are the friends we made along the way. Hence, thanks to all the people from the Observatory, for making me feel part of a group since the first day. And thanks to my friends in Italy, and everyone who reached out in these past months. To Antonio in particular, for being so close to me in a time I should have been close to him.

My gratitude goes towards those people who, in one way or another, have provided material support to the development of this thesis: Valerio, Marie-Julie, Xuan, Jean-Charles Marty and Pascal Rosenblatt. Finally, I would like to thank Wouter van der Wal and Jian Guo for accepting to be part of the thesis committee.

Alfonso Maria Caldiero
Brussels, October 2019

[1] *Seinfeld* (I would rather not have my TurnitIn score ruined by pop-culture references)

Contents

List of Figures

List of Tables

List of Symbols

Latin symbol	Definition	Units
A	Equatorial moment of inertia	kg m^2
A_i	Surface area of plate i	m^2
a	semi-major axis	m
$\boldsymbol{a}$	Acceleration	m s^{-2}
B	Equatorial moment of inertia	kg m^2
C	Polar moment of inertia	kg m^2
c	Speed of light	m s^{-1}
$\boldsymbol{c}$	Vector of consider parameters	-
C_{D_i}	Drag coefficient of plate i	-
e (Ch. 2)	Dynamical ellipticity	-
e	Orbital eccentricity	-
F	Core momentum factor	-
f	Frequency	Hz
G	Gravitational constant	m^{3}s^{-2}kg^{-1}
H	Jacobian matrix	-
h	Measurement	-
i (Ch. 2)	Imaginary unit	-
i	Inclination	deg
J	Inclination of Mars orbit in the ICRF	deg
J (Ch. 3)	Cost function	-
M	Mass	kg
M	Mean anomaly	deg
M_{bd}	Transponder ratio	-
m_x	Wobble variable	mas
N	Right ascension of Mars ascending node in the ICRF	deg
n	Degree of the spherical harmonic	-
n	Mean motion	deg s^{-1}
P	Period	days
P	Covariance matrix	
p	Parameter	depends
Q	Quality factor	
q	Observable	
$\boldsymbol{r}$	Position vector	m
R	Radius	m
R_x	Rotation matrix	-
S_{xc}	Sensitivity matrix	-
t	Time	s
T_n	Transfer function for nutations	-
U	Gravitational potential	m^2 s^{-2}
V	Velocity relative to the atmosphere	m s^{-1}
$\mathcal{V}$	Volume	m^3
W (Ch. 3)	Weighting matrix	dep.
$\boldsymbol{X}$	Vector of unknown parameters	depends
$\boldsymbol{x}$	State vector deviation	depends
X_P	Polar motion parameter	deg
Y_P	Polar motion parameter	deg

Greek symbol	Definition	Unit
α	Right ascension of the martian pole	deg
β	Compliance	-
γ_{MARS}	Vernal equinox of Mars	-
δ	Declination of the martian pole	deg
δ_{0m}	Kronecker delta	-
Δf	Doppler shift	Hz
ε (Ch. 3)	True estimation error	depends
ϵ	Mars obliquity	deg
$\boldsymbol{\epsilon}$	Vector of measurements errors	depends
λ	Longitude in the body-fixed frame	deg
λ'	Wavelength	m
Π	Polar motion matrix	depends
ρ	Range	m
$\rho_{\mathcal{V}}$	Density	kg m^{-3}
σ	Frequency	cpsd
σ (Ch. 3)	Formal error	depends
ϕ	Sidereal angle	deg
$\boldsymbol{\Phi}(t, t_k)$	State transition matrix	-
$\boldsymbol{\chi}$	Angular momentum excitation function	-
ψ	Angle between γ_{MARS} and the Mars ascending node in the ICRF	deg
ω	argument of perigee	deg
Ω	Right ascension of the ascending node	deg
$\boldsymbol{\Omega}$	Vector of the angular velocity of rotation	rad s^{-1}

List of Abbreviations

CMB	Core-mantle boundary
CNES	Centre National d'Etudes Spatiales
CoM	Center of mass
cpsd	Cycles per solar day
CW	Chandler wobble
DTE	Direct to Earth
EME	Earth mean equator
ESA	European Space Agency
FCN	Free core nutation
FICN	Free inner core nutation
FOC	Fluid outer core
FTS	Frequency and timing system
GINS	Géodésie par Intégration Numérique Simultanée
GCM	Global circulation model
GR	General relativity
HGA	High gain antenna
ICRF	International Celestial Reference Frame
ICRS	International Celestial Reference System
ICW	Inner core wobble
InSight	Interior exploration using Seismic Investigations, Geodesy and Heat Transport
JD	Julian Date
LaRa	Lander Radioscience
LOD	Length of day (variations)
LOS	Line of sight
LMD	Laboratoire de Météorologie Dynamique
JPL	Jet Propulsion Laboratory
MGS	Mars Global Surveyor
MMO	Mars mean orbit
MOP	Mars orientation parameter(s)
MRO	Mars Reconnaissance Orbiter
MTE	Mars true equator
NASA	National Aeronautics and Space Administration
ORB	Orbit Reaction Blocs
RISE	Rotation and Interior Structure Experiment
RMS	Root mean square
ROB	Royal Observatory of Belgium
RTN	Radial, tangential, normal
SIC	Solid inner core
TEC	Total electron content
TGO	Trace Gas Orbiter
VLBI	Very Long Baseline Interferometry

Abstract

The Rotation and Interior Structure Experiment (RISE) on the InSight lander and the LaRa experiment on the ExoMars platform will provide precise measurements (accuracies of a few mas) of the rotation of Mars, in terms of the Mars rotation and orientation parameters (MOP). These parameters include the rate of precession and the amplitudes of the nutations, of the length-of-day (LOD) variations, and of the polar motion components. The MOP are sensitive to the interior properties of Mars, particularly to the presence and size of a liquid core. However, uncertainties of current interior models in other physical parameters describing the internal structure of Mars, such as the temperature distribution, the composition, and the elasticity, limit the information on the interior obtainable from the MOP. Current estimates of the core radius have uncertainties of about 100 km, and suggest a fully liquid core.

The improvement of the accuracy of the MOP solution from the landers coming from the inclusion of radio-tracking data from Trace Gas Orbiter (TGO) was studied in this project. Both numerical (through the orbit determination software GINS and Tudat) and analytical (through the ORB software developed at the Royal Observatory of Belgium) methods were employed to asses the sensitivity of the TGO orbit and radio-tracking data to the MOP of interest. In particular, an analytical method based on Kaula's equations was developed to predict the effect of the MOP on a wide range of orbits. The satellites most affected by CW were found to be those in near-circular orbits at about 40° of inclination. The orbiters most sensitive to LOD variations were those in near-equatorial, highly-eccentric orbits.

As for the improvements on the MOP estimation due to TGO data, a covariance analysis was performed with different assumptions on the dynamical and observation models, and on the estimated parameters. The improvement with respect to a lander-only solution is of up to 6 % for the CW components, up to 8 % in the LOD variations components, and up to 20% and 12% on the nutations amplification factor and the FCN frequency (the latter two judged excessively optimistic). However, no definite inference on the resulting core radius accuracy improvement could be made.

1 Introduction

1.1. Motivation

In November 2018, the NASA InSight lander touched down on the surface of Mars, effectively marking a new phase in the rich history of the robotic exploration of the Red Planet. Within 3 years from that date, probes from 4 new missions are expected to reach Mars. These probes will either land on the surface of the planet, as in the case of InSight, or perform science while in orbit around the planets. Belonging to the former category is the probe sent as part of the ExoMars 2020 mission, a joint effort by the European Space Agency (ESA) and Roscosmos. On-board the surface platform of the ExoMars lander is an instrument ideated and developed by the Royal Observatory of Belgium, called LaRa (for Lander Radio Science, Dehant et al., 2009). A similar instrument is also present onboard the InSight lander, as part of the Rotation and Interior Structure Experiment (RISE, Folkner et al., 2018). Both instruments are coherent transponder, which will receive a radio signal coming from Earth and transmit it back. Through shifts in the frequency of this signal due to the relative motion of the instrument and the tracking station on Earth, LaRa and RISE will yield accurate measurements of the Mars rotation and orientation parameters (MOP).

The rotation of a planet and its orientation provide information on the internal state of the body. This is instrumental in the case of Mars, since there are few other options to probe its interior. This is why, although the planet has been the target of several missions in the past years, the internal structure of Mars is as of now still not known precisely. In turn, knowing the present state of the interior of Mars could provide important insight into its formation and evolution, especially since it has not experienced the modifications from plate tectonics as in the case of the Earth (Banerdt et al., 2013).

The mission which will bring LaRa on the surface of Mars is part of the larger ExoMars programme, whose primary objective is to study the present or past habitability of Mars. To do so, another probe was launched as part of the ExoMars programme, and it is orbiting Mars since 2017. This spacecraft, known as Trace Gas Orbiter (TGO), is one of the many currently orbiting the planet, although it has a lower inclination than most of the other probes. Radio-tracking data from TGO is also available. Clearly, an orbiter will not be as sensitive to changes in the rotation of the main body as a lander, which is tied to the planet and follows its motion in space. On the other hand, an orbiter covers a larger area of the main body with its motion, while a lander is only sensitive to variations affecting its landing site. In addition, the peculiar orbital characteristics of TGO may make it more or less sensitive to these effects.

1.2. Research question and goals

In view of this, the main objective of the present study is to propose a way to further improve these estimates by predicting the effect of using tracking data from TGO under different orbital configurations, or from another real or hypothetical orbiting spacecraft. From this main goal, in the literature study phase of this project different sub-goals were deduced:

- Testing the sensitivity of TGO to the MOP, by simulating realistic trajectories and radio science observations;

- Selecting an optimal data combination strategy allowing to maximize the impact of TGO measurements on the combined solution from the landers and the orbiter, by probing different weighting strategies;
- Deducing the effect on the inference of Mars physical characteristic of the inclusion of TGO data in the MOP estimation;
- Proposing a Martian spacecraft orbit which may maximize the accuracy of the MOP estimation from the landers, by evaluating the signature on the MOP on Keplerian orbits obtained by selecting subsets of values from the six orbital elements.

Based on these research goals, the main research question and its sub-questions can be explicited as follows:

- What is the achievable improvement in the accuracy of the MOP solutions obtained from InSight and LaRa when TGO tracking data is included?
  - What is the signature of the different MOP on the trajectory of TGO and the different radio tracking observables?
  - Is there an optimal method of combining data from InSight, LaRa, and TGO for the estimation of MOP?
  - What is the expected improvement in the accuracy of the physical parameters of Mars coming from this improved accuracy on the MOP?
  - What is the set of orbital elements which maximizes the impact of the orbiter tracking data on the combined solution for the MOP?

1.3. Thesis outline

The report starts, in Chapter 2, with a more in-depth explanation of the rotational state of Mars and how it is modelled, as well as a discussion on how geophysical properties of the planet are related to the MOP. Next, Chapter 3 presents the type of measurements which are of interest in this application of radio science, as well as the methods which allow to estimate the parameters and their uncertainties from these observations. Chapter 4, in its first part, outlines the models and assumptions useful to simulate a radio science experiment, and in its second part it describes the implementation of these theoretical expressions into the software employed throughout the project. Verification and validation of the software are presented in Chapter 5, while Chapter 6 lists the principal outcomes of the study. A discussion of the results thus presented is made in Chapter 7, from which the main conclusions are drawn in Chapter 8.

2

The rotation of Mars

This chapter constitutes the main theoretical frame of the report, yielding information about the science related to the research goals of Chapter 1. Section 2.1 presents the main reference frames useful for the description of the rotation and orientation of Mars. Section 2.2 discusses the main Mars rotation and orientation parameters (MOP), which express the relative orientation of these frames, and thus of the planet itself. Then, Section 2.3 outlines the ways by which the geophysical properties of Mars, such as its interior or the atmosphere dynamics, affect the MOP, and consequently how these same geophysical properties could be estimated from the MOP.

2.1. Reference frames

The International Celestial Reference Frame (ICRF), realization of the International Celestial Reference System, is a frame defined from Very Long Baseline Interferometry (VLBI) observation of extra-galactic sources like quasars, its axes being fixed with respect to these distant objects (Wakker, 2015). Its origin is in the barycenter of the Solar System, although in this discussion it will be assumed to be Mars-centered, along with all the other reference frames defined hereafter. The orientation of the ICRF is close to that of the Earth Mean Equator of J2000 (EME2000). The latter frame represents the orientation of the Earth at the epoch J2000 (1 January 2000, 12:00:00), not accounting for nutations. The x-axis of the EME2000 reference frame points to the vernal equinox at the reference date (here called γ_{EARTH}), while the z-axis is aligned to the Earth mean pole of J2000, and the y-axis completes the right-handed frame. The difference between the x-axes of the ICRF and the EME2000 reference frames was estimated to be 78±10 mas (milliarcseconds) in the y-direction and 19±2 mas in the z-direction (Folkner et al., 1994). Therefore, in the following, the terms ICRF and EME2000 (or simply J2000) will be used interchangeably. A representation of the various reference frames relevant to this study is given by Figure 2.1.

The Mars Mean Orbit of the year 2000 (MMO2000) is an inertial reference frame corresponding to the orientation of the mean orbit of Mars (that is, not accounting for the nutations of the orbital angular momentum) at J2000. The z-axis is normal to the Mars mean orbital plane of J2000, while the x-axis points to the ascending node of the orbit of Mars with respect to the xy plane of the ICRF. Such a reference frame can be defined for epochs different from J2000. For example, Konopliv et al. (2006) developed the rotation model of Mars using 1980 as a reference epoch of the MMO frame. The orientation of the MMO frame for the specific epoch is obtained from the ICRF with two rotations, around the z and the x-axes, of angles N and J, respectively. N is the angle between the x-axis of the ICRF and the ascending node of the mean orbit of Mars with respect to the ICRF xy plane. J is the inclination of the mean orbit of Mars with respect to the ICRF xy plane. This means that a vector $\boldsymbol{r}_{ICRF}$ in the ICRF is represented in the MMO frame as:

$$\boldsymbol{r}_{MMO} = R_x(J)R_z(N)\boldsymbol{r}_{ICRF} \tag{2.1}$$

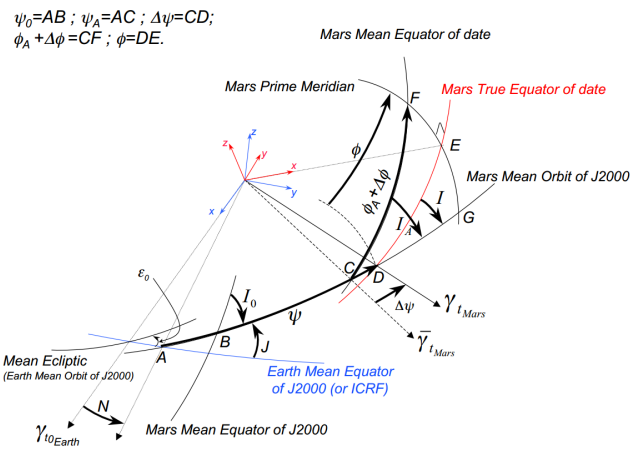

Figure 2.1: Relations between the reference frames used in this study, taken from Le Maistre (2013). The obliquity ϵ is here indicated as I. Similarly, the points γ_{EARTH} and γ_{MARS} are here displayed as $\gamma_{t0_{EARTH}}$ and $\gamma_{t_{MARS}}$, respectively.

Here R_x and R_z are elementary rotation matrices, which for the three axes are defined as:

$$R_x(\theta) = \begin{pmatrix} 1 & 0 & 0 \\ 0 & \cos\theta & \sin\theta \\ 0 & -\sin\theta & \cos\theta \end{pmatrix} \quad R_y(\theta) = \begin{pmatrix} \cos\theta & 0 & \sin\theta \\ 0 & 1 & 0 \\ -\sin\theta & 0 & \cos\theta \end{pmatrix} \quad R_z(\theta) = \begin{pmatrix} \cos\theta & \sin\theta & 0 \\ -\sin\theta & \cos\theta & 0 \\ 0 & 0 & 1 \end{pmatrix} \tag{2.2}$$

Due to the orthogonality of the rotation matrices, the inverse transformation is:

$$\boldsymbol{r}_{ICRF} = R_z(-N)R_x(-J)\boldsymbol{r}_{MMO} \tag{2.3}$$

From the MMO2000 frame (or that relative to any other epoch), another inertial reference frame can be defined. This is the Mars True Equator (MTE) of date, describing the orientation of Mars at an epoch of interest. The node of the Mars true equator with respect to the mean orbit of reference is in the following referred to as γ_{MARS}. The x-axis of the MTE frame is oriented towards the point γ_{MARS}, while the z-axis is parallel to the instantaneous rotation vector. The obliquity of the equatorial plane of Mars with respect to the mean orbit of J2000 is indicated as ϵ, while the angle between the x-axis of the MMO2000 frame and the direction of γ_{MARS} is ψ. The transformation between MMO2000 and MTE coordinates is then:

$$\boldsymbol{r}_{MTE} = R_x(\epsilon)R_z(\psi)\boldsymbol{r}_{MMO} \tag{2.4}$$

The Mars body-fixed frame has its x-axis pointing towards the intersection between the Mars prime meridian and the Mars equatorial plane, while the z-axis points towards the North pole of Mars. The spin angle ϕ is the angle formed by the Mars prime meridian and the direction of γ_{MARS}. The body-fixed frame will differ from the MTE frame because of the rotation of the planet, as expressed by the spin angle, but also because the actual pole is not on the rotation axis, due to polar motion. Hence, a vector $\boldsymbol{r}_{MTE}$ in the inertial MTE frame will be expressed in the Mars body-fixed frame as:

$$\boldsymbol{r}_{BF} = R_x(-Y_P)R_y(-X_P)R_z(\phi)\boldsymbol{r}_{MTE} \tag{2.5}$$

In this expression, the rotation matrix $R_z(\phi)$ rotates the x-axis of MTE to the prime meridian of Mars, while the other two rotations bring the z-axis to the instantaneous position of the pole of Mars. Here X_P and Y_P are the polar motion parameters: to the first order, X_P and $-Y_P$ represent the coordinates of the rotation pole in the body-fixed frame, since the amplitude of the polar motion terms is small and allows to approximate the areocentric angles with the corresponding arcs.

By combining these transformations, it is possible to relate the coordinates in the Mars body-fixed frame to those in the MMO2000 frame:

$$\boldsymbol{r}_{BF} = R_x(-Y_P)R_y(-X_P)R_z(\phi)R_x(\epsilon)R_z(\psi)\boldsymbol{r}_{MMO} \tag{2.6}$$

Some of the terms in this expression are often grouped together, so that:

$$\boldsymbol{r}_{BF} = \Pi\, R\, PN\, \boldsymbol{r}_{MMO} \tag{2.7}$$

Here, $\Pi = R_y(-X_P)R_x(-Y_P)$ is the polar motion matrix, $R = R_z(\phi)$ is the sidereal angle matrix, and $PN = R_x(\epsilon)R_z(\psi)$ is the precession and nutation matrix. From the previous formulas, the relation between a vector in the Mars body-fixed frame and the same vector in the ICRF is given by (Folkner et al., 1997a):

$$\boldsymbol{r}_{ICRF} = R_z(-N)R_x(-J)R_z(-\psi)R_x(-\epsilon)R_z(-\phi)R_y(X_P)R_x(Y_P)\boldsymbol{r}_{BF} \tag{2.8}$$

Alternatively, the position of the Martian pole in the ICRF can be expressed in terms of its right ascension (α) and declination (δ). Moreover, W is the angular distance, in the equatorial plane of Mars, between the Mars prime meridian and the intersection between the Mars True Equator of date and the xy plane of the ICRF. Using these spherical coordinates, the transformation between a vector in the ICRF and one in the body-fixed frame can be expressed as (Le Maistre, 2013):

$$\boldsymbol{r}_{BF} = R_x(-Y_P)R_y(-X_P)R_z(W)R_x\left(\frac{\pi}{2}-\delta\right)R_z\left(\frac{\pi}{2}+\alpha\right)\boldsymbol{r}_{ICRF} \tag{2.9}$$

The angles W and ϕ both describe the rotation of Mars around its spin axis, and are both measured along the Mars true equator of date, in the prograde direction. However, they have a different reference: ϕ is measured starting from the node of the Martian true equator with the mean orbit of the reference epoch, while W is measured starting from its node with the ICRF xy plane. Hence, the difference between these two angles is equal to the angle between the two reference nodes, here indicated as Δ^*:

$$W = \phi + \Delta^*, \tag{2.10}$$

The angle Δ^* varies due to precession and nutations, and using spherical trigonometry it can be shown that (Le Maistre, 2013):

$$d\Delta^* = d\psi \cos\epsilon - d\alpha \sin\delta \tag{2.11}$$

The relation between variation of the Mars orientation in obliquity and longitude ($d\epsilon$ and $d\psi$) and those in right ascension and declination ($d\alpha$ and $d\delta$):

$$d\alpha = -\frac{\sin\psi \sin J}{\cos^2\delta}d\epsilon + \frac{\cos J - \sin\delta\cos\epsilon}{\cos^2\delta}d\psi \tag{2.12}$$

$$d\delta = \frac{\cos\epsilon \sin J \cos\psi - \sin\epsilon\cos J}{\cos\delta}d\epsilon - \frac{\sin\epsilon \sin J \sin\psi}{\cos\delta}\quad d\psi \tag{2.13}$$

In GINS, the inertial reference frame is usually not the Earth Mean Equator of J2000, but the Mars Mean Equator of J2000 (MME2000). This frame is defined by the angles α_0 and δ_0, which are the values of the angles α and δ at the epoch J2000. Consequently, a rotation of a vector from the Mars body-fixed frame to the MME2000 frame is expressed as:

$$\boldsymbol{r}_{BF} = R_x(-Y_P)R_y(-X_P)R_z(W)R_x\left(\frac{\pi}{2}-\delta\right)R_z\left(\frac{\pi}{2}+\alpha\right)R_z\left(-\frac{\pi}{2}-\alpha_0\right)R_x\left(-\frac{\pi}{2}+\delta_0\right)\boldsymbol{r}_{MME2000} \tag{2.14}$$

2.2. Modelling the rotation parameters

Common models for the Mars orientation and rotation parameters are presented in this section. Each parameter is generally described by a constant term, which depends on the reference chosen, a linear term, and periodic terms, represented by finite trigonometric series. Following the partition of the rotation matrix from the inertial to the body-fixed frame (Eq. 2.7), the parameters are separated into precession and nutation parameters (corresponding to the matrix PN), length-of-day variations parameters (corresponding to the matrix R), and polar motion parameters (corresponding to the matrix Π).

2.2.1. Precession and nutations

As the radius of Mars is larger at the equator than at the poles, and since its rotation axis is inclined with respect to the normal to the orbital plane, the gravitational attraction from the other bodies of the Solar System will be uneven over the surface of Mars. This produces a torque which tends to tilt the rotation axis towards the direction normal to the orbital plane. The spinning planet responds with a motion of the rotation axis along a cone centred on the normal to the orbital plane, accompanied by several oscillations of smaller amplitude around this cone, due to the variations in the relative positions of the bodies. The former motion is the precession, while the small oscillations around the precession cone are the nutations. For Mars, precession and nutations are mainly caused by the attraction of the Sun. In the formalization introduced in Section 2.1, the precession and the nutations generate variations in the angles ψ and ϵ. These quantities can then be expressed as a function of time as:

$$\psi(t) = \psi_0 + \dot{\psi}t + \Delta\psi \tag{2.15}$$

$$\epsilon(t) = \epsilon_0 + \dot{\epsilon}t + \Delta\epsilon \tag{2.16}$$

In these equations, ψ_0 and ϵ_0 are the values of the angles at the reference epoch ($t = 0$), here taken to be J2000. The precession term is $\dot{\psi}t$, while $\Delta\psi$ and $\Delta\epsilon$ are the terms relative to the nutations in longitude and in obliquity, respectively. The secular variation of the obliquity of Mars, represented by the term $\dot{\epsilon}t$, is small, with $\dot{\epsilon}$ estimated to be in the order of some mas per terrestrial year (Konopliv et al., 2016). As they depend on the relative positions of the bodies, the main terms in the nutations in longitude and obliquity have frequencies which are multiples of the orbital frequency of Mars. The six prevalent frequencies f_m, for m going from 1 to 6 and representing the number of cycles per Martian year, are (in cycles per Earth solar day) 1/687, 1/343.5, 1/229, 1/171.7, 1/137.4, and 1/114.5. The complete expression of the nutation terms can be approximated by the sum of the terms relative to these 6 frequencies (Le Maistre et al., 2012):

$$\Delta\psi = \sum_{m=1}^{6} \psi_m^C \cos(2\pi f_m t) + \psi_m^S \sin(2\pi f_m t) \tag{2.17}$$

$$\Delta\epsilon = \sum_{m=1}^{6} \epsilon_m^C \cos(2\pi f_m t) + \epsilon_m^S \sin(2\pi f_m t) \tag{2.18}$$

The elliptical motions described by these two series can be each decomposed into two counter-rotating circular motions. These will have the form:

$$p_m e^{2i\pi f_m t} \quad \text{and} \quad r_m e^{-2i\pi f_m t} \tag{2.19}$$

Here $i^2 = -1$, and the complex coefficients $p_m = p_m^R + ip_m^I$ and $r_m = r_m^R + ir_m^I$ are relative to the prograde and the retrograde motion, respectively (with $f_m > 0$). Indicating with $\delta\psi_m$ each term of the sum in Equation 2.17, and with $\delta\epsilon_m$ the corresponding terms in Equation 2.18, the following relation holds (Dehant and Mathews, 2015a):

$$p_m e^{2i\pi f_m t} + r_m e^{-2i\pi f_m t} = \delta\epsilon_m + i \sin\epsilon_0 \delta\psi_m \tag{2.20}$$

From this relation, the coefficients of the circular motions can be found from those of the elliptical motion as:

$$p_m^R = \frac{\epsilon_m^C + \sin\epsilon_0 \psi_m^S}{2} \tag{2.21}$$

$$p_m^I = \frac{-\epsilon_m^S + \sin\epsilon_0 \psi_m^C}{2} \tag{2.22}$$

$$r_m^R = \frac{\epsilon_m^C - \sin\epsilon_0 \psi_m^S}{2} \tag{2.23}$$

$$r_m^I = \frac{\epsilon_m^S + \sin\epsilon_0 \psi_m^C}{2} \tag{2.24}$$

The variation of the angles α and δ with time can be written, similarly to that of ϵ and ψ, as (Le Maistre, 2013):

$$\alpha = \alpha_0 + \dot{\alpha} t + \Delta\alpha, \tag{2.25}$$

$$\delta = \delta_0 + \dot{\delta} t + \Delta\delta, \tag{2.26}$$

where again α_0 and δ_0 are the values of the angle at the reference epoch, at which $t = 0$. Expressed as a truncated trigonometric series, which considers only the principal frequencies (namely the first 6 integer multiples of the orbital frequency of Mars), the nutation terms are:

$$\Delta\alpha = \sum_{m=1}^{6} \alpha_m^c \cos(2\pi f_m t) + \alpha_m^s \sin(2\pi f_m t) \tag{2.27}$$

$$\Delta\delta = \sum_{m=1}^{6} \delta_m^c \cos(2\pi f_m t) + \delta_m^s \sin(2\pi f_m t) \tag{2.28}$$

The amplitudes of the cosine and sine terms are related to the corresponding amplitudes in the series expansion of $\Delta\epsilon$ and $\Delta\psi$ by the same linear expressions (with the same coefficients) relating $d\alpha$ and $d\delta$ to $d\epsilon$ and $d\psi$ (Eqs. 2.12 and 2.13).

2.2.2. Length-of-day (LOD) variations

The length-of-day (LOD) of Mars is defined as (Le Maistre, 2013):

$$LOD(t) = \frac{2\pi}{\Omega(t)} \tag{2.29}$$

where $\Omega(t)$ is the instantaneous angular velocity of rotation of Mars, which in turn is the time derivative of the spin angle ϕ, according to:

$$\Omega(t) = \frac{d\phi}{dt} \tag{2.30}$$

The sidereal angle ϕ is the angle between the Mars vernal equinox and its prime meridian. Hence, its variation is due to the motion in space of these two references. The value of the spin angle at the reference epoch ($t = 0$) is denoted with ϕ_0. The prime meridian of Mars was initially defined as the centre of the Airy-0 crater, while it is currently defined as the meridian 47.95137° east of the one containing the Viking 1 lander (Archinal et al., 2018). The new definition leaves the position of the meridian unchanged, but improves its accuracy, because of the higher precision in the estimated position of a lander compared to that in the position of the centre of a wide crater (Kuchynka et al., 2014). The motion of the prime meridian is related to the rotation of Mars, which consists of a linear term, translating into a variation of the sidereal angle equal to $\dot{\phi} t$, and a periodic term, leading to a term $\Delta\phi$ in the expression of ϕ. The periodic perturbations to the constant rotation of the planet arise mainly from the mass exchange between the atmosphere and the polar caps (matter term of the angular momentum) and from the zonal winds (wind term of the angular momentum) (Defraigne et al., 2000). Therefore, the expression of the sidereal angle at time t, accounting for the motion of the prime meridian, is (Le Maistre et al., 2012):

$$\phi(t) = \phi_0 + \dot{\phi} t + \Delta\phi \tag{2.31}$$

The quantity $\phi_A = \phi_0 + \dot{\phi} t$ is known as the regular term. The seasonal variations of the spin angle are expressed as a finite series (Le Maistre et al., 2012):

$$\Delta\phi = \sum_{m=1}^{4} \phi_m^c \cos(2\pi f_m t) + \phi_m^s \sin(2\pi f_m t) \tag{2.32}$$

The coefficients ϕ_m^c and ϕ_m^s are the amplitudes of the cosine and the sine terms of the series, while f_m is the value of the frequency corresponding to the index m. The frequencies characteristic of the seasonal

spin variations and considered in the series are, in earth solar days, the annual (f_1=1/687 days), the semiannual (f_2=1/343.5 days), the terannual (f_3=1/229 days), and the quaterannual (f_4=1/171.7 days). The motion of the vernal equinox over the mean orbit of J2000 is due to precession and nutations of Mars. Using spherical trigonometry and the considering that $\dot{\epsilon} \approx 0$, the resulting contribution can be approximated by (Le Maistre, 2013):

$$\Delta\phi_\psi = (\dot{\psi}t - \Delta\psi)\cos\epsilon_0 \tag{2.33}$$

The linear term in this expression, which comes from the precession of the rotation axis, may be implicitly included in the linear term of Equation 2.31, so that:

$$\phi(t) = \phi_0 + \dot{\phi}t + \Delta\phi - \Delta\psi\cos\epsilon_0 \tag{2.34}$$

The LOD variations are related to the spin angle variations $\Delta\phi$ (assumed to include also the term $\Delta\psi\cos\epsilon_0$ due to nutations), to the first order in $\frac{1}{\dot{\phi}}\frac{d\Delta\phi}{dt}$, by (Le Maistre, 2013):

$$\Delta LOD = -\frac{2\pi}{\dot{\phi}^2}\frac{d\Delta\phi}{dt} \tag{2.35}$$

The spin angle variations are also described by the variations of the angle W. The seasonal effect due to the matter and wind terms of the angular momentum is the same for W and ψ (that is, $\Delta W = \Delta\psi$), for it affects the motion of the prime meridian, independently from the reference taken for the rotation angles. The terms due to the nutations, instead, are different for the two angles, because of the variation ($d\Delta^*$) of the angle between the corresponding reference nodes. The angle W is thus written as (Le Maistre, 2013):

$$W = W_0 + \dot{W}t + \Delta W - \Delta\alpha\sin\delta_A, \tag{2.36}$$

where $\delta_A = \delta_0 + \dot{\delta}t$, and

$$\Delta W = \sum_{m=1}^{4} W_m^c\cos(2\pi f_m t) + W_m^s\sin(2\pi f_m t). \tag{2.37}$$

2.2.3. Polar motion

The polar motion is the movement of the rotation axis in the body-fixed frame. It is present whenever the rotation axis does not coincide with the axis of maximum angular momentum (Lowrie, 2011). In the case of Mars, this displacement of the axis is due to the atmospheric phenomena and the seasonal mass exchanges between the atmosphere and the polar caps. The position of the rotation pole in the body-fixed frame is described by the two parameters X_P and Y_P, so that its first two coordinates are given by X_P and $-Y_P$. Because of its source, this motion will be mostly characterised by frequencies that are multiples of the Martian orbital frequency. In addition, there is a free mode of Mars, the Chandler wobble (CW), which when excited produces a new periodic component of the polar motion. The rotation axis undergoing polar motion is usually represented in the body-fixed frame as (Dehant and Mathews, 2015a):

$$\boldsymbol{\Omega}(t) = \Omega_0\left(m_x, m_y, 1 + m_z\right) \tag{2.38}$$

where Ω_0 is the angular velocity of the rotation around the axis of maximum angular momentum. The relation between the parameters m_x and m_y and the pole coordinates is clearly:

$$m_x = X_P \quad m_y = -Y_P \tag{2.39}$$

The polar motion parameters X_P and Y_P are represented as a finite series in their most prominent frequencies, like the other MOPs. In particular (Le Maistre et al., 2012):

$$X_P = \sum_{m=1}^{3} X_m^c\cos(2\pi f_m t) + X_m^s\sin(2\pi f_m t) \tag{2.40}$$

$$Y_P = \sum_{m=1}^{3} Y_m^c\cos(2\pi f_m t) + Y_m^s\sin(2\pi f_m t) \tag{2.41}$$

The frequencies involved in this case are the annual (m=1), the semiannual (m=2), and the Chandler wobble frequency (m=3), with values of 1/687, 1/343.5 and around 1/200 days, respectively.

2.2.4. Current estimates

The latest models of the rotation of Mars were provided by Kuchynka et al. (2014) and Konopliv et al. (2016). Both were derived by adjusting tracking data from the landers Viking 1 and 2 and Mars Pathfinder, the Mars Exploration Rover (MER) Opportunity in the 5 months of its radio science campaign, and the orbiters Mars Global Surveyor (MGS), Mars Odyssey, and Mars Reconnaissance Orbiter (MRO). The results from (Konopliv et al., 2016) relied on a larger dataset, due to additional years of observations from Odyssey and MRO. The difference between the two models is roughly 13 m at the surface of Mars (Archinal et al., 2018). Kuchynka et al. (2014) provide a series expansion for the rotation model in the angles α, δ, W. A series expansion in these angles for the model by Konopliv et al. (2016), which is expressed in terms of the angles ψ, ϵ, ϕ, was given by (Jacobson et al., 2018).

The two rotation models are based on the same set of conventions, formulated by Konopliv et al. (2006) in the definition of the Pathfinder model of the rotation of Mars (of which the 2016 model is an update). The expressions of the MOP in the Pathfinder model draw their general form from the analytical models of the precession and nutations of Mars developed by Reasenberg and King (1979). In addition, the model includes terms representing the seasonal variations in spin rate due to the CO_2 mass exchanges between the polar caps and the atmosphere, as given by Folkner et al. (1997b), the polar motion, and the nutations amplification due to the free core nutation (FCN), both found in Folkner et al. (1997a). The obliquity, longitude of the node, and sidereal angle are thus modelled as (Konopliv et al., 2006):

$$\epsilon = \epsilon_0 + \dot{\epsilon}_0 t + \sum_{m=0}^{9} \epsilon_m \cos(\alpha_m t + \theta_m), \tag{2.42}$$

$$\psi = \psi_0 + \dot{\psi}_0 t + \sum_{m=0}^{9} \psi_m \sin(\alpha_m t + \theta_m), \tag{2.43}$$

$$\phi = \phi_0 + \dot{\phi}_0 t - \Delta\psi \cos\epsilon + \sum_{j=1}^{4} \left(\phi_{cj} \cos jl' + \phi_{sj} \sin jl'\right) + \sum_{j=1}^{3} \phi_{rj} \sin jl', \tag{2.44}$$

where $\Delta\epsilon$ and $\Delta\psi$, the nutations in obliquity and longitude, are represented by the trigonometric series in Eqs. 2.42 and 2.43. The angular velocities α_m are equal to mn' for $m \leq 3$ and to $(m-3)n'$ for $3 < m \leq 9$, n' being the mean motion of Mars. The phase terms of the nutations series are given by $\theta_m = ml'_0$ for $m \leq 3$, and $\theta_m = (m-3)l'_0 + q$ for $3 < m \leq 9$, where l' is the mean anomaly of Mars, and the angle q is twice the argument of perihelion of the planet relative to the node of the Mars equator and the Mars mean orbit. The value of q was $142.00°$ at J2000, and varies by $1.3°$ per century (Konopliv et al., 2006). The terms with $m = 0$ correspond to a small and constant correction for the obliquity amplitude (indicated as $\epsilon_{m=0}$ to differentiate it from the initial value of the angle, ϵ_0), equal to -1.4 mas, while $\psi_{m=0} = 0$. (Reasenberg and King, 1979). The equation for ϕ includes the periodic spin variations, of amplitudes ϕ_{cj} and ϕ_{sj}, and the relativistic corrections, of amplitude ϕ_{rj}, which model the slowing of clocks on Mars due to general and special (related to the planetary motion) relativity (Yoder and Standish, 1997).

The trigonometric series of the nutations in longitude and obliquity of the Pathfinder model can be related to those given by Eqs. 2.17 and 2.18 by substituting, for $m \leq 3$ (Le Maistre, 2013):

$$\epsilon_m^c = \epsilon_m \cos\theta_m + \epsilon_{m+3} \cos\theta_{m+3}, \tag{2.45}$$

$$\epsilon_m^s = -\epsilon_m \sin\theta_m - \epsilon_{m+3} \sin\theta_{m+3}, \tag{2.46}$$

$$\psi_m^c = \psi_m \sin\theta_m + \psi_{m+3} \sin\theta_{m+3}, \tag{2.47}$$

$$\psi_m^s = \psi_m \cos\theta_m + \psi_{m+3} \cos\theta_{m+3}, \tag{2.48}$$

and for $m \geq 7$:

$$\epsilon_m^c = \epsilon_m \cos\theta_m, \tag{2.49}$$

$$\epsilon_m^s = -\epsilon_m \sin\theta_m, \tag{2.50}$$

$$\psi_m^c = \psi_m \sin\theta_m, \tag{2.51}$$

$$\psi_m^s = \psi_m \cos\theta_m \tag{2.52}$$

The same can be done for the two trigonometric series in the equation of the spin angle in the Pathfinder model, which become those in Eq. 2.32 if the following substitutions are made (Le Maistre, 2013):

$$\phi_j^c = \phi_{cj} \cos jl'_0 + (\phi_{sj} + \phi_{rj}) \sin jl'_0, \tag{2.53}$$

$$\phi_j^s = (\phi_{sj} + \phi_{rj}) \cos jl'_0 - \phi_{cj} \sin jl'_0 \tag{2.54}$$

The numerical values of the parameters estimated in the aforementioned Mars rotation models are listed in Table 2.1. Of the trigonometric series in the expressions of ϵ, ψ, and ϕ, only the amplitudes of those pertaining to the seasonal variations of the spin angle were estimated. The nutations amplitudes for the rigid Mars were fixed to the values derived by Reasenberg and King (1979). Similarly, the relativistic corrections to the spin angle variation were set to the values found in Yoder and Standish (1997). The values of these non-estimated parameters can be found in Table 2.2.

Parameter	Kuchynka et al. (2014)		Konopliv et al. (2016)	
	Value	Error	Value	Error
ψ_0 (deg)	81.968379	0.000009	81.9683988	0.0000043
$\dot{\psi}_0$ (mas/yr)	-7606.1	3.5	−7608.3	2.1
ϵ_0 (deg)	25.189383	0.000005	25.1893823	0.0000026
$\dot{\epsilon}_0$ (mas/yr)	−1	2	−2.0	1.1
ϕ_0 (deg)	133.386209	0.000043	133.386277	0.000019
$\dot{\phi}_0$ (deg/day)	350.891985294	0.000000006	350.891985307	0.000000003
ϕ_{c1} (mas)	494	13	481	10
ϕ_{s1} (mas)	-195	16	-155	12
ϕ_{c2} (mas)	-114	11	-103	9
ϕ_{s2} (mas)	-105	10	-93	8
ϕ_{c3} (mas)	-34	9	-35	8
ϕ_{s3} (mas)	-1	8	-3	7
ϕ_{c4} (mas)	-4	6	-10	6
ϕ_{s4} (mas)	-22	7	-8	6

Table 2.1: Latest Mars orientation parameters solutions. All values are taken from Konopliv et al. (2016).

As for polar motion, for both models the amplitudes of the X_P and Y_P are set to zero. An estimate of the polar motion amplitudes is found in Konopliv et al. (2006). There, the polar motion parameters are expressed in the form:

$$m_x = \sum_{j=1}^{5} m_{x_j} \sin\left(\alpha_{x_j} t + \theta_{x_j}\right), \qquad m_y = \sum_{j=1}^{5} m_{y_j} \sin\left(\alpha_{y_j} t + \theta_{y_j}\right), \tag{2.55}$$

The first 4 terms of the two series are relative to the seasonal effect, so that $\alpha_{x_j} = \alpha_{y_j} = jn'$ for $j < 5$. The last term, for $j = 5$, is the Chandler wobble (see Section 2.3.2), of angular frequency $\alpha_{x_5} = \alpha_{y_5} = \sigma_{CW}$, corresponding to an assumed period of 205 days. The amplitudes and phase terms of the two series, estimated from the observed values of the gravity field coefficients C_{21} and S_{21} (see Eq. 4.1), are listed in Table 2.3.

2.3. MOP and Mars geophysical properties

2.3.1. Interior models of Mars

Notwithstanding the numerous missions to Mars, the knowledge about its interior is far from being as complete as that of the Earth. Actually, very little is known about the internal structure of Mars. The

m	ϵ_m (mas)	ψ_m (mas)
0	-1.4	0
1	-0.4	-632.6
2	0	-44.2
3	0	-4.0
4	-49.1	-104.5
5	515.7	1097.0
6	112.8	240.1
7	19.2	40.9
8	3.0	6.5
9	0.4	1.0

j	ϕ_{rj} (mas)
1	-176
2	-8
3	-1

Table 2.2: Rigid nutations amplitudes (Reasenberg and King, 1979) and sidereal-angle relativistic corrections (Yoder and Standish, 1997) in mas, as used for the latest Mars rotation models. The values are taken from Konopliv et al. (2006), and are relative to a polar moment of inertia of $C = 0.365$. For a different moment of inertia, these values scale with $C/0.365$.

j	m_{x_j} (mas)	θ_{x_j} (deg)	m_{y_j} (mas)	θ_{y_j} (deg)
1	-12.8	-42	4.5	-92
2	7.8	8	-8.0	0
3	0	0	0	0
4	2.4	-131	2.2	87
5	5 ±3	0	5 ±3	-11

Table 2.3: Amplitudes and phase terms of the Mars polar motion parameters, as estimated by Konopliv et al. (2006).

In this section, the distinction was made between the LOD variations amplitudes of the Pathfinder model, indicated as ϕ_{cj}, ϕ_{sj}, and ϕ_{rj}, and those appearing in Eq. 2.32, indicated with ϕ_j^c and ϕ_j^s. However, in all the applications presented in this report, the expression from Eq. 2.44 is used for the LOD variations, both because it is the notation implemented in Tudat (Section 4.2.2) and because they allow a faster comparison with values from the literature. For polar motion, instead, the formalism from Eqs. 2.40 and 2.41 will be employed, where the amplitudes are X_m^c and X_m^s. Thus, in order to have an agreement between the notations used for the polar motion and the LOD variations amplitudes, the latter will also be expressed as ϕ_j^c and ϕ_j^s, while still referring to the parameters of the Pathfinder model. In particular, this notation will imply $\phi_j^c = \phi_{cj}$, and $\phi_j^s = \phi_{sj} + \phi_{rj}$.

reason is mainly the absence of precise seismic measurements, which have been the major input for the study of the interior of our planet. This could change once data from the Seismic Experiment for Interior Structure (SEIS) on InSight will be available (Lognonné et al., 2019). In the meantime, only hypotheses could be made from the current geodesy measurements.

Mars interior models are usually spherically symmetric, with the parameters only varying as a function of the distance from the centre (Rivoldini et al., 2011). The general structure of the planet consists of three main layers: a crust, a mantle and a core. The cores of terrestrial planets are usually thought evolve with the cooling of the planet, going from an entirely liquid core to a partially solid inner core, and to a fully solid core (Dehant et al., 2003). Several studies favour the hypothesis of Martian core that is at least partially liquid (Yoder et al., 2003). Moreover, recent studies present arguments against the presence of a solid inner core, which may also be confirmed by the absence of a global magnetic field (Rivoldini et al., 2011).

The observations which can give the most information about the state of the planetary interior are those that provide estimates of the radius, the mass, the mean moment of inertia, and the second degree tidal Love number k_2 (Van Hoolst and Rivoldini, 2014). The shape of Mars, and therefore its mean radius, was measured by the Mars Orbiter Laser Altimeter (MOLA) on MGS, while the mass is estimated through the gravity field. The (normalized) mean moment of inertia is (Konopliv et al., 2011):

$$MOI = \frac{I_a}{MR_a^2} = \frac{A+B+C}{3M_aR_a^2} = \left(\frac{C}{3M_aR_e^2} - \frac{2}{3}J_2\right)\left(\frac{R_e}{R_a}\right)^2 \tag{2.56}$$

In this expression, M_a, R_a, and R_e are in the order the mass, the volumetric mean radius, and the equatorial radius, while $A < B < C$ are the principal moments of inertia, C being the polar moment of inertia and the other two the equatorial moments of inertia. The polar moment of inertia is determined from the estimate of the precession rate. The value of the zonal harmonic coefficient J_2 is known to high accuracy, thus the precision of current mean moment of inertia values is limited by the accuracy of the precession estimate. The most recent estimate gives a value of MOI equal to 0.3639 ± 0.0001 (Konopliv et al., 2016). The mean moment of inertia gives information about the internal distribution of the mass. In particular, the current estimate is indicative of a density increasing with depth and a dense core (Rivoldini et al., 2011). However, since it is an integrated quantity, it is not able to constrain local properties like the size of the core.

A better constraint on the interior properties is given by k_2. A planet with a partially liquid interior has a larger response to the tidal forcing than a fully solid one, and in particular, the threshold of 0.08 on the value of k_2 can be used to distinguish between a liquid and a solid core (Rivoldini et al., 2011). Values larger than this threshold could indicate that a portion of the core is liquid. With a Love number of 0.145 ± 0.017, Yoder et al. (2003) inferred a core radius between 1520 and 1840 km, and concluded that at least the outer part of the core should be liquid. Recent estimates of the solar and Phobos tide yield $k_2 = 0.1697 \pm 0.0009$ (Genova et al., 2016). This result is still in agreement with a liquid outer core.

Among the other geophysical parameters that can help constrain the interior of Mars figure the crustal density and thickness. These quantities are estimated from the inversion of topography and gravity field. Wieczorek (2004) computed a crustal thickness of 57 ± 24 km, and a crustal density in the range of $[2700, 3100]$ kg/m^3.

A further constraint is given by the SNC meteorites (shergottites, nakhlites, and chassignites), which are thought to be of Martian origin, and therefore can give information on the composition of the mantle of Mars. In particular, the composition of these meteorites has been employed to infer the bulk composition of the planet, either by assuming abundances equal to those of CI chondrites, or by estimating the isotopic composition of the meteorites (Taylor, 2013). Geochemical models agree on an iron-rich core alloyed with lighter elements, which may be predominantly sulfur (Khan et al., 2018).

Rivoldini et al. (2011) formulated a set of possible interior models for Mars by inferring 8 parameters of the interior structure (core size, crust density and thickness, and 5 parameters characterizing the mantle mineralogy) from the estimates of MOI and k_2 through a Bayesian inversion, since the problem is underdetermined. Knowledge on the parameters, which may come from geochemical models or measured values, is taken into account by the definition of an a priori probability distribution for the parameters. The knowledge about the temperature distribution inside the planet is very limited, which is why the various temperature models were represented by two extremes, a cold and a hot one. This resulted in values for the core radius in the range of $[1729, 1859]$ km, and a sulfur concentration inside

the core in the range of $[14, 18]$ wt%, under the assumption that the core is exclusively composed of Fe and S.

A similar analysis was performed by Khan et al. (2018), leading to core radii between 1730 and 1840 km, as well as a composition of the core of 15 to 18.5 wt% in sulfur. For both studies, the resulting concentration of sulfur in the Fe-S core is close to the eutectic concentration, meaning that the melting point of the core is at a lower temperature than that of an iron-only core. This, compared to the lower limits of the modelled temperatures at the core-mantle boundary, has led in both studies to the conclusion that a solid inner core is absent for Mars. Such a result may not hold if the actual temperatures in the core were lower than the lower bounds of the models used, or for different concentrations of S and other elements within the core.

2.3.2. Signature of the interior on the MOP

As mentioned in the previous section, the internal mass distribution of Mars directly affects the precession rate of the planet. As a matter of fact, in first approximation, the precession rate is given by (Folkner et al., 1997b):

$$\dot{\psi}_0 = -\frac{3}{2}\frac{n'^2}{\Omega\left(1-e'^2\right)^{3/2}}J_2\frac{MR_a^2}{C}cos\epsilon \tag{2.57}$$

Here n' is the Mars mean orbital motion, Ω is the spin rate of Mars, R_a is the mean volumetric radius and e' the orbital eccentricity. This secular rate is the one caused by the solar torque. In the formulation of the secular precession adopted by Konopliv et al. (2011), two additional terms are present: the geodetic precession (Reasenberg and King, 1979), which follows from general relativity and has a value of $\dot{\psi}_g = 6.7$ mas/year, and $\dot{\psi}_p$, which is due to the torque from the other planets (mainly Jupiter), and has a value of -0.2 mas/year. RISE is expected to estimate the precession rate with an accuracy of 2 mas/year, thus bringing a slight improvement to the current uncertainty of 2.1 mas/year which should not improve considerably the information on the interior (Folkner et al., 2018).

The characteristics of the interior of Mars may also affect the nutations and polar motion of the planet, apart from the effect produced by a different polar moment of inertia like for the precession rate. The nutations of a non-rigid planet may present higher amplitudes compared to those of same frequency for a rigid planet. For this reason, it is customary to separate the problem of the determination of the rigid-body nutations, which is purely in the domain of celestial mechanics, from the geophysical problem of the determination of the amplification of these nutations due to the non-rigidity of the planet (Van Hoolst, 2015).

Normal modes of Mars

The conservation of angular momentum states that in an inertial reference frame:

$$\frac{d\boldsymbol{H}}{dt} = \boldsymbol{\Gamma} \tag{2.58}$$

Where $\boldsymbol{H}$ is the angular momentum of the whole planet, and $\boldsymbol{\Gamma}$ is the external torque acting on the body. This equation is independent of the interior structure of the planet. For a rigid planet, the external torque due to the other bodies can be expressed as a function of the positions of these perturbing bodies relative to the planet, and the resulting equations for the nutations in longitude and obliquity can be solved analytically or numerically. Thus, rigid nutations of Mars are known with high accuracy. Roosbeek (1999) computed analytically the rigid nutations of Mars with a truncation level of 0.1 mas. The main nutations of Mars are due to the torque generated by the Sun, hence their frequencies are multiples of the orbital frequency. The contributions from Phobos and Deimos have longer periods (2.26 and 54.75 Earth years, respectively) and much smaller amplitudes due to their size. As a comparison, the long-period (18.6 years) Earth nutation due to the Moon has an amplitude much larger than those due to the Sun (Roosbeek, 1999).

From Eq. 2.58 it is possible to see that even without any external forcing ($\boldsymbol{\Gamma} = 0$) there may be polar motion, that is, a relative motion of the rotation axis with respect to the figure axis (the axis of maximum angular momentum). In the rotating body-fixed frame, the conservation of angular momentum in the absence of external forcing can be expressed as:

$$\frac{d\boldsymbol{H}}{dt} + \boldsymbol{\Omega} \times \boldsymbol{H} = 0 \tag{2.59}$$

Given that the axes of the chosen body-fixed frame are principal axes, the angular momentum of the rigid Mars can be written as $\boldsymbol{H} = \left(A\Omega_x, B\Omega_y, C\Omega_z\right)$, hence the Euler equations are obtained:

$$\begin{aligned} A\dot{\Omega}_x + (C-B)\Omega_y\Omega_z &= 0 \\ B\dot{\Omega}_y + (A-C)\Omega_z\Omega_x &= 0 \\ C\dot{\Omega}_z + (B-A)\Omega_x\Omega_y &= 0 \end{aligned} \tag{2.60}$$

Assuming the body to be an axially symmetric ellipsoidal, so that $B = A$, if the rotation axis is close to the z-axis the angular velocity can be written as $\boldsymbol{\Omega} = \Omega_0\left(m_x, m_y, m_z\right)$. Here Ω_0 is the mean spin rate, m_x and m_y are the wobble variables, and m_z is the spin rate variation. Assuming $B - A = 0$, the component of the rotation vector along the polar axis remains constant. The first two equations in 2.60 become (Dehant and Mathews, 2015a):

$$\begin{aligned} A\Omega_0\frac{dm_x}{dt} + \Omega_0^2\left(C-A\right)m_y &= 0 \\ B\Omega_0\frac{dm_x}{dt} + \Omega_0^2\left(A-C\right)m_y &= 0 \end{aligned} \tag{2.61}$$

The complex combination of these two equations yields a single equation in the complex variable $\tilde{m} = m_x + im_y$:

$$\frac{d\tilde{m}}{dt} = ie\Omega_0\tilde{m} \tag{2.62}$$

where e is the dynamical ellipticity, with $e = \frac{C-A}{A}$. The solution is:

$$\tilde{m}(t) = \tilde{m}(0)e^{ie\Omega_0 t} \tag{2.63}$$

which is a wobble of amplitude $\tilde{m}(0)$, corresponding to the initial displacement of the rotation axis with respect to the figure axis, and frequency $e\Omega_0$, or e cycles per (Mars) solar day (cpsd, since the value of Ω_0 is by definition 1 cpsd). This free wobble (*free* because it takes place without any external forcing) is known as Eulerian wobble, and is the only normal mode of the rigid Mars. For a non-rigid planet, the normal modes may be more than one.

Sasao et al. (1980) studied the effect of a stratified fluid core on the nutations of the Earth, although the same results can be applied to models of Mars involving a mantle and a fluid outer core (FOC). In such models, the rotation axis is taken to be that of the most external solid layer, which in this case is the mantle. The main assumptions in this derivation are the axial symmetry of the body, and the hydrostatic equilibrium at the basic state, which corresponds to a state in which the mantle rotates around its maximum angular momentum axis. Hence:

$$\boldsymbol{\nabla} P_V = \rho_V \boldsymbol{\nabla}\zeta \tag{2.64}$$

where P_V is the pressure, ρ_V the density, and ζ the gravitational and centrifugal potential. They hypotesis of hydrostatic equilibrium implies that the core-mantle boundary (CMB) is non-spherical, with the ellipticity varying as a function of radius as expressed by the Clairaut's equation (Le Maistre et al., 2012). The conservation of angular momentum is written for both the whole planet and the core:

$$\begin{aligned} \frac{d\boldsymbol{H}}{dt} + \boldsymbol{\Omega}\times\boldsymbol{H} &= \boldsymbol{\Gamma} \\ \frac{d\boldsymbol{H_f}}{dt} - \boldsymbol{\omega_f}\times\boldsymbol{H_f} &= \boldsymbol{\Gamma_b} \end{aligned} \tag{2.65}$$

In the equation relative to the sole fluid core, $\boldsymbol{\omega_f}$ is the difference between the angular velocity of the core $\left(\boldsymbol{\Omega_f} = \Omega_0\left(m_{f_x}, m_{f_y}, m_{f_z}\right)\right)$ and that of the mantle ($\boldsymbol{\Omega}$), so that $\boldsymbol{\omega_f} = \boldsymbol{\Omega_f} - \boldsymbol{\Omega}$. The principal moments of inertia of the core are $A_f = B_f$ and C_f. The equatorial moments of inertia of the mantle are $A_m = B_m$, with $A_m = A - A_f$. The forcing $\boldsymbol{\Gamma_b}$ is that due to interactions at the CMB, and is null for the equation relative to the whole planet, since the equal contributions from the core and from the mantle have opposite signs. This coupling torques may come from electromagnetic interactions between the two layers, or from other boundary effects. A detailed explanation of the solution of these equations

can be found in Dehant and Mathews (2015a). When the $\boldsymbol{\Gamma_b}$ term is neglected, the solutions of the two equations in the frequency domain (hence as a function of the frequency, σ), are (Dehant and Mathews, 2015b):

$$\begin{aligned}[\sigma - e + (\sigma+1)\kappa]\tilde{m}(\sigma) + (\sigma+1)\left(A_f/A + \xi\right)\tilde{m}_f(\sigma) &= -\left[e - (\sigma+1)\,k\right]\tilde{\zeta}(\sigma) \\ \sigma(1+\gamma)\tilde{m}(\sigma) + (\sigma + 1 + \beta\sigma + e_f)\tilde{m}_f(\sigma) &= \sigma\gamma\tilde{\zeta}(\sigma)\end{aligned} \tag{2.66}$$

The factors κ, ξ, γ, and β are the compliances, expressing the deformability of the whole planet and of the core under different wobbles. In particular, the value of β is expected to be between 0.00015 and 0.00045 (Folkner et al., 2018). The term e_f is the dynamical ellipticity (or flattening) of the core, equal to $(C_f - A_f)/A_f$. The unknowns are the wobble amplitudes at the frequency σ for the mantle ($\tilde{m}(\sigma)$) and for the core ($\tilde{m}_f(\sigma)$).

The normal modes can be obtained from the eigenvalues of the associated homogeneous system of equations, namely the one resulting from imposing $\tilde{\zeta} = 0$. To the first order in the ellipticities and the compliance parameters, the eigenfrequencies are, in cpsd, (Dehant and Mathews, 2015b):

$$\sigma_1 = \sigma_{CW} = \frac{A}{A_m}(e - \kappa) \tag{2.67}$$

$$\sigma_2 = \sigma_{NDFW} = -\left(1 + \frac{A}{A_m}(e_f - \beta)\right) \tag{2.68}$$

The first frequency is that of the Chandler Wobble (CW). This normal mode is the equivalent of the Eulerian wobble of a rigid planet, which is equal to e. It is a long-period motion in the body-fixed frame. The second frequency is the nearly diurnal free wobble (NDFW), so called because it has a frequency close to 1 in the body-fixed frame.

A motion of the rotation axis in the inertial space causes the figure axis to move in inertial space as well, and the displacements for the two axes are not the same Van Hoolst (2015). Therefore, periodical motions in the body-fixed frame (wobbles) are related to periodical motions in the inertial frame (nutations) by the kinematic equations, that imply Van Hoolst (2015):

$$\tilde{\eta}(\sigma_n) = -\frac{1}{\sigma_n}\tilde{m}(\sigma_w) \quad \text{and} \quad \sigma_w = \sigma_n - 1, \tag{2.69}$$

with $\tilde{\eta}(\sigma_n)$ and σ_n the amplitude and frequency of the nutation, and $\tilde{m}(\sigma_w)$ and σ_w the amplitude and frequency of the corresponding wobble.

The nutation in the inertial frame relative to the nearly diurnal free wobble is known as free core nutation (FCN). This normal mode is present only for planets with a (partially) fluid core. The frequency of the FCN can be found from that of the NDFW by adding 1 cpsd, hence:

$$\sigma_{FCN} = -\frac{A}{A_m}(e_f - \beta) \tag{2.70}$$

The FCN is a long-period retrograde motion in the inertial frame. It is important due to its vicinity in frequency to the major long-term nutations, which may then be amplified by the resonance with this normal mode.

For interior models which include a solid inner core (SIC), two other normal modes are expected: the inner core wobble (ICW), describing a relative rotation between the figure axis of the SIC and the rotation axis of the mantle, and the free inner core nutation (FICN), emerging from the relative rotation of the inner core and the mantle. For a small inner core, the FICN induces amplifications on the nutations which are below the predicted accuracy of the radio science experiments considered here, which is in the order of few mas (Le Maistre et al., 2012). This is true unless the period of the FICN is very close to the annual prograde nutation, in which case the signature of the inner core on the amplitude of that nutation would be detectable (Defraigne et al., 2003). This condition is verified for a narrow interval of compositions and values of the inner core radius. For a large inner core, the amplification of the nutations due to the FICN is detectable with the expected precision. However, in that case the resonance of the semiannual prograde nutation with the FCN is almost cancelled by the resonance with the FCN (Defraigne et al., 2003). Therefore, the presence of a large solid inner core could be evinced from the FCN resonance of the nutations (thus without considering the FICN), if the amplification measured for the semiannual prograde nutation is negligible. For these reasons, along

with the fact that recent interior models tend to exclude the presence of a SIC, the ICW and FICN normal modes will not be considered in the following derivations.

The solution of Equations 2.66 for the wobble of the mantle is (Dehant and Mathews, 2015b):

$$\tilde{m}(\sigma) = \frac{(\sigma+1)\left[eA + \gamma\sigma A_f - (1+\sigma)\kappa A\right]}{A_m(\sigma-\sigma_1)(\sigma-\sigma_2)}\tilde{\zeta}(\sigma) \tag{2.71}$$

It can be seen that there are resonances close to the eigenfrequencies, as expected.

The ratio between the non-rigid wobble (or nutation) and its rigid counterpart (i.e., with the same frequency and relative to the same external forcing) is the transfer function (Dehant and Mathews, 2015b):

$$T_w(\sigma_w) = \frac{\tilde{m}(\sigma_w)}{\tilde{m}_R(\sigma_w)} \tag{2.72}$$

Here σ_w is the frequency of the wobble, and $\tilde{m}_R(\sigma_w)$ is the wobble for a rigid planet. Moreover, $T_w(\sigma_w) = T_n(\sigma_n)$, where $T_n(\sigma_n)$ is the transfer function of the nutation of frequency σ_n associated to the wobble of frequency σ_w. This ratio can be simplified through partial fraction decomposition, so that (Dehant and Mathews, 2015b):

$$T_w(\sigma_w) = R_0 + R_0'(1+\sigma_w) + \frac{R_1}{\sigma_w - \sigma_1} + \frac{R_2}{\sigma_w - \sigma_2} \tag{2.73}$$

The coefficients R_i, with $i = 1, 2$, are found by multiplying $T_w(\sigma_w)$ times $\sigma_w - \sigma_i$, and then evaluating this expression for $\sigma_w = \sigma_i$. The other two coefficients can be found from the fact that $T_w(-1) = -1$ (property known as gyrostatic rigidity, for which the planet behaves as a rigid body when $\sigma_w = 1$) and that $T_w(e) = 0$. The same expression of the transfer function is valid for the nutations, after substituting σ_w with $\sigma_n - 1$, since $T_w(\sigma_w) = T_n(\sigma_n)$.

Amplification of the principal nutations

If only the principal nutations are considered (that is, those for which $\sigma << 1$), the expression for the transfer function of a planet with an elastic mantle and a fluid core is found in Le Maistre et al. (2012) as:

$$T_n(\sigma_n) = 1 + F\frac{\sigma_n}{\sigma_n - \sigma_{FCN}}, \tag{2.74}$$

with F the core momentum factor, equal to:

$$F = \frac{A_f}{A - A_f}\left(1 - \frac{\gamma}{e}\right) \tag{2.75}$$

This formulation is justified by the fact that principal nutation will not show resonance with the Chandler wobble eigenmode: the nutation corresponding to the Chandler wobble, which is a long-period wobble in the body-fixed frame, is a short-period motion in the inertial frame ($\sigma_{CW} + 1 \approx 1$), thus outside the range of frequencies of the principal nutations. Sometimes, the transfer function is expressed as an amplification factor, equal to the transfer function minus 1 (Le Maistre et al., 2012). The amplification factor represents the contribution of the fluid core to the nutation amplitude.

The amplitudes of the trigonometric series in the expressions of the nutations in obliquity and longitude given by Eqs. 2.18 and 2.17 are amplified by the free-core nutation according to (Le Maistre, 2013)

$$\epsilon_m^{c\prime} = \epsilon_m^c\left(1 + F\frac{\sigma_m^2}{\sigma_m^2 - \sigma_{FCN}^2}\right) + \sin\epsilon_0\psi_m^s F\frac{\sigma_m\sigma_{FCN}}{\sigma_m^2 - \sigma_{FCN}^2} \tag{2.76}$$

$$\epsilon_m^{s\prime} = \epsilon_m^s\left(1 + F\frac{\sigma_m^2}{\sigma_m^2 - \sigma_{FCN}^2}\right) - \sin\epsilon_0\psi_m^c F\frac{\sigma_m\sigma_{FCN}}{\sigma_m^2 - \sigma_{FCN}^2} \tag{2.77}$$

$$\psi_m^{c\prime} = \psi_m^c\left(1 + F\frac{\sigma_m^2}{\sigma_m^2 - \sigma_{FCN}^2}\right) - \frac{\epsilon_m^s}{\sin\epsilon_0}F\frac{\sigma_m\sigma_{FCN}}{\sigma_m^2 - \sigma_{FCN}^2} \tag{2.78}$$

$$\psi_m^{s\prime} = \psi_m^s\left(1 + F\frac{\sigma_m^2}{\sigma_m^2 - \sigma_{FCN}^2}\right) + \frac{\epsilon_m^s}{\sin\epsilon_0}F\frac{\sigma_m\sigma_{FCN}}{\sigma_m^2 - \sigma_{FCN}^2} \tag{2.79}$$

$$\tag{2.80}$$

Similar expressions are given for the amplifications of the nutations parameters of the Pathfinder model in the presence of the FCN (Konopliv et al., 2006):

$$\epsilon'_m = \epsilon_m \left(1 + F\frac{\sigma_m^2}{\sigma_m^2 - \sigma_{FCN}^2}\right) + \sin\epsilon_0 \psi_m F \frac{\sigma_m \sigma_{FCN}}{\sigma_m^2 - \sigma_{FCN}^2} \tag{2.81}$$

$$\psi'_m = \psi_m \left(1 + F\frac{\sigma_m^2}{\sigma_m^2 - \sigma_{FCN}^2}\right) + \frac{\epsilon_m}{\sin\epsilon_0} F \frac{\sigma_m \sigma_{FCN}}{\sigma_m^2 - \sigma_{FCN}^2} \tag{2.82}$$

The values of ψ_m and ϵ_m, the nutation amplitudes for a rigid Mars, are those shown in Table 2.2, corrected for the value of the polar moment of inertia. In the two models by Kuchynka et al. (2014) and Konopliv et al. (2016), the factor F and the FCN period were set to 0.07 and -240 days, respectively, to get the non-rigid Mars nutation. However, the nutation amplitudes, and thus the values of F and σ_{FCN} have never been measured (Folkner et al., 2018).

From the expressions of the core momentum factor (Eq. 2.75), it can be seen that F increases with increasing core size, because the moment of inertia of the core (A_f) increases, and the term $A - A_f$ decreases (Folkner et al., 2018). Similarly, for a larger core radius the frequency of the FCN increases in magnitude (that is, becomes more negative), since the dynamical ellipticity of the core increases and A_m decreases. Therefore, the period of the FCN decreases in magnitude (that is, becomes less negative) for increasing radius of the CMB. A similar conclusion was obtained by Van Hoolst et al. (2000b). There, several interior models were considered, generated by interpolating between the two models from Sohl and Spohn (1997) for different core radii. The conclusion was that the FCN period ($P_{FCN} = 2\pi/\sigma_{FCN}$) is sensitive to both the core radius and the density jump at the CMB, decreasing (in absolute value) from 287 to 230 days for a core radius increasing from 1268 to 1768 km.

The FCN period predicted by most interior models lies between the semiannual (-343.5 days) and the terannual (-229 days) periods (Folkner et al., 2018). In particular, recent estimates of the k_2 parameter are consistent with an FCN period of about -230 days (Le Maistre et al., 2012), which would lead to large amplifications of the terannual nutation terms due to resonance. This resonance effect is clearly visible in Figure 2.2a, taken from Le Maistre et al. (2012), which represents the difference between the amplitudes of the rigid and non-rigid nutations as a function of the FCN period, for the first four terms of the series of prograde and retrograde nutations. This difference is equal to $\tilde{\eta}(\sigma_n) - \tilde{\eta}_R(\sigma_n) = [T_n(\sigma_n) - 1]\,\tilde{\eta}_R(\sigma_n)$, where $\tilde{\eta}_R(\sigma_n)$ is the amplitude of the rigid nutation of frequency σ_n. Figures 2.2b and 2.2c plot the same quantity for the nutations in obliquity and longitude, respectively. The large width of the curves is due to the uncertainties on the compliances β and γ, which have a significant influence. For example, setting β and γ to 0 changes the FCN period by 10 days (Le Maistre et al., 2012). It can be seen that the semiannual sine amplitude of the nutations in longitude presents a large amplification from the FCN, whichever its period. The same can be said of the prograde semiannual nutation, which has an amplification larger than 10 mas for all the FCN periods considered. The non-rigid nutations can be determined either by estimating σ_{FCN} and F, or by solving for the amplitudes of the trigonometric expressions in Section 2.2. The first method relies on non-linear equations in σ_{FCN}. As shown by Le Maistre et al. (2012), since the estimation methods are usually linear (see Section 3.2), solving for σ_{FCN} and F when the FCN period is close to the resonance leads to biased values for these parameters. The moment of inertia and the dynamical ellipticity of the core (A_f and e_f) can be computed from the FCN period and the core momentum factor, if assumptions are made on the compliances γ and β. However, close to the resonance, these quantities will be themselves biased, due to the incorrect values of σ_{FCN} and F. This is not the case if the nutation amplitudes are estimated directly, since only linear equations in the amplitudes are involved in that estimation. Therefore, for an FCN period close to -229 days, it is preferable to determine the liquid-core amplification by estimating directly the nutations amplitudes. Sufficiently far from the resonance (e.g. already for a period of -240 days), the method involving the solution of σ_{FCN} and F is favoured, because it requires the determination of fewer parameters (Le Maistre et al., 2012).

Figure 2.3, taken from (Folkner et al., 2018), shows the the variation of the CMB radius as a function of σ_{FCN} and F, and of A_f/A as a function of F, all for different mantle mineralogy models and two mantle temperature profile end-members, a cold and a hot one. The FCN period shows larger variations in CMB radius for different mineralogy models than the factor F, because of its proportionality to e_f, which varies considerably for different core and mantle compositions (Folkner et al., 2018). The blue-shaded areas represent the solutions expected for F and for the FCN period after one Martian year of

RISE measurements. The uncertainty on the FCN period depends on its value and the vicinity to the resonance periods, but for a period of -240 days it is estimated to be around 5 days. This corresponds to an uncertainty on the core radius of 100 km, taking into account all the models and the two extreme temperature profiles and in the assumption of hydrostatic equilibrium for the core shape. The expected uncertainty on F is 0.013 for a core momentum factor of 0.07, leading to an uncertainty of 150 km on the core radius estimate, which is less sensitive to assumptions on e_f (Folkner et al., 2018). Similar results are expected from LaRa, which should lead to uncertainties on the FCN period in the non-resonant case of 5 days after 600 days of tracking, and reaching up to 1 day in the resonant case (Le Maistre et al., 2012).

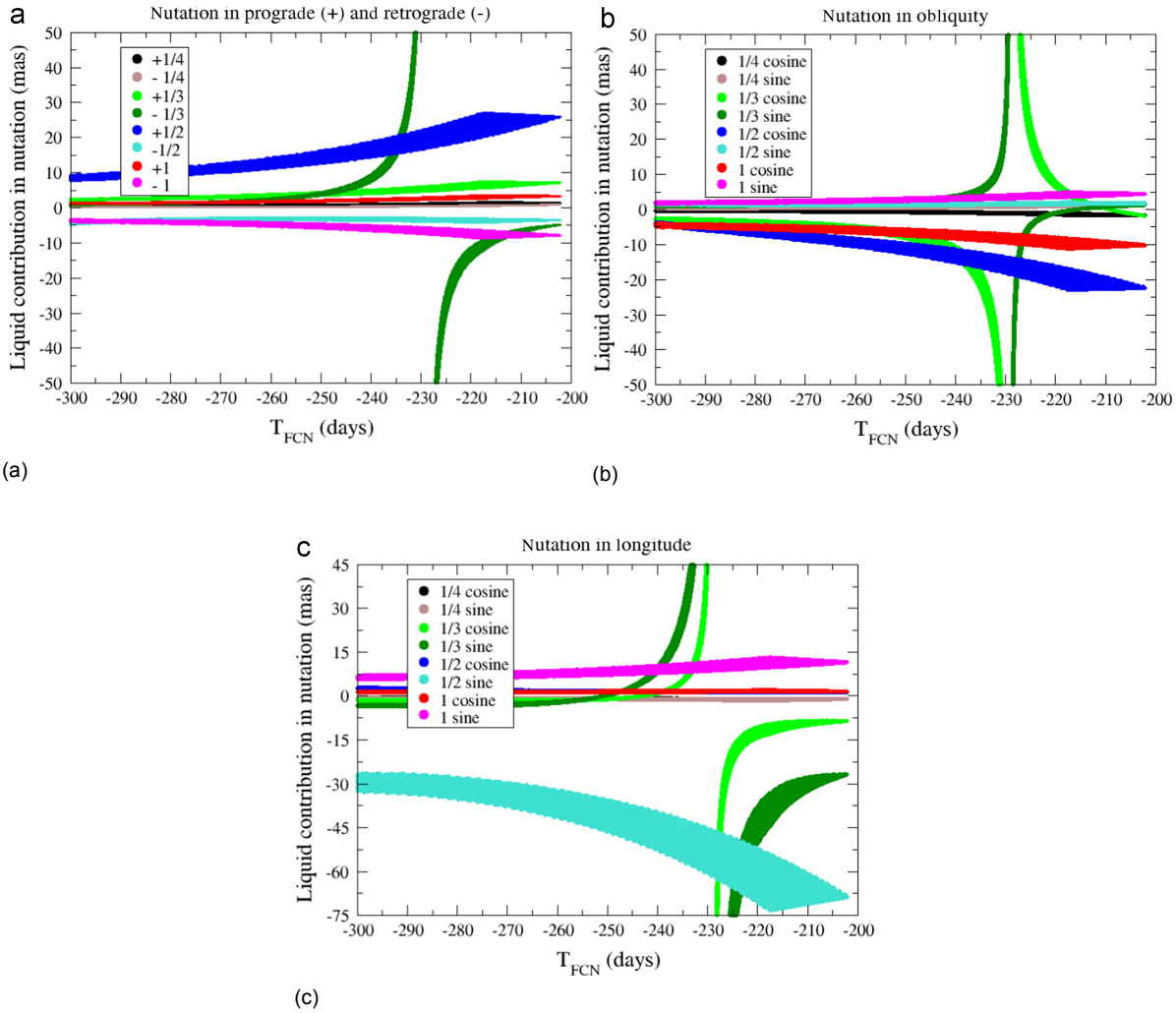

Figure 2.2: Influence of the FCN period, in terms of the difference with the corresponding rigid-body value, for prograde and retrograde nutations (a), nutations in obliquity (b), and nutations in longitude (c). The period P_{FCN} is in these plots indicated as T_{FCN}. Taken from Le Maistre et al. (2012)

Effect on polar motion

The polar motion is mainly caused by surface mass redistribution, in particular by the condensation and sublimation of CO_2 between the polar caps and the atmosphere (Dehant et al., 2003). This is a seasonal process, with predominantly annual and semiannual frequencies, and involves a third of the total atmospheric mass (Dehant et al., 2006). These seasonal effects are treated more in detail in Section 2.3.3. Apart from these harmonic forcings, the polar motion excitation may also come from stochastic forcing by the atmosphere and from marsquakes. The latter are expected to have a low energy, so that the polar motion excited by marsquakes is expected to be below the measurement noise (Dehant et al., 2006). If excited, the free wobble is subject to dissipation by friction. The rate

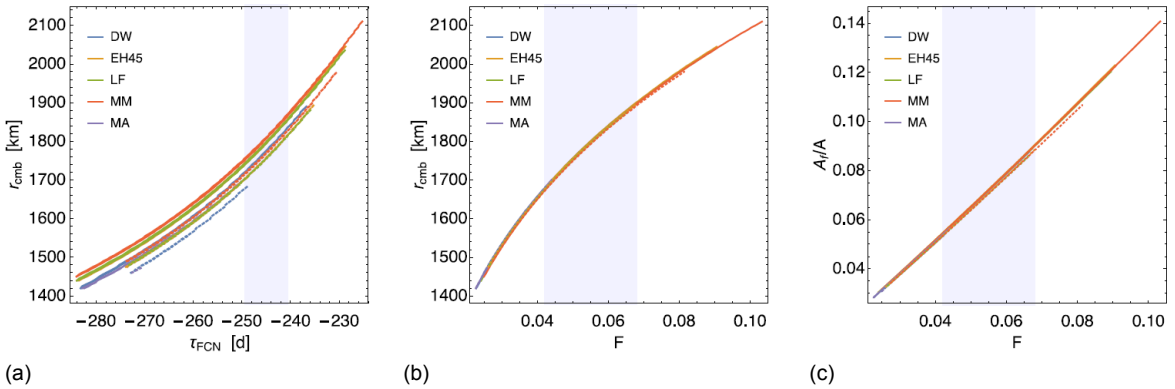

Figure 2.3: Variation of the core radius with the FCN period (a), here indicated as τ_{FCN}, and F (b), and variation of the ratio A_f/A as a function of F (c). The curves of different color represent different mantle mineralogy models, while solid curves and dashed curves indicate a hot and a cold model for the temperature profile of the mantle, respectively. The blue-shaded regions are the values and uncertainties expected after a year of InSight measurements. Taken from Folkner et al. (2018).

of dissipation of the mode is expressed through the quality factor, Q_W. With a value of the wobble quality factor equal to that measured from tidal effects on Phobos orbit, Yoder and Standish (1997) found that the wobble decay time would be around 60 years. However, the tidal forcing on Phobos has a period of 5.6 hours, considerably smaller than that the Chandler wobble, which for a rigid Mars would be (Van Hoolst et al., 2000b; Konopliv et al., 2006):

$$P_{CW} = \frac{2\pi}{\Omega}\sqrt{\frac{AB}{(C-A)(C-B)}} = 190.8 \pm 0.3 \text{ days} \tag{2.83}$$

Consequently, the quality factors at the two frequencies may have substantially different values.

The actual CW period of Mars was estimated to be between 190 and 210 days (Van Hoolst, 2015). Applying the same method used for the FCN period, Van Hoolst et al. (2000b) concluded that the Chandler wobble period is weakly sensitive to the radius and the density of the core, decreasing from 219 to 213 days for a core radius increasing from 1268 to 1768 km. Mantle inelasticity, as indicated by a low value of Q, leads to a period up to 7 days larger (Van Hoolst et al., 2000b). Moreover, the CW period is sensitive to the seismic velocities of the mantle, increasing of 0.5 days and 5 days for changes in V_P and V_S of 10% and 21%, respectively (Van Hoolst et al., 2000a). Thus, the accuracy on the measured CW period should be lower than 1 day in order to be able to infer interior properties from it (Van Hoolst, 2015).

The amplitude of the CW was estimated by Yoder and Standish (1997) to be around 10 mas from Viking pressure measurements, although values as large as 50 mas were deemed possible. As shown in Table 2.3, Konopliv et al. (2006) estimated a CW amplitude of 5 mas, assuming a period of 205 days and models of the ice caps shape. The result was obtained from the time-variable tesseral degree 2 coefficients of the gravity field solution, although the difficulty in the separation of this signal from the 1/3-year wobble makes this solution not reliable.

2.3.3. Seasonal effects

The study of the effect of the seasonal changes involving the atmosphere and the ice caps on the polar motion and the rotation rate of Mars generally starts from the assumption of no external torque. Hence, the variations in the angular momentum of the atmosphere are balanced by the variations of the angular momentum of the solid planet (Defraigne et al., 2000). Similarly to what was shown for the normal modes of the planet, the total angular momentum is expressed as the product of a variable tensor of inertia and the global angular velocity ($\boldsymbol{\Omega}$), plus the angular momentum associated with the relative motion between the atmosphere and the solid Mars. Substituted in the conservation of the total angular momentum, this expression leads to the Liouville equations. The solution of these equations for the polar motion, $\tilde{m} = m_x + im_y$, is (Defraigne et al., 2000):

$$\tilde{m} = \left[-\frac{eA(\sigma+1)\tilde{\chi}^{load}}{A_m(\sigma-\sigma_{CW})}\left(1+k_2'\right) - \frac{eA(\sigma+1)\tilde{\chi}^{wind}}{A_m(\sigma-\sigma_{CW})}\right]\left(1+\frac{A_f}{A}\frac{\sigma_{FCN}}{(\sigma+1)-\sigma_{FCN}}\right) \tag{2.84}$$

Here, the forcing was separated into a matter and a wind component, namely $\tilde{\chi}^{load}$ and $\tilde{\chi}^{wind}$. The matter term is due to the variations in the inertia tensor, while the wind term corresponds to the variation in the relative angular momentum. The matter term also includes the mass redistribution within the planet caused by the surface mass redistribution, which is accounted for by the second degree Love load number, k_2'. The forcings $\tilde{\chi}^{load}$ and $\tilde{\chi}^{wind}$ are the complex sum of the first two components of the atmospheric angular momentum excitation functions $\boldsymbol{\chi}^{load}$ and $\boldsymbol{\chi}^{wind}$, for which expressions are given in Defraigne et al. (2000). The third component of the excitation function is responsible for the length of day variations, according to (Acker et al., 2002):

$$\frac{\Delta LOD}{LOD} = -\frac{C}{C_m}\left[\left(1+k_2'\right)\chi_z^{load} + \chi_z^{wind}\right] \tag{2.85}$$

The various terms of the angular momentum excitation functions can be computed given a global circulation model (GCM) of the atmosphere of Mars, which gives the effect of the change in both the atmosphere and the surface ice (Konopliv et al., 2011). Examples of such models are the NASA/Ames (Haberle et al., 1999) and the LMD (Laboratoire de Météorologie Dynamique, Forget et al., 1999). Sanchez et al. (2003) computed the LOD variations using the Ames GCM, although with a different approach than the one presented here, relying on a torque model. The torque approach leads to LOD variations almost twice as large as those obtained from the total angular momentum approach, mainly due to a larger annual harmonic in the case of the torque method. Of the two methodologies, the total angular momentum approach is considered more reliable for the measurements of LOD variations (Sanchez et al., 2003). The results from Sanchez et al. (2003), when using the angular momentum approach, are similar to those obtained by Acker et al. (2002) with the LMD GCM, the differences being mostly due to the two distinct atmospheric models. The ΔLOD amplitudes found by Sanchez et al. (2003) do not take into account the internal properties of Mars, meaning that the load factor and the amplification from the FCN are neglected. However, Karatekin et al. (2006) showed that the effects of the liquid core on the LOD variations are small. In particular, an accuracy on ΔLOD better than 2% would be needed to be able to distinguish a planet with a solid core from one with a liquid core.

The wind component accounts for around 30% of the total LOD variations. These contributions are given by (Konopliv et al., 2011), using a total angular momentum approach and the two different GCM models, as:

$$\Delta LOD^{wind}_{Ames} = 0.0565\sin l' + 0.1093\cos l' - 0.1265\sin 2l' - 0.0732\cos 2l', \tag{2.86}$$

$$\Delta LOD^{wind}_{LMD} = 0.0277\sin l' + 0.0762\cos l' - 0.0784\sin 2l' - 0.0772\cos 2l', \tag{2.87}$$

where the amplitudes are in ms, and l' is the mean anomaly of Mars. According to Le Maistre et al. (2012), a precision of less than 0.05 ms on the total ΔLOD is necessary to select, between the two GCMs, the one in better agreement with the measurements. However, the precision of the available rotation models, found from that of $\Delta\phi$ using Eq. 2.35, did not allow to easily distinguish between the two models, although being right below this threshold. The current uncertainties on $\Delta\phi$ (Table 2.1) are up to 50% smaller than those from the rotation model by (Konopliv et al., 2011), considered by (Le Maistre et al., 2012), hence they may provide a better constraint for the GCMs. Future atmospheric measurements, such as those from InSight (Spiga et al., 2018), will lead to more precise GCMs, and tracking from landers like InSight and LaRa will allow to reach an accuracy on ΔLOD 50% smaller than the current one (Folkner et al., 2018), and good enough to distinguish between the two current atmospheric models (Le Maistre et al., 2012).

The matter contribution to the LOD variations is proportional to the variation of the second degree zonal coefficient of the gravity field (Chao and Rubincam, 1990):

$$\Delta LOD^{load} = \dot{\phi}\frac{2}{3}\frac{MR_e^2}{C}\Delta J_2 \tag{2.88}$$

Hence, the wind contribution can be found by subtracting this term to the total estimated ΔLOD. However, the result is limited by the uncertainties on the normalized polar moment of inertia and on ΔJ_2, which is the variation of the degree 2 zonal harmonic coefficient.

The seasonal variations of the gravity field of Mars due to the CO_2 cycle consist mainly of variations in the zonal coefficients. In particular, the odd degree coefficients have variation amplitudes about 20%

larger than those of even degrees. The temporal variation of the Stokes coefficients is related to the temporal variation of the density distribution of the planet by (Smith et al., 2009):

$$\overline{C}_{nm} + i\overline{S}_{nm} = \frac{1}{(2n+1)\,MR_e^n} \int_{\mathcal{V}} \rho_{\mathcal{V}}(r, \phi_{lat}, \lambda, t) r^n Y_{nm}(\phi_{lat}, \lambda) d\mathcal{V}, \tag{2.89}$$

where $Y_{nm}(\phi_{lat}, \lambda) = P_{nm} \sin(\phi_{lat}) (\cos(m\lambda) + i \sin(m\lambda))$, and $\mathcal{V}$ is the volume.

Studies of the seasonal variations of these coefficients were performed by Smith et al. (2001), who tracked the topography evolution related to the mass exchange at the ice caps using data from the MOLA instrument, and estimated the variation of Mars flattening from MGS tracking data. MGS data was also employed by Yoder et al. (2003) to estimate the seasonal variation of the low-degree gravity field coefficients from their effect on the eccentricity and argument of pericenter of the spacecraft orbit (for the odd zonal harmonics) and on the right ascension of the ascending node (for the even zonal harmonics). Tracking data from a single spacecraft allows to distinguish between the signature of the odd and the even harmonics, but it is generally not possible to separate the effects of the different even or odd degrees (Karatekin et al., 2005). Thus, the observed time-variable coefficients are generally lumped coefficients, being the sum of zonal coefficients from different degrees, each multiplied by a weighting factor (Yoder et al., 2003).

The largest seasonal variations, as computed from GCM models, affect the C_{10} coefficient, leading to displacements of the CoM of Mars of up to 27.5 mm in the z-direction (Sanchez et al., 2006). However, these terms are generally not detected from spacecraft tracking data, because they are hard to separate from the errors on the ephemerides of the central body.

By performing simulations with MGS tracking data, Karatekin et al. (2005) concluded that of neglecting the zonal coefficients C_{40} and C_{50} results in a 50% error in the estimated annual amplitudes of C_{20} and C_{30}. Thus, high-degree zonal coefficients have to be considered in the determination of the seasonal gravity field variations. In addition, they computed the variations of the zonal coefficients from the Ames GCM, the LMD GCM, and the measurements of the thickness of the polar deposits by the High Energy Neutron Detector (HEND) on Mars Odyssey. The results from these three models differed by about 30% in the amplitude of the coefficients. Compared to the previous estimations by Smith et al. (2001) and Yoder et al. (2003), the coefficients estimated from MGS tracking data showed differences of up to 40% for CO_2, hence it was not possible to discriminate between the two GCMs and HEND data from the MGS tracking solutions. Thus, they simulated data from an additional spacecraft at an inclination of $50°$, showing that this resulted in lower uncertainties on the estimated coefficients and a better separability of the even zonal coefficients.

More recent estimates of the time-varying gravity field of Mars were obtained by Smith et al. (2009), from a larger MGS Doppler and range dataset, and by (Konopliv et al., 2011), using also Odyssey and MRO data. The latter results showed good agreement with those from the Ames and LMD GCMs. Konopliv et al. (2016) estimated the time-varying odd zonal lumped coefficient, but fixed the variation of the even zonal lumped coefficient to that given by the Ames GCM. Genova et al. (2016) used the same dataset but estimated also the even zonal degrees, with a monthly-batch mission by mission analysis. This method allowed to limit the instability on the C_{20} solution, largely caused by MGS and MRO data. The time-variable gravity coefficients were retrieved over 11 years, and since the contribution of the atmosphere to their variations was modelled before the estimation using the Mars-GRAM2010 atmospheric model (Justh, 2011), these variations were only caused by the change of the polar caps masses. The polar caps, assumed to be point masses in their geometric centre, were then found from the estimated zonal coefficients with the simple formulas:

$$M_{NP} = \frac{C_{20} + C_{30}}{2} M, \tag{2.90}$$

$$M_{SP} = \frac{C_{20} - C_{30}}{2} M, \tag{2.91}$$

where M_{NP} is the mass of the north polar cap, M_{SP} the mass of the south polar cap, and M the mass of Mars. The negative of the variation of the total ice caps mass showed good agreement (correlation of about 0.85) with the variation of the atmospheric mass as computed from the Mars-GRAM2010 pressure fields. This was expected, since the increase in atmospheric mass is due to the sublimation of the ice caps mass, and vice versa.

3

Orbit determination and covariance analysis

This chapter deals with radio-tracking measurements and how physical parameters can be retrieved from them. Therefore, a description of the radio-tracking observables which will be considered in this project is given in Section 3.1. Then, Section 3.2 presents the linear regression method employed for the parameter estimation in Chapter 6, namely a weighted least squares filter with a priori information. Furthermore, Section 3.3 discusses the consider covariance analysis, a powerful technique allowing to get more realistic estimates of the actual uncertainties of the parameters obtainable from a least squares estimation with real data.

3.1. Radio-tracking observables

This section deals with the different tracking data types that will be considered throughout the thesis project, namely ranging (Section 3.1.1 and Doppler (Section 3.1.2), giving formulations for the corresponding observables. In the literature study phase, other kinds of radio-tracking observables, such as Very-long-baseline interferometry (VLBI) or Same beam interferometry (SBI) were deemed not precise enough to provide a considerable contribution to the accuracy of the final MOP solution.

3.1.1. Range observables

The range is a measure of the distance between the tracked object and the tracking station. The geometric range is the instantaneous distance between the ground station (with position vector $\boldsymbol{r}_{GS}$) and the spacecraft (at $\boldsymbol{r}_S$), namely (Tapley et al., 2004):

$$\rho = \sqrt{(\boldsymbol{r}_{GS} - \boldsymbol{r}_S)(\boldsymbol{r}_{GS} - \boldsymbol{r}_S)} \tag{3.1}$$

Such an ideal observation is limited by the finite speed of light. Therefore, the actual range measurement is relative to the position of the two bodies at different times.

The one-way range measures the light-time from the tracking station to the satellite, or vice versa. If t_T is the time of transmission of the radio signal from one body and t_R the time of reception of the signal at the other body, the quantity to be measured will be:

$$\rho = \left|\boldsymbol{r}_S(t_R) - \boldsymbol{r}_{GS}(t_T)\right| \tag{3.2}$$

In an ideal case, the difference between t_R and t_T would be the time taken by the light to travel the distance ρ, hence $t_R = t_T + \rho/c$. In a real measurement, the difference between the transmission and the reception times will deviate from the simple light-time, either due to a speed of the signal lower than c, or to a disagreement between the clocks at the two bodies (Tapley et al., 2004).

In a two-way range measurement, the round-trip light time between the tracking station and the spacecraft is observed. This provides a more accurate value, since the clock offsets are not to be taken into account (Tapley et al., 2004). The ranging signal is modulated over the uplink carrier at the ground station, which is then transponded coherently by the spacecraft. The signal is then received by

the station, and is used to infer the light-time. The uplink frequency can be either ramped or unramped. In the general case of ramped uplink signal, the range observable can be expressed as (Moyer, 2003):

$$q_\rho = \int_{t_T}^{t_R} F_\rho(t)dt \tag{3.3}$$

where $F_\rho(t)$ is the conversion factor from seconds to range units, which is proportional to the transmitted frequency. The range measurement is affected by an ambiguity equal to an integer number of wavelengths of the ranging signal (Montenbruck and Gill, 2012). This ambiguity may be solved if other range observations are available, or using Doppler observations.

3.1.2. Doppler observables

Range-rate observations measure the relative velocity of the station and the spacecraft along the line-of-sight (LOS). The formula for the instantaneous two-way Doppler shift is, in a first-order approximation (Le Maistre, 2013):

$$\Delta f = 2M_{bd} f_T \frac{v_r}{c} \tag{3.4}$$

where $v_r = \dot{\rho}$ is the range-rate and f_T is the transmitted frequency, while M_{bd} is the transponder turnaround ratio. The signal is transponded at the spacecraft in order to avoid interference between the uplink and the downlink (Montenbruck and Gill, 2012). In practice, the Doppler shift is integrated over a time interval $t_C = t_{R_e} - t_{R_s}$, defined at the station of reception. The subsctipts s and e refer to the starting time and to the ending time of the interval t_C. The Doppler observable is then derived from the Doppler count, defined as (Montenbruck and Gill, 2012):

$$N_{dop} = \int_{t_{R_s}}^{t_{R_e}} (f_R - f_{ref})dt, \tag{3.5}$$

where f_R is the frequency of the received signal and f_{ref} is a reference frequency. The number of transmitted cycles of $M_{bd}f_T$ over the time interval at transmission corresponding to t_C at reception must be equal to the number of cycles of f_R received over t_C:

$$\int_{t_{R_s}}^{t_{R_e}} f_R dt = M_{bd} \int_{t_{T_s}}^{t_{T_e}} f_T dt \tag{3.6}$$

Then, if the reference frequency is taken to be $f_{ref} = M_{bd}f_T$, the Doppler count can be written as:

$$N_{dop} = M_{bd}\left[\int_{t_{T_s}}^{t_{T_e}} f_T dt - \int_{t_{R_s}}^{t_{R_e}} f_T dt\right] = M_{bd} f_T \left(t_{T_e} - t_{T_s} - t_{R_e} + t_{R_s}\right) \tag{3.7}$$

The time between the transmission and the reception at either the start of the interval or the end is the round-trip light time. Therefore:

$$\begin{aligned} t_{R_s} - t_{T_s} &= \frac{\rho_{u_s} + \rho_{d_s}}{c} \\ t_{R_e} - t_{T_e} &= \frac{\rho_{u_e} + \rho_{d_e}}{c} \end{aligned} \tag{3.8}$$

Here, ρ_u and ρ_d are the range along the uplink leg and the downlink leg, respectively, while the subsctipts s and e indicate that the ranges are relative to the starting time and to the ending time of the interval t_C. The Doppler observable is then (Le Maistre, 2013):

$$q_{DOP} = \Delta f = \frac{N}{t_C} = M_{bd}\frac{f_T}{ct_C}\left[(\rho_{u_e} + \rho_{d_e}) - (\rho_{u_s} + \rho_{d_s})\right] \tag{3.9}$$

In this expression, N_{dop} is taken to be the opposite of that given by Eq. 3.7, in agreement with the convention for which a positive range rate leads to a positive Doppler shift (Moyer, 2003). Since the range observable represents the difference in phase between the transmitted and the received signal, and the signal is transponded coherently, the turnaround ratio of the transponder does not appear in the expression of q_ρ, which measures the phase shift (Montenbruck and Gill, 2012).

3.1.3. Noise budget and corrections

As mentioned in the previous section, the science return of lander and orbiter radio tracking is limited by the accuracy of the measurements, since a geophysical signature below the noise threshold can generally not be determined from the observations. Errors in the measurements can be due to instrumental noise, propagation noise, or systematic errors (Asmar et al., 2005). Current accuracy levels are in the order of 0.1 mm/s for Doppler at 60s integration time and 1-5 m for ranging measurements (Iess et al., 2014), as measured from post-fit residuals. These values vary a lot with the tracking system and the orbital configuration, and may be larger in the presence of systematic errors.

Instrumental noise stems from mechanical and thermal instability of the ground and spacecraft electronics, as well as from errors in the frequency and timing system (FTS). The instrumentation instability can be expressed in terms of fractional fluctuations in the reference frequency, $y(t) = \Delta f(t)/f_0$. The Allan variance (and the corresponding deviation $\sigma_y(\tau)$) is a measure of the stability of the reference frequency, and is defined as (Thornton and Border, 2003):

$$\sigma_y^2(\tau) = \frac{1}{2}\langle (y_{k+1} - y_k)^2 \rangle \tag{3.10}$$

where y_k and y_{k+1} are the average values of the fractional frequency fluctuation $y(t)$ over two adjacent intervals of length τ, and the angle brackets represent an ensemble average. This expression is more properly known as the two-sample Allan variance with no dead time (because two adjacent time intervals are considered), τ being the averaging time.

For two-way Doppler tracking, where the reference frequency is provided for example by hydrogen masers at the DSN station, the Allan deviation of the FTS errors is better than 10^{-15} at $\tau = 1000$ s (Asmar et al., 2005). This value is generally limited by the stability of the on-board transponder, for which $\sigma_y \sim 1.8 \cdot 10^{-14}$ at $\tau = 60$ s in the case of Cassini, corresponding to a noise of 0.006 mm/s (Iess et al., 2014). For one-way range-rate, the ultrastable oscillators (USO) on-board the spacecraft achieve a worse performance, with $\sigma_y \sim 10^{-13}$ for 1000 s integration time, but in any case FTS noise and instrumental noise in general is not the dominant contribution to the total noise (Asmar et al., 2005).

Other instrumental contributions to the noise are the ground antenna thermal and mechanical noise. The thermal noise corresponds to a finite signal-to-noise ratio (SNR) on the link due to the non-zero temperature of the antenna, and is a white noise on the phase. The associated Allan deviation was estimated to be in the order of $\sigma_y \sim 10^{-16}$ at $\tau = 1000$ s by Asmar et al. (2005), and 0.005 mm/s at Doppler integration times of 60 s for the MRO Ka-band signal (Zuber et al., 2007). Antenna mechanical noise can be due to wind, gravitational loading, or thermal expansion, and is roughly $\sigma_y \sim 1.6 \cdot 10^{-14}$ at $\tau = 60$ s, or 0.005 mm/s (Iess et al., 2014). In addition, there is a numerical truncation error, which for Cassini and Juno was estimated to be up to $6 \cdot 10^{-2}$ mm/s at $\tau = 60$ s (Zannoni and Tortora, 2013).

For range measurements, the random errors are dominated by the thermal noise. The systematic errors for range data are considerably larger than those for Doppler measurements (which are negligible and mostly of low frequency), and mainly consist in biases due to delays induced by various effects, like multipath (Iess et al., 2014).

Propagation noise is caused by the fact that the electromagnetic signal does not travel in vacuum, but through media with different refractive indices. The main sources of this noise for a probe targeting Mars are therefore the interplanetary and solar plasma, the Earth ionosphere and troposphere, and, in minor part, the Martian atmosphere. The plasma and ionosphere are dispersive media, because their refractive index (n_p) depends on the carrier frequency of the signal (f_c), approximately as (Le Maistre, 2013):

$$n_p = 1 - 40.3\frac{N_e}{f_c^2} \tag{3.11}$$

N_e is the electron density, namely the number of free electrons per unit of volume, expressed in m^3. The interaction between the electromagnetic wave and the charged particles leads to a reduction of the group velocity and an increase of the phase velocity. The range correction due to plasma and ionospheric noise is (Montenbruck and Gill, 2012):

$$\Delta\rho = 40.3\frac{TEC}{f_c^2} \tag{3.12}$$

The total electron content (TEC) is the total number of free electrons in the path of the signal, and is

therefore obtained as (Montenbruck and Gill, 2012):

$$TEC = \int_{S_{tot}} N_e ds \tag{3.13}$$

Here S_{tot} represents the path of the signal, and ds is the infinitesimal element of length along the path. The correction for carrier phase measurements is equal and opposite in sign, due to the increase of phase velocity (Montenbruck and Gill, 2012):

$$\Delta\varphi = -40.3\frac{TEC}{f_c^2} \tag{3.14}$$

The correction in the Doppler shift, which is proportional to the rate of change of the range, is (Le Maistre, 2013):

$$\Delta f_{ion} = \frac{40.3}{cf_c}\frac{d(TEC)}{dt} \tag{3.15}$$

Therefore, the Doppler shift correction depends on the time variation of the TEC along the signal path. The TEC for interplanetary plasma depends on the distance from the Sun, which is why an important parameter in the measurement noise is the Sun-Earth-probe (SEP) angle, that is, the angle between the Sun and the spacecraft as seen from the Earth. Models of the distribution of the electron density in the ionosphere and in the interplanetary plasma are available, but the most precise method to correct the dispersion effects is to use two different carrier frequencies. Usually, the uplink signal in a single band gets transponded in two separate bands. Assuming the paths of the two signals through the dispersive media to be the same, the correction can be found by applying Equation 3.15 for the two signals with different f_c Le Maistre (2013).

The troposphere is non-dispersive, so its index of refraction does not depend on the carrier frequency (Montenbruck and Gill, 2012). Its effects on the signal can be divided into those coming from dry air, the properties of which are easy to model because they change slowly with time, and those due to water vapour. For both components, a zenith delay is computed, which is then extended to the different elevations of the radio link through mapping functions (Petit and Luzum, 2010). These mapping functions will generally be close to the cosecant of the elevation of the satellite as seen from the station (Tapley et al., 2004). In addition, the dependence on the azimuth of the signal is taken into account through tropospheric gradients in the North-South and the East-West directions (Petit and Luzum, 2010). Therefore, the tropospheric delay along the line-of-sight is modelled as (Petit and Luzum, 2010):

$$\Delta\rho_T = m_h(el)D_{hz} + m_w(el)D_{wz} + m_g(el)[G_N\cos(az) + G_E\sin(az)], \tag{3.16}$$

where the hydrostatic (dry) and wet zenith delays are D_{hz} and D_{wz}, while m_h and m_w are their respective mapping functions. The angles el and az are the elevation and the azimuth of the satellite, as seen from the station. The terms G_N and G_E are the tropospheric gradients in the N-S and E-W directions, and m_g is the total gradient mapping function.

Other errors which typically have to be considered in the radio tracking of a spacecraft are the unmodeled displacements of the satellite antenna phase centre, that cause a shift in the spacecraft CoM, with respect to which the dynamical equations are integrated (Genova et al., 2016). Table 3.1 lists the contributions to the Doppler noise for the (X-band) radio tracking of the LaRa instrument, in terms of the error on the radial velocity (Δv_r), given by Le Maistre (2013) for a Doppler integration time of 60 s. It can be seen that the major error source is the Earth tropospheric delay, and that the total noise is below 0.1 mm/s. The average data noise for MRO, MGS, and Mars Odyssey at 10 s integration time and SEP angles larger than 60° is 0.053, 0.056, and 0.040 mm/s, with Odyssey data reaching up to 0.03 mm/s of accuracy (Konopliv et al., 2011).

3.2. Least squares filter

This section presents the method used to determine the physical parameters of interest from the measurements, namely the least-squares estimation. Only the batch least squares method is described here, since it is the one implemented in the software used for the project. Further information on the topic can be found, for example, in (Tapley et al., 2004) or (Montenbruck and Gill, 2012), which are

Error source	Δv_r (mm/s)
Thermal noise	0.03
Ground station	0.04
Solar plasma	< 0.09
Earth ionosphere	0.02
Earth troposphere	0.14
Mars ionosphere	0.0016
Mars troposphere	0.002
Total RMS	<0.066

Table 3.1: Doppler noise contributions at t_c = 60 s for LaRa, as estimated by Le Maistre (2013).

the main references used for this chapter. In Section 3.3, some details are given about the covariance analysis in a batch least-squares, which allows to evaluate the influence of a parameter on the uncertainties of the estimated parameters.

The orbit determination problem consists of the solution of two nonlinear relations:

$$\dot{\boldsymbol{X}}(t) = F(\boldsymbol{X}(t), t) \tag{3.17}$$

$$\boldsymbol{Y}_i = G(\boldsymbol{X}_i, t_i) + \boldsymbol{\epsilon}_i \tag{3.18}$$

$\boldsymbol{X}$ represents the vector of the n unknown parameters, which include the state vector of the spacecraft, $\boldsymbol{S}$. The elements of the state vector are the three components of the position of the satellite and the three components of its velocity. However, in the following, the entire vector of parameters, $\boldsymbol{X}$, will often be referred to simply as "state vector". The propagation of the vector of parameters, as expressed by Eq. 3.17, is obtained from the dynamical model presented in Section 4.1. $\boldsymbol{Y}_i$ is a vector of p_i elements, representing the measurements available at the epoch t_i, where $i = 1, ..., l$. The vector $\boldsymbol{X}_i$ is the vector of parameters at the epoch t_i, thus $\boldsymbol{X}(t_i)$. These measurements are of the same kind as those described in section 3.1, and generally $p_i < n$. The p_i-dimensional vector of errors, $\boldsymbol{\epsilon}_i$, can be either due to an incorrect formulation of the function G, which relates the real measurements to the parameters to estimate, or to wrong values of the estimated parameters, or to the noise proper of the measurement technique.

The functions F and G are usually nonlinear functions of $\boldsymbol{X}$. However, the problem can be linearized around a reference trajectory $\boldsymbol{X}^*$, so that, neglecting terms of order higher than the first in $\boldsymbol{x}(t) = \boldsymbol{X}(t) - \boldsymbol{X}^*(t)$, the two equations become (Tapley et al., 2004):

$$\dot{\boldsymbol{x}} = A(t)\boldsymbol{x}(t) \tag{3.19}$$

$$\boldsymbol{y}_i = \tilde{H}_i \boldsymbol{x}_i + \boldsymbol{\epsilon}_i \tag{3.20}$$

with

$$A(t) = \left[\frac{\partial F(\boldsymbol{X}(t), t)}{\partial \boldsymbol{X}(t)}\right]^*, \quad \text{and} \quad \tilde{H}_i = \left[\frac{\partial G(\boldsymbol{X}_i, t_i)}{\partial \boldsymbol{X}}\right]_i^* \tag{3.21}$$

The asterisk means that these partial derivatives are evaluated at the reference trajectory.

The deviation in the state vector at time t, $\boldsymbol{x}$(t), may be related to that at a reference epoch t_k through the state transition matrix $\boldsymbol{\Phi}(t, t_k)$, with:

$$\boldsymbol{\Phi}(t, t_k) = \frac{\partial \boldsymbol{x}(t)}{\partial \boldsymbol{x_k}} \tag{3.22}$$

Then, using Eq. 3.19, the differential equation yielding the variation of the state transition matrix as a function of t can be written as:

$$\dot{\boldsymbol{\Phi}}(t, t_k) = A(t)\boldsymbol{\Phi}(t, t_k) \tag{3.23}$$

The initial condition of this equation derives from the fact that the state vector deviation at the reference epoch (t_k) is not modified by the state transition matrix, so, indicating with I the identity matrix (in this case with dimensions $n \times n$):

$$\boldsymbol{\Phi}(t_k, t_k) = I \tag{3.24}$$

The state transition matrix can be used to relate the observations equation at the different epochs to the state deviation at the reference epoch, by substituting $\boldsymbol{x}_i$ in Eq. 3.19 with $\boldsymbol{\Phi}(t, t_k)\boldsymbol{x}_k$:

$$\boldsymbol{y}_i = H_i \boldsymbol{x}_k + \boldsymbol{\epsilon}_i, \tag{3.25}$$

where $H_i = \tilde{H}_i \boldsymbol{\Phi}(t_i, t_k)$. All the measurement residuals at the l different epochs can be regrouped in a single vector $\boldsymbol{y}$, which will have $m = \sum_i p_i$ elements. If the same is done for the errors and for the measurement Jacobian matrices H_i, obtaining the $m \times 1$ vector of residuals $\boldsymbol{\epsilon}$ and the $m \times n$ Jacobian matrix H, the observations equation is written in a more compact form as:

$$\boldsymbol{y} = H \boldsymbol{x}_k + \boldsymbol{\epsilon}, \tag{3.26}$$

The least squares solution for $\boldsymbol{x}$ in 3.26 is the one minimizing the cost function

$$J(\boldsymbol{x}_k) = \frac{1}{2}\boldsymbol{\epsilon}^T \boldsymbol{\epsilon} = \frac{1}{2}(\boldsymbol{y} - H\boldsymbol{x}_k)^T (\boldsymbol{y} - H\boldsymbol{x}_k) \tag{3.27}$$

If $m \geq n$ and the Jacobian has full rank (hence if its n columns are independent), the cost function minimum is found by setting $\partial J / \partial \boldsymbol{x}$ to 0. The resulting value for the state vector deviation at the reference epoch is obtained by solving the following linear system of equations, known as *normal equations*:

$$\left(H^T H\right) \boldsymbol{x}_k = H^T \boldsymbol{y} \tag{3.28}$$

The $n \times n$ matrix $\left(H^T H\right)$ is known as the *normal matrix*, and is invertible given the assumptions made on H, so that:

$$\hat{\boldsymbol{x}}_k = \left(H^T H\right)^{-1} H^T \boldsymbol{y} \tag{3.29}$$

In the solution here presented, all the measurements are treated equally, while in reality, when combining different observations (especially of different types), these may be affected by errors of different magnitudes. The non-uniformity the measurements can be taken into account by assigning to each equation in the system of normal equations a weight, inversely proportional to the uncertainty of the corresponding observation. This is generalized in the weighted least squares problem, where the cost function to minimize is:

$$J(\boldsymbol{x}_k) = \frac{1}{2}\boldsymbol{\epsilon}^T W \boldsymbol{\epsilon} \tag{3.30}$$

The solution is then given by the system of equations:

$$\left(H^T W H\right) \boldsymbol{x}_k = H^T W \boldsymbol{y} \tag{3.31}$$

Here W is an $m \times m$ weighting matrix. If $\left(H^T W H\right)$ is positive definite, the weighted least squares solution is:

$$\hat{\boldsymbol{x}}_k = \left(H^T W H\right)^{-1} H^T W \boldsymbol{y} \tag{3.32}$$

The measurements errors may be assumed to be random variables with zero mean, so that:

$$E[\boldsymbol{\epsilon}] = 0 \quad \text{and} \quad E[\boldsymbol{\epsilon}\boldsymbol{\epsilon}^T] = R, \tag{3.33}$$

where the operator $E[]$ represents the expected value, and R is the auto-covariance matrix of the random vector of errors $\boldsymbol{\epsilon}$. In these assumptions, the weighted least squares solution is a linear and unbiased estimate of $\boldsymbol{x}_k$. It is linear because it is obtained as a linear combination of the observations, and unbiased because its expected value is $\boldsymbol{x}_k$:

$$E[\hat{\boldsymbol{x}}_k] = E\left[\left(H^T W H\right)^{-1} H^T W \boldsymbol{y}\right] \overset{\text{Eq. } 3.26}{=} E\left[\boldsymbol{x}_k + \left(H^T W H\right)^{-1} H^T W \boldsymbol{\epsilon}\right] = \boldsymbol{x}_k \tag{3.34}$$

Moreover, it is possible to show that if the weighting matrix is taken to be $W = R^{-1}$, the weighted least squares estimate is the one for which the *estimation error*, $\hat{\boldsymbol{x}}_k - \boldsymbol{x}_k$, has the minimum variance (see

e.g. Kuchynka et al., 2014, although there the errors were assumed to be uncorrelated, in accordance to the hypoteses of the Gauss-Markov theorem). The auto-covariance matrix of the estimation error is in this case:

$$P_k = \left(H^T W H\right)^{-1} \tag{3.35}$$

It can be shown (e.g. Montenbruck and Gill, 2012) that any other linear unbiased estimator will lead to a covariance matrix of the estimation error, P_k^*, for which $P_k^* - P_k$ is positive semi-definite, confirming the minimum variance property of the least squares solution.

There may be a priori information about the initial state vector deviation in terms of its value, $\overline{\boldsymbol{x}}_k$, and its uncertainty, as expressed by the weighting matrix $\overline{W}_k$ (i.e. the inverse of its auto-covariance matrix, P_k). In this case, the cost function is modified to penalize large deviations from the a apriori values:

$$J(\boldsymbol{x}_k) = \frac{1}{2}\boldsymbol{\epsilon}^T W \boldsymbol{\epsilon} + \frac{1}{2}\left(\overline{\boldsymbol{x}}_k - \boldsymbol{x}_k\right)^T \overline{W}_k \left(\overline{\boldsymbol{x}}_k - \boldsymbol{x}_k\right) \tag{3.36}$$

The corresponding normal equations are:

$$\left(H^T W H + \overline{W}_k\right)\boldsymbol{x}_k = H^T W \boldsymbol{y} + \overline{W}_k \overline{\boldsymbol{x}}_k \tag{3.37}$$

Leading to the estimate:

$$\hat{\boldsymbol{x}}_k = \left(H^T W H + \overline{W}_k\right)^{-1}\left(H^T W \boldsymbol{y} + \overline{W}_k \overline{\boldsymbol{x}}_k\right) \tag{3.38}$$

The covariance of the estimated vector is:

$$P_k = \left(H^T W H + \overline{W}_k\right)^{-1} \tag{3.39}$$

The resolution of the normal equations and the computation of the covariance matrix require that the information matrix $\left(P_k^{-1}\right)$ be non-singular. The knowledge about the uncertainties of the a priori parameters allows to add the weighting matrix $\overline{W}_k$ to the normal matrix $\left(H^T W H\right)$, so that a non-singular information matrix can be obtained even if the normal matrix itself is singular or close to singular. Therefore, the effect of the a priori weighting matrix is to stabilize the information matrix.

This approach to the orbit determination problem is called *batch estimation*, because observations from several epochs are accumulated and then processed at the same time. *Sequential estimation*, on the other hand, allows to update the state vector with each new observation, and is therefore useful for near-real-time applications.

In general, a reference state vector at the initial epoch, $\boldsymbol{X}^*(t_0)$, is given, and along with it an a priori deviation $\overline{\boldsymbol{x}}_0$ with covariance matrix P_0. The value of $\overline{\boldsymbol{x}}_0$ is usually set to 0, hence P_0 is a measure of the uncertainties of the elements of $\boldsymbol{X}^*(t_0)$. From the initial state vector, the reference orbit is obtained by integrating Eq. 3.17 over the epochs of interest, with the given $\boldsymbol{X}^*(t_0)$ as initial condition. At the same time, the variational equation for the state transition matrix (Eq. 3.23) is integrated, evaluating the term $A(t) = \partial F(\boldsymbol{X}(t), t)/\partial \boldsymbol{X}(t)$ over the reference trajectory at each integration step. Once the reference trajectory and the state transition matrix have been propagated, the estimate of the initial state, $\boldsymbol{X}(t_0)$, is obtained by adding the solution of Eq. 3.37, $\hat{\boldsymbol{x}}_0$, to the reference value, $\boldsymbol{X}^*(t_0)$.

The least squares estimate of $\boldsymbol{X}(t_0)$ obtained in this way is that relative to the linearized dynamical and observation equations. Therefore, it may not accurately reflect the true behaviour of the spacecraft. For this reason, the process is iterated multiple times, by taking the estimated initial state as the reference initial state of the subsequent iteration. Convergence is reached if the RMS of the difference between two consecutive estimations of $\hat{\boldsymbol{x}}_0$ falls below a fixed threshold (although equivalent convergence criteria are often used).

Usually, the complete set of observations is divided into several smaller subsets, corresponding to time intervals, or data arcs, which can be in the order of days (Konopliv et al., 2011). This allows to limit the impact on the estimated parameters of forces which are poorly known, and, if dynamical parameters relative to these forces are among those estimated, to more precisely model these effects. Examples of these poorly constrained forces may be the atmospheric drag or the solar radiation pressure, for which usually scale factors are estimated as part of the state vector. This method is known as the multi-arc approach (Milani and Gronchi, 2010). The elements of the state vector are split into local parameters and global parameters. The local parameters are estimated at each arc, with each time

different initial conditions, and independently from the local parameters relative to the other arcs. The global parameters, instead, are estimated over the whole dataset. Typically, local parameters include the position and velocity of the spacecraft, the surface forces scale factors, thrust corrections, and range biases, while global parameters may be the static gravity field coefficients, the rotation and orientation parameters, and the tidal Love number (Konopliv et al., 2011).

3.3. Covariance analysis

The covariance matrix of the estimated parameters, given by Eq. 3.39, does not take into account the systematic errors, which may arise from inaccuracies in the dynamical and measurements model. The formal errors decrease with the number of observations, roughly as $1/\sqrt{m}$ (Dirkx et al., 2014), while this is not true for the systematic errors, which thus put a limit to the accuracy obtainable in the orbit determination process (Montenbruck and Gill, 2012). Hence, the formal errors of the estimated parameters, which correspond to the square roots of the elements on the diagonal of P_k, are a too optimistic representation of the uncertainty of the solution. The true errors (i.e., the difference between the estimated parameters and their actual values), which are not known when dealing with real observations, may be several times larger than the formal uncertainties (Marty et al., 2009).

The true errors are known in simulations, since they can be found by comparing the estimated parameters to those used to generate the synthetic measurements. Then these errors may be used to calibrate the estimated uncertainties, for example by multiplying the formal errors by the amplification factor (Le Maistre et al., 2012):

$$k_{calib} = \frac{1}{N_{simu}} \sum_{j=1}^{N_{simu}} \left(\frac{\varepsilon(j)}{\sigma(j)} \right)^2 \tag{3.40}$$

Here, N_{simu} is the total number of simulations performed, and $\varepsilon(j)$ and $\sigma(j)$ are the true errors and the estimated formal errors for the j-th simulation and the parameter of interest. However, this process can be time consuming and computationally intensive, since it requires many instances of the least squares estimation.

Another way to investigate the influence of systematic errors on the least squares solution is though the consider covariance analysis. In this method, an additional vector of parameters, $\boldsymbol{c}$, is selected, consisting of the force and measurement model parameters which are affected by uncertainties, but are not estimated. These quantities are called *consider parameters*. The reason why the consider parameters are chosen not to be estimated but fixed to a reference value could be due to computation speed and memory requirements, or to an instability of the information matrix when there is only a small number of independent observations (Tapley et al., 2004).

Using a linearized model, the vector $\boldsymbol{c}$ represents the displacement of the consider parameters from their nominal values, so that the observation equations can be written as (Bierman, 1977):

$$\boldsymbol{y} = H_x \boldsymbol{x} + H_c \boldsymbol{c} + \boldsymbol{\epsilon} \tag{3.41}$$

The cost function with the a priori information of the reference state deviation $\boldsymbol{x}_k$ is this time:

$$J(\boldsymbol{x}_k) = \frac{1}{2}(\boldsymbol{y} - H_x \boldsymbol{x}_k)^T W (\boldsymbol{y} - H_x \boldsymbol{x}_k) + \frac{1}{2}\left(\overline{\boldsymbol{x}}_k - \boldsymbol{x}_k\right)^T \overline{W}_k \left(\overline{\boldsymbol{x}}_k - \boldsymbol{x}_k\right) \tag{3.42}$$

Setting the derivative of the cost function with respect to $\boldsymbol{x}$ equal to 0 leads to the least squares solution:

$$\hat{\boldsymbol{x}}_k = \left(H_x^T W H_x + \overline{W}_k\right)^{-1} \left(H_x^T W \boldsymbol{y} + \overline{W}_k \overline{\boldsymbol{x}}_k\right) \tag{3.43}$$

Substituting for $\boldsymbol{y}$ its (linearized) expression as a function of the state and consider parameters deviation vectors (Eq. 3.41), the estimate with the inclusion of the consider parameters becomes:

$$\begin{aligned} \hat{\boldsymbol{x}}_k &= \left(H_x^T W H_x + \overline{W}_k\right)^{-1} \left(H_x^T W \left(H_x \boldsymbol{x}_k + H_c \boldsymbol{c} + \boldsymbol{\epsilon}\right) + \overline{W}_k \overline{\boldsymbol{x}}_k\right) \\ &= \left(H_x^T W H_x + \overline{W}_k\right)^{-1} \left(H_x^T W \left(H_x \boldsymbol{x}_k + H_c \boldsymbol{c} + \boldsymbol{\epsilon}\right) + \overline{W}_k \left(\overline{\boldsymbol{x}}_k + \boldsymbol{x}_k - \boldsymbol{x}_k\right)\right) \\ &= \boldsymbol{x}_k + P_k \left(H_x^T W \left(H_c \boldsymbol{c} + \boldsymbol{\epsilon}\right) + \overline{W}_k \left(\overline{\boldsymbol{x}}_k - \boldsymbol{x}_k\right)\right) \end{aligned} \tag{3.44}$$

with $P_k = \left(H_x^T W H_x + \overline{W}_k\right)^{-1}$. The autocovariance of the estimation error $(\hat{\boldsymbol{x}}_k - \boldsymbol{x}_k)$ is:

$$\begin{aligned} &E[(\hat{\boldsymbol{x}}_k - \boldsymbol{x}_k)(\hat{\boldsymbol{x}}_k - \boldsymbol{x}_k)^T] = \\ &= E\left[P_k H_x^T W \boldsymbol{\epsilon}\boldsymbol{\epsilon}^T W H_x P_k^T + P_k H_x^T W H_c \boldsymbol{c}\boldsymbol{c}^T H_c^T W H_x P_k^T + P_k \overline{W}_k (\overline{\boldsymbol{x}}_k - \boldsymbol{x}_k)(\overline{\boldsymbol{x}}_k - \boldsymbol{x}_k)^T \overline{W}_k^T P_k^T\right] \\ &= P_k + P_k H_x^T W H_c \overline{P}_{cc} H_c^T W H_x P_k^T \end{aligned} \tag{3.45}$$

where $\overline{P}_{cc} = E[\boldsymbol{c}\boldsymbol{c}^T]$ is the a priori covariance matrix of the consider parameters. The consider covariance can be written as:

$$P_{xx} = P_k + S_{xc} \overline{P}_{cc} S_{xc}^T \tag{3.46}$$

The matrix S_{xc} is known as the sensitivity matrix (Tapley et al., 2004), with:

$$S_{xc} = P_k H_x^T W H_c \tag{3.47}$$

Another matrix of interest in the consider covariance analisis is the perturbation matrix, given by:

$$\Gamma = S_{xc}[diagonal(\sigma_c)] \tag{3.48}$$

The perturbation matrix expresses the contribution to the uncertainty of the estimated parameters due to a 1σ error in the consider parameters.

4

Simulation setup

This chapter covers the development of the simulation environment for TGO, starting from a theoretical description of the forces involved in its motion in space and the way these can be modeled, given in Section 4.1. Then, Section 4.2 explains how this theory is implemented in the software used to simulate the trajectory and the measurements of TGO.

4.1. Dynamical model

In order to correctly describe the motion of the spacecraft in space, a precise modelling of the forces acting on it is necessary. These forces, and the corresponding accelerations, can be either of gravitational or non-gravitational nature. The primary accelerations of these two kinds are described in the next two sections. A lander is assumed to be fixed on the surface of Mars, hence its motion will simply be that of a point of the surface of the planet. For this reason, no integration of the dynamical equations strictly relative to the lander is performed in the orbit determination process. The motion of the lander is obtained by solving for the global motion of the planet, along with the surface displacements from tides and loading (given, in a linear approximation of the response to the forcing, by the corresponding Love numbers). It is clear, then, that the forces described here are intended to be applied to the orbiter, since for the lander they are, if present, counterbalanced by the reaction of the surface of Mars, and have no effect on the motion of the probe in inertial space.

The integration of the dynamical equations of the satellite is usually performed in an inertial frame, so as to avoid the inclusion of fictitious forces in the model. If $\boldsymbol{r} = (x, y, z)$ is the position vector of the spacecraft in an inertial frame, such as the MMO frame, its acceleration will be $\boldsymbol{a} = \ddot{\boldsymbol{r}}$, where the dots represent time derivatives.

4.1.1. Gravitational accelerations

The gravitational forces acting on a Mars orbiter are principally due to the planet itself. If Mars were a homogeneous sphere, its gravitational attraction on the spacecraft would be always on the direction connecting the centres of mass of the two bodies (assuming the satellite to be a homogeneous sphere as well). If no other force were present, the spacecraft would be in a Keplerian orbit, which is perfectly described by a conic. However, inhomogeneities in the shape and mass distribution of the central planet generate perturbations on the Keplerian trajectory of the satellite feeling its attraction. In particular, the gravitational potential at a point outside of a body with a generic shape and mass distribution, can be written as (e.g. Kaula, 2000):

$$U = \frac{GM}{r} + \frac{GM}{r} \sum_{n=2}^{\infty} \sum_{m=0}^{n} \left(\frac{R_e}{r} \right)^n \overline{P}_{nm} (\sin \phi_{lat}) \times \left[\overline{C}_{nm} \cos m\lambda + \overline{S}_{nm} \sin m\lambda \right] \tag{4.1}$$

In this expression of the spherical harmonics expansion of the gravitational potential, G is the gravitational constant and M the mass of the central body, R_e is the equatorial radius of the body, and $\overline{C}_{nm}$ and $\overline{S}_{nm}$ are the (fully) normalised harmonic coefficients of degree n and order m. The first term on

the right-hand-side of the equation is the central term, corresponding to the gravitational potential of a homogeneous spherical body. The spherical coordinates r, ϕ_{lat}, λ are the radial distance, the latitude, and the longitude in a reference system fixed to the body. The functions $\overline{P}_{nm}(\theta)$ are the (fully) normalised associated Legendre polynomials. The spherical harmonics coefficients are normalised since they vary considerably in magnitude depending on the degree and order, while their normalised counterparts allow for an easier comparison between different harmonics. The normalised coefficients $\overline{C}_{nm}$ are obtained from the spherical harmonics coefficients C_{nm} as (Kaula, 2000)

$$\overline{C}_{nm} = \sqrt{\frac{(n+m)!}{(n-m)!\ (2n+1)\ (2-\delta_{0m})}} C_{nm} \tag{4.2}$$

The same formula holds for the normalisation of the S_{nm} coefficients, while the inverse formula is used to normalize the associated Legendre polynomials, namely by dividing the unnormalized value by the square-root term. The Kronecker delta δ_{0m} is 1 for m=0,s and 0 otherwise. Nonetheless, this formalism will not be maintained throughout the report. Since in most of the applications considered here the fully normalised coefficients are used, the bar above their symbol is dropped. Thus, in the following C_{nm} and S_{nm} are intended as fully normalised gravity field coefficients, and not their unnormalised counterparts, unless stated otherwise. Moreover, is some parts of the report, like in Section 4.2.3, the symbol n for the degree of the gravity field harmonic is substituted by the symbol l, to avoid confusion with local parameters with similar notation. The meaning of the subscript will anyway be made clear when this happens.

The gravitational potential at the orbiter's position due to the central body is given by Eq. 4.1, so that the two-body acceleration acting on the spacecraft is given by (Tapley et al., 2004):

$$\boldsymbol{a}_{cen} = -M^{(x,y,z)}_{(r,\phi_{lat},\lambda)} \boldsymbol{\nabla} U_{MARS} \tag{4.3}$$

The rotation matrix $M^{(x,y,z)}_{(r,\phi_{lat},\lambda)}$ is needed because the gravitational potential in Eq. 4.1 is defined in the body-fixed frame, and in the set of spherical coordinates $(r,\ \phi_{lat},\ \lambda)$. The gravitational potential is commonly represented in the body-fixed frame because then the harmonic coefficients are constant for a rigid planet (i.e., the static gravity field is constant in the body-fixed frame). Therefore, the gradient of the potential will itself be in the body-fixed frame, and in spherical coordinates. The rotation matrix transforms the components of the gradient in the directions of the body-fixed spherical coordinates to cartesian components in the inertial frame of integration. Hence, it is found as the product of two matrices, one transforming body-fixed spherical coordinates to body-fixed cartesian coordinates, and the other, which was already introduced as $PNR\Pi$ (Eq. 2.7), transforming cartesian coordinates in the body-fixed frames to cartesian coordinates in the inertial frame.

The static gravitational potential, as displayed in Eq. 4.1 assuming constant harmonic coefficients, is however perturbed by the gravitational attraction of other bodies on Mars (mostly the Sun) and by the non-rigidity of the planet. This generates tidal deformations of the planet, which in turn modify the Mars gravitational potential experienced by the orbiter. The tidal potential can be expressed in terms of variations of the gravity field harmonic coefficients (that is, those in the expansion of U_{MARS}), which in the general case can be written as (Dirkx et al., 2014):

$$\Delta\overline{C}_{nm} - i\Delta\overline{S}_{nm} = \frac{k_{nm}}{2n+1} \sum_j \frac{GM_j}{GM} \left(\frac{R_e}{r_j(\tilde{t}_{nj})}\right)^{n+1} \overline{P}_{nm}(\sin\phi_{lat_j}(\tilde{t}_{nj})) e^{-im\lambda_j(\tilde{t}_{nj})}, \tag{4.4}$$

The angles ϕ_{lat_j} and λ_j are the latitude and longitude of the perturbing body, while the term $r_j(\tilde{t}_{nj})$ is the distance of the perturbing body j from the center of Mars at the time $\tilde{t}_{nj} = t - \Delta t_{nj}$. If Mars were a completely elastic body, a perturbation at time t would cause an instantaneous response from the planet, and therefore a corresponding term in the tidal potential at time t. The dissipation inside the planet causes a delay in the deformation of the planet, hence the component of the tidal potential of degree n and due to the body j at time t will be relative to a perturbation at time $\tilde{t}_{nj}$. The other terms in the expression are the mass, the latitude, and the longitude (M_j, ϕ_j, and λ_j, respectively) of the perturbing body j. The Love numbers estimated from satellite orbits include the effect of both the solid and the atmospheric tide (Konopliv et al., 2011). Yoder et al. (2003) identified k_2 with the value

of k_{22}, since for the MGS orbit the uncertainties on k_{20} and k_{21} were 20 times and 7 times larger than those estimated for k_{22}.

The other Solar System bodies affect the orbit of the spacecraft not only in an indirect way (that is, through tidal deformation of Mars), but also through their direct gravitational attraction on the orbiter. These third-body effects are usually modelled by considering the perturbing body as a point mass, or truncating its gravity field to low degrees, given its large distance from the affected body when compared to their dimensions. These perturbing bodies include also several asteroids, which have small but non-negligible effects on the orbit of Mars (Konopliv et al., 2011).

In the modelling of third-body effects and tidal interactions, the orbits of the perturbing bodies are assumed to be known. Therefore, the accurate prediction of these gravitational interactions requires precise ephemerides of the bodies involved. The standard for high-precision ephemerides is found in the Development Ephemerides (DE) provided by JPL (e.g. Folkner et al., 2014), obtained by fitting the orbits of planets and other Solar System bodies to observations of different kinds (spacecraft, astrometry, radar, VLBI, laser ranging and occultation measurements). The uncertainties are reported to be in the order of hundreds of meters for terrestrial planets, tens of km for Jupiter and Saturn, and thousands of km for the other planets. As for the Martian moons, accurate ephemerides are provided by Lainey et al. (2007) and Jacobson (2010) . Both ephemerides are affected by errors of hundreds of meters, with those from Lainey et al. (2007) showing a better agreement with optical observations (Ziese and Willner, 2018).

In addition, variation of the gravitational potential of Mars with respect to the static solution are caused by the sublimation and deposition of CO_2 ice at the poles, as discussed in Section 2.3.3. This seasonal mass exchange between the atmosphere and the polar caps causes seasonal variations in the harmonic coefficients of the gravity field, especially the zonal terms (Sanchez et al., 2006). The time-varying gravity harmonic coefficients are then expressed as trigonometric series, similarly to the periodic variations of the MOP. The main effects have annual, semiannual, and annual frequency (Sanchez et al., 2006), thus the seasonal variation of the normalized coefficient $\overline{C}_{nm}$ is modeled as (Genova et al., 2016):

$$\Delta\overline{C}_{nm} = \sum_{j=1}^{3} A^{j}_{\overline{C}_{nm}} \cos(2\pi f_j t) + B^{j}_{\overline{C}_{nm}} \sin(2\pi f_j t), \tag{4.5}$$

where $f_j = jf_1$, f_1 being the orbital frequency of Mars (1/687 Earth days). The same formula holds for $\overline{S}_{nm}$. Values of the amplitudes are found from GCMs, as in (Sanchez et al., 2006), where expressions for the variations of coefficients up to degree and order 40 are computed.

The contributions from the atmospheric mass change to the time-varying gravity coefficients can be modeled separately, so that the equations in 4.5 are only relative to the mass variations of the polar caps. The variations of $\overline{C}_{nm}$ due to atmospheric pressure variations are then given by (Genova et al., 2016):

$$\Delta\overline{C}^{a}_{nm} = \frac{3}{R_a \rho_a g_0} \frac{1+k'_n}{2n+1} \overline{C}^{P}_{nm}, \tag{4.6}$$

where R_a is the mean radius of Mars, ρ_a the mean atmospheric density, g_0 is the mean surface gravity, and k'_n is the load Love number of degree n. The coefficient $\overline{C}^{P}_{nm}$ is the spherical harmonic coefficient of the surface pressure field, derived from atmospheric model like the Mars-GRAM2010. An equivalent formula can be used for $\Delta\overline{S}^{a}_{nm}$.

For high-precision applications of orbit determination, correction to the Newtonian dynamic model have to be applied to take into account the relativistic effects, as predicted by the theory of general relativity (GR). The main correction to the force model due to the relativistic effects comes from the Schwarzschild term, which models the difference in the central gravitational attraction of the main body with respect to the Newtonian mechanics (*e.g.* Dirkx, 2015), and can be expressed as:

$$\boldsymbol{a}_g = \frac{\mu}{c^2 r^3} \left\{ \left[2\left(\beta_{PPN} + \gamma_{PPN}\right) \frac{\mu}{r} - \gamma_{PPN} \left(\dot{\boldsymbol{r}} \cdot \dot{\boldsymbol{r}}\right) \right] \boldsymbol{r} + 2\left(1 + \gamma_{PPN}\right) \left(\boldsymbol{r} \cdot \dot{\boldsymbol{r}}\right) \dot{\boldsymbol{r}} \right\}, \tag{4.7}$$

with $\mu = GM$ the gravitational parameter of Mars. The coefficients β and γ are the parameterized post-Newtonian (PPN) parameters (which are 1 in the GR), c is the speed of light, and the other symbols have been already introduced. The main effect of this acceleration is a secular variation of the argument

of perigee of the orbit, which can be in the order of 10 arcsec/yr (Tapley et al., 2004). Other relativistic effects on the gravitational attraction are the Lense-Thirring precession and the geodesic precession, the corresponding acceleration being at least 10 times smaller than $\boldsymbol{a}_g$ (Petit and Luzum, 2010).

4.1.2. Non-gravitational accelerations

The principal non-gravitational forces acting on a spacecraft orbiting Mars include the atmospheric drag, the solar radiation pressure, and the angular momentum wheel desaturation (AMD) thrusting (Genova et al., 2016). Many of those non-conservative forces depend not only on the mass of the probe, but also on its shape, and generate from interactions with its exposed surfaces. For this reason, a model of the shape of the satellite is often needed to correctly estimate the non-gravitational effects. The spacecraft is generally approximated by a box-wing model, consisting of multiple flat plates, each with its own physical characteristics, that approximate the spacecraft bus (e.g. 6 panels forming a box), the solar panels (e.g. two or more moveable plates), and the high-gain antenna (HGA) (Genova et al., 2016). The HGA may be moveable, like for TGO, or fixed, like for the Mars Express spacecraft, the fixed configuration being easier to model but limiting the possibility of tracking from Earth (Mazarico et al., 2009). Each plate of this macro model will be described by its surface area (A_i), its normal vector, $\boldsymbol{n}_i$, which defines its orientation in space, and its physical and optical properties.

Nonetheless, limiting the geometry of the spacecraft to the sole surface area and orientation of the plates composing the macro model leads to a mismodeling of three-dimensional effects due to the interaction between the plates, such as the self-shadowing (Mazarico et al., 2009). This effect consists in a reduction of the effective exposed surface area of a plate due to the partial obscuration by another plate. The consequences of neglecting the self-shadowing depend on the spacecraft configuration, and are generally small but important in the parameter estimation.

The general expression of the acceleration coming from the atmospheric drag is (Genova et al., 2016)

$$\boldsymbol{a}_{drag} = -\frac{1}{2}\frac{\rho_a V^2}{m}\sum_i C_{D_i} A_i (\boldsymbol{n}_i \cdot \boldsymbol{n}_V)\boldsymbol{n}_V \tag{4.8}$$

The unit vector $\boldsymbol{n}_V$ is in the direction of the velocity of the spacecraft relative to the atmosphere, the norm of which is V. This velocity will have components due to the rotation of Mars and the wind speed. The drag acceleration is in the direction of the relative velocity itself, but the total aerodynamic acceleration due to the interactions with the atmosphere will also include a term perpendicular to the velocity, that is, the atmospheric lift. The parameter C_{D_i} represents the adimensional drag coefficient of the plate i. The drag acceleration depends on the local density of the atmosphere. This parameter can be determined from models of the density and temperature distribution in the Martian upper atmosphere, such as DTM-Mars (Bruinsma and Lemoine, 2002). The temporal variations in density predicted by the model are due to the diurnal variation of the local insolation, the intensity of the solar activity, and the seasonal cycle of the partial densities of CO_2 and O (Genova et al., 2015).

The solar radiation pressure is an acceleration caused by the exchange of angular momentum between photons emitted by the Sun reaching the satellite and the plates of the satellite, in the finite element model. The total acceleration acting on the spacecraft will be the sum of the contribution from all the plates of the macro model, and can be expressed as (Gobinddass et al., 2009):

$$\boldsymbol{a}_{SRP} = -\frac{G'}{mc}\sum_i A_i \cos\theta_i \left[2\left(\frac{\delta_i}{3} + \varrho_i \cos\theta_i\right)\boldsymbol{n}_i + (1-\varrho_i)\,\boldsymbol{n}_S\right] \tag{4.9}$$

Here, G' is the solar flux at the spacecraft position, m is the total mass of the satellite, and c the speed of light. The unit vector $\boldsymbol{n}_S$ points towards the Sun, and the angle it forms with the surface normal ($\boldsymbol{n}_i$) is the incidence angle, θ_i. The parameter ϱ_i is the specular reflectivity of the plate, while δ_i is its diffuse reflectivity. This formulation assumes the incoming flux to be parallel.

For a Mars orbiter, the solar radiation reflected by the surface of the planet and the black-body radiation emission have a considerable effect on the trajectory of the spacecraft. Due to the vicinity of the source, this radiation cannot be considered as made up of parallel rays. Hence, the surface of Mars is approximated with a series of surface elements, each with a specific albedo and emissivity.

The acceleration on the spacecraft due to this radiation pressure is then Marshall and Luthcke (1994):

$$\boldsymbol{a}_{RadMars} = -\sum_j \frac{G'_j}{mc} \sum_i A_i \cos\theta_{ij} \left[2\left(\frac{\delta_i}{3} + \varrho_i \cos\theta_{ij} \right) \boldsymbol{n}_i + (1-\varrho_i)\, \boldsymbol{n}_{S_j} \right] \tag{4.10}$$

The flux G'_j is that emitted or reflected by the j-th Mars surface element, $\boldsymbol{n}_{S_j}$ is the unit vector going from the i-th plate to the surface element j, and the incidence angle θ_{ij} is the angle between this vector and the normal to the plate, $\boldsymbol{n}_i$.

Another major acceleration acting on the spacecraft is that due to thrust in the case of manoeuvres or angular momentum wheel desaturation (AMD) events. The direction and intensity of these forces can be reconstructed from navigation data, but still the uncertainties in the AMDs are the limiting factor for the determination of the seasonal J_2 and J_3 variations and a considerable source of error in the detection of k_2 from the solar tide (Konopliv et al., 2006).

4.2. Software

What follows is a general description of the three major programs relevant to this project: GINS, in Section 4.2.1; Tudat, in Section 4.2.2; and ORB, in Section 4.2.3. Particular attention is given to the functions used to generate the results which will be presented in Chapter 6. While this is all external software (that is, not developed in the frame of this project, nor by the author), additional tools were built in support of these programs, to either prepare the necessary environment files (mainly in the case of GINS), process their outputs (mainly for Tudat), or expand and adapt some of their functionalities to the specific problem (mainly for ORB).

4.2.1. GINS

The GINS (Géodésie par Intégration Numérique Simultanée, Marty et al., 2011) orbitography software was developed by the GRGS (Groupe de Recherches de Géodésie Spatiale) team at CNES (Centre National d'Études Spatiales). Unless otherwise stated, all the information comes from the algorithmic documentation of the software (CNES/GRGS, 2018).

The development of GINS started in the 1970s, when it was used to process data from the first space geodesy missions targeting the Earth. In the 1990s it was extended to support the analysis of data from GPS satellites and from missions targeting other bodies of the Solar System, which currently include the 8 planets, Pluto, the Moon, Phobos, Eros, the comets Wirtanen and Churymov-Gerasimenko, and the Sun. The types of observations supported by GINS include Doppler and range (in 1, 2, or 3-way configuration), VLBI, laser ranging, optical, and altimetric measurements.

The DYNAMO package consists of various tools which allow to perform algebraic operations on the outputs provided by GINS. These may be used to combine data from different arcs, or different measurements types. Because no estimation was performed with GINS, and thus no use of DYNAMO was necessary, this package will not be discussed in the following.

The principal input of GINS is the *director* file, coded in YAML. This file lists the values of the processing options selected for the run, as well as the names and locations of the environment files and the measurements. The environment files include force models, the satellite macro model, rotation and orientation models for the central body and the principal perturbing bodies, as well as all the ephemerides and atmospheric models required.

Each GINS run is made up of two phases. The first phase is performed remotely on a CNES server at the Observatoire Midi-Pyrénées, in Toulouse. Here, the *director* file is read by the programs inside the PREPARS package, which retrieve all the relevant models and data, that may be stored locally or on the server. The a priori information on the parameters to estimate is given by the user in a *vap* file (*valeurs a priori*, French for "a priori values"). Here and throughout the whole of GINS, each parameter is identified by a specific signaletic element, a string of 24 characters. As well as by indicating the value and uncertainty, the a priori knowledge about a quantity to be estimated can also be expressed in the form of linear constraints between one or more parameters. After eventual preprocessing operations, the values are stored on the local computer in a *fic* (*fichier d'entrée*, French for "input file") text document. An additional input of the PREPARS processing is the *listing* file, which provides information on the steps executed and on the *director* read.

The *fic* file is given as an input to the functions of the GINS package as such, that perform the orbit

determination. This second phase of the processing is executed on the local computer, and yields several outputs, depending on the choices selected in the *director* file. Of these, the most relevant are:

- a *listing* file, which, similarly to the one produced in the PREPARS processing, lists the principal operations performed. Moreover, the values and uncertainties of the parameters, as well as the statistics of the measurements residuals, are reported here
- an *orbite* file, which stores the ephemeris of the spacecraft, along with the accelerations acting on it, depending on the format selected in the *director*
- a *mes* file, where each observation is stored along with its time stamp (at the time of reception), along with other relevant quantities like the receiving and transmitting station identifier, the reference frequency of the link, and its elevation at the ground station.

Other files, like the *statistique* (storing the post-fit residuals) and the *eqna* (storing the system of normal equations in binary format), are produced when a parameter estimation is performed. However, it was not possible to estimate the MOP from TGO simulated data using GINS.

GINS has been extensively used in the estimation of the rotation parameters of planetary bodies, both in simulation studies and in the analysis of real radio-tracking data from landers. Nonetheless, partial derivatives of the observables with respect to the rotation parameters are different depending on whether the planetary probe is orbiting the planet or fixed on its surface. In the latter case, the influence of the parameter on the observable is purely kinematic, while in the case of orbiters there is also a dynamical term to be included in the formulation of the partials. Partials of radio-tracking measurements with respect to the rotation parameters are currently not implemented in the GINS toolbox, and both due to time constraints and the fact that the source code of the software was not made available, it was not possible to add this functionality to GINS.

Still, GINS allowed to implement very accurate dynamical and observation models for TGO, which is why it was employed for the propagation of the spacecraft orbit and the simulation of radio-tracking observations. These outputs were in turn used in the forward approach presented in Section 6.1, to evaluate the signature of the various MOP on the TGO trajectory and radio-tracking measurements.

The dynamical model taken as nominal in the GINS simulations is shown in the first part of Table 6.1. It includes most of the gravitational accelerations mentioned in Subsection 4.1.2, namely the static gravity field of Mars up to degree and order 120, the central gravity of both Martian moons, the solid tide potential, the third-body effects from the other Solar System planets, and the Schwarzschild relativistic correction. Attempts to include a time-varying component of the Mars gravity field due to surface mass redistribution and atmospheric pressure variations (Eqs. 4.5 and 4.6) were unsuccessful. Yet, the amplitudes of these variations in the gravity field coefficients are way smaller than the coefficients themselves (up to 6 orders of magnitude smaller for C_{20} and S_{20}), and since the resulting accelerations are proportional to the coefficients, the forces not included in the dynamical model of TGO equally smaller compared to those due to the static part of the gravity field. The seasonal gravity field influences a spacecraft orbit enough for it to be detected from Doppler data (Genova et al., 2016), but since the interest here is not in the absolute orbit, but in differential orbits coming from mismodeling of the rotation of Mars, the exclusion of these effects from the simulation model should not affect the results substantially.

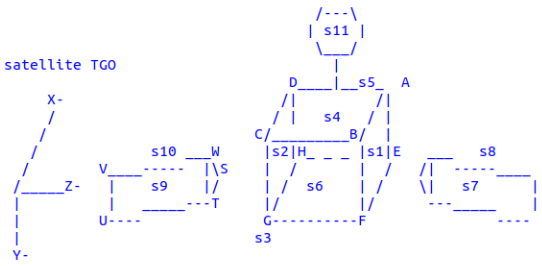

Figure 4.1: ASCII schematization of the box-wing model of TGO used by GINS for the computation of the surface forces

The accelerations modelled in the nominal case of GINS simulations are those given by Eqs. 4.8, 4.9, and 4.10. The use of these formulae in GINS required the modelization of the shape and physical properties of TGO through a macromodel, as introduced in the first paragraph of Subsection 4.1.2. Such models were present in GINS for other orbiters, but not for TGO. Hence, the TGO shape model was based off the one available for MRO, mainly because of the presence of a steerable HGA in both spacecraft. The resulting macromodel consists of a box-wing model with 4 panels for the spacecraft body and 2 for the solar panels (although the optical properties are different

G I N S	
Dynamical model	
Gravitational accelerations	
Type	Specification
Mars static gravity	MRO120D, up to degree and order 120
Phobos gravity	Central term, GM = 7.084E+05 kg m^3/s^2
Deimos gravity	Central term, GM = 9.800E+04 kg m^3/s^2
Mars solid tide from the Sun	Degree 2, $k_{20} = k_{21} = k_{22}$ =0.3
Gravity from the other planets	Central terms, DE430 ephemeris
Relativistic correction	Schwarzschild term
Non-gravitational accelerations	
Type	Specification
Atmospheric drag	TGO box-wing shape model, DTM-Mars atmospheric model
Direct solar pressure	TGO box-wing shape model
Mars radiation pressure	TGO box-wing shape model
Observation model	
Property	Specification
Ground stations	DSN-32 (New Norcia)
Measurements simulation step	300 s
Doppler integration time	60 s
Measurement noise	None
Tropospheric correction	None
Minimum elevation at G/S	5°
Integration/propagation settings	
Property	Specification
Propagator	Cowell
State vector elements	Cartesian components in MME2000
Propagation length	10 days
Integration order	8
Integration step	60 s (fixed)

Table 4.1: Nominal TGO dynamical model (gravitational and non-gravitational accelerations), observation model, and integrator and propagator settings, as used in GINS simulations

on opposite sides of the same panel), plus a paraboloid representing the HGA. The computation of the surface forces with the dynamical model presented here does not take into account the self-shadowing of the plates.

As shown in the ASCII sketch of the TGO macromodel of Figure 4.1, a total of 11 exposed surfaces characterize this shape model, and for each surface the values of the optical coefficients (emissivity, specular reflectivity, diffuse reflectivity) were taken directly from the corresponding values of the MRO model (although the values for surfaces of the same type were found to be consistent for models of different orbiters). GINS being a proprietary software, it was chosen not to list here the values of the optical coefficients assumed for each plate. The dimensions of each plate and of the antenna were loosely based off information available on the size of the real spacecraft[1]. The axes of the body-fixed frame were defined relative to the shape model in accordance to the definition of the TGO body-fixed frame in the SPICE *fk* kernel[2].

The attitude of the spacecraft body, of the solar array, and of the HGA is input in GINS through three time series of quaternions, describing the rotation from the corresponding element-fixed frame (that is, a frame fixed relative to the body, the solar panels, and the HGA, respectively) to the MME2000 inertial frame. The conversion of the *ck* SPICE kernels to series of quaternions recognized by GINS was performed by means of Fortran routines available at ROB.

Similar scripts were used to generate other environment files required for the propagation of the orbit of TGO. For example, a script allowed to convert the orbit of TGO, as given by the *spk* SPICE kernel, to a time series of cartesian coordinates expressed in the MME2000 frame. From the resulting file, GINS read the initial state of the spacecraft at each run. The ephemerides of the Martian moons, as distributed by Lainey et al. (2007) in the form of *spk* kernels, were converted to series of Chebyshev polynomials of degree 15 (a format used by GINS for the ephemerides of natural satellites), using yet another Fortran routine available at ROB.

The information on the rotation of the central body can be introduced in GINS through a *rotorcc* file. More information on the format of this text file can be found in its description by Le Maistre (2013). For the following, it is sufficient to say that this is the same file format used to input a planetary rotation model in GINS, and that is divided into different sections. The first section lists the parameter of the main rotational motion, namely a rotation with constant spin velocity and constant precession rate. Each of the ensuing sections of the file lists the parameters relative to a specific perturbation of the main rotational motion. In the *rotorcc* file relative to the nominal rotational model, based on the model from Konopliv et al. (2016) presented in Section 2.2.4, there are 4 blocks after the one describing the steady rotation of the planet with constant precession rate. These blocks are relative, in the order, to the rigid nutation series, the amplification of rigid nutations due to the FCN, the motion of the pole, and the spin angle variations.

Accelerations due to manoeuvres and AMD events are not included in the dynamical model of GINS, due to missing knowledge about their predicted magnitudes and times. Completely disregarding these effects, however, leads to unrealistic predictions of the orbital evolution of the spacecraft, which without corrective manoeuvres may be unstable (due to the atmospheric drag, or to the build-up of other kinds of perturbations). Large manoeuvers are therefore taken into account by propagating the orbit for periods smaller than 10 days, assumed to be the maximum time that the satellite can go without the need of major orbital corrections.

Hence, in a nominal simulation case, the TGO orbit is integrated over 10 days. To do so, a Cowell propagator is used, along with an integrator of order 8 and a fixed step-size (since the orbit is nearly-circular) of 60 s. When observations are simulated, a single Earth ground station is used, namely the DSN station of New Norcia, Australia. For both range and range-rate, measurement points are generated every 5 minutes. No corrections due to troposphere and ionosphere, nor any other kind of noise, was added to the data. Measurements corresponding to a radio-link at an elevation lower than 5° at the ground station were automatically removed from the dataset. The nominal GINS settings and observation model used for the simulations are shown in the second part of Table 6.1.

4.2.2. Tudat

Part of the work was performed using the TU Delft Astrodynamics Toolbox (Tudat), a multi-purpose, modular, software suite written in C++ and developed by the Astrodynamics & Space Missions group

[1] http://spaceflight101.com/exomars/trace-gas-orbiter/

[2] All the TGO SPICE kernels were obtained from the dedicated page of the ESA SPICE Service FTP

of Delft University of Technology (Dirkx et al., 2019). Tudat was essential in the second part of this sensitivity study, regarding the computation of estimation errors for the MOP using simulated observations. The modularity of Tudat made the implementation of the expressions for the partials with respect to Mars rotation parameters relatively straightforward. The code for the MOP partials in Tudat was written, verified, and validated in the frame of a timely master thesis work performed by another student, almost in parallel with the present study. Therefore, by the time this study entered its second phase, the functionalities needed for the covariance analysis were already available in Tudat.

The one at hand is a very standard orbit determination problem, which is why a Tudat tutorial application about the orbit determination of an Earth satellite was taken as reference for the main code, with very few modifications being necessary to adapt it to the specific case of TGO. Table 4.2 shows the relevant settings used in this application. In particular, the box-wing model of the spacecraft was discarded here in favour of a more simple spherical shape with equivalent mass and surface area, and unitary drag and radiation pressure coefficients. The atmosphere of Mars was simulated by interpolating tabulated values of different physical properties (density, pressure, temperature, gas constant, specific heat ratio and molar mass) averaged over latitude, longitude, and time. These values were already included in the Tudat toolbox and based on the LMD (Laboratoire de Météorologie Dynamique, Forget et al., 1999) Global Circulation Model (GCM) for Mars. A simplified cannonball model was used for the radiation pressure as well, the resulting force acting always along the direction connecting the satellite and the Sun.

As for the gravitational accelerations, only the static gravity field of Mars was accounted for in the dynamical model implemented in the Tudat script. Therefore, neither third-body effects, nor tidal interactions, nor seasonal variations of the gravity field coefficients were considered. Moreover, the relativistic effects were also assumed to be absent. The static gravity field coefficients are those of the MRO120D model (Konopliv et al., 2016). The highest degree and order of the Martian gravity field included in the force model was set to 40. A Cowell propagator was selected for the simulation of the trajectory of TGO, while a Runge-Kutta-Fehlberg 7(8) variable step-size integrator is chosen, with an initial step-size of 60 s and a minimum of 15 s. Absolute tolerances as high as 1 s were selected, since in a near-circular orbit the step-size needed is relatively constant (hence why in Table 4.2 it is listed as fixed).

The output from Tudat, including the information matrix and the measurement errors, is loaded into Python scripts, which have been written to perform the covariance analysis. Through permutation and recombination of the rows and columns of the information matrix, is it possible to obtain the formal and the consider uncertainties for a wide range of estimation strategies.

4.2.3. ORB

A first impression of the sensitivity of the TGO radio-tracking data to the MOP is given by the signature of these parameters on the satellite orbit, as well as on the particular observable. What is intended here by signature of a parameter on a specific quantity is the difference between that quantity computed using the nominal dynamical model, and another evaluation of that quantity obtained with a dynamical model where the parameter of interest is set to 0. In this sense, signatures of MOP on a radio tracking observable generally overestimate the sensitivity of the measurement to the parameter, because they ignore the correlations between parameters. Nonetheless, very small signatures may indicate a parameter that can hardly be retrieved from the observations, and thus help focus the attention of the linear regression to a restricted set of parameters.

The most straightforward method to compute the signatures of MOP is by numerical propagation of the satellite orbit using a nominal and a reduced force model. This process, while providing accurate orbits and therefore signatures, may result too computationally intensive for a simple initial phase of a full sensitivity study. Here a different technique is presented, with the advantage of being mostly analytical.

T u d a t	
Dynamical model	
Gravitational accelerations	
Type	Specification
Mars static gravity	MRO120D, up to degree and order 40
Non-gravitational accelerations	
Type	Specification
Atmospheric drag	Homogeneous sphere, LMD atmospheric model
Direct solar pressure	Cannonball model
Observation model	
Property	Specification
Ground stations	DSN-32 (New Norcia)
Measurements simulation step	300 s (range), 60 s (range-rate)
Doppler integration time	Instantaneous Doppler
Measurement noise	1 m (range), 0.1 mm/s (range-rate)
Tropospheric correction	None
Minimum elevation at G/S	None
Integration/propagation settings	
Property	Specification
Propagator	Cowell
State vector elements	Cartesian components in J2000
Propagation length (arc)	10 days
Integration order	7-8
Integration step	60 s (fixed)

Table 4.2: Nominal TGO dynamical model (gravitational and non-gravitational accelerations), observation model, and integrator and propagator settings, as used in estimations with Tudat

Kaula's theory

The method is based on the first-order integration of the Lagrange planetary equations, with a disturbing potential R equal to the non-central terms of the gravity field potential of Mars (Eq. 4.1):

$$\begin{aligned}
\frac{da}{dt} &= \frac{2}{na}\frac{\partial R}{\partial M} \\
\frac{de}{dt} &= \frac{1-e^2}{na^2 e}\frac{\partial R}{\partial M} - \frac{\left(1-e^2\right)^{1/2}}{na^2 e}\frac{\partial R}{\partial \omega} \\
\frac{di}{dt} &= \frac{\cos i}{na^2(1-e^2)^{1/2}\sin i}\frac{\partial R}{\partial \omega} - \frac{\left(1-e^2\right)^{1/2}}{na^2(1-e^2)^{1/2}\sin i}\frac{\partial R}{\partial \Omega} \\
\frac{d\omega}{dt} &= -\frac{\cos i}{na^2(1-e^2)^{1/2}\sin i}\frac{\partial R}{\partial i} + \frac{\left(1-e^2\right)^{1/2}}{na^2 e}\frac{\partial R}{\partial e} \\
\frac{d\Omega}{dt} &= \frac{1}{na^2(1-e^2)^{1/2}\sin i}\frac{\partial R}{\partial i} \\
\frac{dM}{dt} &= n - \frac{1-e^2}{na^2 e}\frac{\partial R}{\partial e} - \frac{2}{na}\frac{\partial R}{\partial a}
\end{aligned} \tag{4.11}$$

For small deviations of the orbital elements from those of a Keplerian ellipse, corresponding to a central gravity field, the elements of the Keplerian orbit can be taken as the coordinate system in which to express the perturbing potential. Hence, the pertubations to the central gravity field can be written as (Kaula, 2000):

$$R = \sum_{l=1}^{\infty}\sum_{m=0}^{l}\frac{\mu a_e^l}{a^{l+1}}\sum_{p=0}^{l}F_{lmp}(i)\sum_{q=-\infty}^{\infty}G_{lpq}(e)S_{lmpq}(\omega, M, \Omega, \theta) \tag{4.12}$$

where

$$S_{lmpq} = X_{lm}\cos\Theta_{lmpq} + Y_{lm}\sin\Theta_{lmpq} \tag{4.13}$$

and

$$\begin{cases} X_{lm} = C_{lm}, & Y_{lm} = S_{lm}, \text{ if } l-m \text{ even} \\ X_{lm} = -S_{lm}, & Y_{lm} = C_{lm}, \text{ if } l-m \text{ odd} \end{cases} \tag{4.14}$$

The phase angle is given by:

$$\Theta_{lmpq} = (l-2p)\,\omega + (l-2p+q)\,M + m\,(\Omega-\theta) \tag{4.15}$$

The dependence of the perturbing potential on the inclination of the osculating orbit is represented by the *inclination function*, $F_{lmp}(i)$, with:

$$F_{lmp}(i) = \sum_{t}\frac{(2l-2t)!}{t!\,(l-m-2t)!\,2^{2l-2t}}\sin^{l-m-2t}i\sum_{s=0}^{m}\binom{m}{s}\cos^s i\sum_{c}\binom{l-m-2t+s}{c}\binom{m-s}{p-t-c}(-1)^{c-k} \tag{4.16}$$

where k is the integer part of $(l-m)/2$, the limits of the sum over t are 0 and the smaller between p and k, and the sum over c is extended to all the permissible values of this index, namely those leading to nonzero binomial coefficients.

The eccentricity of the reference orbit appears in the expression of the perturbing potential as the argument of the eccentricity function, $G_{lpq}(e)$. In the case of long period terms, i.e. those for which $l-2p+q=0$ and the contribution of M to the phase angle disappears, it can be computed as:

$$G_{lpq}(e) = \frac{1}{(1-e^2)^{l-(1/2)}}\sum_{d=0}^{p'-1}\binom{l-1}{2d+l-2p'}\binom{2d+l-2p'}{d}\left(\frac{e}{2}\right)^{2d+l-2p'} \tag{4.17}$$

Since $G_{lpq}(e)$ is of the order of $e^{|q|}$, for near-circular orbits like that of TGO, the sum over q can be truncated to a few terms. The main assumption of the first-order theory developed by Kaula is that the

only time dependent terms in the planetary equations are the orbital elements ω, Ω, and M, and the Greenwich mean sidereal time (θ), all with a constant time derivative. In other words, the reference orbit is assumed to vary in time due to the secular variations of the argument of perigee, the right ascension of the asceding node, and the mean anomaly ($\dot{\omega}, \dot{\Omega}$, and $\dot{M}$, respectively). Moreover, the central body is assumed to be in steady rotation, with angular velocity $\dot{\theta}$. With this assumption, the phase angle can be written as

$$\Theta_{lmpq} = \dot{\Theta}_{lmpq} t \tag{4.18}$$

with $\dot{\Theta}_{lmpq} = (l-2p)\,\dot{\omega} + (l-2p+q)\,\dot{M} + m\left(\dot{\Omega} - \dot{\theta}\right)$, constant. Because the phase angles are the only terms in the system of differential equations 4.11, and their dependence on time is linear, the Lagrange planetary equations can be easily integrated analytically, yielding the deviation of the orbital elements from those of the secularly-precessing osculating orbit:

$$\begin{aligned}
\Delta a_{lmpq} &= \mu a_e^l \frac{2F_{lmp}G_{lpq}\,(l-2p+q)\,S_{lmpq}}{na^{l+2}\dot{\Theta}_{lmpq}} \\
\Delta e_{lmpq} &= \mu a_e^l \frac{F_{lmp}G_{lpq}\left(1-e^2\right)^{1/2}\left[\left(1-e^2\right)^{1/2}(l-2p+q) - (l-2p)\right]S_{lmpq}}{na^{l+3}e\dot{\Theta}_{lmpq}} \\
\Delta i_{lmpq} &= \mu a_e^l \frac{F_{lmp}G_{lpq}\left[(l-2p)\cos i - m\right]S_{lmpq}}{na^{l+3}\left(1-e^2\right)^{1/2}\sin i\dot{\Theta}_{lmpq}} \\
\Delta \omega_{lmpq} &= \mu a_e^l \frac{\left[\left(1-e^2\right)^{1/2}e^{-1}F_{lmp}\left(\partial G_{lpq}/\partial e\right) - coti\left(1-e^2\right)^{-1/2}\left(\partial F_{lmp}/\partial i\right)G_{lpq}\right]\overline{S}_{lmpq}}{na^{l+3}\dot{\Theta}_{lmpq}} \\
\Delta \Omega_{lmpq} &= \mu a_e^l \frac{\left(\partial F_{lmp}/\partial i\right)G_{lpq}\overline{S}_{lmpq}}{na^{l+3}\left(1-e^2\right)^{1/2}\sin i\dot{\Theta}_{lmpq}} \\
\Delta M_{lmpq} &= \mu a_e^l \frac{\left[-\left(1-e^2\right)e^{-1}\left(\partial G_{lpq}/\partial e\right) + 2\,(l+1)\,G_{lpq}\right]F_{lmp}\overline{S}_{lmpq}}{na^{l+3}\dot{\Theta}_{lmpq}}
\end{aligned} \tag{4.19}$$

where $\overline{S}_{lmpq}$ is the integral of S_{lmpq} with respect to its argument:

$$\overline{S}_{lmpq} = X_{lm}\sin\Theta_{lmpq} - Y_{lm}\cos\Theta_{lmpq} \tag{4.20}$$

Rotation of spherical harmonics

The assumption of uniform for the central body is certainly too strict for the application here considered, where the focus is on the impact of small differences in detailed rotation models. Nonetheless, the formalism of the equations expressing the variations of the orbital elements relative to the osculating orbit can be kept, and the perturbations to the steady rotation induced by precession, nutation, length-of-day variations, and polar motion be considered by modifying the values of the gravity field coefficients, which are considered constant in the classical derivation by Kaula. The coefficients C_{lm} and S_{lm} appearing in Eq. 4.19 will still be relative to a frame rotating with a constant rate $\dot{\theta}$, which however is now different from the body-fixed frame, due to the non-uniform rotation of the central body. Since the spherical harmonics coefficients are constant in a body-fixed frame, the coefficients in Eq.4.19 will vary with time. The approach of taking into account the full rotation model in Kaula's perturbing potential by modifying the gravity field coefficients is directly derived from Kudryavtsev (1997). In that study, orbital perturbations due to the Earth orientation parameters were computed by expressing the rotated gravity coefficients as trigonometric series, and then integrating analytically the Lagrange equations up to the fifth order. Here, a simplified version of this method is tested. The main difference between the method from Kudryavtsev (1997) and the one presented in the following is that here no attempt is made to approximate the rotated spherical harmonics coefficients with trigonometric series or any other analytical function of the MOP. In fact, no integration of these coefficients is performed at all, which is why analytical expressions are not necessary. The perturbations to the osculating orbit due to the gravitational potential of a body in non-uniform rotation are found by substituting directly the values of the rotated coefficients in Eq. 4.19. In doing so, the implicit assumption that the variation in time of the spherical harmonic coefficients is negligible compared to that of the terms $\cos\Theta_{lmpq}$ and $\sin\Theta_{lmpq}$. Thus, the

dependence on time of the right-hand sides of the Lagrange planetary equation can still be effectively considered equal to that of S_{lmpq} and its derivatives. This assumption is only valid when the angles of rotation involved in the transformation of the gravity coefficients are small. This is true of the MOP of interest for this study, although the assumption will be verified a posteriori. The two frames involved here in the transformation of the spherical harmonic coefficients are the Mars body-fixed frame and a frame describing a steady rotation of the planet around a fixed axis, which for simplicity is henceforth referred to as Kaula's frame. The z-axis of this frame is that of the GINS MME2000 reference frame, defined by the angles α_0 and δ_0. The Kaula's frame is assumed to be coincident with the MME2000 frame at $t = 0$ s from J2000. Kaula's frame rotates with respect to the MME2000 frame around their common z-axis, with a constant rate equal to $\dot{W}$. At each time step t, the rotation from the body-fixed frame to Kaula's frame is given by the matrix:

$$R_{bf}^{kaula} = R_{ICRF}^{Kaula} R_{bf}^{ICRF} \tag{4.21}$$

with R_{ICRF}^{Kaula} the matrix describing the rotation from the ICRF to the Kaula's frame:

$$R_{ICRF}^{kaula} = R_z\left(-W_{kaula}\right) R_x\left(-\frac{\pi}{2} + \delta_0\right) R_z\left(-\frac{\pi}{2} - \alpha_0\right) \tag{4.22}$$

and R_{bf}^{ICRF} the matrix relative to a rotation from the Mars body-fixed frame to the ICRF:

$$R_{bf}^{ICRF} = R_z\left(\frac{\pi}{2} + \alpha\right) R_x\left(\frac{\pi}{2} - \delta\right) R_z\left(W\right) R_x\left(-Y_P\right) R_y\left(-X_P\right) \tag{4.23}$$

The angles α, δ, W, X_P, Y_P all vary with time, and specify the Martian rotation model.

It will be shown that analytical expressions of the variation with time of the spherical harmonic coefficients in the perturbing potential and the subsequent integration of the resulting planetary equations are not necessary for the purpose of the current study. In particular, since the interest is on the order of magnitude of the signatures of the MOP on TGO's orbit, and how it changes for different satellite orbits, a first-order approximation of these quantities is deemed sufficient. Kudryavtsev (1997) provides expressions for the variations of the spherical harmonic coefficients under an elementary rotation. A method of transformation of the spherical harmonic coefficients from a body-fixed reference frame to another with generic orientation is also presented by Dirkx et al. (2019), as developed by Boué (2017). The two methods are equivalent, and described in Appendix A. For this application, the latter was preferred: although the formulas provided by Kudryavtsev (1997) have a simpler analytical expression, in that they consist of trigonometric series of the angle of rotation, they are valid for an elementary rotation around one of the 3 orthogonal axes of the frame with respect to which the rotation takes place. This means that for a relative orientation between the body-fixed and Kaula's frame which is described by a series of elementary rotations, the expressions for the rotation of the gravity coefficients have to be evaluated for each of these elementary rotations. The formulas provided by Dirkx et al. (2019) instead, while having a less explicit dependence on the rotation angles (and therefore on time), allow as input a generic rotation matrix, which thus can be the one describing the full rotation from the body-fixed to the steadily rotating frame. For this reason, while requiring more processing power and computation time for a single elementary rotation, the method from Dirkx et al. (2019) is better performing from a time and power point of view in the case of a full rotation.

Algorithm

A numerical algorithm implementing Kaula's equations in a MATLAB toolkit was already available a the Royal Observatory of Belgium, distributed internally under the name of *Orbit Reaction Blocs (ORB)*. Minor changes to the original scripts allowed for a reduction of the running time and memory usage, while keeping the general structure of the already validated software unchanged. This algorithm is stored in a single function, taking as input a vector of times at which Kaula's equations are to be evaluated, the values of the rotation angles at each time step, the initial orbital elements of the osculating orbit, and the fully normalized gravity coefficients. The output of the function is the matrix of the perturbed orbital elements at each time step.

In order to guarantee compatibility with GINS, which is used to get the numerical results and for verification of the analytical method, the rotation angles characteristic of the Mars rotation model are read from the same input file that is used in GINS, namely the *rotorcc* file mentioned in Subsection

4.2.1. The rotation model thus read was validated by comparing the corresponding body-fixed rotation matrix with that output by GINS, showing differences attributable to numerical noise (see Section 5.1.1).

Generally, the signatures of the MOP on the orbital elements of TGO are obtained by calling this function twice, with the same time vector but different rotation angles, and then subtracting the two outputs. Particular attention has to be reserved to the choice of the reference orbital elements. A the start time, the MOP signature should be zero, as was the case in the numerical results. This is because the initial states in the two cases are assumed to be the same, so that the different evolution of the orbit under a different Mars rotation model can be effectively studied. Setting the same initial osculating orbits for the two function runs, however, will not lead to the same perturbed orbital elements at the initial time. Indeed, the two body-fixed reference frames will generally not be overlapping at the initial time, due to the Mars rotation model being relative to the J2000 epoch. Therefore, the values of the gravity field coefficients in Kaula's frame will be different for the two rotation models, and this will lead to different perturbations of the orbital elements: applied to the same reference orbit, they will result in different initial states and thus non-zero MOP signatures at the initial time. Hence the correct set of reference orbital elements for each rotation model is found through a simple iterative process. First, the values of the initial *perturbed* keplerian elements, and not the osculating orbit, are selected, and set to be equal for the two rotation models. Then, the function is called for the initial time step only, using the desired perturbed initial elements as input. The resulting perturbations are subtracted from the perturbed initial elements, to obtain a new set of reference elements to be used as input for another call of the function, at the same time step. The process is repeated until the root-sum-squared (RSS) of the relative difference between sets of input orbital elements at two consecutive iterations falls below the threshold value of 10. Hence the resulting input elements are taken as initial elements of the precessing osculating orbit. The initial iterations are performed for both rotation models, so as to have two sets of osculating Keplerian elements yielding the same perturbed elements at the initial time. While the iterative process takes away from the property of the method to be analytical, it is considered necessary for a precise comparison of the signatures thus obtained with the numerical results. Nonetheless, the iterations are only used to define the input parameters, while the function itself remains fully analytical.

5 Verification and Validation

5.1. Verification

In this section, the correctness of the implementation of the theory and of the functioning of the software will be gauged. This is done separately for the two main programs developed for this thesis (see Chapter 4): the use of Kaula's equations to get the signatures of the MOP on the spacecraft trajectory and observables, as performed with ORB, and the handling of the information matrix output by Tudat to perform the covariance analysis, through the use of Python scripts. There is no verification involving GINS, since no functionalities were added to the software. Hence, Section 5.1.1 covers the verification of the most relevant functions added to the ORB package, while Section 5.1.2 is devoted to the verification of the part of the covariance analysis involving the Python scripts written for the project.

5.1.1. Verification of the analytical MOP signatures algorithms

Three main functions written in MATLAB for ORB will be verified here. The first is a function allowing to read the Mars rotation model from a *rotorcc* file, of the format used by GINS (see Section 4.2.1). The second function is used for the rotation of the spherical harmonic coefficients, which are then substituted to the constant gravity coefficients in Kaula's equations 4.19 to model perturbations in the rotation model of Mars. Finally, the third function to be verified is the one used for the conversion of the keplerian elements to LOS velocity.

Input of rotation model

The accuracy of the body-fixed Mars reference frame defined by the rotation model taken as input by the ORB scripts is tested here. The rotation matrices from the MME2000 frame and from the J2000 frame to the body-fixed frame are compared to those used in GINS for the same rotation model. The rotation matrices used in the GINS propagation can be read in the *listing* file of the execution. The two matrices reported there (one for the transformation from the body-fixed frame to the J2000 frame, the other for the transformation from the body-fixed frame to the MME2000 frame) are relative to the initial time of the propagation (since the body-fixed frame varies with time). These matrices output by GINS transform vectors in the two frames, and not the axes of the reference frames, as was the case for all the rotation matrices defined in Section 2.1. In order to obtain matrices which transform vectors and not frame axes, the formulas expressing them as successions of elementary rotations (Eqs. 2.9 and 2.14) can still be used, but the elementary matrix are in this case the transpose of those defined in Eq. 2.2.

Therefore, once the MOP values are read from the *rotorcc* file and the values of the angles α, δ, W, X_P, Y_P at a specific time t_0 are computed, the two rotation matrices are constructed in ORB using Eqs. 2.9 and 2.14, with all the angles changed of sign so that the elementary rotation matrices are transposed. Then, GINS is used to propagate the orbit of TGO, with initial time t_0, and using the same *rotorcc* as that read in ORB. The nominal settings are used for this propagation, although the settings themselves do not matter for this comparison, since only the body-fixed rotation matrices at the initial time are relevant. After the GINS execution, the rotation matrices at t_0 are retrieved from the listing file, and compared to those computed with ORB given the same *rotorcc* file (thus the same MOP).

The comparison of the rotation matrices is performed for different rotation files, all derived from the nominal, described in Section 4.2.1. These new *rotorcc* files are obtained from the nominal one by setting to 0 one or more terms in the different blocks. In particular, here four additional *rotorcc* files are generated, by setting to 0 all the polar motion amplitudes, all the LOD variations amplitudes, the core factor F, and the polar motion amplitudes at the Chandler wobble frequency, respectively. The resulting 5 rotation models are labeled as "nom", "noPM", "noLOD", "noFCN", and "noCW", respectively. The reference time is here $t_0 = 25110.6918$ JD50 (days from 01/01/1950, 00:00).

Table 5.1 show a comparison of the GINS and the ORB body-fixed rotation matrix relative to both base inertial frames, and for the 5 rotation models described by the different *rotorcc* files. The first and third columns ("Max ΔR") list the maximum, over the 9 matrix elements, of the element values given by the two programs, divided by the value output by GINS. The second and fourth columns ("Max ΔR_{nom}") display the maximum relative difference between the GINS rotation matrix linked to the specific rotation model and the GINS rotation matrix obtained for the nominal rotation model.

	MME2000		J2000	
	Max ΔR	Max ΔR_{nom}	Max ΔR	Max ΔR_{nom}
Rotation model				
nom	2.87e-11	-	2.87e-11	-
noPM	2.86e-11	5.69e-04	2.89e-11	4.74e-08
noLOD	2.95e-11	4.19e-06	2.95e-11	4.19e-06
noFCN	3.25e-11	6.14e-04	3.23e-11	4.77e-07
noCW	2.88e-11	3.25e-04	2.89e-11	2.62e-08

Table 5.1: Difference between the ORB and the GINS rotation matrices

The relative differences between the matrices generated by ORB and GINS for the different rotation models are all at the same level of 1e-11. This difference is thought to originate from the limited precision of the reference time t_0, since it was found to decrease for a shift of 1e-5 s in the t_0 value used for ORB. However, as the relative differences between the various rotation models show, the error of 1e-11 between GINS and ORB is several orders of magnitude smaller than the effect of the MOP on the rotation matrix. Therefore, the rotation model implemented in ORB from a generic *rotorcc* file is considered reliable enough to allow for a precise evaluation of the effects of the MOP on the rotation of Mars and thus on the orbit of a spacecraft.

Rotation of spherical harmonic coefficients

Here the rotation of the gravity coefficient is verified, by testing the consistency of the two equivalent methods presented in Section 4.2.3, and described in Appendices A.1 (method from Kudryavtsev, 1997) and A.2 (method from Dirkx et al., 2019). Table 5.2 shows the maximum relative difference in the variations of the coefficients coming from the two rotation algorithms, over the same time period of 2 days (from $t_i = 25116.6944$ JD50 to $t_f = 25118.6944$ JD50) and with a time step of 60 s. In other words, the quantities compared there are the deviations of the spherical harmonic coefficients from their initial value, due to the nominal rotation of Mars. For each coefficient, the difference between the deviations from the two methods (which is a function of time) is then scaled by the values of the deviations obtained with the method in A.2, and the maximum of the resulting vector forms the corresponding entry of Table 5.2. The nominal Mars rotation model implies the input of the rotation matrix from Eq. 4.21 for the method in A.2, or equivalently the succession of elementary rotations given in Eqs. 4.22 and 4.23 for the method in A.1. The time series of angles are those computed from the MOP retrieved in the nominal *rotorcc* file.

The difference in the output of the two methods is negligible, except for the order zero sine coefficients, where the relative difference is up to 1. This result stems from the comparison criterion, and from the fact that the implementation of the method from Dirkx et al. (2019) generates non-zero values of the zonal sine coefficients due to numerical errors, although these values are in the order of 1e-28. The method from Kudryavtsev (1997) does not produce this effect, since the rotations of the coefficients are described by formulas specific for each degree and order, and for the zonal sine coefficients

	C_{nm}		S_{nm}	
Degree	2	3	2	3
Order				
0	3.99e-05	6.00e-09	1	1
1	5.06e-11	1.99e-08	1.90e-09	3.67e-09
2	6.19e-06	1.39e-08	7.64e-07	1.13e-07
3	-	5.87e-09	-	2.89e-09

Table 5.2: Maximum relative difference between the deviation of the C_{nm} and S_{nm} from their initial value using the two rotation methods, over a period of 2 days

these formulas reduce to a constant 0 value. Hence, the difference between the two methods for these coefficients will be strictly equal to the numerical errors in the first method, and the relative difference will always yield 1.

As for the other coefficients, the two algorithms differ at most by about 0.005% in the computed deviations of $C_{nm}(t)$ and $S_{nm}(t)$ from $C_{nm}(t_i)$ and $S_{nm}(t_i)$ over 2 days. These differences are acceptable, and show that both methods give an accurate representation of the evolution of the gravity coefficients in Kaula's frame, with a nominal rotation model. At the same time, there is reason to believe that the same level of accuracy and consistency between the two algorithms will be reached also with a different rotation model (e.g. one of those mentioned in Table 5.1), because then the only thing to change would be the numerical values of the elementary rotation angles and of the elements of the full rotation matrix.

LOS projection

Here the verification involves the LOS projection function, which allows to convert the set of perturbed orbital elements output by the ORB main script to LOS velocity. The function is tested by comparing the signature of polar motion on GINS simulated Doppler measurements with the signature of the same parameter on the projected LOS velocity. For this, GINS is used to propagate 2 TGO orbits, one with the nominal *rotorcc* file, and the other with a *rotorcc* file where all the polar motion terms are set to 0 (labelled as "noPM" in Table 5.1). Apart from the rotation models, all the other options for the GINS execution are the nominal ones listed in Table 6.1. The propagation is carried on over 10 days, from $t_i = 25110.4684$ JD50 to $t_f = 25120.4615$ JD50. Hence, the signature of polar motion is obtained by subtracting the synthetic measurements output by GINS for the two runs. The orbits relative to the two measurement simulations are stored in the *orbite* GINS file. From there, the cartesian components of the velocity are projected to the line-of-sight using the function implemented in ORB. The signature of polar motion on the LOS velocity is then found by subtraction of the two LOS velocity vector thus computed.

Figure 5.1 shows the comparison between the signature of polar motion on the GINS simulated Doppler measurements and on the LOS velocity projected from the corresponding GINS orbits. For the sake of this plot, the time stamps associated with the GINS orbits had to be converted from ET to UTC, by means of the SPICE *deltet* routine[1]. Moreover, the Doppler points were converted to LOS velocity according to Eq. 3.4, dividing the frequency shift by $2M_{bd}f_T/c$, where the reference downlink frequency in the nominal GINS execution is $M_{bd}f_T = 8.419$ GHz, and c is the speed of light. The bottom part of the Figure shows the difference between the two sets of points, relative to the maximum value of the signature on the Doppler observations. This relative difference is below 0.5%. This error is justified by the fact that the Doppler measurements are integrated over 60 s, while the LOS projection is proportional to the instantaneous Doppler. In view of this, the agreement is considered sufficient to justify the use of the projected LOS velocity as a measure of the signature on the Doppler observable itself.

In ORB, before the LOS projection, the perturbed Keplerian elements are converted to cartesian components using the SPICE *conics* routine[2].

[1] https://naif.jpl.nasa.gov/pub/naif/toolkit_docs/FORTRAN/spicelib/deltet.html
[2] https://naif.jpl.nasa.gov/pub/naif/toolkit_docs/FORTRAN/spicelib/conics.html

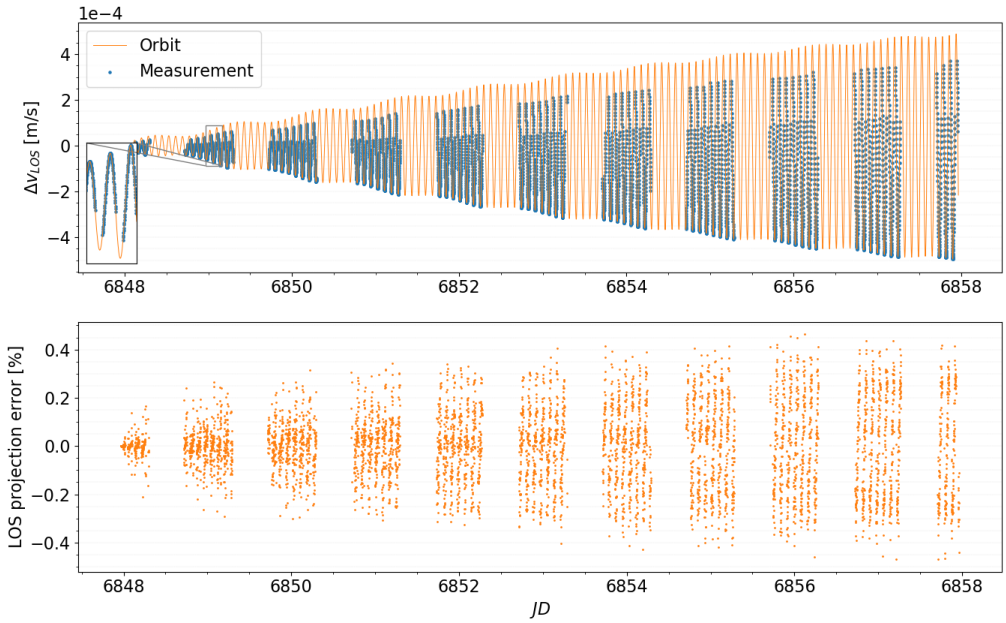

Figure 5.1: Top: signature of polar motion on the projected LOS velocity (solid orange line), and on the simulated two-way Doppler measurements (points in blue). Bottom: difference between the polar motion signature on the GINS Doppler measurements and that on the corresponding LOS projected velocity, as a percentage of the former.

5.1.2. Verification of the covariance analysis algorithms

Observation partials

The verification of the observation partials implemented in Tudat is performed by comparing the elements of a column of the observation matrix to the numerical approximation of the partial derivatives of the observable with respect to the parameter corresponding to said column. Here, a central finite difference over 2 points is used to approximate the partials of the observables with respect to the parameter of interest (p). This means that the numerical derivative is computed as:

$$\frac{\partial h}{\partial p} \approx \frac{h(p_0 - \Delta p) - h(p_0 + \Delta p)}{2\Delta p} \tag{5.1}$$

where the notation $h(p_0 - \Delta p)$ indicates an observable obtained using a dynamical model where the parameter of interest differs by a small quantity Δp from its nominal value, p_0. The numerical derivation is performed by simulating sets of observables relative to same observation and dynamical models, except for the value of the parameter of interest, and then combining these two vectors according to the expression of the finite difference method. The perturbations are symmetrical with respect to the nominal value, which corresponds to the parameter value used to generate the information matrix with Tudat. It is stressed here that none of the partials used to get the results presented in the next chapter were implemented in Tudat in the frame of this study. Hence, a systematic verification of the expressions for all the partials is outside of the scope of this project. Still a single case is analyzed here, since an equivalence between the numerical partials and the information matrix entries, apart from confirming the validity of the expressions used for the partials, can be interpreted as a positive feedback about the overall functioning of the estimation process setup in Tudat.

The parameter chosen for the verification of the partials is the cosine term of the CW harmonic of the X_P polar motion component. Its nominal value is here assumed to be 55 mas. The choice of this parameter is due to the fact that polar motion is the main focus of the project, and this amplitude is expected to be the largest among the polar motion ones. The value of Δp is taken to be 5 mas, so that two sets of Doppler measurements are generated, using a value of 50 mas and 60 mas for X^c_{CW}, respectively. The estimation interests a single arc of 2 days.

The comparison of the two types of partials (that is, those output by Tudat and stored in the information matrix, and those computed by numerical differentiation) for each measurement point is shown in Figure 5.2. Each point in this plot represents the difference between the two partials at a specific observation time, scaled by the maximum (absolute) value of the information matrix column relative to X^c_{CW}. The choice of the scaling factor is justified by the fact that the partials oscillate around zero, thus scaling the difference at each observation by the corresponding information matrix element would lead to divergence problems. Moreover, the partials diverge to high positive values towards the end of the estimation arc, which is why the last 5 observations are discarded for both sets of partials. The divergence is due to loss of accuracy of the interpolations algorithms used in Tudat towards the edge of the estimation domain. It can be seen that the relative difference between the two types of partials is below 1% after two days, indicating consistency in the modelling of the dependence of the observables on the parameter of interest.

The difference between the two types of partials is presumably due to the discretization error, and could be lower if methods with orders of accuracy higher than the second in Δp are used.

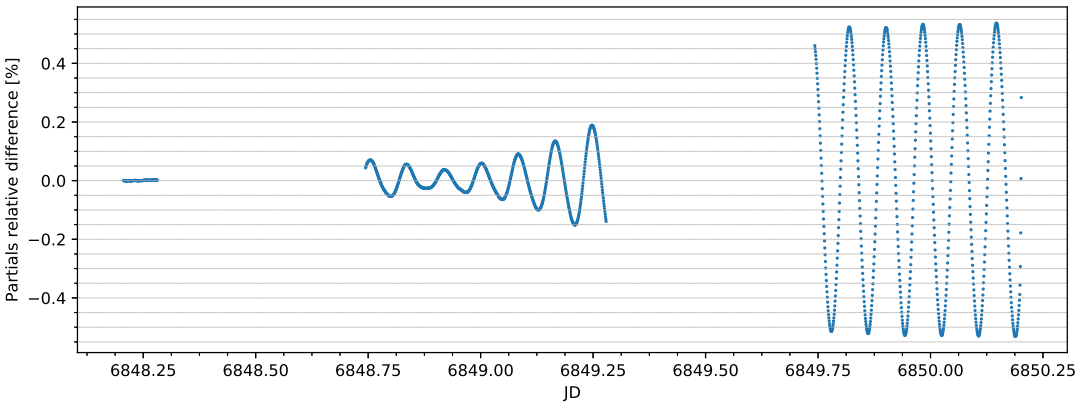

Figure 5.2: Relative difference between the Doppler partials with respect to X^c_{CW} obtained by numerical differentiation and those retrieved from the information matrix, expressed as a percentage of the maximum value of the information matrix partials

Normal matrix inversion

The covariance matrix of the estimated parameters is one of the outputs of the Tudat script. Yet, most of the times the set of parameters estimated in Tudat is not the same as the set of parameters to estimate in the covariance analysis performed with the Python scripts (the results of which are presented in Section 6.3). This is true, for example, when a subset of the parameters is shifted to the consider parameters and fixed to their a priori value. Moreover, sometimes it is preferred to use Tudat to estimate only a subset of parameters at a time, to reduce the memory usage and avoid memory errors, which can happen due to the large amount of measurements (about 6000 observations per day, over 700 days) and of parameters (up to about 600). Hence, generally the covariance matrix output by Tudat cannot be employed to retrieve the uncertainties of the parameters to estimate. Instead, a new normal matrix has to be created in Python, starting from an observation matrix obtained by combination and rearrangement of one or more observation matrices computed with Tudat. The covariance matrix is then found by inversion of this normal matrix, through the *linalg.inv* function[3] of the *NumPy* Python library. The accuracy of this process, which includes the parameters selection (through permutation of the observation matrix columns) and the numerical inversion of the normal matrix, is tested here.

This is done by comparing the correlations matrix generated with the Python script to the one output by Tudat. Only a subset of the parameters mentioned in Section 6.3 is selected for the estimation in this verification process, with the assumption that a positive result for this reduced normal matrix could be expanded to the inversion of the full one. Specifically, the Mars gravity field coefficients are excluded from the set of parameters, which is therefore reduced to 582 elements. These include: the 6 cartesian components of the initial TGO state at each of the 70 10-day arcs (420 elements); the drag and radiation pressure coefficients for each arc (140 elements); the F and σ_{FCN} parameters of the

[3] https://docs.scipy.org/doc/numpy/reference/generated/numpy.linalg.inv.html

nutation amplification transfer function (2 elements); the LOD variations amplitudes (sine and cosine) for the first four multiples of the annual frequencies (8 elements); the sine and cosine amplitudes of the X and Y polar motion components, at the annual, semiannual, and Chandler wobble frequencies (12 elements).

The first thing to be verified is the method of selection of the parameters to estimate and the consider parameters, since in this case there are no consider parameters and the full information matrix is to be used to construct the normal matrix. This can be achieved by setting to 0 the value of the corresponding variable in the Python script, and leaving the rest of the script unchanged. Then, the normal matrix is inverted, and the corresponding normalized covariance matrix is subtracted to the reference correlations matrix (i.e., the one given by Tudat). The resulting matrix is divided, element-wise, by the reference correlation matrix. These operations yield the matrix of the relative differences between the two normalized covariance matrices. Multiplying the entries of this last matrix by 100 gives the difference between the two matrices expressed as a percentage of the reference matrix. The entries of this 582x582 matrix have a mean of -0.022% and a standard deviation of 4.7%, with roughly 0.03% of the elements being outside the 3σ interval. However, the statistics of these relative error drop to 7.53e-5% for the mean and 0.005% for the standard deviation when only the matrix blocks relative to the MOP are compared (i.e. the intersection of the last 22 rows and columns).

The difference between the two numerical inversions can be explained by the high condition number of the normal matrix, which is about 1e10, making the inversion solution affected by numerical noise. Still, the agreement between the covariances computed for the MOP is accurate enough to not compromise the results obtained for the uncertainties of the parameters. Moreover, the level of agreement between the two matrices indicates a correct selection of the parameters to estimate in the Python script. Hence, the inversion method in Python can be used to compute the formal uncertainties from the one or more Tudat observation matrices.

5.2. Validation

As for the verification, the validation only interests applications related to ORB and to Tudat, since nothing was developed for GINS. Still, GINS is here used as a reference, in the sense that the ORB results are validated against equivalent numerical GINS solutions, in Section 5.2.1. As for the Tudat application and the corresponding Python script, they are validated in Section 5.2.2.

5.2.1. Validation of the analytical MOP signatures algorithms

Nominal orbit

The TGO trajectory generated by ORB with the nominal rotation model, expressed in terms of the set of perturbed Keplerian elements, is compared to the orbit propagated by GINS with the same dynamical model. The rotation model is read from the nominal *rotorcc* file, and includes the contributions from all the MOPs, in all their harmonics. The same *rotorcc* file is input in GINS to model the rotation of Mars. Both the GINS and the ORB orbit predictions are obtained with a gravitational potential of Mars truncated to degree and order 10 as the only source of perturbation to the Keplerian orbit. Since the GINS results are assumed to be the more precise of the two sets, these differences are also referred to as errors.

Figure 5.3 presents a comparison of the two TGO orbits over the 2 days of orbit propagation, from t_i = 6854.1918 JD to t_f = 6856.1973 JD. The difference between the two sets of orbital elements is given as a percentage of the maximum value of the GINS solution (and not the GINS solution itself, in order to avoid divergence for values of the elements close to 0).

The ORB perturbed orbital elements follow closely those propagated by GINS, at least over this time span. Both i and Ω present a noticeable drift along with the oscillations typical of the errors on the other elements, that may lead to error 10 times as large after the nominal 10 days of propagation assumed for GINS and Tudat. Over 2 days, the most conspicuous exception to the good accuracy of the ORB solution is the evolution of the argument of perigee. This orbital element shows similar spectral components for the two orbits, but with amplitudes about twice as large for the GINS trajectory, as can be seen in Figure 5.4. Such large differences in the ω variation amplitudes come from a mismodeling on the part of ORB, but the precise cause of this error was not pinpointed and the problem is still unsolved. Given the low eccentricity of the orbit, the errors in the ω amplitude result mostly in a shift in the tangential position of the spacecraft as predicted by ORB with respect to the GINS trajectory.

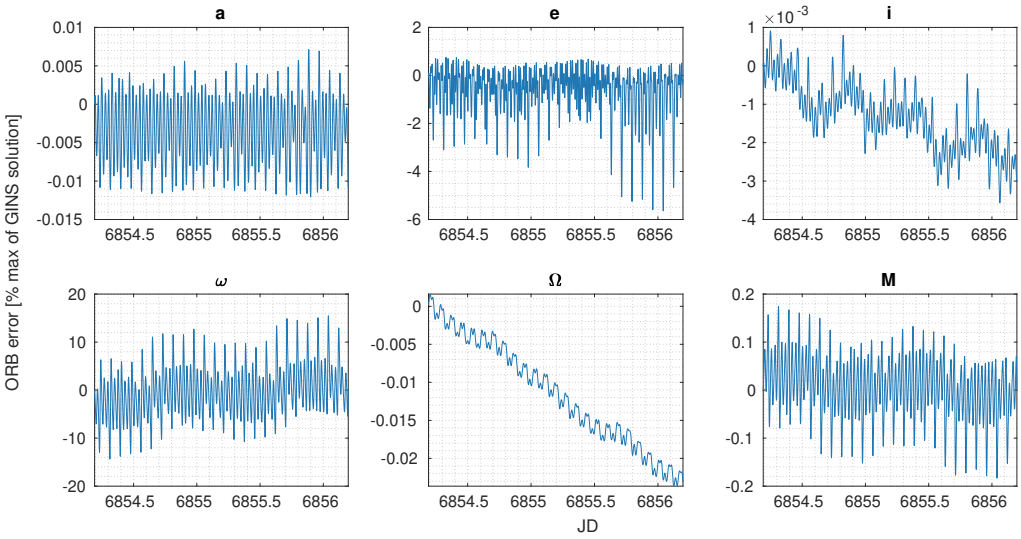

Figure 5.3: Difference between the TGO Keplerian elements obtained with ORB and GINS over 2 days, expressed as a percentage of the maximum value of the GINS solution for each orbital element

A shift in the tangential direction is also given by errors in the value of the mean anomaly (M), which in this case are in the order of 0.1% of the maximum GINS value (although the mean anomaly assumes values in the range 0°-360° over less than 2 hours, hence the errors relative to the instantaneous value of M, and not to 360°, may be at least one order of magnitude larger for about 30% of the time). The low eccentricity of TGO may justify an ambiguity in the mean anomaly, with the errors in ω which should in that case be absorbed by those in M. Yet, the low level of the errors in M indicates that this is not the (main) cause of the mismodeling by ORB.

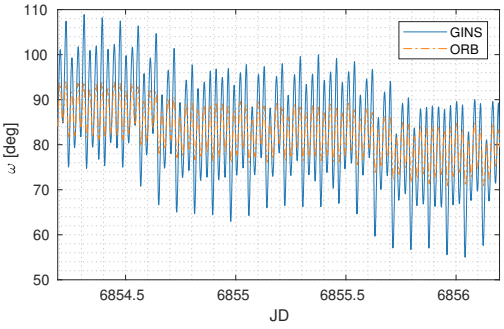

Figure 5.4: Comparison of GINS and ORB propagation of the TGO argument of perigee (ω), over 2 days

Nonetheless, the computation of the orbital elements is only an intermediate step of the ORB algorithm, for which the output is the signature of the MOP on the LOS velocity. Since an a priori prediction of how these errors on ω and the other elements propagate to the final LOS signature result is not straightforward, it is not possible to draw conclusions on the feasibility of ORB for the computation of MOP signatures from these large errors alone.

Thus, the verification process is not abandoned, and the ORB trajectory is converted to cartesian coordinates, expressed in the MME2000 inertial frame. The differences between the cartesian states in this frame from the two programs are depicted in Figure 5.5, again as a percentage of the maximum value output by GINS for each quantity. Even with the same initial conditions, and a dynamical model consisting solely of the Mars gravity field, these differences reach up to 20 km in the position components after only 2 days, and are in the order of tens of m/s for the velocity components. Clearly, effects of order higher than the first in the time variable (Kaula's main assumption is that the phase angle varies linearly with time) have an important impact on the precise state of TGO.

As discussed previously for the Keplerian elements errors, the main intent of this ORB application is not so much to accurately predict the absolute orbit of the spacecraft, as to asses the magnitude of the orbital perturbations due to small variations in the Mars rotation model. Hence, even if the absolute TGO trajectory generated with ORB is tens of km away from the more precise GINS orbit, the differences between two ORB orbits may still prove close enough to those from GINS to make the results useful to the research goals.

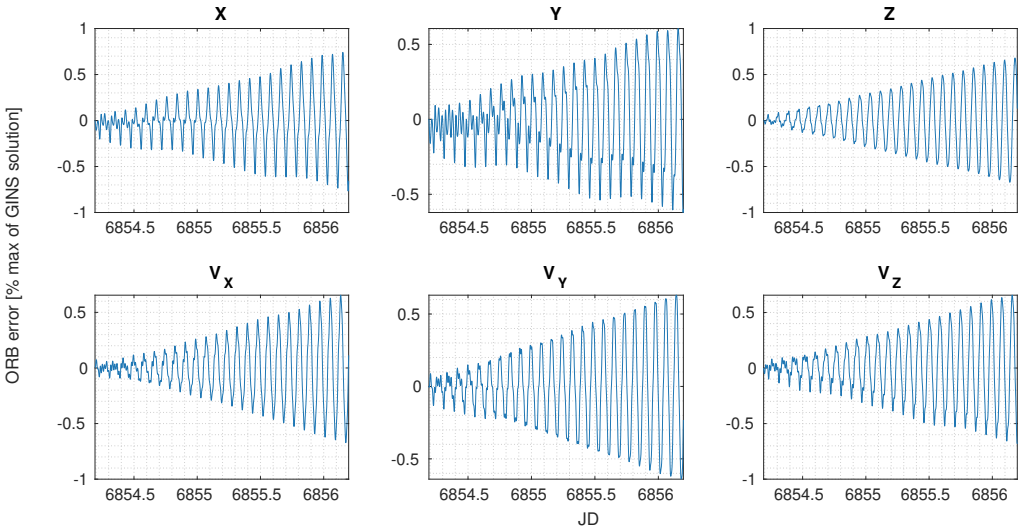

Figure 5.5: Difference between the cartesian components of the TGO position and velocity obtained with ORB and GINS over 2 days, expressed as a percentage of the maximum value of the GINS solution for each component

MOP signatures

Looking at the curve in Figure 5.6, this seems to be the case. The plot shows the difference between the signature of polar motion on the LOS velocity (Δv_{LOS}) given by GINS and ROB. The relative difference referred to in the y-axis on the right is the error in Δv_{LOS} scaled by the maximum value of the GINS LOS velocity signature (to avoid division by 0, which is also the value of Δv_{LOS} at the start time). The difference between the two signatures reaches up to 10% of the GINS maximum after 2 days. This error is considered small enough to allow ORB to be used for a preliminary study of the magnitude of these signatures.

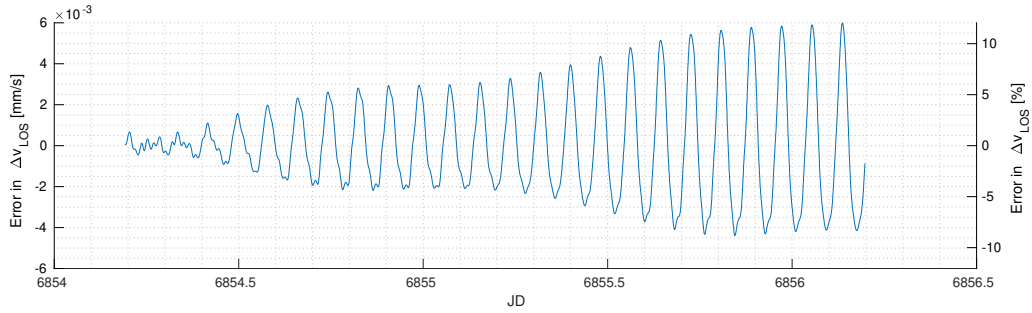

Figure 5.6: Difference in the signature of polar motion on the LOS velocity between the ORB and the GINS orbits of TGO over 2 days. The y-axis on the left shows the absolute values of the signature, while the values on the right y-axis are scaled by the maximum value of the GINS signature

The difference between the results from the two programs can be clearly seen when comparing the signatures of polar motion on the Keplerian elements, as in Figure 5.7. The outputs from GINS and ORB are similar for the signatures on the elements a, i, and Ω. For the other three elements, the two sets of signatures have sizeable differences in their trend, possibly due to different amplitudes of long-period terms. Yet, the errors in these in-plane elements, which can be more than twice the reference values, do not propagate with the same order of magnitude in the projection to LOS.

In order to substantially reduce the execution time of ORB, the signatures of the MOP shown above are compared with those obtained by truncating the gravity field of Mars at degree and order 3. The two sets of signatures on the Keplerian elements are plotted in Figure 5.8, while Figure 5.9 shows the error on the LOS velocity signature of the low-degree gravity solution compared to the one given by a 10-by-10 potential. These errors reach up to 3% of the maximum LOS velocity signature after 2 days. Based on this, a gravity field model truncated at degree and order 3 is taken as nominal.

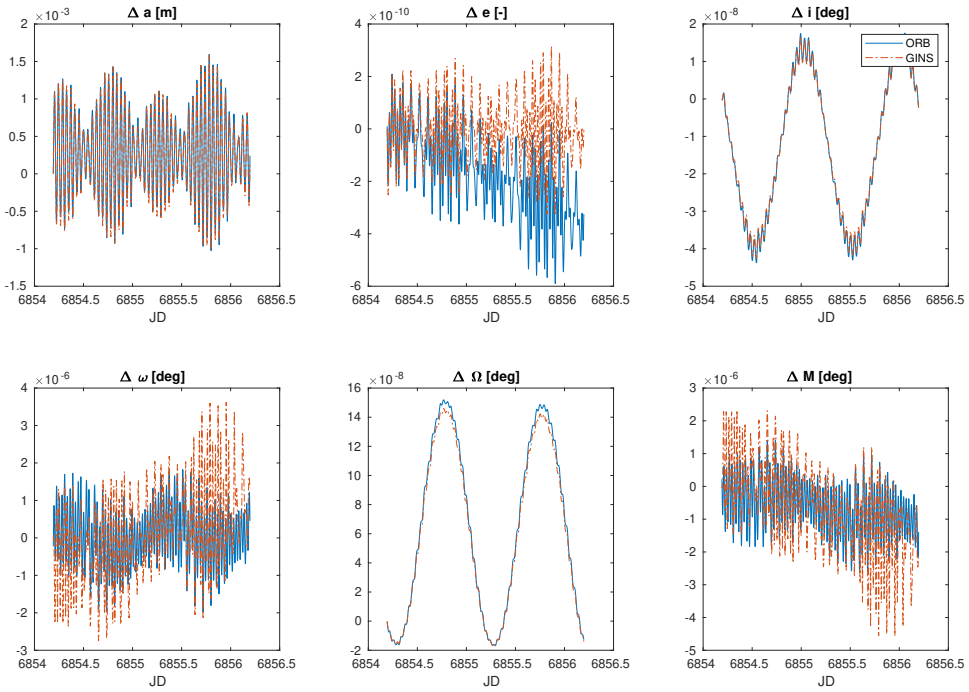

Figure 5.7: Comparison between the polar motion signature on the TGO Keplerian elements as given by ORB (blue solid line) and GINS (orange dashed line), over 2 days

Finally, a comparison between the GINS and ORB polar motion signatures over 10 days, both obtained with a degree-3 gravity field, is presented in Figure 5.10. Here it is more clear how for the elements e, ω, and M, the ORB results misrepresent long-period (in the order of tens of days) perturbations by the polar motion parameters.

Still, even after 10 days, the difference in the v_{LOS} signature from the two methods is below 10% of the GINS value, as shown in Figure 5.11.

While a similar agreement with the GINS signature is found for the LOD variations, the same is not true for the FCN parameters and the precession rate. This is shown in Figure 5.12, which, like Figure 5.7 for polar motion, plots the signatures of the core factor F on the keplerian elements of TGO, as obtained with GINS and with ORB. It is clear how the two solutions diverge immediately, mostly due to secular terms in the i and Ω signatures which are not modelled by GINS. Unmodelled effects of the same kind also appear when ORB is used to predict the signature of the precession rate on the spacecraft trajectory. This is possibly due to the large value of these angles compared to those associated with polar motion and LOD variations. Consequently, ORB will only be used to predict the signature of polar motion and LOD variations.

Truncation of the eccentricity series

Some assumptions made in the development of the ORB scripts may not hold for spacecraft in orbits different from that of TGO. It is the case for the truncation of the series expansion of the eccentricity function, $G_{lpq}(e)$ in Eq. 4.12, for which only terms of q comprised between $-l$ and $+l$ were considered. This was a sound approximation for TGO, given that its eccentricity is below 0.1 and the terms excluded were smaller than e^l, thus below 0.01 (the degree 1 coefficients in the static gravity field model used are all 0). For orbits with different eccentricities, however, the limits of the summation over q may need to be larger to avoid neglecting significant contributions to the perturbations of the orbital elements. These limits are parameterized through the factor q_{max}, so that the summation limits lie between $-q_{max}l$ and $q_{max}l$. Ten different orbits are then considered, all with inclination $i = 5°$ and periapsis distance $h_p = 400$ km, but with eccentricities linearly spaced between $e = 0.01$ and $e = 0.7$. The signatures of LOD variations on each of these orbits are computed over 2 days, using values of q_{max} between 1 and

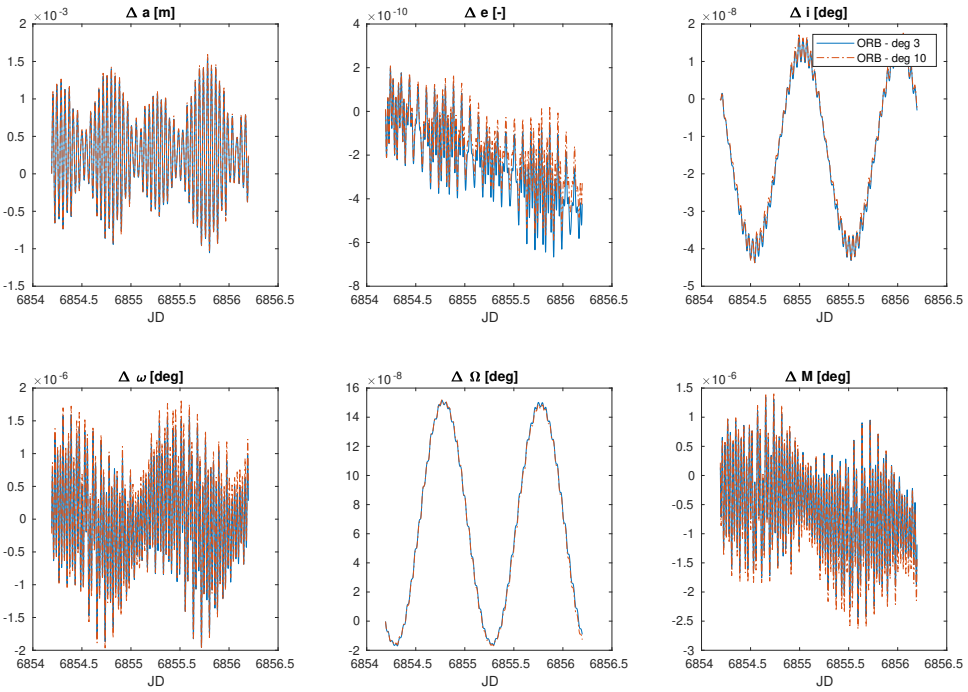

Figure 5.8: Comparison between the polar motion signature on the TGO Keplerian elements given by ORB with the Mars gravity field truncated at degree 3 (blue solid line) and at degree 10 (orange dashed line), both over 2 days

5. The maximum of each signature over the whole time span is then compared to the maximum of the LOD signature given by GINS for the same orbits. Table 5.3 shows the ratio between the maximum Δv_{LOS} given by ORB and those given by GINS. The closer this value is to 1, the more precise is the ORB result.

The table cells are colour coded depending on the time required to generate the result with ORB. Larger range of values for q imply a larger number of terms in the expansion of the potential, and consequently larger execution times. The execution time reported here includes also the time required for the iterative adjustment of the Keplerian elements of the reference orbits, as described in Section 4.2.3. The first two rows of the Table confirm the fact that for eccentricities smaller than $e = 0.1$, using values of q_{max} larger than 1 provides insignificant (if at all) improvement in the accuracy of the Δv_{LOS} solution. On the other hand, for eccentricities larger than about $e = 0.5$, not even using $q_{max} = 5$ ensures that all the significant contributions from the $G_{lpq}(e)$ are considered, since the difference between the solution with $q_{max} = 4$ is still high and no convergence is reached. In particular, for the orbit with $e = 0.7$, it was found that a q_{max} of 10 was needed to get a solution which was roughly 80% of the GINS one, while still not converging to a constant value with larger q_{max}. The inclusion of limits so large for q makes the ORB script extremely slow, and takes away the major advantage of using the analytical method with respect to the more precise numerical propagation. For this reason, only orbits with eccentricities lower than $e = 0.5$ are considered in the following.

The first two plots in Figure 5.13 show the maxima of the polar motion signature on the LOS velocity for an array of 80 orbits characterized by the values of the eccentricities from the first 8 rows of Table 5.3, and 10 different inclinations, linearly spaced between $i = 5°$ and $i = 85°$. The first plot contains the results from ORB, the second those from GINS. The colour scales for the two plots are the same, and the colour distribution in each tile is the linear interpolation of the corner values. The third plot shows the difference between the two matrices of Δv_{LOS}, expressed as a percentage of the GINS matrix. The ORB matrix has a peak in the same location as the peak seen in the GINS matrix, and the overall data distribution is also similar to the GINS one. The errors are considerably large for high inclinations and eccentricities, reaching up to 70% of the reference value. This region corresponds to the area of the plots where the Δv_{LOS} is the smallest, hence these errors do not affect the search for the pair of orbital

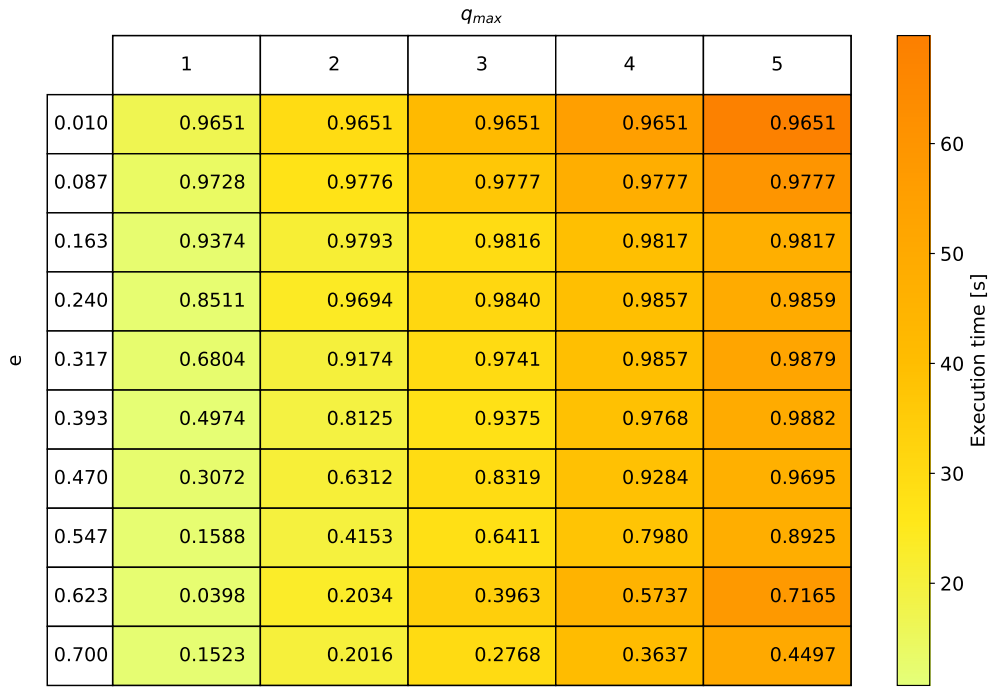

Table 5.3: Maximum Δv_{LOS} given by ORB over the same quantity as computed with GINS, for 10 orbits with the same inclination ($5°$) and eccentricities linearly spaced between 0.01 and 0.7. The values along each row vary due to the different limit for the eccentricity function $G_{lpq}(e)$ series expansion, as expressed by q_{max}. The cells are color coded depending on the ORB execution time

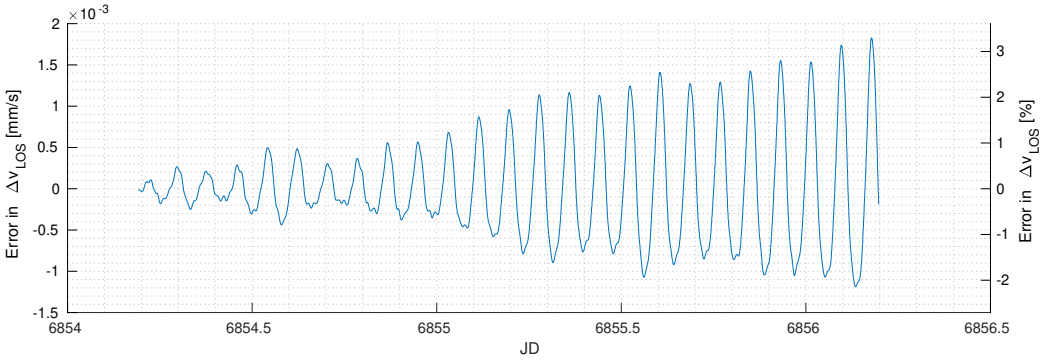

Figure 5.9: Difference in the signature of polar motion on the LOS velocity between two ORB orbits obtained with a Mars gravity field up to degree and order 3 and up to degree and order 10, respectively. The y-axis on the left shows the absolute values of the signature, while the values on the right y-axis are scaled by the maximum value of signature relative to the degree-10 orbit

elements yielding the maximum Δv_{LOS}.

The same comparison, on the same set of orbits, is made for the signatures of LOD variations on the LOS velocity, as shown in Figure 5.14. Again, the values predicted by ORB are fairly similar to those from GINS. The largest errors are again in the region corresponding to large inclinations and eccentricities of the nominal orbit, although the maximum value of the errors is smaller than for the polar motion signature.

5.2.2. Validation of the covariance analysis algorithms

Consider covariance computation

In this section, the computation of the contribution of the consider parameters to the final consider uncertainty is verified. Hence, the formula from Eq. 3.46 is subject to validation. The implementation of the consider covariance algorithm in the Python scripts is tested by solving the simple Example problem in Tapley et al. (2004, pp. 410-416), and comparing the results with the solutions given therein. While a step-by-step solution is given in the reference, the equations involved are also listed here. In fact, an approach which is formally slightly different is followed here, because it better reflects the logic behind the Python scripts, which takes as input the full information matrix and then partitions it depending on the choice of the consider parameters. The problem is that of a point mass in free fall. The only force acting on the mass is the gravity, assumed to cause a constant acceleration g on the particle, so that the equation of motion is written as:

$$\ddot{x} = g \tag{5.2}$$

where x is the vertical position of the particle, which moves with a vertical velocity v. The full state vector is:

$$\boldsymbol{X} = \begin{bmatrix} x \\ v \\ g \end{bmatrix} \tag{5.3}$$

The equation representing the dynamics of the system is linear:

$$\dot{\boldsymbol{X}} = F\left(\boldsymbol{X}, t\right) = \begin{bmatrix} v \\ g \\ 0 \end{bmatrix} = A\boldsymbol{X} \tag{5.4}$$

where

$$A = \frac{\partial F}{\partial \boldsymbol{X}} = \begin{bmatrix} 0 & 1 & 0 \\ 0 & 0 & 1 \\ 0 & 0 & 0 \end{bmatrix} \tag{5.5}$$

Three observations of the position of the particle are available at times $t_0 = 0$s, $t_1 = 1$ s, and $t_2 = 2$ s. The equation relating the measurements taken at time t_i to the corresponding state vector $\boldsymbol{X}_i = \boldsymbol{X}(t_i)$ is written as in Eq. 3.18, and is also linear:

$$\boldsymbol{Y}_i = G\left(\boldsymbol{X}_i, t_i\right) + \boldsymbol{\epsilon}_i = x + \epsilon_i = \tilde{H}_i \boldsymbol{X}_i \tag{5.6}$$

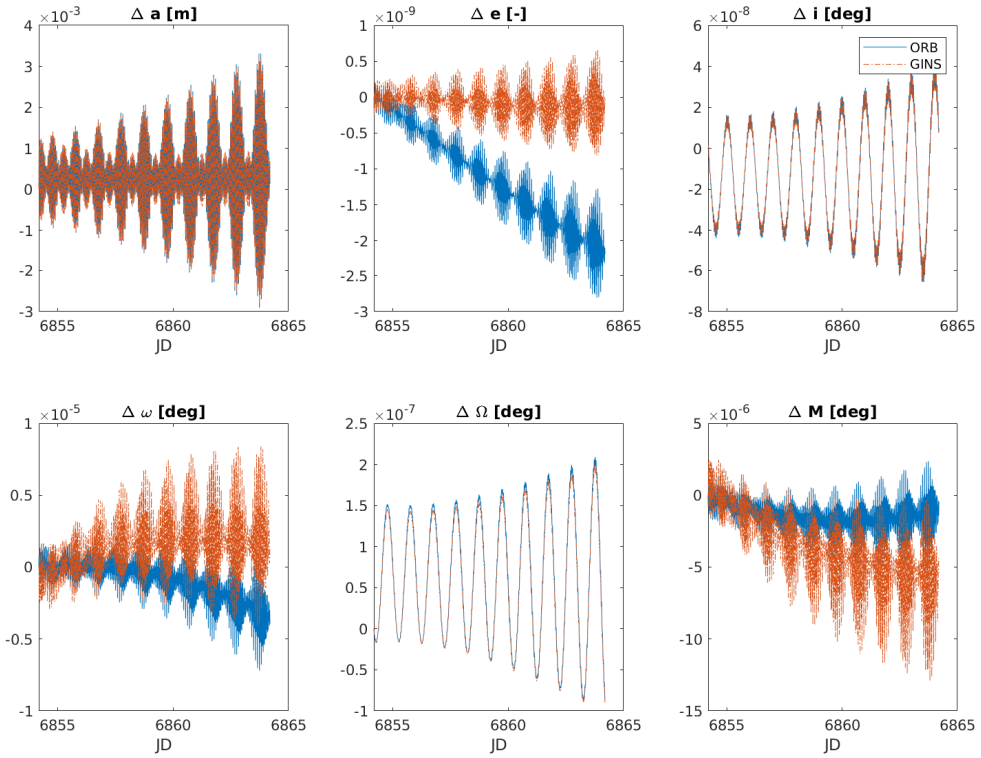

Figure 5.10: Comparison between the polar motion signature on the TGO Keplerian elements as given by ORB (blue solid line) and GINS (orange dashed line), over 10 days and with a degree-3 Mars gravity field

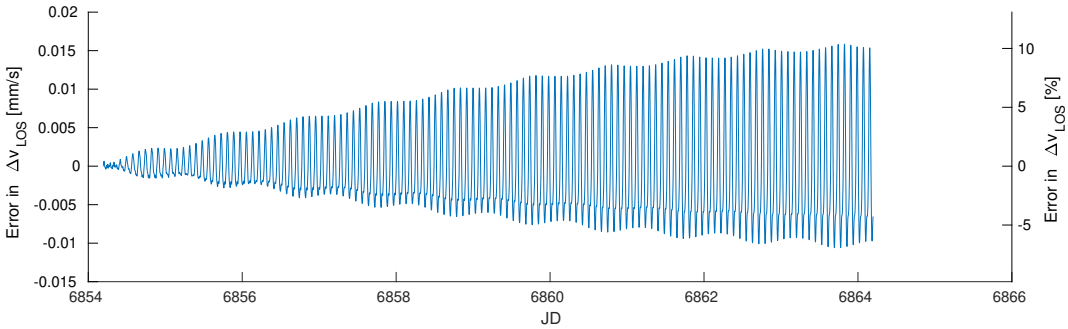

Figure 5.11: Difference in the signature of polar motion on the LOS velocity between the ORB and the GINS orbits of TGO, computed over 10 days and with a degree-3 Mars gravity field. The y-axis on the left shows the absolute values of the signature, while the values on the right y-axis are scaled by the maximum value of the GINS signature

with ϵ_i the (scalar) measurement error and

$$\tilde{H}_i = \frac{\partial G(\boldsymbol{X}_i, t_i)}{\partial \boldsymbol{X}_i} = \begin{bmatrix} 1 & 0 & 0 \end{bmatrix} \tag{5.7}$$

If the state at $t_0 = 0$s is chosen as reference, the vectors $\boldsymbol{X}_I$ at the other observation times can be ralated to it through the state transition matrix (see Eq. 3.23). Since this matrix is the solution of the differential equation

$$\dot{\boldsymbol{\Phi}}(t, t_0) = A\boldsymbol{\Phi}(t, t_0) \tag{5.8}$$

it has the form:

$$\boldsymbol{\Phi}(t, t_0) = Ke^{A(t-t_0)} \tag{5.9}$$

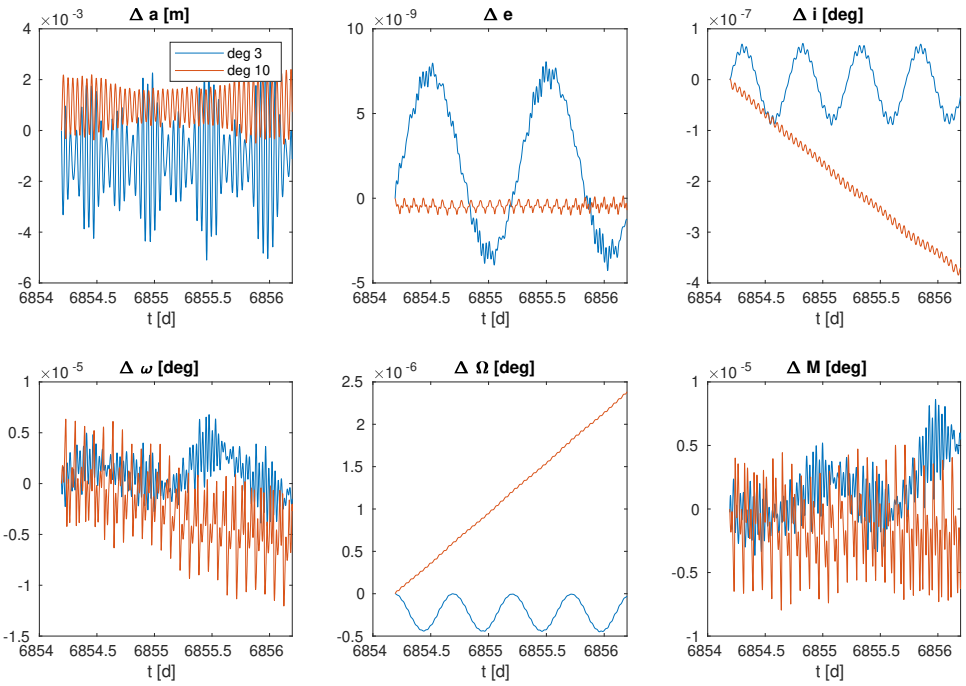

Figure 5.12: Difference in the signature of polar motion on the LOS velocity between the ORB and the GINS orbits of TGO, computed over 10 days and with a degree-3 Mars gravity field. The y-axis on the left shows the absolute values of the signature, while the values on the right y-axis are scaled by the maximum value of the GINS signature

Given the initial condition $\boldsymbol{\Phi}(t_0, t_0) = I$, the scaling factor is $K = 1$, and:

$$\boldsymbol{\Phi}(t, t_0) = e^{A(t-t_0)} = I + A\,(t - t_0) + \frac{A^2}{2}(t - t_0)^2 = \begin{bmatrix} 1 & (t-t_0) & (t-t_0)^2/2 \\ 0 & 1 & (t-t_0) \\ 0 & 0 & 1 \end{bmatrix} \tag{5.10}$$

since powers of A higher than the second are equal to the null matrix. The full design matrix is finally:

$$H = \begin{bmatrix} \tilde{H}_0 \boldsymbol{\Phi}(t_0, t_0) \\ \tilde{H}_1 \boldsymbol{\Phi}(t_1, t_0) \\ \tilde{H}_2 \boldsymbol{\Phi}(t_2, t_0) \end{bmatrix} = \begin{bmatrix} 1 & 0 & 0 \\ 1 & 1 & 1/2 \\ 1 & 2 & 2 \end{bmatrix} \tag{5.11}$$

The state vector is then partitioned in parameters to estimate and consider parameters, g being the only consider parameter. Accordingly, the matrix of the observation partials is separated in a component relative to the parameters to estimate (H_x), and one relative to the consider parameter (H_c), so that

$$H_x = \begin{bmatrix} 1 & 0 \\ 1 & 1 \\ 1 & 2 \end{bmatrix} \qquad H_c = \begin{bmatrix} 0 \\ 1/2 \\ 2 \end{bmatrix} \tag{5.12}$$

The a priori covariance of the parameters to estimate is taken to be the identity matrix, just like the a priori covariance of the measurement errors, that is, $W = \overline{W}_0 = I$. The a priori covariance of the consider parameter, g, is taken here to be 3 m/s^2, so that $\overline{P}_{cc} = [9]$ The result obrained for covariance of the estimated parameters without consider parameters is then:

$$P_0 = \left(H_x^T W H_x + \overline{W}_0\right)^{-1} = \begin{bmatrix} 0.4 & -0.2 \\ -0.2 & 0.267 \end{bmatrix} \tag{5.13}$$

The sensitivity matrix is found to be:

$$S_{xc} = P_0 H_x^T W H_c = \begin{bmatrix} 0.1 \\ 0.7 \end{bmatrix} \tag{5.14}$$

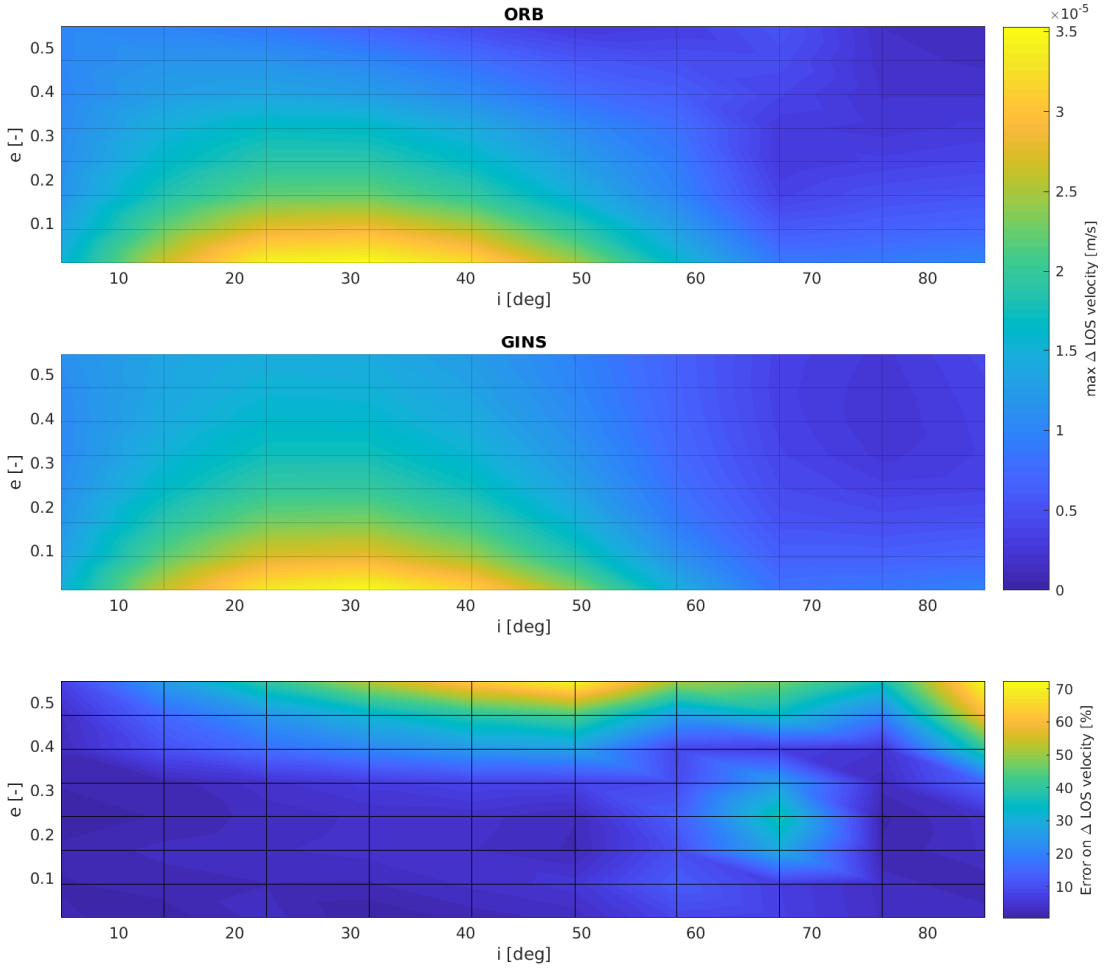

Figure 5.13: Comparison between ORB (top panel) and GINS (middle panel) matrices of the maximum PM signature on v_{LOS} as a function of the orbit inclination and eccentricity. The difference between the two matrices, as a percentage of the GINS values, is shown in the bottom panel

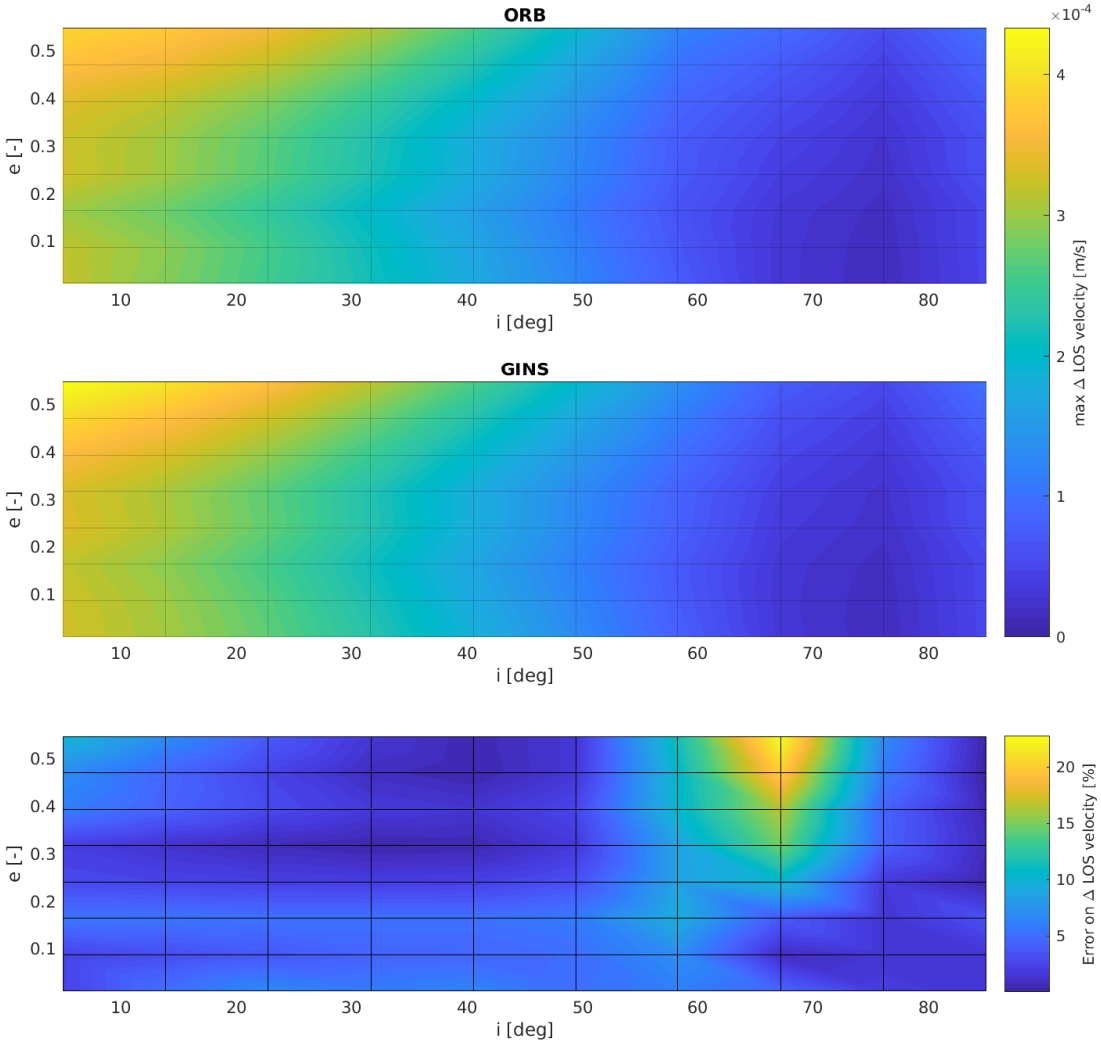

Figure 5.14: Comparison between ORB (top panel) and GINS (middle panel) matrices of the maximum LOD signature on v_{LOS} as a function of the orbit inclination and eccentricity. The difference between the two matrices, as a percentage of the GINS values, is shown in the bottom panel

Hence, the matrix of the consider covariances is:

$$P_{xx} = P_0 + S_{xc}\overline{P}_{cc}S_{xc}^T = \begin{bmatrix} 0.49 & 0.43 \\ 0.43 & 4.68 \end{bmatrix} \tag{5.15}$$

These results are in agreement with the reference solutions for the corresponding matrices given in the reference (Tapley et al., 2004, pp.413-414), when $\overline{P}_{cc} = [9]$ is substituted for the a priori covariance of the consider parameters.

TGO orbit propagation

The validation of the TGO orbits propagated with Tudat is performed by comparing the cartesian states of the spacecraft with orbits propagated with GINS, using similar dynamical model and initial states. The full dynamical model selected in GINS (shown in Table 6.1) is simplified to agree with the full model of the Tudat propagation (shown in Table 4.2), which only includes the Martian gravity field up to degree 40, the aerodynamic drag, and the radiation pressure, where the spacecraft is modelled as a uniform sphere. The differences between the cartesian components of the position of TGO predicted, with this dynamical model, by GINS and Tudat are shown in Figure 5.15. The position components are relative to the MME2000 inertial frame. The disagreement between the two orbits after 10 days is in the order of 100 m in the cartesian components. This difference is mostly due to the modelling of the non-gravitational forces, since the Mars atmosphere and the solar flux models used in the two runs are not the same (although the spacecraft shape and physical properties are modelled in the same way).

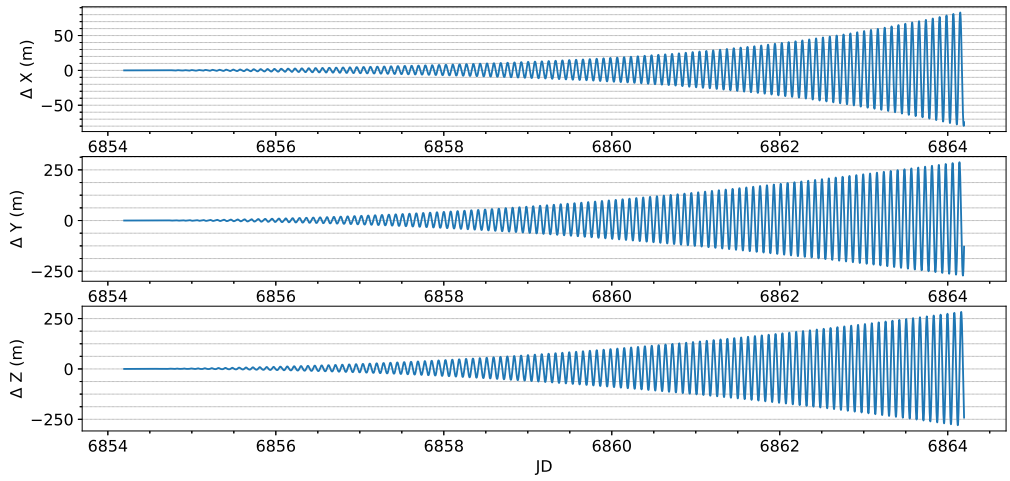

Figure 5.15: Differences in the MME2000 position component of TGO between the orbit propagated by Tudat with the full dynamical model and the orbit propagated by GINS with an equivalent dynamical model

Indeed, when the dynamical model is restricted to the sole degree-40 gravity field of Mars, the differences are at the meter level (Figure 5.16). Here, the deviations are explained by differences in the integrator settings (although both are of the same order and with the same step-size, as shown in Tables 6.1 and 4.2) and eventual small disparities in the two initial states.

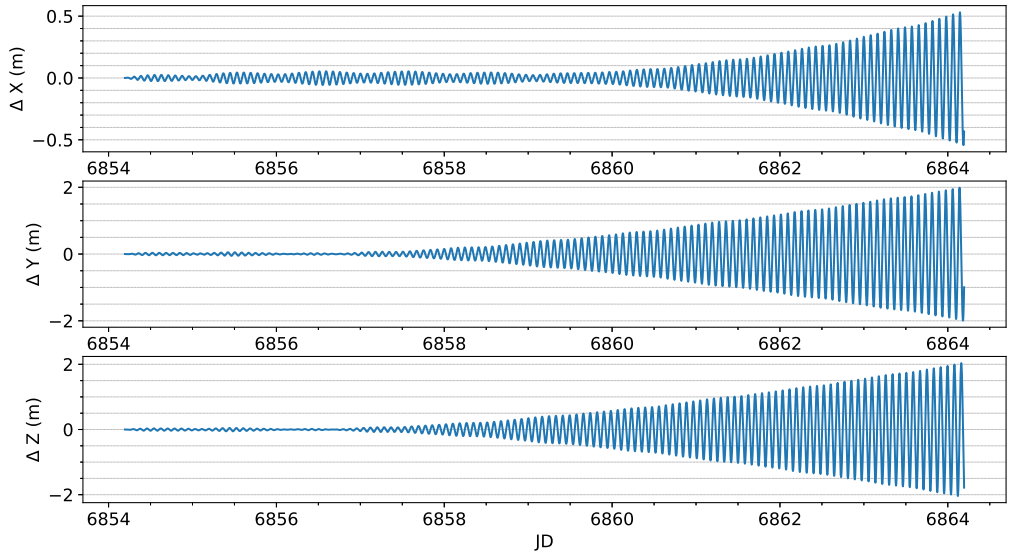

Figure 5.16: Differences in the MME2000 position component of TGO between the orbit propagated by Tudat and the one propagated by GINS with a dynamical model consisting of only the Mars gravity field up to degree 40

6 Results

In this Chapter, the main results obtained from the software described in Chapter 4 and validated in Chapter 5 are presented. Each of the following three sections mainly focuses on the outputs of one of the three main programs employed in this project: GINS, ORB, and Tudat. Specifically, GINS was used to perform high-precision simultations of the trajectory and measurements of TGO, given the accurate dynamical model described in Section 4.2.1. Hence, Section 6.1 treats the signatures of the MOP on the spacecraft trajectory and tracking data, as computed with GINS.

ORB, instead, was used to develop an analythical method to assess those same signatures with a simpler dynamical model but with an improvement in execution speed and insight in the process. Thus, the outcome of this analytical study is found in Section 6.2.

Finally, Tudat was employed for the assessment of the accuracy of the MOP estimation from radio-tracking data. This was done through a covariance analysis, the results of which are presented in Section 6.3.

6.1. MOP signatures: numerical approach

In this section, the signatures of the relevant Mars orientation and rotation parameters will be presented, as obtained numerically with GINS. Both the signatures in the TGO trajectory (Section 6.1.1) and in the radio-tracking observables (Section 6.1.2) will be considered, the latter being compared to the noise level for the specific observable in order to asses the detectability of the signal. Moreover, Section 6.1.3 will show a comparison with the polar motion signature on MRO, which should give a preliminary assessment of if and to what extent TGO is more sensitive than MRO to the polar motion parameters.

6.1.1. Signatures on TGO trajectory

The impact of variations in the rotation model of Mars on the state of TGO can be expressed in different sets of coordinates. Depending on the chosen coordinates in which the state of TGO is expressed, it may result for a parameter to affect a subset of these coordinates more than the rest. This kind of information may reveal details about the most favourable spacecraft configuration and observable type for the retrieval of the parameter. Here, the effects on the RTN (radial, tangential, and normal) components of the spacecraft position, velocity, and acceleration are analyzed. The RTN frame is that relative to the nominal orbit of TGO, that is, the one obtained with a full rotation model. The state of TGO throughout the nominal orbit is expressed in the areocentric MME2000 frame. Hence, the rotation matrix transforming a vector in the MME2000 frame to RTN coordinates is given, at each timestep, by:

$$R^{RTN}_{MME2000} = \left[\frac{\boldsymbol{r}}{|\boldsymbol{r}|} \quad \frac{\boldsymbol{t}}{|\boldsymbol{t}|} \quad \frac{\boldsymbol{h}}{|\boldsymbol{h}|}\right]^T \tag{6.1}$$

with $\boldsymbol{r}$ and $\boldsymbol{v}$ the position and velocity vectors of the spacecraft, $\boldsymbol{h} = \boldsymbol{r} \times \boldsymbol{v}$, and $\boldsymbol{t} = \frac{\boldsymbol{h}}{|\boldsymbol{h}|} \times \frac{\boldsymbol{r}}{|\boldsymbol{r}|}$. While varying with time, the rotation matrix from the MME2000 to the RTN frame is assumed to be constant at each time step, that is, $R^{RTN}_{MME2000} = 0$, so that the components of the velocity and the acceleration vectors can be obtained just like for the position vector by left-multiplication of the corresponding vector in the MME2000 frame by $R^{RTN}_{MME2000}$.

Figure 6.1 shows the signatures of the Chandler wobble on the radial, tangential, and normal components of the position, velocity, and acceleration of TGO over 10 days, from $t_i = 6847.98$ JD to $t_f = 6857.96$ JD. The two orbits used to generate these signatures are computed with the nominal settings for GINS, as listed in Table 6.1. The only difference between the dynamical model in the two cases is the rotation model of Mars, read once from the nominal *rotorcc* file and the other from the *rotorcc* file labelled as ”noCW” in Table 5.1.

The largest effect on the position is by far in the along-track direction, building up to more than 10 cm over the 10 days period. The signature in the radial position builds up with time as well, but is two orders of magnitude lower than that in the tangential direction. The signature in the normal direction, instead, oscillates without diverging, with a constant amplitude of about 5 mm. The effects on the radial and tangential component of the velocity are inverted with respect to those on the position, the largest signature being in the radial velocity component and building up to 0.1 mm/s. The behaviour of the signatures in the acceleration RTN components reflects that in the position components, with a maximum signature of 10^{-7} m/s^2.

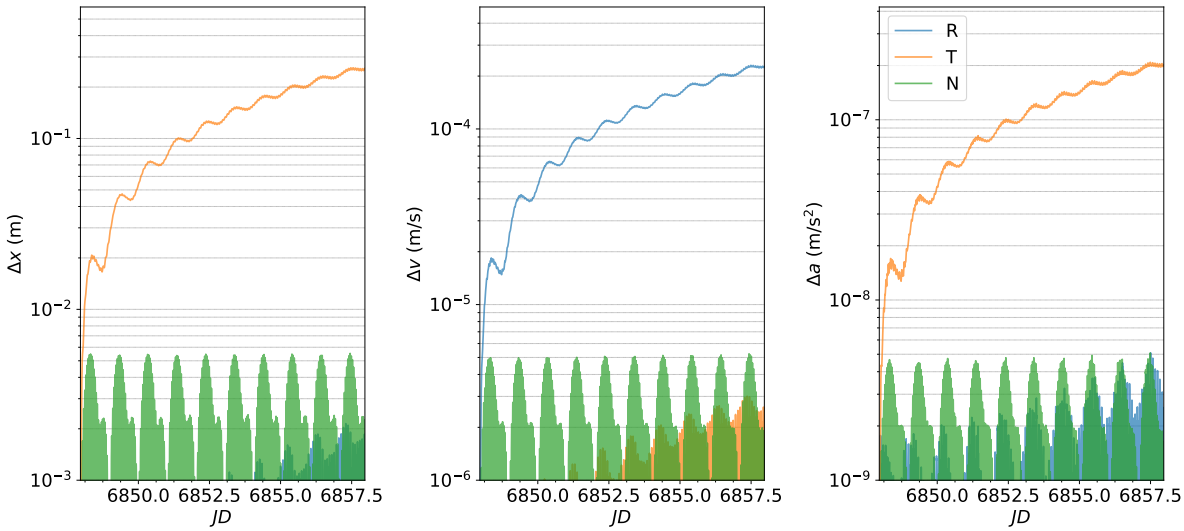

Figure 6.1: Signature of CW on the RTN components of TGO trajectory in the MME2000 frame

The reason for the similarity among curves across the plots in Figure 6.1 is to be found in the choice of the reference frame in which these signatures are displayed, namely the RTN frame relative to the nominal orbit. The overlap between the signature on the position in the tangential direction and the one on the velocity in the radial direction can be visualized in the simplified case of a purely circular orbit for TGO, and assuming the module of the velocity (v) to be the same for the two orbits at each time step. Then, a small shift (Δx_T) in the tangential position of the spacecraft following the mismodeling of the CW, as shown in the leftmost plot, would imply that, at a generic time, the two predictions of the spacecraft position are separated by a small angle θ. The assumption of equal v for both predictions means that the difference between the two velocity vector is all in the radial direction, and is roughly equal to $v\theta$. As $\theta = \Delta x_T/x$, x being the position of TGO (all in the radial direction), the radial component of the differential velocity is $\Delta v_R = v/x\Delta x_T$. It happens that for TGO the ratio of the module of the velocity and the range from Mars (about 3.35 x 10^3 m/s versus 3.8 x 10^6, both varying little along the orbit because of the low eccentricity) is roughly 10^{-3}. Hence, $\Delta v_R \approx 10^3 \Delta x_T$, as seen in the plots. The same argument can be made for the acceleration, which in a circular orbit is in the radial direction, so that the difference in acceleration between two points at a small distance along-track is on the tangential direction.

In the real case, where the two compared orbits are not perfectly circular, the small-angles approximations are still valid for a Δx_T of a few centimetres, when compared to the thousands of km of x. Nonetheless, the CW will also produce a signature on the norm of the velocity, v, meaning that the differential velocity will not be all in the radial direction. Yet, the position displacement builds up faster than the error on v (since it the corresponding integrated quantity), so that in the case of Figure 6.1 its effects (in generating a radial velocity signature) are larger than the direct error on the v value, which

may lead to a velocity signature in any direction. This may not be true in the case of signatures from other parameters, hence in the following the plots for Δx, Δv, and Δa are all shown, even if there may be redundancy, as seen for the CW.

Similar is the relation between the signatures in the position, velocity, and acceleration due to LOD variations, as shown in Figure 6.2. The GINS options are the same as above, except the non-nominal *rotorcc* file is in this case the one labelled as "noLOD" in Table 5.1. The magnitude of the perturbations, however, is larger than for the CW, with the signature in the position building up to about 1 m in the along-track direction. The signatures in the two other directions are larger as well, with that in the normal component twice as large as with the CW, and that in the radial component one order of magnitude larger than the CW signature. The same observations could be made for the signatures of LOD variation on the velocity and acceleration RTN components, the velocity perturbation reaching a maximum of 1 mm/s after 10 days.

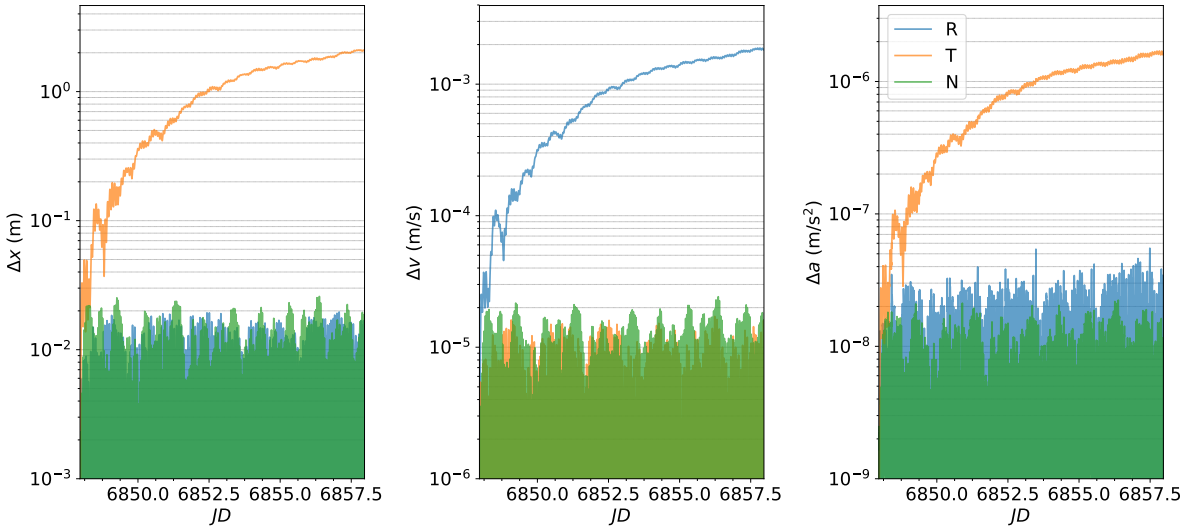

Figure 6.2: Signature of LOD variations on the RTN components of TGO trajectory in the MME2000 frame

Figure 6.3 displays the signatures of non-rigid nutations (obtained by setting $F = 0$ in one of the two rotation models, hence using the "noFCN" *rotorcc* file). The largest signatures are again in the tangential direction for the position and the acceleration of TGO (up to almost 3 m and roughly 10^{-6} m/s^2, respectively) and in the radial direction for the velocity (up to 2 mm/s). Moreover, the signature in the normal direction is larger than for the previous parameters, and has an amplitude increasing with time.

Finally, the signatures of the precession on the state and acceleration of TGO are presented in Figure 6.4. Here the non-nominal *rotorcc* file is generated by setting to zero the precession rate. The general behaviour is similar to the previous cases, in that most of the position error is in the tangential direction. Nonetheless, the magnitude of these signatures is very large in all directions, reaching more than 1000 m, and the signature in the radial and normal components is larger than before relative to the tangential one.

6.1.2. Signatures on the observables

The results presented here concern the signatures of the MOP of interest on the radio-tracking observables. Only range and range-rate observations are considered, since the signatures on the position seem to be too small to generate a sensible signal in the angular separation measurements. In particular, for VLBI with phase referencing, the realistic accuracy of 1 nrad (e.g. Bocanegra Bahamon, 2019) translates into an uncertainty in the position of TGO in the order of 100 m (assuming a distance of the spacecraft from Earth in the order of 100 million km). Such an uncertainty in the plane-of-sky position of TGO (normal to the LOS direction) is well above the perturbation on the orbit arising by a mismodeling of the MOP seen in Figures 6.1 to 6.4 (generally less than a few meters), with the exception of the precession rate signature.

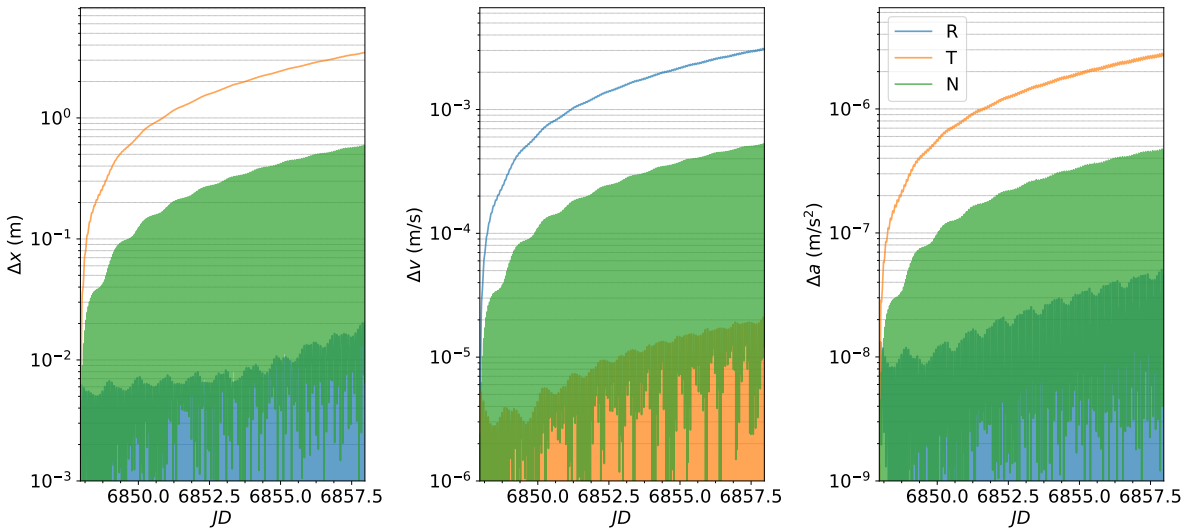

Figure 6.3: Signature of non-rigid nutation amplification on the RTN components of TGO trajectory in the MME2000 frame

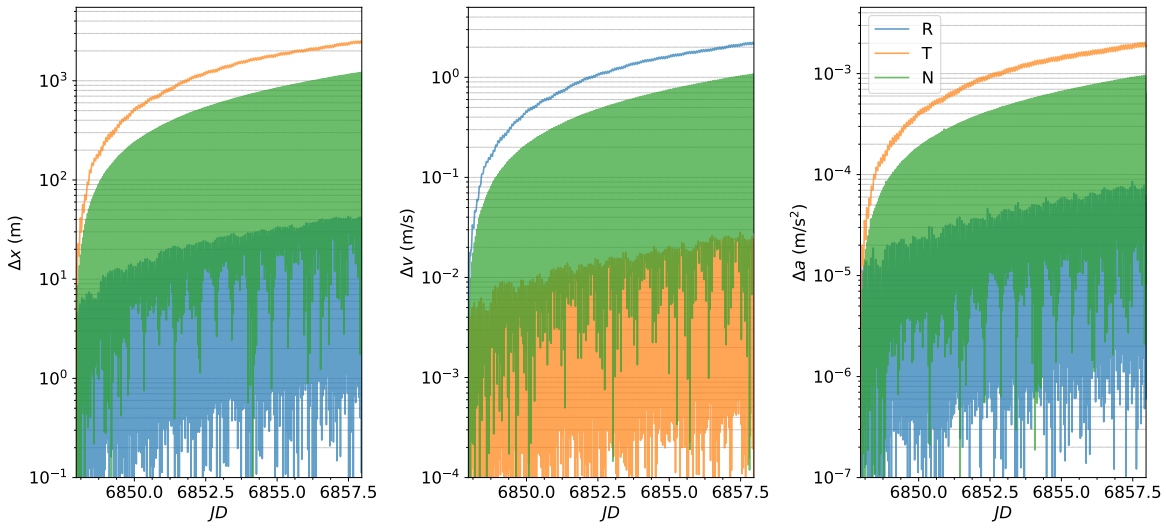

Figure 6.4: Signature of precession on the RTN components of TGO trajectory in the MME2000 frame

For both observable types, only one ground station on Earth is assumed to maintain a radio link with TGO, and that is the ESTRACK New Norcia station, in accordance with the nominal options of GINS in Table 6.1. The TGO dynamical and observation, as well as the integration and propagation settings, are also those listed in said table.

The results for each observable will be compared to a reference noise level. As a general rule of thumb, parameters responsible for a signal in the data lower than the noise level will be hard to extract from the measurements. This is not always true, as there is not a linear relation between the signature in the measurements and the achievable uncertainty of the parameter: estimation of parameters with signatures above the noise level may not be possible due to high correlations with other variables, and a signal from a parameter could be extracted even if it is below the noise floor. Still, the signatures on the measurements can be used as a preliminary assessment of the accuracy to be expected for the parameter relative to others.

Range

Figure 6.5 displays the signature of the different MOP of interest on the range measurements, over a period of 10 days. The shaded area represents the typical noise level of this type of measurements,

supposed to be 1 m. For the Chandler wobble, the maximum signature in the range data is around 10 cm, thus well below the noise level of the observations. Both LOD variations and non-rigid amplification of the nutations, instead, have signatures which rise above the signal noise after 2 to 4 days of tracking, although reaching a maximum value which is right above the noise level. Different is the effect of the precession rate on the range data, with a signal-to-noise ratio (SNR) of about 10^3. Therefore, range data could definitely prove useful in the estimation of the precession rate from TGO, but the estimation of the other MOP from this kind of data is challenging.

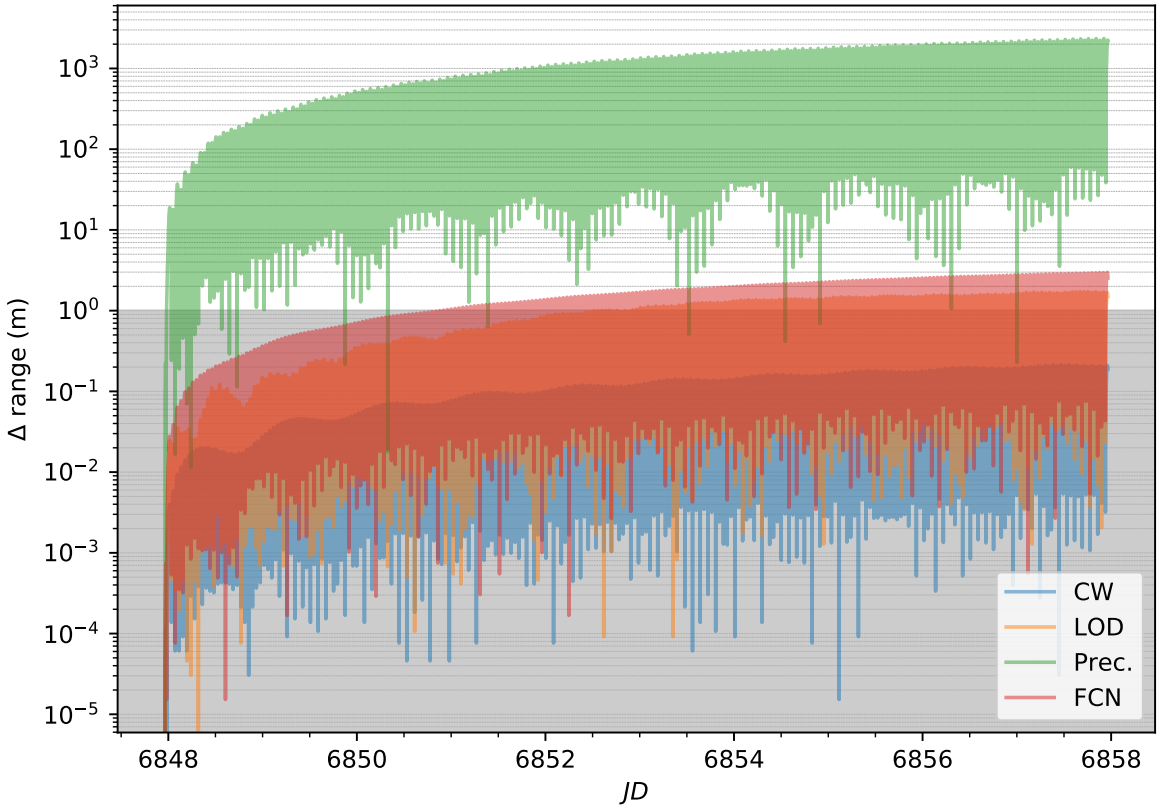

Figure 6.5: Signature of different MOP on the TGO range observable

Range-rate

Figure 6.6 shows the signature of the Chandler wobble (CW), the LOD variations (LOD), the precession rate (Prec), and the liquid-core amplification of the nutations (FCN) on the simulated TGO range-rate observations at the ESTRACK station of New Norcia. Along with the signatures, plotted as a function of the observation times, two angles characterizing the geometry of the observations are plotted. The β angle is the angle formed by the orbital plane and the direction connecting the satellite and the ground station. It is 0° for an edge-on orbit, and $\pm$90° for a face-on orbit. The second angle plotted in the upper part of the figure, Ω, is the right ascension of the ascending node of TGO. Because of its inclination, TGO has a relatively short period for the precession of the orbital nodes compared to other (mainly polar) orbiters. This period is around 140 days, and this is why the variation of the β angle is mostly modulated by the variations of Ω (as opposed to the relative motion of the Earth and Mars).

The measurements are simulated using arcs of 10 days, covering a total of about 150 days, so that the full nodal precession period of TGO is probed. The noise level is set to 6 mHz, or about 0.1 mm/s, which is a conservative value (see Section 3.1.3). All the MOP considered have a signature in the Doppler which is above the noise in most of the arcs. The LOD variations, the Chandler wobble, and the non-rigid nutations amplification have signatures with generally an SNR of 10 and higher. The SNR is the lowest for very negative values of β, and is maximum when β is close to 0°, i.e. for edge-on orbits. The high signature of the precession rate is in agreement with the results from other orbiters: an

uncertainty of less than 0.04% of the nominal value of this parameter was obtained using only range and Doppler data from orbiters (Konopliv et al., 2016).

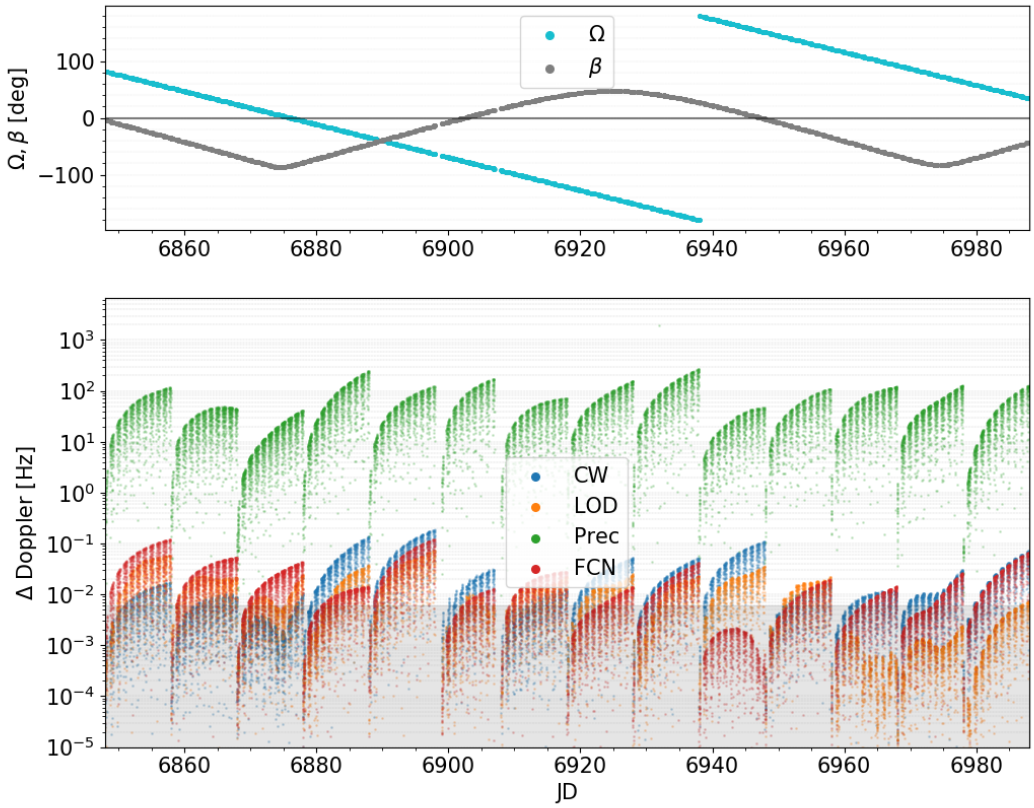

Figure 6.6: Top: evolution of the angles Ω and β describing the orientation of the TGO orbital plane and the LOS direction. Bottom: signature of different MOP on the TGO Doppler observable

6.1.3. Comparison with MRO

Once the magnitude of the MOP signatures on the radio-tracking data from TGO has been assessed in an absolute sense, it seems interesting to investigate how these signatures compare to those relative to a spacecraft in a different orbit. Whether and to what extent the orbital configuration of TGO is more favourable than others for what concerns the estimation of a specific MOP is one of the research questions mentioned in Section 1.2. Several spacecraft have been orbiting Mars and providing radio-tracking data, thus it's important to establish the improvement to this dataset given by TGO.

A comparison between the signature of polar motion (all 3 frequencies) on the Doppler observable of TGO and that of Mars Reconnaissance Orbiter (MRO) is shown in Figure 6.7. MRO is on a nearly circular orbit at an inclination of about 93° and a lower altitude than TGO, around 300 km from the Martian surface. The higher inclination is responsible for a longer period of nodal precession, which is why the Ω angle for MRO shows little variation in the 30 days spanned by the plots. The evolution of the β angle was not included in the Figure, because it followed closely that of Ω for both spacecraft (hence, at least in this short time span, the variations of β are modulated mostly by the motion of the spacecraft orbital plane, and not by the relative motion of the Earth and Mars). The two sets of TGO observations are obtained using the GINS nominal settings from Table 6.1, and with the rotation models labeled as "nom" and "noPM" in Table 5.1, respectively. The same settings are used for the two MRO simulations, and this required the generation of the spacecraft ephemeris and attitude input files from SPICE (the macromodel was already available in GINS), as done for TGO (Section 4.2.1).

The maximum value of the signature is larger for TGO, but overall the difference between the two signatures is relatively small, and probably not enough to justify a preference for TGO data in the MOP estimation. However, only a small time period was analyzed, and although the two values of Ω intersect in one point, the two satellites are not in the same configuration relative to Earth. Moreover, there might be a significant improvement from the combination of both datasets that is not quantifiable from the measurement signatures alone (nor will it be investigated further in this report). A more general study of how the MOP signature in the observable varies with the spacecraft orbit, with a better-suited method, will be presented in Section 6.2.

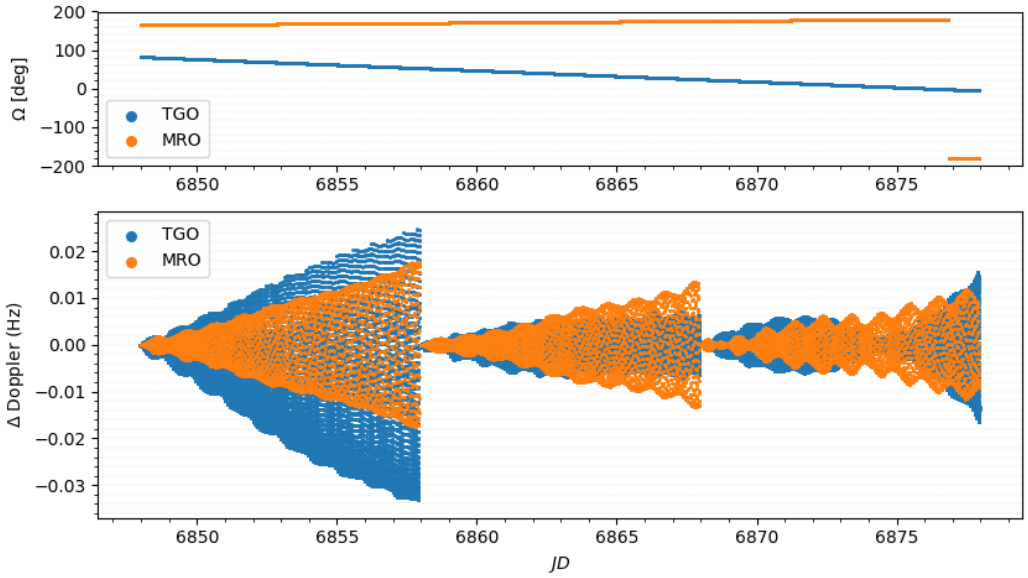

Figure 6.7: Top panel: evolution of the right ascension of the ascending node for TGO (blue points) and MRO (orange points) over 30 days. Bottom panel: signature of PM on the Doppler observable from TGO (blue points) and MRO (orange points) over 30 days

6.2. MOP signatures: analytical approach

The main results obtained from the analytical method for the assessment of the MOP signatures on spacecraft radio-tracking measurements are presented in this section. These results were obtained using the functionalities implemented in the ORB package through the functions verified and validated in Sections 5.1.1 and 5.2.1, respectively. Only the signatures of polar motion and length-of-day variations will be considered, since for the other parameters the ORB results were found to be in disagreement with those from GINS. Moreover, the only type of measurement analyzed here is the range-rate, given the low signature on the range observations seen in Section 6.1.2 for CW and LOD variations.

Unless otherwise specified, the only force acting on the spacecraft is the gravitational attraction of Mars, with its non-central component expanded up to degree and order 3. In Section 6.2.1 the spacecraft is TGO, so the results can be compared with those obtained numerically with GINS, presented in Section 6.1. In Section 6.2.2, instead, the methods are applied to a range of spacecraft orbits.

6.2.1. Results for TGO

This section lists the principal results obtained for the analytical signatures of the MOP on the trajectory and radio-tracking observables of TGO, as obtained with the ORB scripts. The results are generally displayed alongside equivalent quantities computed numerically with GINS, with a dynamical model consisting only of the degree-3 gravity potential of Mars. This serves both as a case-specific validation of the analytical signatures (the general validation was presented in Section 5.2.1) and as an indication of the extent by which errors on various intermediate results influence the final solution. A detailed verification and validation of the analytical method are however discussed in Chapter 5. The initial

Element	a	e	i	ω	Ω	M
Unit	m	-	deg	deg	deg	deg
Value	3781287.53	0.0067	73.57	63.75	49.17	239.05

Table 6.1: Mean orbital elements of the nominal ORB orbit over 10 days

state is the same for both the GINS and the ORB orbits: this is achieved by fitting the reference orbit in ORB iteratively, as described in the ”Algorithm” part of Section 4.2.3.

Figure 6.8 shows the perturbation in the orbital elements of TGO due to the polar motion (which includes the annual, semiannual, and Chandler wobble harmonics). Hence, the quantities plotted are the relative differences between the keplerian elements of two TGO orbits: one orbit is obtained with the nominal rotation model (i.e. by using the nominal *rotorcc* file), while the other is generated after removing the polar motion terms from the rotation model (i.e., using the *rotorcc* file labelled as ”noPM” in Table 5.1). The orbits span 10 days, from $t_i = 6847.98$ JD to $t_f = 6857.96$ JD (same as the GINS orbits of Section 6.1.1). For each orbital element, the relative difference here plotted is equal to the ratio of the difference between the elements in the two orbits and the mean value of the element in the nominal orbit (i.e., the one with a nominal rotation model) given by ORB. These mean elements are the same for all the cases analyzed in this section, since the nominal orbit is the same, and are listed in Table 6.1. The normalization is applied in order to correctly compare such different quantities as the signatures on the semi-major axis, the eccentricity, and the angular elements. From this figure, the parameters which are affected the most by polar motion are the eccentricity and the argument of perigee, both showing relative variations in the order of 10^{-6}%. For these same parameters, as well as for the mean anomaly, the analytical solution (shown in blue) deviates the most from the numerical one (in red). More specifically, the eccentricity solution presents a trend which is absent in the numerical results, while the analytical perturbations of both ω and M have long-period (tens of days) components that are different from those of the numerical solution. These errors in the analytical prediction of Δe, $\Delta, \omega,$ andΔM are presumably due to the ambiguities coming from the near-circularity of the TGO orbit, and could be reduced by the use of an unambiguous set of orbital elements.

Converting the keplerian elements of both orbits to cartesian coordinates, projecting the velocity vector along the direction connecting the spacecraft and the New Norcia station on Earth, and then subtracting these two line-of-sight (LOS) velocities, yields the results of Figure 6.9. The variations of the LOS velocity are equivalent to the instantaneous Doppler observable. Nevertheless, the GINS solution (again in red) is still generated by projecting the orbital elements, and not by simulating directly the observable. It can be seen that the numerical and the analytical solutions for the perturbation in the LOS velocity present a good agreement. This is in spite of the important differences in the perturbations of the orbital elements e, ω, and M described above. Hence, although the eccentricity and the argument of perigee show the largest (relative) perturbations due to polar motion, the impact of these perturbations on the signatures of the MOP on the Doppler observable must not be as significant as that from the semi-major axis and the out-of-plane perturbations of the angles i and Ω. If the latter perturbations are shown to be the prevalent contribution to the LOS velocity perturbation, it could mean that more than the absolute position of TGO it is the orientation of its orbit with respect to the Earth which is responsible for the signature from the figure. The period of the main spectral component of the LOS velocity signature is around 2 hr, close to the orbital period of TGO.

The same process is repeated for the LOD perturbations on the orbital elements and the LOS velocity. Figure 6.10 shows the relative perturbations of the keplerian elements. The agreement between the GINS solution and the analytical results is better than for polar motion, especially for the eccentricity. Still, the amplitudes of the perturbations on both ω and M are underestimated by the analytical method. Overall, the signatures in the parameters show more complex modulations than for polar motion. This is possibly due to the fact that for polar motion the Chandler wobble harmonic was dominant because of its amplitude, 10 times larger than the others. All orbital elements present relative perturbations due to LOD variations which are 2 or 3 times larger than those due to polar motion.

The perturbations on the projection of the cartesian components of the velocity along the LOS caused by LOD variations are displayed in Figure 6.11. Here as well the two different methods show better agreement than for the polar motion signature. With the initial conditions selected (given by the

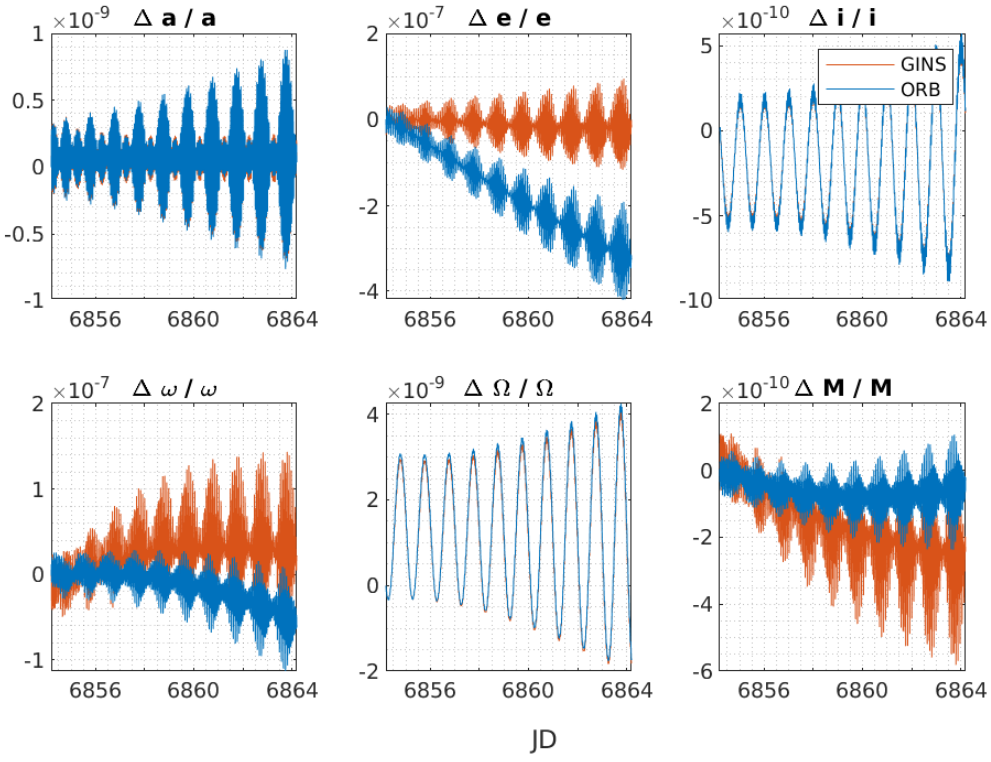

Figure 6.8: Signature of PM on the TGO perturbed keplerian elements, as given by ORB (blue curve) and GINS (red curve)

TGO state of epoch from the SPICE spk kernel), the signature of LOD variations on the LOS velocity is, at its peak, about twice the maximum of the same perturbation due to polar motion. The period of the main sinusoidal component is similar to that of the CW signature, and close to the orbital period of TGO.

6.2.2. Extension to different orbits

The main application of the analytical method developed here is the evaluation of the MOP signatures on different orbits and over long periods of time in a faster and lighter way compared to a numerical propagation of the orbits. With this goal in mind, the code is expanded to allow for a grid of two parameters to be created, and then to evaluate the analytical signatures at each point of this grid. The parameters used for the construction of the grid are in this case the eccentricity and the inclination of the osculating orbit. Moreover, the altitude at the pericenter of the orbit is set to $h_{PER} = 400$ km for all the orbits, so that the semi-major axis is given by the value of the eccentricity, according to $a = h_{PER}/(1 - e)$. The other three orbital elements, however, are free to vary. They are set initially all to $0°$.

In what is effectively a bi-dimensional grid search optimization of the signature of the MOP on the LOS velocity, the quantity to maximize is set to be the maximum of the absolute value of the signature (a curve of the kind shown in Figure 6.9).

The grid for the following figures was generated with 10 linearly spaced points for the eccentricity, with values comprised between 0.01 and 0.5, and 10 linearly spaced points for the inclination, with values ranging from $5°$ to $85°$. Since the method utilized the classical Keplerian elements, the minimum values of the eccentricity and inclinations are rigorously different than 0, in order to avoid the ambiguities typical of circular and of equatorial orbits. The upper limit on the eccentricity values is mostly due to a poor performance of the algorithm at high values of e. As mentioned before, the eccentricity function in Kaula's expression of the potential is a power series of the eccentricity. If the eccentricity is small, the series can be truncated at the first three terms. For larger and larger eccentricities, more and more terms of the series are needed for an accurate reconstruction of the orbit. The current version of the algorithm implements a variable number of terms of the eccentricity series, starting from $2l + 1$ up to

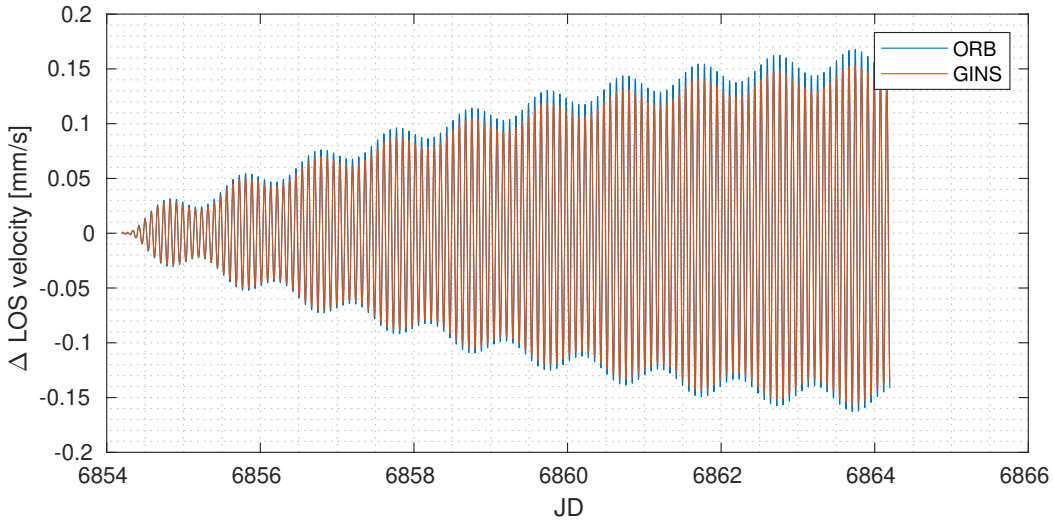

Figure 6.9: Signature of PM on the TGO LOS velocity, as given by ORB (blue points) and GINS (red points)

$10l+1$, l being the degree of the gravity field. Higher numbers of terms in the series make the algorithm too slow to be of any advantage with respect to a numerical propagation, which is why eccentricities larger than 0.5 are not considered here.

The value plotted for each of the 100 points in Figure 6.12 is the maximum of the polar motion signature on the LOS velocity. According to this plot, with the assumptions made on the values of the four others elements of the osculating orbit, the signature of polar motion on the LOS velocity is largest for nearly-circular orbits (inclination around 0.01) with an inclination close to about $40°$. The maximum of the signature for orbits with e and i close to these values is at least twice that of orbits with different eccentricities and inclinations. Thus the orbit of TGO, with its inclination of about $74°$ degrees, would not be the most sensitive one to the polar motion parameters of Mars. Yet it would be more sensitive than many other spacecraft, which are mostly in near-polar orbits.

The same grid of values of e and i is used to obtain the plot in Figure 6.13, representing the maxima of the signature in the LOS velocity caused by the LOD variations.

Additional plots of this kind can be found in Appendix B. In particular, Figure B.1 shows that the result obtained for the PM signature does not vary significantly if the perigee altitude is set to 600 km instead of 400 km. Similarly, from Figure B.2 it can be seen that the same maximum for the PM signature on the LOS velocity is found even if the orbits are extended over a single 700 days arc (although in this case the quantity plotted is the RMS of the signature, since the time steps are larger and the data more sparse). On the other hand, Figure B.3 shows that just by fixing the values of the remaining orbital elements to $45°$ instead of $0°$, a completely different result is obtained for the optimal orbit, which is in that case one with high inclination and an eccentricity of about 0.3. Therefore, conclusive results about the optimal orbital configuration for the estimation of PM and LOD cannot be inferred from the bidimensional case. Instead, the optimization process should interest all six of the orbital elements.

6.3. TGO covariance analysis results

This section presents the results of the covariance analysis performed with Tudat, with the aim of assessing the uncertainties of the MOP solution obtainable from TGO alone and from combination of TGO data with those from landers. The Tudat settings and the spacecraft dynamical model are those listed in Table 4.2. In the nominal case, the synthetic Doppler measurements from TGO are simulated over 700 days, divided in arcs of 10 days with 2-hours overlap. The initial state of the spacecraft at each arc is retrieved from the SPICE *spk* kernel. The spacecraft orbit is propagated assuming a nominal rotation model for Mars, that is, equivalent to the one listed in the nominal *rotorcc* file for the GINS and ORB executions. Hence, this rotation model includes the constant precession rate, the non-rigid nutations, the polar motion, and the length-of-day variations, with the same parameter values (and the same number of harmonics for the trigonometric series) as in the *rotorcc* file. In Section 5.2.2, the

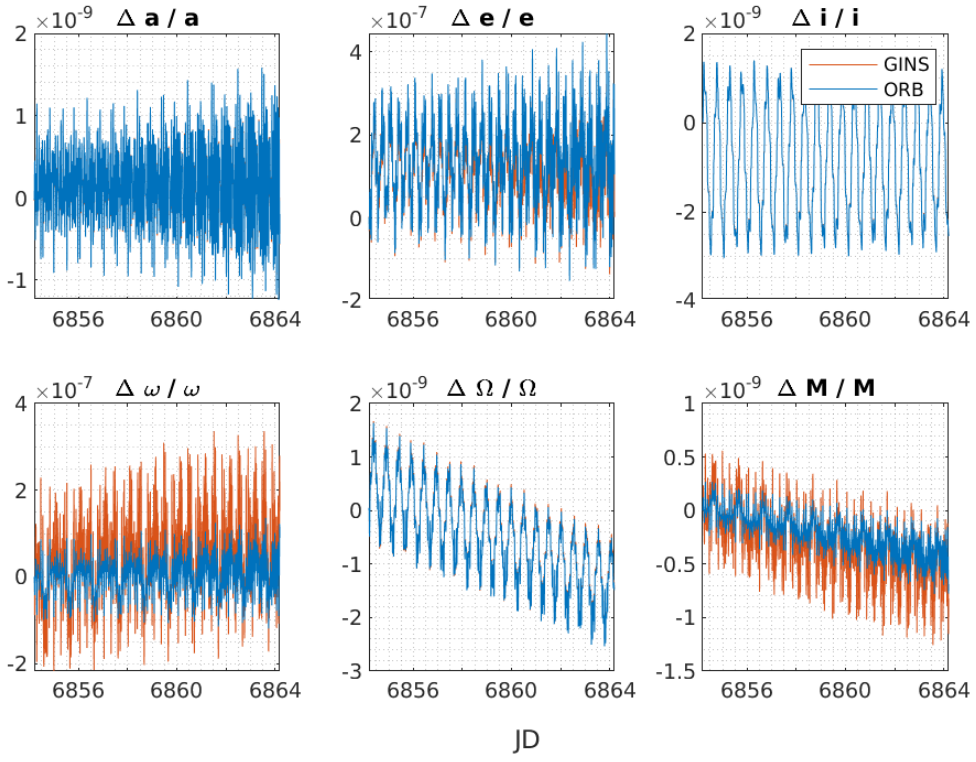

Figure 6.10: Signature of LOD on the TGO perturbed keplerian elements, as given by ORB (blue curve) and GINS (red curve)

orbit propagated by the Tudat application was validated through comparison with the GINS orbit, both propagations using the nominal settings and rotation model.

The simulated measurements are then used to compute the partial derivatives with respect to the full set of parameters to estimate, which form the elements of the information matrix. The least squares algorithm in Tudat is stopped at the first iteration, and the outputs, including the full information matrix, are fed to the Python scripts described in Section 4.2.2, which yield the final formal and consider uncertainties.

The set of parameters to estimate is large: along with the sine and cosine amplitudes of the polar motion components and the LOD variations, and the F and σ_0 parameters of the nutation transfer functions, the degree-2 and 3 gravity field coefficients are also estimated, because significant correlations are expected between some of those coefficients and the rotation parameters of Mars. In addition to this set of global parameters, the initial state and the C_D and C_R coefficients also need to be estimated in order to ensure a correct reconstruction of the spacecraft orbit over each 10-days arc. Attempting to solve for this complete set of parameters with just the 700 days of TGO observations leads to considerably high values of the condition number for the normal matrix ($P_{COND} = 1.495\text{x}10^{11}$ for the normalized matrix), and therefore to results which are heavily affected by numerical noise. More reliable solutions for the uncertainties of the MOP estimates are obtained by including a priori information about the parameters. However, adding a diagonal a priori covariance matrix only lowers the condition number to $P_{COND} = 1.490\text{x}10^{11}$. Further precision could be obtained by restricting the estimation to only a subset of the parameters, and leaving the rest fixed to their a priori value, while still taking into account their assumed uncertainties and the way those affect the estimated parameters. As explained in Section 3.3, the parameters of the latter subset will be referred to as consider parameters in the following. Depending on the choice of the consider parameters, the restricted normal matrix has condition numbers as low as $P_{COND} = 10^{10}$, leading to a reduction of the numerical noise in the solution.

In order to select which parameters to estimate and which to consider, the normal matrix relative to the complete set of unknowns is constructed. Here it is assumed that the formal errors for the full-set solution, while degraded by numerical noise, are still representative of the order of magnitude of the actual uncertainties of the least squares solution. Then the formal errors thus obtained are

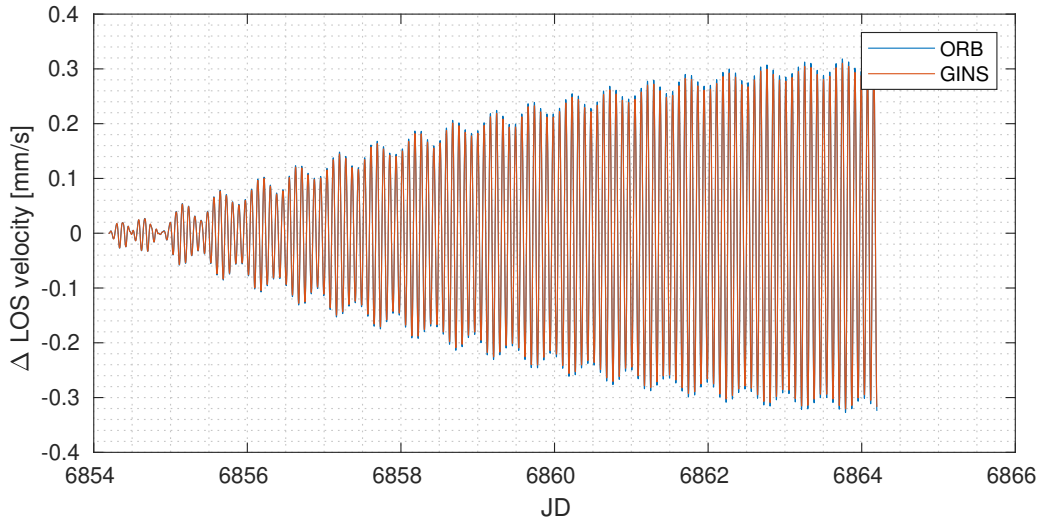

Figure 6.11: Signature of LOD on the TGO LOS velocity, as given by ORB (blue points) and GINS (red points)

divided by the a priori standard deviation of the corresponding parameters. Figure 6.14 shows this ratio as computed for the global parameters. Excluded from this figure are the 4 Chandler wobble amplitudes and the 8 amplitudes (2 for each frequency) of the LOD variations, as these parameters are the main focus of the study. The parameters for which the resulting formal error is more than 1% of the initial uncertainty are moved to the set of consider parameters, while the others are kept in the parameters to estimate. The threshold is arbitrary, but the rationale behind the selection criteria is that for the parameters for which the final uncertainty is close to the a priori one, fixing the error to the initial estimate will not influence the covariance analysis solution considerably. On the other hand, fixing the uncertainties of such parameters allows to reduce the total number of unknown to solve for, making the system of normal equations potentially more stable. As indicated by the shaded area, the variables included in the estimation are the FCN frequency and the core factor F, as well as the zonal gravity coefficients of degree 2 and 3.

The a priori uncertainties assumed for the parameters are generally half of their nominal value, except for the initial state parameters (1 km and 1 m/s on the position and the velocity components, respectively) and the static gravity coefficients, for which the uncertainties published alongside the MRO120D solution are used. Moreover, the a priori errors of the PM and LOD amplitudes are set to 10 mas when their nominal value is lower than 20 mas, to avoid having uncertainties lower than the nominal ones shown in Table 2.1. What is told by Figure 6.14, namely that the C_{20} and C_{30} solutions could be reduced by 100 times using 700 days of TGO data alone, is quite unrealistic. However, no gravity coefficients of degree higher than 3 were estimated. As mentioned in Section 2.3.3, even and odd zonal gravity coefficients show high correlations among them, because they perturbation on the orbit may have the same phase angle (Eq. 4.15). Therefore, estimating the full gravity field should lead to more realistic formal errors for the zonal gravity coefficients. Similar is the situation for the F and σ_0 parameters, since their uncertainties are 10 lower than the expected by RISE after 1 year of operations (Folkner et al., 2018). While here as well the case could be made that in a real estimation, correlation with other parameters would raise the formal errors considerably, a software error cannot be excluded. The handling of the information matrix by the Python scripts, leading to the normal matrix and consequently, after inversion, the formal uncertainties, was verified in Section 5.1.2. Moreover, the results shown here were found to remain unchanged when singular value decomposition was employed for the inversion of the normal matrix. Thus, an eventual problem could be in the Tudat application created for the project. The computation of the partial derivatives was also verified (although not for these parameters), and the implementation of the TGO dynamical model and Mars nominal rotation model was validated with GINS (Section 5.2.2). Hence, the source of these overly optimistic uncertainties is still undetected.

The next sections will present the formal uncertainties solutions for the subset of MOP included in

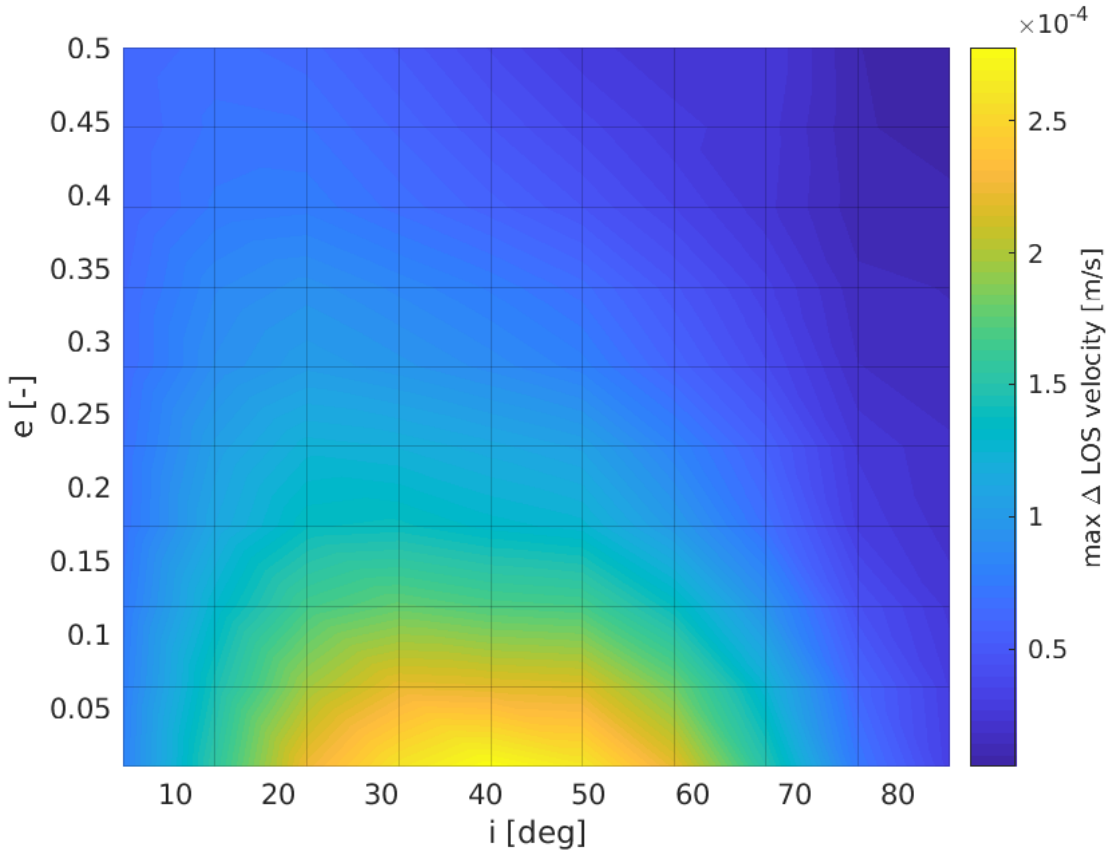

Figure 6.12: Maximum signature of PM on the LOS velocity computed with ORB, as a function of the orbit eccentricity and inclination, assuming a fixed pericenter altitude of 400 km

the parameters to estimate, with and without the contribution of the consider parameters thus selected. Specifically, Section 6.3.1 describes the formal and consider uncertainties of the Chandler wobble obtained in the nominal TGO estimation, and similar results for LOD variations and the FCN amplification of the nutations are found in Sections 6.3.2 and 6.3.3, respectively. Section 6.3.4 discussed the effect of including TGO range measurements in the dataset, while Section 6.3.5 reports the effects of different changes in the nominal estimation settings on the final uncertainties. Finally, Section 6.3.6 presents a comparison of the TGO only solution with that from an ideal lander, and with the combined solution of TGO and lander data.

6.3.1. Chandler wobble

This section presents the formal error solutions obtained for the amplitudes of the Chandler wobble harmonic of the Martian polar motion, assuming a period of 200 d. The results for the X and Y components are shown in Figure 6.15. The solid lines represent the evolution of the formal errors over the tracking period when the uncertainties of the consider parameters are not taken into account. The dashed lines, instead, show the formal error solutions including the effect of the consider parameters. The final results, after the full 700 days of TGO tracking, are displayed in Table 6.2, along with the a priori values and errors.

The consider uncertainties are substantially larger than those obtained when ignoring the consider parameters uncertainties. The formal errors decrease steadily with the increasing number of tracking data, due to the increasing number of observations. This is typical of the pure formal uncertainties, which, assuming that the addition of data does not affect the correlations between the parameters, depend on the number of measurements N approximately as $\sqrt{1/N}$ (Dirkx et al., 2014). On the other hand, the consider uncertainties decrease steeply during the first 200 days of tracking, and then plateau around values one order of magnitude larger than the formal uncertainties. The steep initial decrease

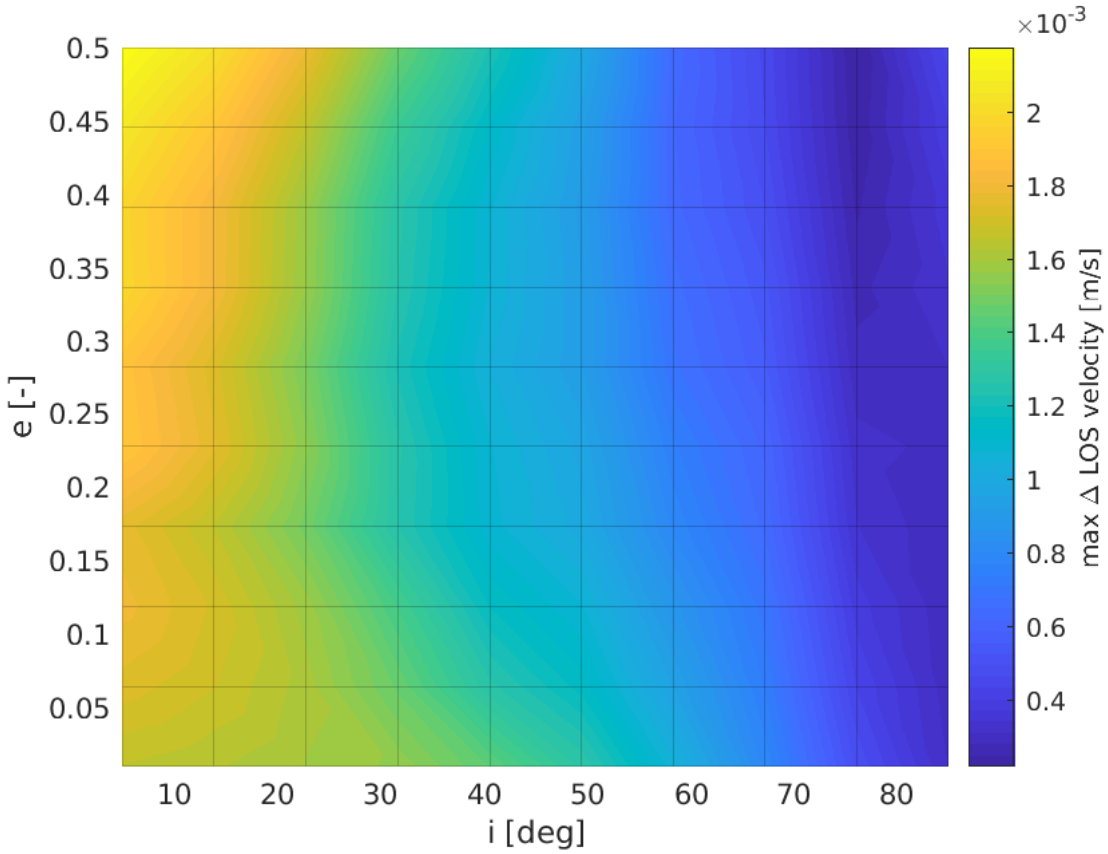

Figure 6.13: Maximum signature of LOD on the LOS velocity computed with ORB, as a function of the orbit eccentricity and inclination, assuming a fixed pericenter altitude of 400 km

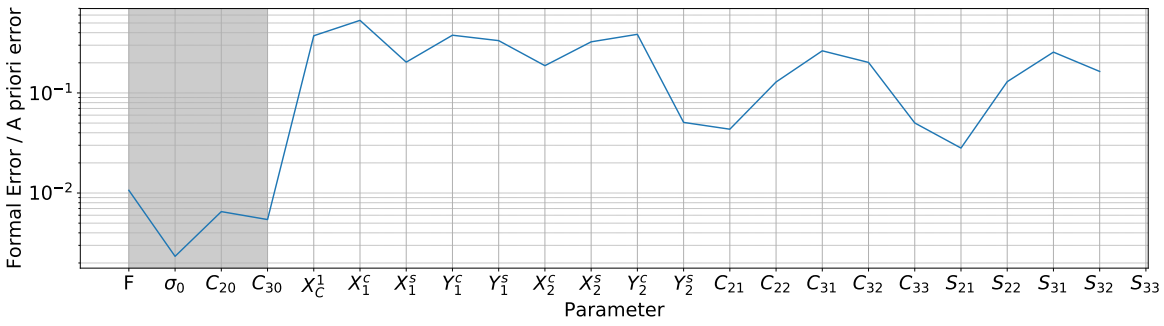

Figure 6.14: Ratio of the formal errors with the full set of unknowns and the a priori uncertainties of the unknowns themselves. The shaded area indicates the subset of parameters which is added to those to estimate, leaving all the others as consider parameters.

is due to the ability of the filter to decorrelate more and more the CW amplitudes from the consider parameters as the number of observations increase and the variability of configurations by which these data are obtained increases. Once the full period of the signal is sampled, and in the case of the CW it is indeed 200 days, most of the correlations are resolved and the consider uncertainties decrease less rapidly.

Figure 6.16 plots the rows of the perturbation matrix relative to each CW amplitude. The perturbation matrix is computed from Eq. 3.48, by multiplying the sensitivity matrix (Eq. 3.47) by a diagonal matrix containing the formal errors assumed for the consider parameters. The elements of each row of the perturbation matrix represent the contribution of each consider parameter to the total consider

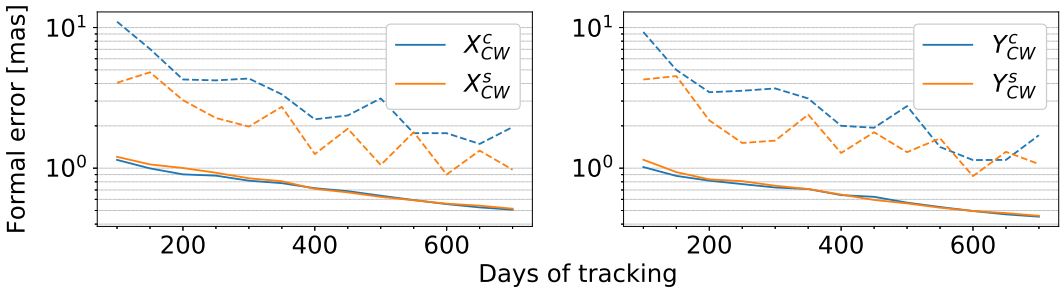

Figure 6.15: Formal error solutions for the CW amplitudes without (solid lines) and including (dashed lines) the consider parameters uncertainties in the estimation

Parameter	A priori [mas]		Formal error [mas]	
	Value	Error	Without CP	With CP
X^c_{CW}	54.6551	27.3275	0.5068	1.9602
X^s_{CW}	0.7346	10	0.5154	0.9760
Y^c_{CW}	-33.2059	16.6029	0.4521	1.7174
Y^s_{CW}	-7.4894	10	0.4593	1.0724

Table 6.2: Chandler wobble amplitudes: a priori values and uncertainties, and formal errors with and without consider parameters after 700 days

uncertainty of the estimated parameter corresponding to the row. In particular, for each amplitude, the difference between the consider uncertainty and the pure formal error is equal to the RSS of the contributions from each of the consider parameters (i.e. the elements of the perturbation matrix row, as plotted in the figure). It can be seen that for both the X and Y components, most of the contribution to the solution is due to the uncertainties on the amplitudes of the corresponding polar motion components at the other two frequencies, and to the error on the tesseral and sectorial gravity field coefficients of degree 2. In particular, the X component is overall more sensitive to the uncertainty in the C_{21} and C_{22} coefficients, while the contribution of the gravity field uncertainties to the Y component is mostly due to the S_{21} and S_{22} coefficients. The tesseral coefficients are non-zero when the body-fixed frame and the frame used for the expression of the gravity potential are oriented differently, which is the case for a mismodeling of polar motion. Specifically, using approximated formulas from (Petit and Luzum, 2010):

$$\begin{aligned} C_{21}(t) &= \sqrt{3}X_P(t)C_{20} - X_P(t)C_{22} + Y_P(t)S_{22} \\ S_{21}(t) &= -\sqrt{3}Y_P(t)C_{20} - Y_P(t)C_{22} - X_P(t)S_{22} \end{aligned} \tag{6.2}$$

These expressions are a simplification of the results that the algorithms in Appendix A would give (as discussed in Kudryavtsev, 1997). They show how the polar motion parameters are related to the tesseral and sectorial gravity field coefficients. Hence, correlations between these spherical harmonic coefficients and the polar motion amplitudes are expected.

6.3.2. Length-of-day variations

Figure 6.17 shows the evolution of the formal errors for the amplitudes of the 4 LOD variations harmonics taken into account. As in the previous section, the formal errors are displayed as solid lines, while the consider uncertainties are represented by dashed lines. Table 6.3 shows the values of the a priori values and uncertainties and the two sets of solutions with the full 700 days of tracking data.

As with the CW amplitudes, the formal errors are a too optimistic estimate of the true uncertainties of the parameters, and the introduction of the consider parameters leads to an increase of final uncertainties, albeit not as large as the previous case. The formal errors generally display an initial steep

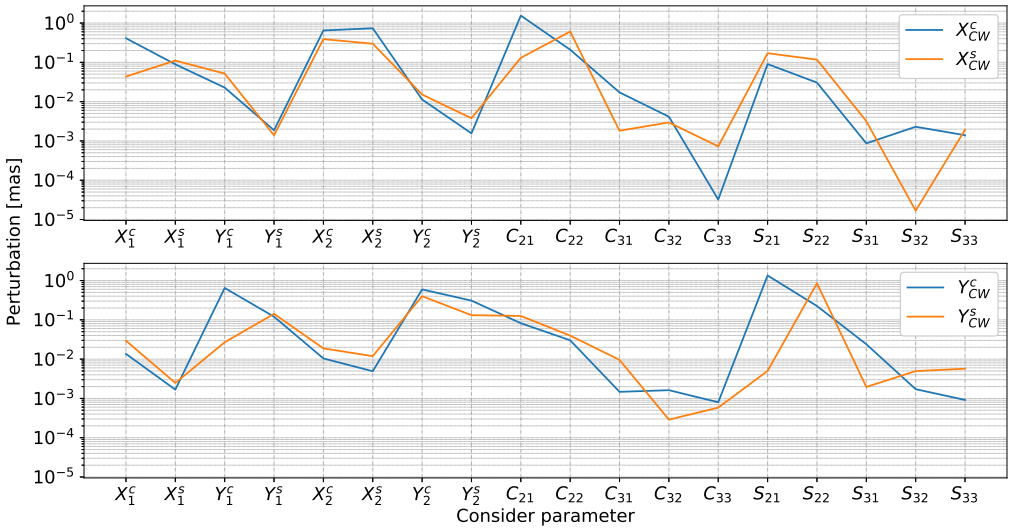

Figure 6.16: Perturbation matrix elements for the CW variations amplitudes

decrease followed by a further decrease with the days of tracking which is due only to the addition of observations. After 700 days, all formal errors converge to similar final values, with the consider uncertainties being around twice this value or less.

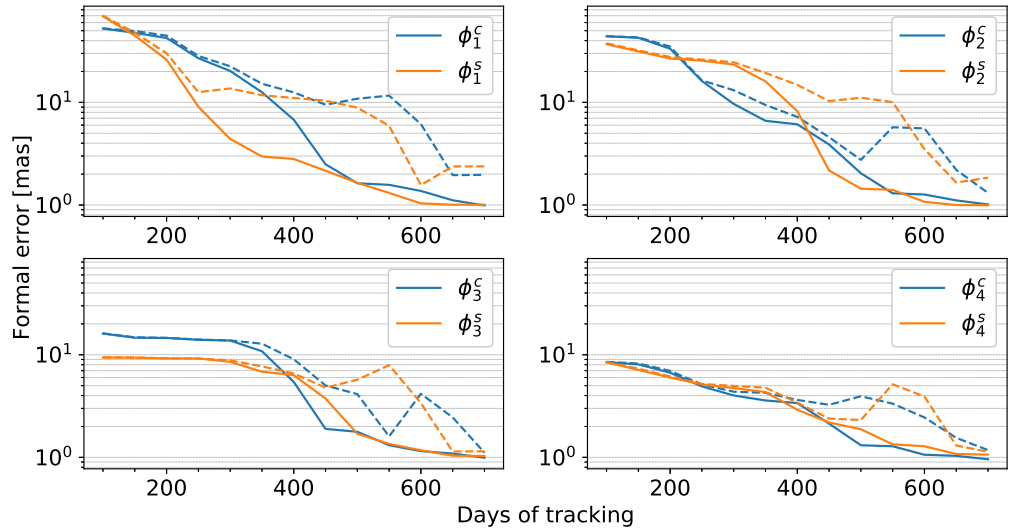

Figure 6.17: Formal error solutions for the LOD amplitudes without (solid lines) and including (dashed lines) the consider parameters uncertainties in the estimation

The rows of the perturbation matrix corresponding to each amplitude of the LOD variations are plotted in Figure 6.18. Overall, most of the contribution to the consider uncertainties is due to the error on the spherical harmonic coefficients of degree 2 and order 2. These coefficients are indeed the most representative of a mismodelling of the rotation of the planet around the rotation axis, thus significant correlations between C_{22} and S_{22} and the LOD variations amplitude are expected.

Parameter	A priori [mas]		Formal error [mas]	
	Value	Error	Without CP	With CP
ϕ_1^c	481	240.5	0.98941	1.9672
ϕ_1^s	-331	165.5	1.0064	2.3770
ϕ_2^c	-103	51.5	1.0117	1.3106
ϕ_2^s	-101	50.5	0.9942	1.8451
ϕ_3^c	-35	17.5	0.9921	1.1102
ϕ_3^s	-4	10	1.0317	1.1442
ϕ_4^c	-10	10	0.9582	1.1762
ϕ_4^s	-8	10	1.0634	1.1310

Table 6.3: LOD variations amplitudes: a priori values and uncertainties, and formal errors with and without consider parameters after 700 days

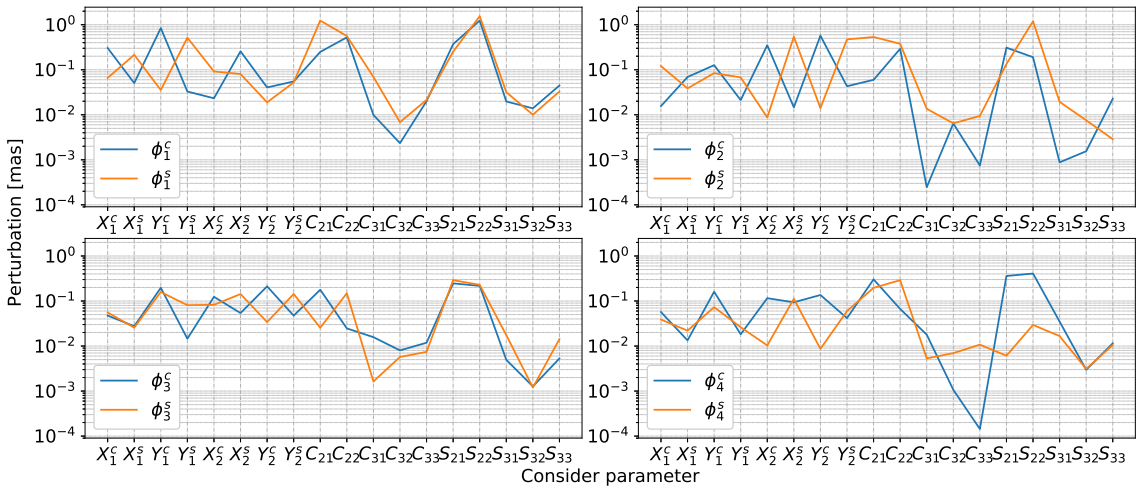

Figure 6.18: Perturbation matrix elements for the LOD variations amplitudes

6.3.3. Nutations transfer function parameters

The evolution of the F and σ_0 uncertainties as a function of the days from the start of the data acquisition are displayed in Figure 6.19. The values of the errors after the full 700 days of tracking can be found in Table 6.4. The impact of the consider parameters is smaller for these parameters than for the CW and the LOD variations amplitudes. Both the formal and the consider uncertainties results are very close to the relative values shown in Figure 6.14 for the solution without a priori constraints, being close to 1% and 0.1% of the a priori error, respectively. As mentioned when commenting Figure 6.14, these values are almost two orders of magnitude too low compared to results from other studies (37% and 3% relative to the same a priori errors, according to Folkner et al., 2018), and in light of the fact that these parameters have never been estimated from radio-tracking data.

Parameter	A priori		Formal error	
	Value	Error	Without CP	With CP
F [-]	0.07	0.035	3.7210e-4	3.9233e-4
σ_0 [deg/day]	1.5	0.75	9.2969e-4	9.8728e-4

Table 6.4: Nutation transfer function parameters: a priori values and uncertainties, and formal errors with and without consider parameters after 700 days

The contribution of the each consider parameter to the final consider covariance of the two nuta-

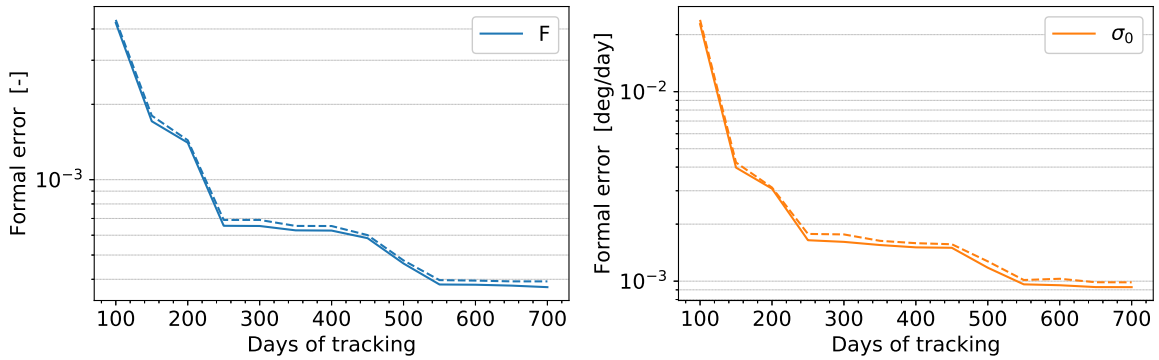

Figure 6.19: Formal error solutions for the FCN parameters without (solid lines) and including (dashed lines) the consider parameters uncertainties in the estimation

tion function parameters is represented in Figure 6.20, which plots the rows of the perturbation matrix relative to the two estimated MOP. The contributions to the consider covariance of the polar motion amplitudes have the same shape for both parameters, with a peak at the sine amplitude of the semiannual harmonic. The semiannual period is 343.5 days, while the one hypothesized for the FCN is 240 days. Hence, while the two periods are still very far apart, the interactions between the signals could explain why the effect of the semiannual polar motion component is larger than the annual one. As for the gravity field, most of the contribution to the consider covariance is due to the C_{21} and C_{22} coefficients for F, and to S_{22} for both parameters.

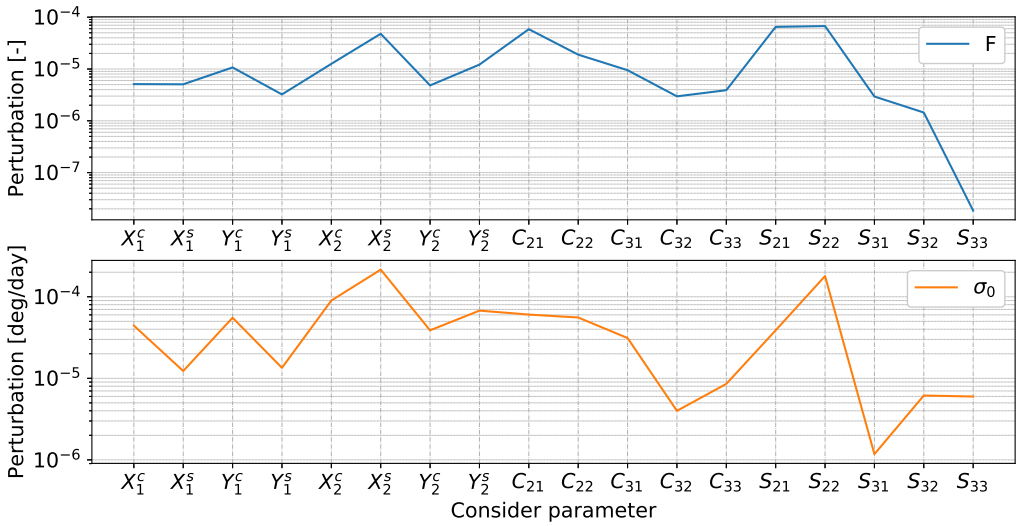

Figure 6.20: Perturbation matrix elements for the FCN parameters

6.3.4. Impact of range measurements

All the results presented above are obtained using only two-way Doppler data. Here the impact of the addition of range measurements to the set of Doppler observations is tested. The range measurements are assumed to be roughly 5 times less frequent than the Doppler ones, with one data point every 5 minutes. The relative variation of the formal error solution for the CW and the LOD variations amplitudes is shown in Figures 6.21 and 6.22, respectively. On the y-axis in both figure is plotted the difference between the formal errors with both Doppler and range data and those with Doppler data only, expressed as a percentage of the Doppler-only solution. As usual, solid lines are relative to the pure formal errors, while dashed lines indicate quantities related to the consider uncertainties. The

variations in the solution following the addition of range measurements are well below 1% for both sets of MOP. This holds true whether the consider parameters are included or not. Such a result was to be expected from the comparison between the signatures of these parameters on the range observables (just above the noise level), and those of the same parameters on the Doppler measurements, as shown in Section 6.1. The same conclusion could also have been reached using the analytical approach in Dirkx et al. (2018), for the comparison of the range and range-rate sensitivity to a parameter. While the method is valid in general, the specific formula derived these applies to parameters which lead to sinusoidal partials for the range data, of the type $\partial\rho/\partial p = A\sin\omega t$ (where ρ is the range observable and p the parameter. The partials in the instantaneous range-rate are simply the first derivative of those in the range, so that for such a parameter $\partial\dot{\rho}/\partial p = A\omega\cos\omega t$. Then, the ratio of the sensitivity of the Doppler to the parameter compared to that of the range measurements is proportional to the figure of merit (Dirkx et al., 2018):

$$\Xi_q = \frac{\sigma_\rho}{\sigma_{\dot{\rho}}}\omega \tag{6.3}$$

with σ_ρ and $\sigma_{\dot{\rho}}$ being the noise levels of the range and Doppler measurements, respectively.

The signatures of polar motion and LOD variations on the LOS velocity of TGO, shown in Figures 6.9 and 6.11 can, in a first approximation (since they represent the variation of the range-rate observable for a 100%-variation of the parameter), be taken as representative of the behaviour of the range-rate partials. Both curves show a main sinusoidal component with a period of about 2 hours, modulated mainly by a trend and another sinusoidal, which make the amplitude increase and oscillate with time. However, these two additional effects should not affect the validity of Eq. 6.3 (at least for the trend, a confirmation is given by Dirkx et al., 2018). Hence, assuming a range noise at the 1 m level and a Doppler noise of 0.1 mm/s, given $\omega = 2\pi/2$ hr $= 8.73$ s^{-1}, the figure of merit from Eq. 6.3 is $\Xi_q = 8.73$. Hence, Doppler data is roughly 10 times more sensitive than range data for these parameters.

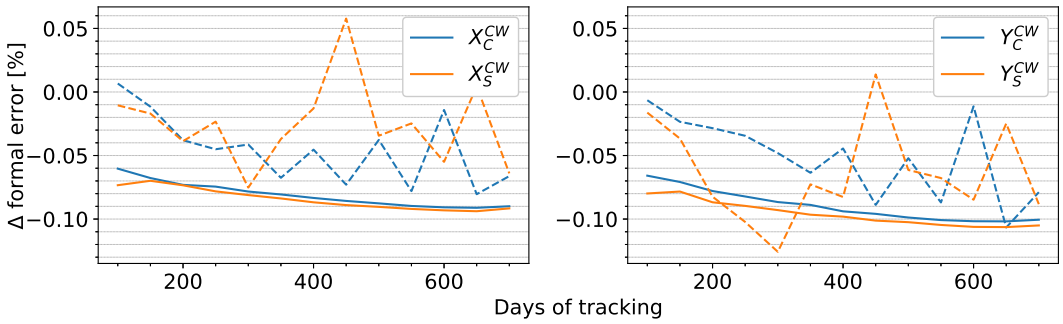

Figure 6.21: Relative variation of the CW amplitudes uncertainties following the addition of range data to the Doppler

6.3.5. Stability of the solution

In order to establish to what extent the solution obtained is dependent on the settings chosen, different estimation conditions are tested, and the resulting formal errors are compared to those from the nominal case. The variations of the formal error solutions both with and without the inclusion of the consider parameters are expressed, for each estimated parameter discussed above, in terms of the ratio between the case-specific solution and the nominal one. In the following, several cases are presented, characterized by different estimation models and assumptions.

Case 1: Inclusion of Mars occultations in the viability conditions

The observations used in the nominal estimation case include those at times where Mars is along the LOS, between TGO and the ground station. Clearly, in real tracking conditions, no Doppler measurements are produced at these times, since there is no direct radio link between the spacecraft and the Earth. However, an unsolved software error causes the inclusion of Mars occultations in the Tudat viability conditions to entail the removal about twice the points normally affected by the type of occultation mentioned above. The observations removed are not only those obtained when Mars is on the LOS

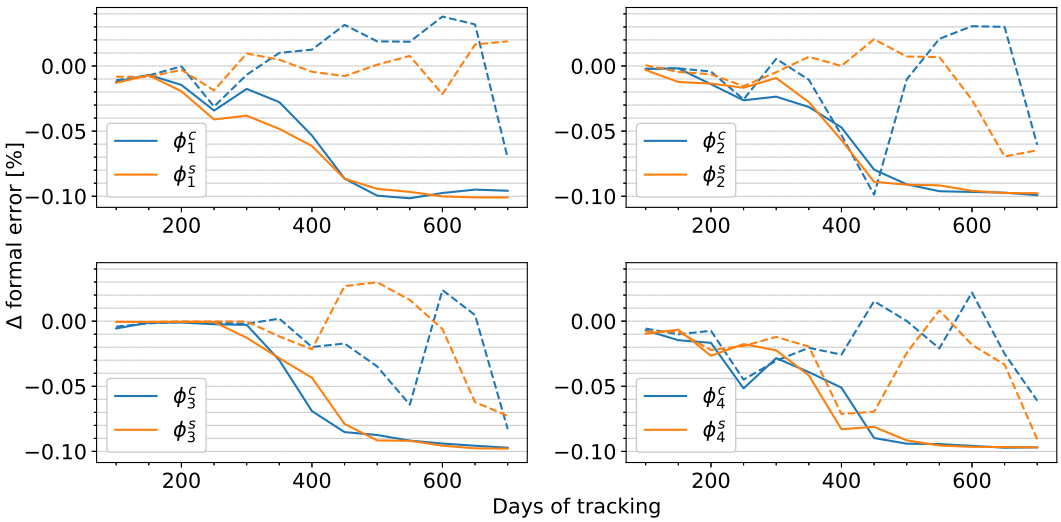

Figure 6.22: Relative variation of the LOD amplitudes uncertainties following the addition of range data to the Doppler

and in front of TGO as seen from Earth, but also those corresponding to the opposite configuration of the spacecraft and Mars on the LOS, with TGO in front of Mars as seen from Earth. With this latter geometry, the radio link with the spacecraft is unobstructed, and measurements can be generated. Therefore, while removing the Mars occultations from the data selection criteria leads to optimistic results, because of a larger number of data compared to what is achievable in real conditions, including them, with the current state of the scripts used, yields conservative solutions, at least for what concerns this particular aspect.

The ratio between the conservative solution, given by a synthetic dataset from which those points where Mars is on the LOS are excluded, and the nominal one are plotted in Figure 6.23. The solid line connects the ratios between the two formal errors for each MOP, while the dashed line connects ratios of the consider covariances for the two cases. The ratios between the formal errors are larger than 1 for all the parameters. Thus, the formal errors obtained when the Mars occultations are included in the viability conditions are larger than the nominal solutions, as expected from the inverse proportionality of the formal uncertainties and the square root of the number of data points. The ratios for the consider uncertainties are more erratic, suggesting sigmas smaller than for the nominal case for three different parameters. Nevertheless, the formal error ratios are close to unity, and the largest deviation in the consider errors is 150% of the nominal solution. Hence, the lack of removal of data points corresponding to an occultation is here judged to not compromise the reliability of the nominal solution.

Case 2: No overlap between consecutive arcs

In this case, the 2-hours overlap between one arc and the next is removed, making the end time of one arc correspond to the start time of the one after. The overlap removal degrades the solution for all the parameters, as shown by the errors ratios in Figure 6.24, which are all larger than 1. Again, the solid line connects points corresponding to the formal errors without consider parameters, and the dashed line connects ratios between errors which include the consider parameters, both curves showing similar behaviour. The FCN frequency presents a large error ratio compared to the other parameters, yet all the deviations stay well below 1% of the nominal errors.

Case 3: Variation of the measurements errors

Here, the standard deviation of the Gaussian noise added to the simulated measurements is increased from the already conservative value of 0.1mm/s to 0.5mm/s. Such a noise value is about an order of magnitude larger than what is currently achievable with an X-band radio link, and its use in a realistic scenario can be justified possibly for arcs with very low SEP angles, where the quality of the signal is severely degraded by solar plasma (see Eq. 3.15 and the related discussion). Still, this new noise

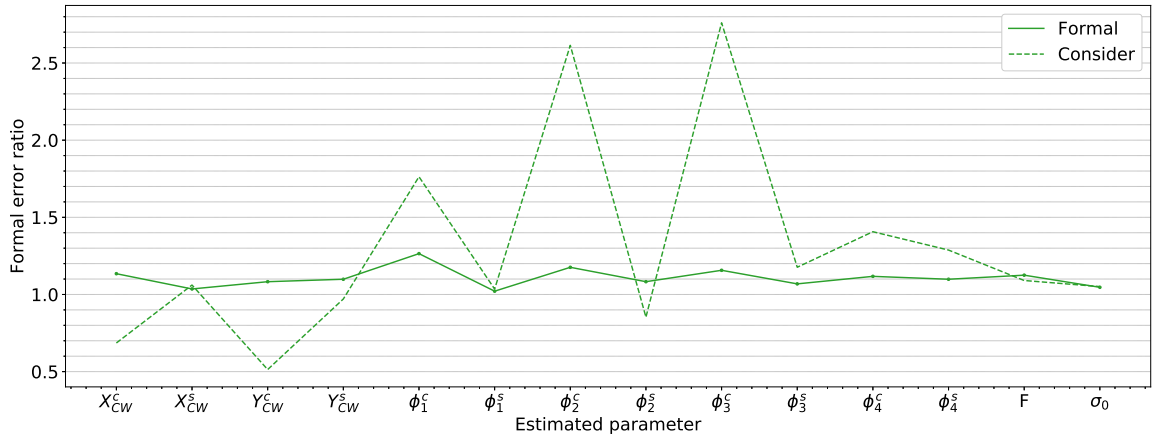

Figure 6.23: Uncertainties of the estimation case including Mars occultations relative to the nominal solution

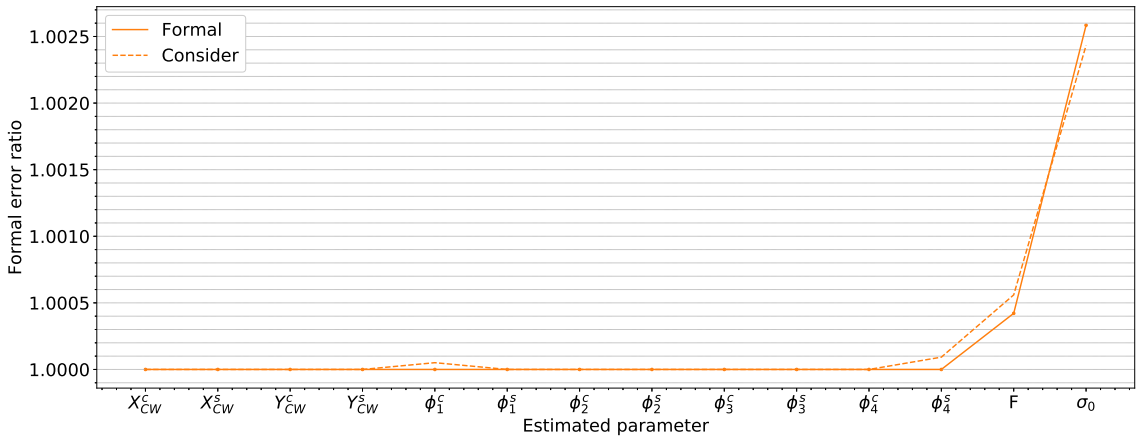

Figure 6.24: Uncertainties of the estimation case without arc overlap relative to the nominal solution

value is not used as much to get realistic estimates of the uncertainties, but to test the relation between the (single) measurement error and the resulting formal error. From the formulas in Section 3.2, it can be seen that without a priori information, the ratio between the formal errors obtained using two different measurements sigmas is equal to the ratio of these sigmas. In this case, this ratio is 5. Indeed, most the formal error ratios shown in Figure 6.25 are around the value of 5 for most of the parameters, with some exceptions which are presumably due to the influence of the a priori covariance on the solution. Thus, approximate values of the formal errors corresponding to a different noise level of the measurements can be inferred by scaling the nominal errors by the ratio of the two noise levels. In particular, a Doppler noise of 0.05 mm/s should lead to formal uncertainties which are roughly half of the values presented here for the nominal case.

Case 4: Reduced arc length

Up until now, arcs of 10 days of length have been considered. Figure 6.26 shows the effect on the estimated uncertainties of reducing this length, by dividing the whole tracking period into arcs of 5 days. While the formal errors (solid line) of the Chandler wobble parameters remain more or less unchanged, those of the LOD variations amplitude are double the nominal solution, and those of the non-rigid nutations transfer function parameters become three times as large as in the nominal case. The consider uncertainties ratios are close to those of the formal errors, except for the LOD variations parameters, where they are up to two times the ratios of the errors without consider parameters.

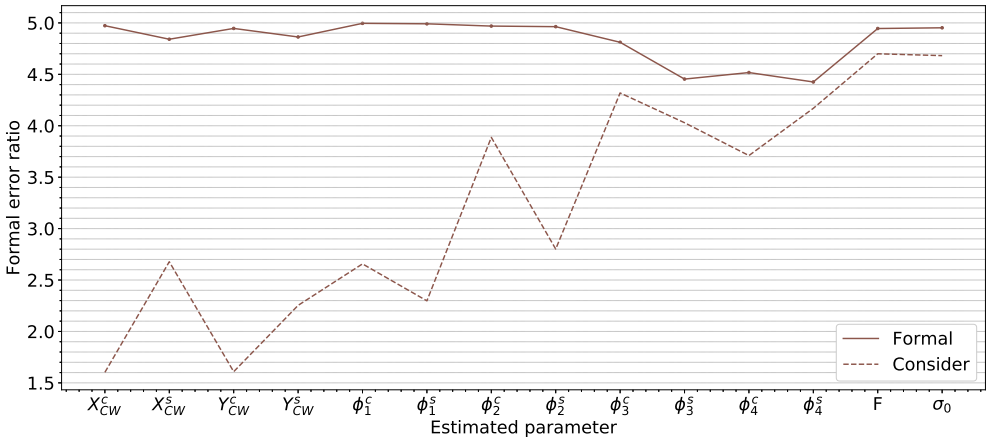

Figure 6.25: Uncertainties of the estimation case with measurements error 5 times larger than the nominal, relative to the nominal solution

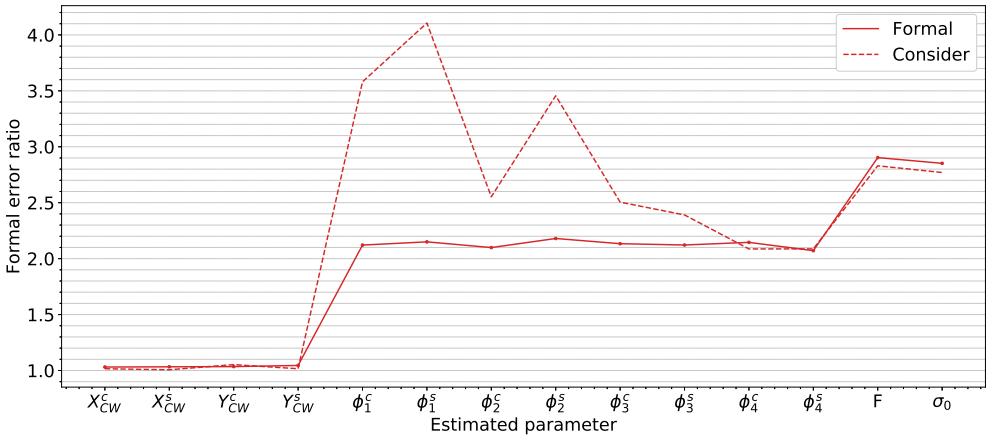

Figure 6.26: Uncertainties of the estimation case with arcs of 5 days relative to the nominal solution

Case 5: Reduced tracking time per day

Here the number of hours in which the measurements are taken each day is varied from the nominal value of 12 hr. Figure 6.27 displays the error ratios relative to a tracking window of maximum 10 hours each day, always from the New Norcia ground station. The same results are presented in Figure 6.28, but for an even shorted maximum daily tracking time of 6 hours, which is generally half the value of the nominal case. A shorter tracking time means a smaller number of observations, and thus larger formal errors. For both tracking lengths, however, the change in the uncertainties is at most 120% of the nominal value.

Case 6: Estimation of Mars variable gravity field

The zonal gravity field coefficients C_{20} and C_{30} estimated in the nominal case are assumed to be global parameters, meaning that only the static gravity field of Mars is estimated. Nonetheless, the same processes tied to some of the MOPs, like the seasonal mass exchanges between the ice caps and the atmosphere, are also responsible for variations in the gravitational potential of Mars, due to the mass redistribution. This variability of the gravity is mostly expressed in the zonal spherical harmonic coefficients (Karatekin et al., 2005). Hence, substantial correlations are expected between the variable zonal gravity coefficients and, for example, LOD variations amplitudes. The spacecraft accelerations due to the gravitational potential are linear in the spherical harmonic coefficients, and so are the Doppler

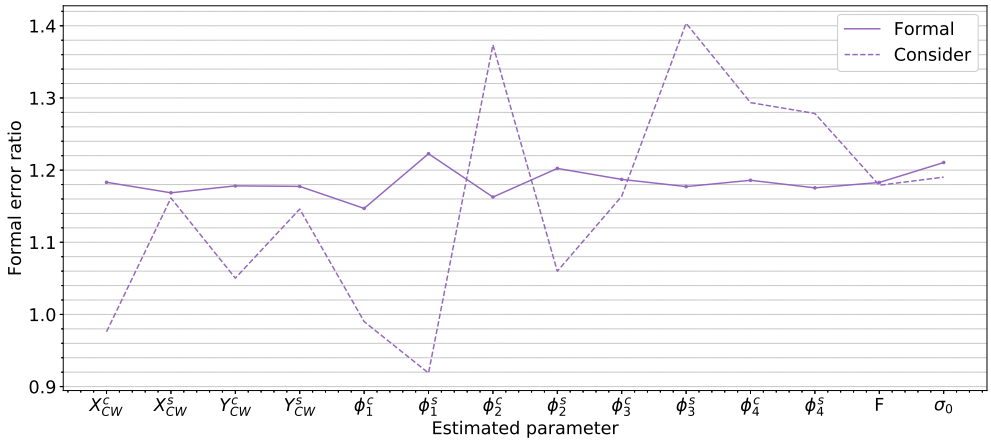

Figure 6.27: Uncertainties of the estimation case with 10 hr/day of tracking, relative to the nominal solution

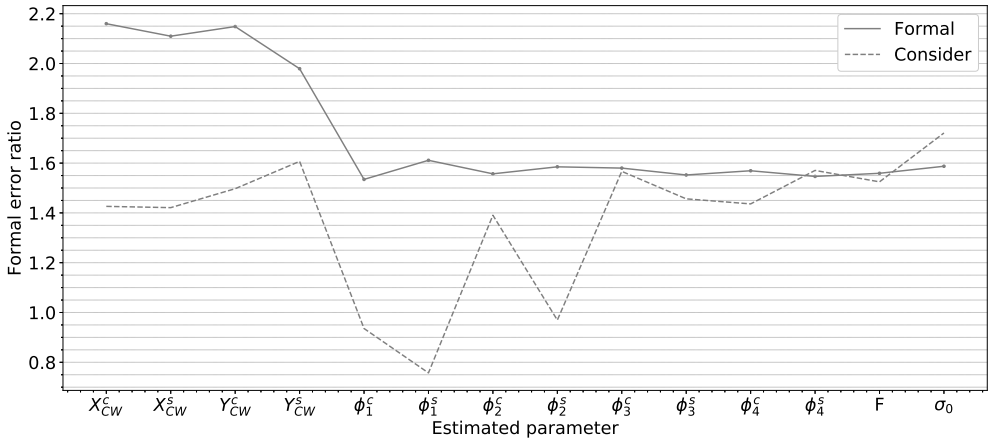

Figure 6.28: Uncertainties of the estimation case with 6 hr/day of tracking, relative to the nominal solution

partials. Thus, the same elements of the information matrix used in the estimation of the static zonal coefficients can be used for the estimation of the time-varying coefficients. In this estimation case, the C_{20} and C_{30} coefficients are treated as local parameters, meaning they are estimated at each arc. This is done by substituting the information matrix column corresponding to each zonal coefficient with as many columns as there are arcs, and distributing the partials from the removed column over these new columns according to the arc to which each measurement belongs. The nominal values and a priori uncertainties of the zonal coefficients are the same at every arc, and equal to those of the static gravity field (Konopliv et al., 2016).

The ratios thus obtained are shown in Figure 6.29. While the formal errors of both the polar motion and the LOD variations parameters (which are thought to be strongly correlated to the variable gravity field) stay close to the nominal solutions, the errors for the non-rigid nutation parameters are more than 10 times the nominal solutions. This means that a more realistic prediction for these parameters is obtained by estimating them together with the variable gravity field coefficients.

6.3.6. Comparison with lander estimates

The TGO Doppler data are now combined with those from a single lander on Mars, in order to assess the impact of the orbiter observations on the precision of the joint solution. The lander properties are chosen in such a way as to replicate as closely as possible those predicted for LaRa. Therefore, the landing site is fixed at 18.20° N of latitude and 335.45° E of longitude on the Martian surface. The radio

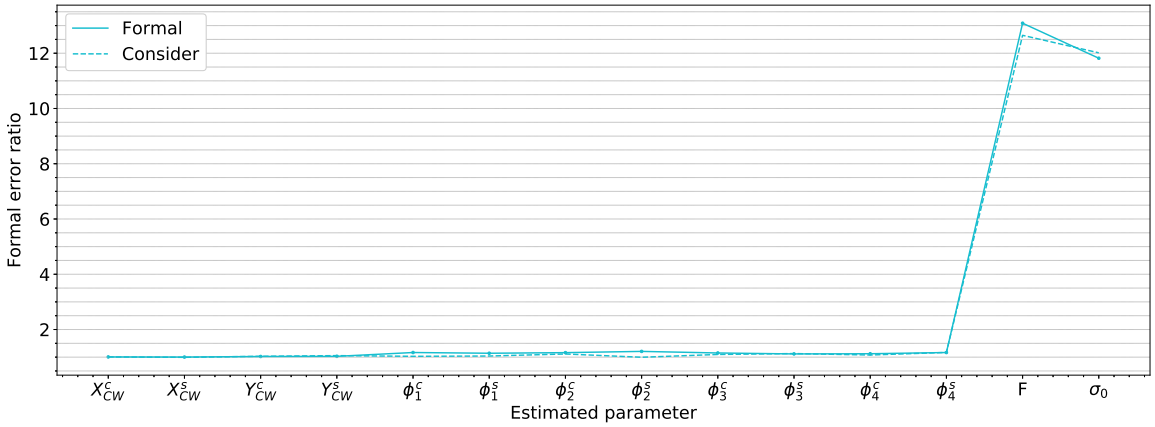

Figure 6.29: Uncertainties of the estimation case including Mars variable gravity field relative to the nominal solution

link with Earth is assumed to be in the X-band, hence the same noise level as TGO data is taken for the simulated two-way Doppler observations from the lander. Like for TGO, in these simulations the lander is tracked by the sole New Norcia ground station. The observation schedule consists of 1 hour of tracking per week, with one measurement point per minute. The complete set of lander measurements spans the same 700-days period as the TGO data used for the previous results, which is a little more than 1 Martian year.

First, the formal errors resulting from the lander data alone are computed. The estimated parameters for the lander include the same set of MOP estimated with TGO, as well as the cartesian position of the lander. As in the orbiter case, the amplitudes of the first two polar motion frequencies are moved to the consider parameters. Therefore, a total of 17 parameters is estimated from the lander observations, while the number of consider parameters is 8. The a priori errors for the estimated MOP are once again equal to half their nominal value, or equal to the minimum value of 10 mas. As for the lander position components, instead, their a priori uncertainty is set to 1 km.

Table 6.5 lists, along with the a priori statistics, the formal errors with and without the consider parameters of the CW amplitudes, the LOD variations amplitudes, and the rest of the parameter set. All the uncertainties are obtained with synthetic data from the full tracking period of 700 days. The last two columns of the table list the solution obtained from synthetic RISE data by Folkner et al. (2018), in terms of the nominal values used in the simulation and the formal errors. These formal uncertainties are in general agreement with those predicted for RISE, if not for too optimistic estimates of the LOD variations amplitudes, which are 2 to 3 times larger than those provided there. This despite the higher latitude of the lander with respect to that of RISE, which should yield a worse sensitivity LOD variations (Le Maistre et al., 2012), and the higher amount of data for RISE, given its 1-hr per day tracking schedule, compared to the 1-hr per week assumed here. However, the RISE estimation included parameters not part of those estimated here, above all the precession rate of Mars, which may justify the degradation of the solution compared to the one obtained here. Moreover, the noise profile in the RISE simulation was more complex than the white noise used here, with time-correlated noise due to solar plasma. This more realistic noise budget may also contribute to the larger values of the RISE uncertainties for the LOD variations amplitudes.

Of particular interest is the error on the nutation transfer function parameters, which are about twice as large as those expected from RISE, but are still a more reasonable result than the excessively optimistic estimates obtained with the orbiter simulations. In this case, the higher frequency of the RISE observations could help explain the differences between the two solutions (Table 6.4).

The combination of orbiter and lander data can be justified by looking at the correlation matrices of the orbiter-only solution and the lander only-solution, as shown in Figures 6.30 and 6.31, respectively. The TGO estimated parameter show much lower correlations than in the lander estimation. This is thanks to the richer geometry relative to Mars provided by the orbiter, allowing to better separate the signals in the Doppler of different parameters.

Thus, the orbiter and lander datasets are merged, and the POD algorithm is applied to this full set

Parameter	Unit	A priori		Formal error		Folkner et al. (2018)	
		Value	Error	Without CP	With CP	Nominal	Uncertainty
X^c_{CW}	mas	54.6551	27.3275	4.5182	4.5239	-	-
X^s_{CW}	mas	0.7346	10	3.6170	3.6221	-	-
Y^c_{CW}	mas	-33.2059	16.6029	2.5334	2.5356	-	-
Y^s_{CW}	mas	-7.4894	10	2.3423	2.3440	-	-
ϕ^c_1	mas	481	240.5	2.9406	3.0453	481	6
ϕ^s_1	mas	-331	165.5	1.7178	1.7879	-331	4
ϕ^c_2	mas	-103	51.5	2.4864	2.5512	-103	5
ϕ^s_2	mas	-101	50.5	2.4427	2.6000	-101	4
ϕ^c_3	mas	-35	17.5	2.0229	2.0242	-35	4
ϕ^s_3	mas	-4	10	2.0299	2.0326	-4	3
ϕ^c_4	mas	-10	10	1.6138	1.6197	-10	2
ϕ^s_4	mas	-8	10	1.7965	1.7971	-8	2
X	m	2920272	1000	0.0173	0.0175	-	-
Y	m	-1350573	1000	0.0234	0.0235	-	-
Z	m	1066231	1000	19.0081	19.0083	-	-
F	-	0.07	0.035	0.0270	0.0282	0.07	0.013
σ_0	deg/day	1.5	0.75	0.0473	0.0490	1.5	0.023

Table 6.5: Lander-only solution: a priori values and uncertainties, and formal errors with and without consider parameters after 700 days of tracking. The last column reports the accuracy expected from RISE on the LOD variations and FCN parameters, as obtained by Folkner et al. (2018)

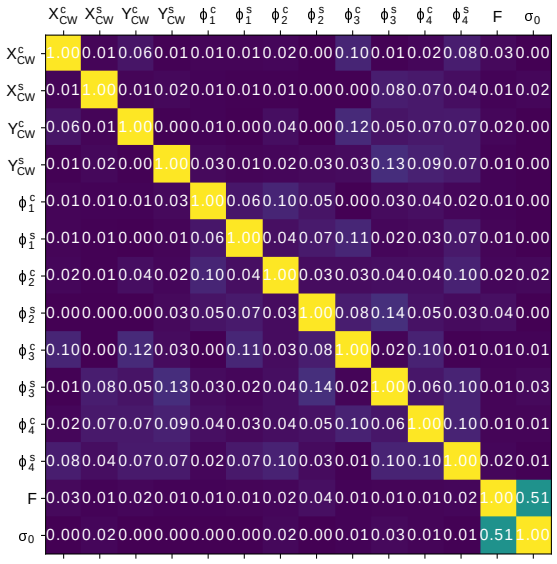

Figure 6.30: Correlations between the MOP estimated as part of the TGO solution

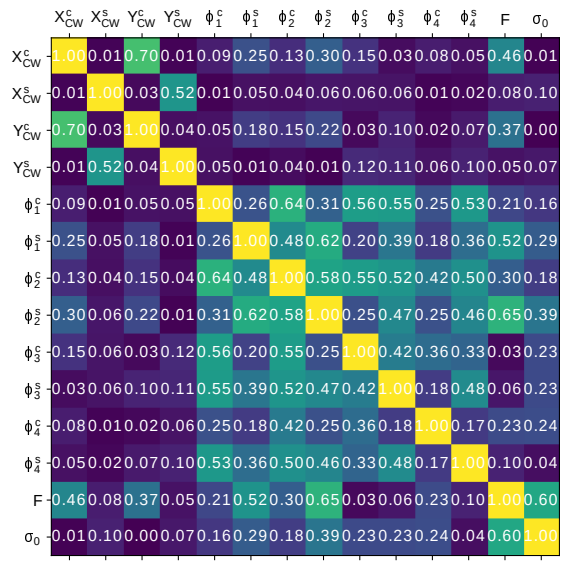

Figure 6.31: Correlations between the MOP estimated as part of the lander solution

of observations. This is achieved by combining the two information matrices. The parameters solved for in the joint estimation are the states of TGO at the beginning of each arc, the aerodynamic drag and solar radiation pressure coefficients of TGO for each arc, the cartesian position of the lander, and the MOP estimated in the previous results. As before, the amplitudes of the annual and semiannual harmonics of the forced polar motion are taken as consider parameters. For simplicity, there is no estimation of the Mars gravity field, although this means that the orbiter contribution to the final solution will be overestimated. Hence, the TGO information matrix has a smaller number of columns. On the other hand, three columns of zeroes are added to this matrix, representing the partials of the TGO observable with respect to the lander position. In the same way, columns of zeros are added to the lander information matrix, one for each of the states and surface-forces coefficients estimated for TGO. Consequently, the two information matrices have the same number of columns, and are stacked vertically to generate the information matrix for the joint estimation. The two matrices are stacked by using the same weight, as the noise level of the orbiter and lander measurements are assumed to be the same.

The solutions for the MOP and the lander position, as estimated from the full combined dataset, are listed in Table 6.6. The formal errors for the CW amplitudes are very close to those part of the TGO-only solution (Table 6.2), due to the lower sensitivity of the lander to polar motion. The formal uncertainties for the LOD variations amplitudes are instead about 10% smaller than those obtained exclusively from the spacecraft measurements (Table 6.3). The final formal errors for the F and σ_0 parameters are again unrealistically low, and very close to the orbiter-only solution (Table 6.4). In the same Table, it can be seen that the errors on the lander position are smaller than for the lander-only solution (Table 6.5), because in the combined solution the other parameters are known with higher accuracy.

Parameter	Unit	A priori		Formal error	
		Value	Error	Without CP	With CP
X^c_{CW}	mas	54.6551	27.3275	0.4994	1.1568
X^s_{CW}	mas	0.7346	10	0.5087	0.7116
Y^c_{CW}	mas	-33.2059	16.6029	0.4326	0.9614
Y^s_{CW}	mas	-7.4894	10	0.4416	0.6067
ϕ^c_1	mas	481	240.5	0.8451	1.0170
ϕ^s_1	mas	-331	165.5	0.7834	0.8263
ϕ^c_2	mas	-103	51.5	0.8247	0.9232
ϕ^s_2	mas	-101	50.5	0.7947	0.9721
ϕ^c_3	mas	-35	17.5	0.8007	0.8088
ϕ^s_3	mas	-4	10	0.8176	0.8378
ϕ^c_4	mas	-10	10	0.7805	0.8006
ϕ^s_4	mas	-8	10	0.8366	0.8480
X	m	2920272	1000	0.0151	0.0152
Y	m	-1350573	1000	0.0155	0.0164
Z	m	1066231	1000	17.4700	17.6470
F	-	0.07	0.035	3.5770e-4	4.0000e-4
σ_0	deg/day	1.5	0.75	9.2961e-4	9.6641e-4

Table 6.6: Lander and TGO combined solution: a priori values and uncertainties, and formal errors with and without consider parameters after 700 days of tracking.

Given the equal weighting of the two datasets, the combined solution for the MOP is led by the heavily optimistic results of TGO (as discussed in Section 6.3.3). However, both the consider uncertainties and the errors obtained when including the variable gravity in the estimation, suggest that in reality the errors may be one order of magnitude larger than the nominal solution. For this reason, another combined estimation is performed, this time weighting the two datasets differently. In particular, the noise level of the TGO observations is raised tenfold, while that for the lander is kept the same. The evolution

over time of the uncertainties of the estimated parameters resulting from this new dataset is presented in Figures 6.35 to 6.34. The corresponding final uncertainties are listed in Table 6.7. Rescaling the information matrices when combining data from different orbiters and landers is a common practice in the processing of real data (Konopliv et al., 2016; Kuchynka et al., 2014). In particular, the factors used by Konopliv et al. (2016) for the rescaling of orbiter data in the MRO120D solution are between 10 and 15, hence the same order of magnitude as the one used here. Konopliv et al. (2016) also rescaled the lander data, by a factor of 15. However, the radio-tracking data from LaRa will be whitened, and no meaningful systematic errors are expected in the real case (Le Maistre et al., Submitted), which is why the weighting of the lander observation in this new combined dataset is kept to 1. The weighting factors assumed here are more or less arbitrary values. More accurate scale factors for each set of measurements can be obtained with techniques such as the Helmert's method (Sahin et al., 1992), which is an iterative method solving for the optimal weighting by comparison of the a priori observation errors and the post-fit residuals. However, because of time constraints, it was not possible to operate a similar analysis for the combination of the two simulated datasets.

The results of the weighted solution are discussed in Chapter 7, as they are considered the main (numerical) results of this project.

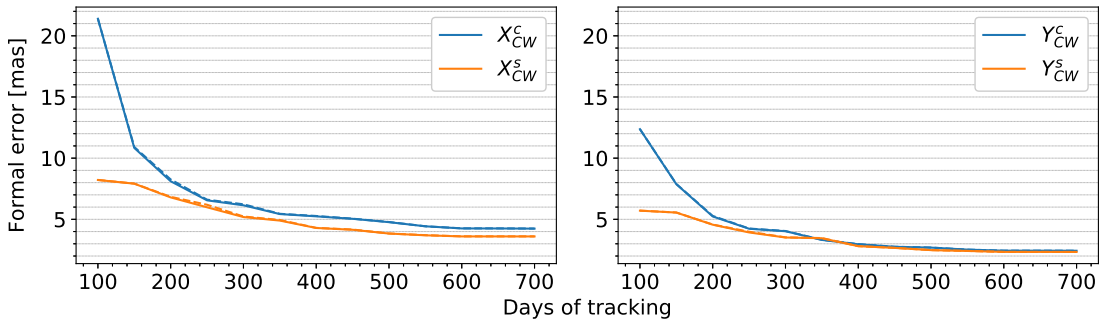

Figure 6.32: Formal error solutions for the CW amplitudes with (solid lines) and without(dashed lines) including the consider parameters uncertainties in the estimation, as obtained from the weighted combined dataset

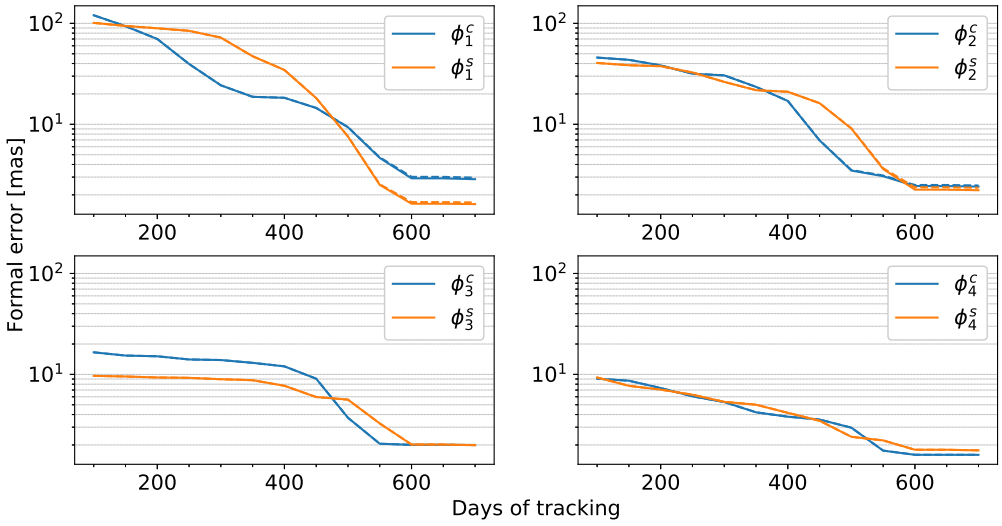

Figure 6.33: Formal error solutions for the LOD amplitudes with (solid lines) and without(dashed lines) including the consider parameters uncertainties in the estimation, as obtained from the weighted combined dataset

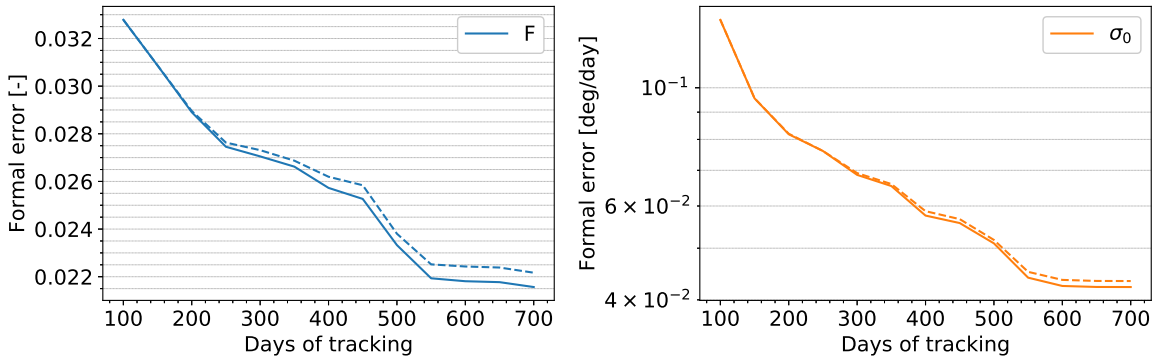

Figure 6.34: Formal error solutions for the nutation amplification parameters, with (solid lines) and without(dashed lines) including the consider parameters uncertainties in the estimation, as obtained from the weighted combined dataset

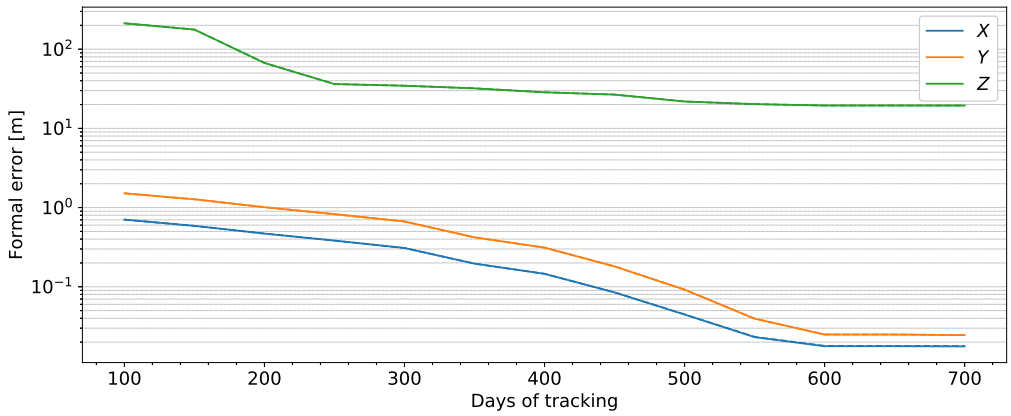

Figure 6.35: Formal error solutions for the cartesian components of the lander position, with (solid lines) and without(dashed lines) including the consider parameters uncertainties in the estimation, as obtained from the weighted combined dataset

Parameter	Unit	A priori		Formal error	
		Value	Error	Without CP	With CP
X_{CW}^{c}	mas	54.6551	27.3275	4.2390	4.2450
X_{CW}^{s}	mas	0.7346	10	3.6011	3.6057
Y_{CW}^{c}	mas	-33.2059	16.6029	2.4315	2.4246
Y_{CW}^{s}	mas	-7.4894	10	2.3337	2.3353
ϕ_1^c	mas	481	240.5	2.8582	2.7114
ϕ_1^s	mas	-331	165.5	1.6188	1.6108
ϕ_2^c	mas	-103	51.5	2.4161	2.2805
ϕ_2^s	mas	-101	50.5	2.2230	2.1940
ϕ_3^c	mas	-35	17.5	1.9968	1.8919
ϕ_3^s	mas	-4	10	1.9890	1.4089
ϕ_4^c	mas	-10	10	1.5963	1.5278
ϕ_4^s	mas	-8	10	1.7676	1.5537
X	m	2920272	1000	0.0170	0.0172
Y	m	-1350573	1000	0.0226	0.0227
Z	m	1066231	1000	18.9959	19.0000
F	-	0.07	0.035	0.0215	0.0221
σ_0	deg/day	1.5	0.75	0.0416	0.0427

Table 6.7: Lander and TGO combined and weighted solution: a priori values and uncertainties, and formal errors with and without consider parameters after 700 days of tracking. The orbiter data is rescaled by a factor of 10

For better clarity, Table 6.8 lists the formal errors (without consider parameters) obtained from the four different datasets: the orbiter measurements, the lander measurements, the combination of lander and orbiter data, and the combined dataset with weighting.

Parameter	Unit	A priori		Formal error			
		Value	Error	TGO	Lander	Combined	Weighted
X_{CW}^{c}	mas	54.6551	27.3275	0.5068	4.5182	0.4994	4.2390
X_{CW}^{s}	mas	0.7346	10	0.5154	3.6170	0.5087	3.6010
Y_{CW}^{c}	mas	-33.2059	16.6029	0.4521	2.5334	0.4326	2.4315
Y_{CW}^{s}	mas	-7.4894	10	0.4593	2.3423	0.4416	2.3337
ϕ_1^c	mas	481	240.5	0.9894	2.9406	0.8451	2.8582
ϕ_1^s	mas	-331	165.5	1.0064	1.7178	0.7834	1.6188
ϕ_2^c	mas	-103	51.5	1.0117	2.4864	0.8247	2.4161
ϕ_2^s	mas	-101	50.5	0.9942	2.4427	0.7947	2.2230
ϕ_3^c	mas	-35	17.5	0.9921	2.0229	0.8007	1.9968
ϕ_3^s	mas	-4	10	1.0317	2.0299	0.8176	1.9890
ϕ_4^c	mas	-10	10	0.9582	1.6138	0.7805	1.5963
ϕ_4^s	mas	-8	10	1.0634	1.7965	0.8366	1.7676
F	-	0.07	0.035	3.7210e-4	0.0270	3.5770e-4	0.0221
σ_0	deg/day	1.5	0.75	9.2969e-4	0.0473	9.2961e-4	0.0416

Table 6.8: MOP estimation: a priori values and uncertainties, and formal errors without consider parameters after 700 days of TGO-only tracking, of lander-only tracking, of TGO-lander combined non-weighted observations, and of TGO-lander combined weighted observations

7

Discussion

Here the principal results shown in Chapter 6 are examined, in order to gain insight on their significance and plausibility and their connection to the research question and subquestions, which will be answered in Chapter 8. First, Sections 7.1, 7.2, and 7.3, discuss the impact of TGO data on the uncertainties estimated from the lander-orbiter combined datasets for the CW amplitudes, the LOD amplitudes, and the FCN parameters, respectively. Then, Sections 7.4 and 7.5 investigate how the conclusions from the first three sections affect the knowledge about the interior and the atmosphere of Mars, respectively.

7.1. Impact of TGO on the CW solution

Once rescaled by a factor of 10 (to take into account the fact that the TGO solution is expected to be about one order of magnitude larger than that obtained from the Tudat, as discussed in Section 6.3.6), the formal uncertainties of the CW amplitudes given by the orbiter measurements are close to those corresponding to the lander-only solution, as shown in Table 7.1. In particular, the two solutions differ at the decimal level for the X component of polar motion, while for the Y component the orbiter estimates are almost twice those from the lander. A lander detects the wobble through a change in its distance from the rotation axis of the planet (Konopliv et al., 2006), hence it is logical to think that the lander data may be sensitive to one polar motion component more than the other. On the other hand, the orbiter can detect both components of the polar motion, hence its sensitivity is the same for both. Thus for the component to which it is more sensitive, the lander data provides twice the precision given by the orbiter, while for the other component the precision from the two datasets is the same.

Parameter	Formal error [mas]	
	Orbiter	Lander
X^c_{CW}	4.9645	4.5182
X^s_{CW}	4.5721	3.6170
Y^c_{CW}	4.3408	2.5334
Y^s_{CW}	4.1490	2.3423

Table 7.1: Chandler wobble amplitudes: comparison of the TGO-only values, after rescaling by a factor of 10, and lander-only solution.

The TGO uncertainties can then be compared to the only available estimates of the CW amplitudes from real tracking data of orbiters (MGS and Odyssey), given by Konopliv et al. (2006). There, uncertainties of about 6 mas (when scaling by 10 the 1-sigma error) were obtained, although with a nominal CW period of 205 d (compared to the 200 d period assumed here), and with estimated values of the amplitudes an order of magnitude smaller than those taken as nominal values in this study. Still, as the expression of the Doppler observable is linear in the CW amplitudes, and thus the observation partials do not depend on the value of the parameter, the formal uncertainties corresponding to a different nominal model for the CW should not vary significantly from those presented here. Moreover,

as seen in Figure 6.6, the CW signature on the Doppler with the current nominal model have an SNR higher than 10 over 10 days of tracking. Hence, the signal due to a forced polar motion at the Chandler frequency with amplitudes 10 times lower than those assumed here should still have an SNR larger than 1, although whether it can actually be estimated from the data depends from other parameters, as discussed in Section 6.1.2.

The improvement of the CW amplitudes solution following the addition of TGO measurements to the lander dataset is then presented in Figure 7.1, in terms of the ratio between the uncertainties of the combined solution (listed in Table 6.8, in the "Weighted" column) and those of the lander-only solution (Table 6.8 or 7.1). The maximum reduction is in the formal uncertainty of the X^c_{CW} amplitude, for which the two datasets appeared to have a similar sensitivity (and which has also the largest nominal value in the rotation model assumed for Mars). For this parameter, the formal error from the combined dataset is roughly 6% smaller than that obtained from lander data alone.

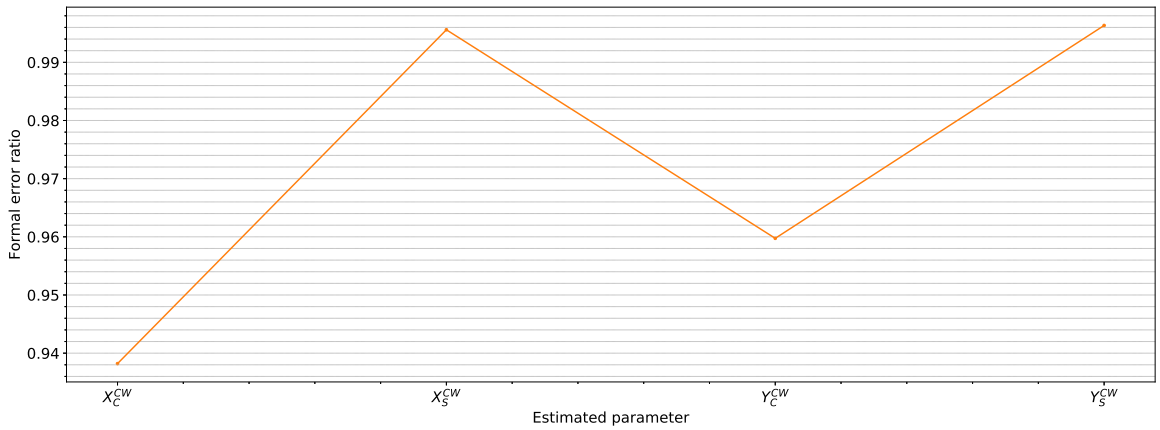

Figure 7.1: Ratio of the CW amplitudes formal errors from the combined weighted dataset and the lander-only solution

7.2. Impact of TGO on the LOD solution

The solution for the LOD variations amplitude obtained with the rescaled TGO-only full dataset can be compared to the uncertainties for the same parameter given in the orbiters-only solution of Konopliv et al. (2016). The two sets of uncertainties are shown in Table 7.2. Although the formal errors from TGO are lower than those from the MRO120D orbiter solution, it's hard to conclude on the better sensitivity of the first dataset to the LOD variations amplitude. Indeed, the scaling factor of 10 chosen for TGO, while justified in its order of magnitude by the study of the effects of some of the systematic errors and the inclusion of more parameters in the estimation, is an arbitrary value. A factor of 15 would be equally plausible, and produce uncertainties which are closer to those of MRO120D. Still, the differences between the two solutions may be simply due to them coming from very different estimation conditions. For the MRO120D, years of data MGS, Odyssey, and MRO are combined, meaning that the data points are about 50 times as much as those used for the TGO estimation. This should lead to uncertainties equal to or smaller than those from TGO. However, the set of parameters estimated as part of the MRO120D solution is way larger than those included in the TGO estimation, comprising the gravity field coefficients up to degree and order 120, the degree-2 Love number, and the Mars precession rate.

As for the impact of TGO measurements on the LOD amplitudes solution of the combined datasets, it can be assessed by computing the ratio between this combined solution and that obtained from the lander alone. These ratios are displayed in Figure Figure 7.2, for each of the LOD variations amplitudes. Due to the high accuracy expected from the LaRa data, the contributions of the spacecraft observation to the total solution for LOD are limited. The maximum reduction of the formal uncertainties following the inclusion of the orbiter data is about 8% of the corresponding lander-only solution, for the semiannual sine amplitude. For frequencies higher than the semiannual, the impact of the TGO data is minimal, with about 1% of improvement obtained using the combined dataset instead of the lander data alone.

Parameter	Formal error [mas]	
	TGO-only solution	MRO120D, orbiter (Konopliv et al., 2016)
ϕ_1^c	9.8646	17
ϕ_1^s	10.0044	17
ϕ_2^c	9.8872	16
ϕ_2^s	9.6867	17
ϕ_3^c	8.6142	15
ϕ_3^s	7.1734	16
ϕ_4^c	6.9090	15
ϕ_4^s	7.2797	15

Table 7.2: LOD variations amplitudes: comparison of the TGO-only values, after rescaling by a factor of 10, and the orbiter-only solution from Konopliv et al. (2016).

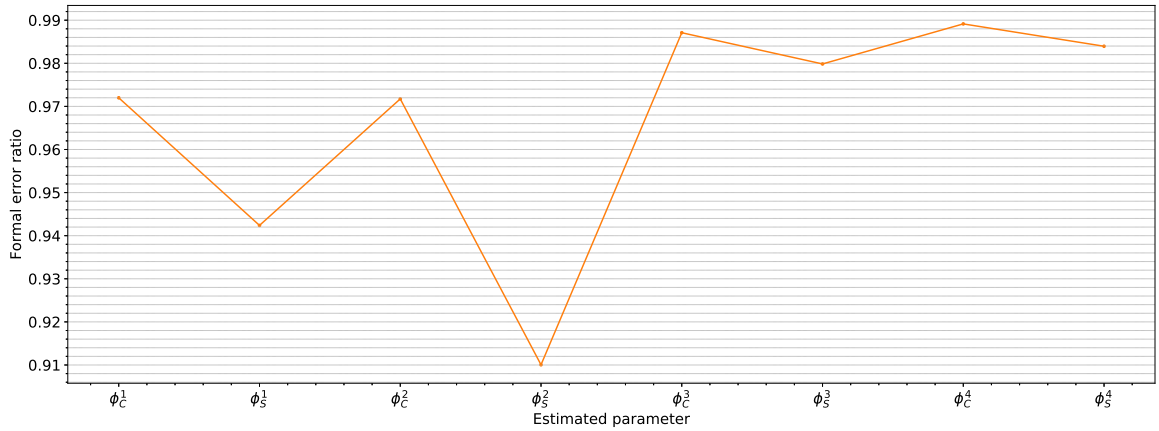

Figure 7.2: Ratio of the LOD variations amplitudes formal errors from the combined weighted dataset and the lander-only solution

7.3. Impact of TGO on the nutation transfer function solution

The solutions for the non-rigid nutation parameters given by the orbiter data are overly optimistic. Even after scaling the orbiter information matrix by the factor of 10, the uncertainties of these parameters are about one order of magnitude below those obtained from the lander data, as shown in Table 7.3. These solutions are once again obtained by using a priori errors equal to 10 times those used in the nominal TGO estimation. The F and σ_0 estimates from lander data, instead, are consistent with the expected RISE solution provided by Folkner et al. (2018), of 0.013 and 0.023 deg/day, respectively. The larger uncertainties estimated here for the lander compared to the RISE solution are possibly due to the larger amount of data expected from RISE, for which 1 hr of tracking per day is planned (compared to 1 hr per week in the observation schedule hypothesized here). No reference values for the estimation of these parameters from orbiter data is available in the literature, meaning their retrieval from spacecraft Doppler data is difficult. Hence, the formal errors for the orbiter case seem very unrealistic when compared to those from the lander, which are supposedly obtainable by experiments like RISE or LaRa. The very low formal errors obtained from TGO data can be ascribable to the non-inclusion of correlations with other parameters (such as the degree 2 Love number, or the precession rate), which are not part of the set of parameters and which may cause the formal errors to be far larger, or to possible software errors, as discussed in Section 6.3.

For completeness, considerations on the impact of TGO on the combined solution are made for these parameters as well, however unbelievable the correctness may be. Thus, Figure 7.3 plots the formal errors from the combined solution as a fraction of those from the lander-only solution. Although the sensitivity of TGO data to those parameters is overestimated, the combined solution is still driven

Parameter	Formal error [mas] Orbiter	Lander
F [-]	0.0036	0.0272
σ_0 [deg/day]	0.0090	0.0482

Table 7.3: Nutation amplification parameters: comparison of the TGO-only values, after rescaling by a factor of 10, and lander-only solution.

by the lander observations, with uncertainties that are closer to the lander-only ones than to those from TGO. Thus, the uncertainties for the combined solution have still reasonable values. The addition of TGO data results in a reduction of about 20% for the F error, and of about 12% for the σ_0 solution.

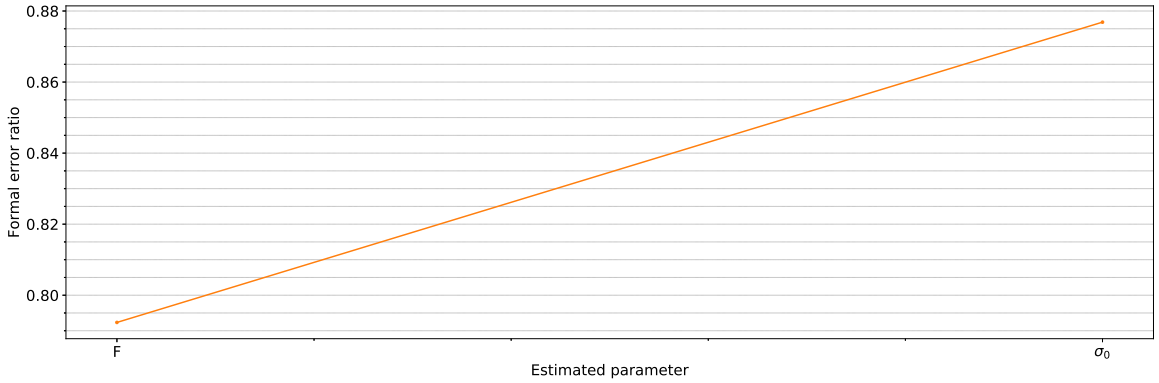

Figure 7.3: Ratio of the nutation amplification parameters formal errors from the combined weighted dataset and the lander-only solution

7.4. Impact of TGO on the knowledge of Mars interior

Without a reliable assessment of the improvement of the F and σ_0 solutions coming from TGO, it is hard to draw any conclusions with regards to the effect of TGO data on the uncertainty of the core-mantle boundary radius. Based on a qualitative analysis of Figure 2.3b, an improvement of 20% on an uncertainty of 0.0270 would translate in an improvement on the knowledge of the CMB radius anywhere from 20 km to 100 km, depending on the nominal value of F. However, the lander-only solution is about twice as large as that expected for RISE (0.013). Thus, even if the results from the previous Section were to be trusted, combination of TGO data with a more accurate lander dataset (better reflecting the expected precisions of both LaRa and RISE) would presumably yield a considerably reduced impact of TGO on the combined solution. This would in turn correspond to a reduced effect on the accuracy of the CMB radius estimate.

It was not possible to include the period of the CW in the parameters to estimate. As mentioned in Section 2.3.2, the period of this normal model is also dependent on the core radius, although a precision lower than 1 day would be required to infer interior properties with sufficient accuracy. A tentative assessment of the sensitivity of the TGO measurements to the CW period is made by comparing the LOS velocities outputs by ORB for two Mars rotation model which differ only in the period of this mode, 200 d for one and 201 d for the other. This way a signature on the LOS velocity of 0.3 mm/s is obtained, well above the noise level of 0.1 mm/s. It's not possible however, based just on this, to conclude that the CW period can be retrieved from TGO data with an uncertainty lower than 1 d.

7.5. Impact of TGO on the knowledge of Mars atmosphere

Detection of the CW on Mars may reveal information about the atmosphere dynamics at frequencies close to the CW period: a continuous forcing is needed to overcome the dissipation and sustain this normal mode, otherwise will disappear over time scales of tens of years, as mentioned in Section

2.3.2. Detecting the CW on Mars could prove the existence of this forcing, which should plausibly come from interactions between the atmosphere and the surface. This is of particular interest because this frequency is not multiple of the annual frequency, for which the processes are relatively well known from GCM models. TGO should be able to detect such a mode, as long as it is excited and has sufficient amplitude. However, in the combination with LaRa data, the improvement coming from TGO to the CW estimation is fairly limited (no more than 6%, as seen in Section 7.1). An orbit more sensitive to these parameters, and therefore having a larger effect on the accuracy of the combined solution, could be found by optimization of the LOS velocity signatures as given by the ORB method 6.2.2.

8

Conclusions and recommendations

This chapter presents the main conclusions which can be drawn from the results and the relative discussions shown in Chapters 6 and 7, respectively. The results are here shown in relation to the corresponding research (sub-)question.

- *What is the signature of the different MOP on the trajectory of TGO and the different radio tracking observables?*
  In Section 6.1, the LOD variations were found to have a signature in the order of 1 m in the position of the spacecraft and of 1 mm/s in its inertial velocity after 10 days of propagation. The signature of the non-rigid amplification of the nutations had a similar magnitude, while that of the Chandler wobble components of polar motion, with the assumed amplitude of up to 50 mas, was 10 times smaller. This translated to signatures on the range observables of up to about 1 m for LOD and FCN, and up to 10 cm for the CW. The signatures on the LOS velocity (and thus on the Doppler observable) for both CW and LOD variations were shown to be at least 10 times larger than the conservative value assumed for the measurement noise level of 0.1 mm/s. As suggested by this high signature in the LOS velocity, the LOD, FCN, and CW parameters were all retrieved from simulated TGO data (Sections 6.3.1 to 6.3.2) with accuracies generally smaller than 10% of the a priori uncertainties.

- *Is there an optimal method of combining data from InSight, LaRa, and TGO for the estimation of MOP?*
  Combination of the TGO and a LaRa-like lander with unitary weighting generated results judged too optimistic in comparison to those from similar studies, as discussed in Section 6.3.6. This solution was mainly driven by the low uncertainties from TGO (when compared to the lander-only solution and to values from literature), especially for the nutation amplification parameters. Therefore, the stability of the orbiter-only solution was tested in Section 6.3.5, by varying some of the estimation settings. Based on these results and the comparison with previous estimations and expected uncertainties of LaRa and RISE measurements, a weighting factor of 10 was adopted for the rescaling of the TGO observations when combined to those from a single lander. As shown in Section 6.3.6, this configuration resulted in an improvement of up to 6% in the accuracy of the amplitudes of the CW components with respect to the lander-only solution. For the LOD variations, the improvement following the inclusion of TGO data was maximum for the sine amplitude of the annual and semiannual harmonics, up to a decrease of 8 % in the uncertainties. An even higher improvement resulted for the nutation transfer function parameters, with a variation of 20 % on the value of F and of 12 % on the frequency of the FCN.

- *What is the expected improvement in the accuracy of the physical parameters of Mars coming from this improved accuracy on the MOP?*
  As discussed in Chapter 7, the improvement in the accuracy of the nutation transfer function parameters is considered too optimistic to be used for reliable estimations of the impact of the orbiter data on the inference of the core radius. At the same time, it was not possible to gauge the

accuracy of the CW period estimation, which is why overall no clear conclusions on the improvement of the core radius estimation can be made. On the other hand, the improvement on the CW and LOD estimation will prove useful in the characterization of Mars atmospheric dynamics both at seasonal time scales (cycle of CO_2) and at the CW period, assuming that this free mode is excited and sustained at a sufficient amplitude.

- *What is the set of orbital elements which maximizes the impact of the orbiter tracking data on the combined solution for the MOP?*
  In Section 5.2.1 it was shown that a simple first-order analytical method based on Kaula's equations and on algorithms of rotation of the spherical harmonics can be used to accurately predict the effect of a mismodeling of the complex rotation of the central body on the trajectory of an orbiting spacecraft. This faster method was preferred to the numerical propagation of the orbits in studying the variation of the maximum signature of CW and LOD on the LOS velocity, leading to the results shown in Section 6.2.2. Although the method was advantageous only for orbits with eccentricities lower than 0.5, being based on series expansions, it determined in this range two orbits which should maximize the science return in terms of MOP estimation. These two orbits had an eccentricity of about 0.01 and an inclination close to 40° for the CW, and a high eccentricity (close to 0.5) and near-equatorial inclination (5°) for the LOD estimation. Thus, spacecraft with orbital elements different than those of TGO could provide better improvement to the combined solution, although estimation with these hypothetical orbiters was not performed here. Still, these results proved valid only for a specific set of the other orbital elements. Hence, an optimization extended to all six orbital elements would be more adequate to the goal.

Overall, most of the goals mentioned in Chapter 1 were only partially met. The sensitivity of TGO to the MOP was tested extensively through simulations of orbits and radio-tracking data (Section 6.1), including a comparison with a different spacecraft to asses the relative level of this sensitivity. However, for what concerns the optimal weighting of the combined dataset, only two cases were considered (Section 6.3.6): the unitary weighting and an arbitrary value for the scaling of TGO. This process should be carried out more rigorously, possibly using iterative methods like Helmert's method, mentioned in that section.

The inference of Mars interior and atmosphere parameters was hindered by the unreliability of the MOP estimates for the FCN parameters. Finding the source of these problems, whether it is a model error or simply due to a too-small set of estimated parameters, should be the first step before embarking in a more precise inference of parameters like the CMB radius from these uncertainties.

Finally, ORB has shown to be successful in determining, from a wide array of orbits the one most sensitive to a specific parameter. However, as mentioned in Section 6.2.2, the optimization should involve all the Keplerian elements. Moreover, investigating the use of a different set of orbital elements for ORB could lead to the resolution of the differences with GINS seen for the perturbations on ω, M, and e. In any case, from what came out of the preliminary solution in Section 6.2.2, the TGO orbit should not be the optimal one in terms of sensitivity to the MOP. It was shown that polar motion should be obtainable from TGO data with an accuracy close to that of the lander solution, while previous orbiter missions have generally failed to give a reliable estimate of these parameters. Still, this is not a conclusive indication that the inclusion of TGO data to the lander measurements is advantageous with respect to that of other orbiters.

Bibliography

E. V. d. Acker, T. V. Hoolst, O. d. Viron, et al. Influence of the seasonal winds and the CO_2 mass exchange between atmosphere and polar caps on Mars' rotation. *Journal of Geophysical Research: Planets*, 107(E7):9–1–9–8, 2002. ISSN 2156-2202. doi:10.1029/2000JE001539.

B. A. Archinal, C. H. Acton, M. F. A'Hearn, et al. Report of the IAU Working Group on Cartographic Coordinates and Rotational Elements: 2015. *Celestial Mechanics and Dynamical Astronomy*, 130 (3):22, February 2018. ISSN 1572-9478. doi:10.1007/s10569-017-9805-5.

S. W. Asmar, J. W. Armstrong, L. Iess, and P. Tortora. Spacecraft Doppler tracking: Noise budget and accuracy achievable in precision radio science observations. *Radio Science*, 40(2), 2005. ISSN 1944-799X. doi:10.1029/2004RS003101.

W. B. Banerdt, S. Smrekar, P. Lognonné, et al. InSight: A Discovery Mission to Explore the Interior of Mars. volume 44, page 1915, March 2013.

G. J. Bierman. *Factorization Methods for Discrete Sequential Estimation*. 1977.

B. B. Bocanegra Bahamon. *Planetary Radio Interferometry and Doppler Experiment (PRIDE) for radio occultation studies: A Venus Express test case*. PhD thesis, Delft University of Technology, 2019.

G. Boué. The two rigid body interaction using angular momentum theory formulae. *Celestial Mechanics and Dynamical Astronomy*, 128(2):261–273, June 2017. ISSN 1572-9478. doi:10.1007/s10569-017-9751-2.

S. Bruinsma and F. G. Lemoine. A preliminary semiempirical thermosphere model of Mars: DTM-Mars. *Journal of Geophysical Research: Planets*, 107(E10):15–1–15–13, 2002. ISSN 2156-2202. doi:10.1029/2001JE001508.

B. F. Chao and D. P. Rubincam. Variations of Mars gravitational field and rotation due to seasonal CO2 exchange. *Journal of Geophysical Research: Solid Earth*, 95(B9):14755–14760, 1990. ISSN 2156-2202. doi:10.1029/JB095iB09p14755.

CNES/GRGS. Algorithmic documentation of the GINS software. Technical report, CNES, 11 2018.

P. Defraigne, O. d. Viron, V. Dehant, T. V. Hoolst, and F. Hourdin. Mars rotation variations induced by atmosphere and ice caps. *Journal of Geophysical Research: Planets*, 105(E10):24563–24570, 2000. ISSN 2156-2202. doi:10.1029/1999JE001227.

P. Defraigne, A. Rivoldini, T. V. Hoolst, and V. Dehant. Mars nutation resonance due to Free Inner Core Nutation. *Journal of Geophysical Research: Planets*, 108(E12), 2003. ISSN 2156-2202. doi:10.1029/2003JE002145.

V. Dehant and P. Mathews. Earth Rotation Variations. In *Treatise on Geophysics*, pages 263–305. Elsevier, 2015a. ISBN 978-0-444-53803-1. doi:10.1016/B978-0-444-53802-4.00066-X.

V. Dehant, T. V. Hoolst, O. d. Viron, et al. Can a solid inner core of Mars be detected from observations of polar motion and nutation of Mars? *Journal of Geophysical Research: Planets*, 108(E12), December 2003. ISSN 2156-2202. doi:10.1029/2003JE002140.

V. Dehant, O. d. Viron, O. Karatekin, and T. V. Hoolst. Excitation of Mars polar motion. *Astronomy & Astrophysics*, 446(1):345–355, January 2006. ISSN 0004-6361, 1432-0746. doi:10.1051/0004-6361:20053825.

V. Dehant, W. Folkner, E. Renotte, et al. Lander radioscience for obtaining the rotation and orientation of mars. *Planetary and Space Science*, 57(8-9):1050–1067, 2009.

V. Dehant and P. M. Mathews. *Precession, nutation and wobble of the Earth*. Cambridge University Press, Cambridge, 2015b. ISBN 978-1-107-09254-9. OCLC: 912476491.

D. Dirkx, L. L. A. Vermeersen, R. Noomen, and P. N. A. M. Visser. Phobos laser ranging: Numerical Geodesy experiments for Martian system science. *Planetary and Space Science*, 99:84–102, September 2014. ISSN 0032-0633. doi:10.1016/j.pss.2014.03.022.

D. Dirkx. *Interplanetary laser ranging—analysis for implementation in planetary science mission*. PhD thesis, Delft University of Technology, 2015.

D. Dirkx, I. Prochazka, S. Bauer, et al. Laser and radio tracking for planetary science missions—a comparison. *Journal of Geodesy*, July 2018. ISSN 1432-1394. doi:10.1007/s00190-018-1171-x.

D. Dirkx, E. Mooij, and B. Root. Propagation and estimation of the dynamical behaviour of gravitationally interacting rigid bodies. *Astrophysics and Space Science*, 364(2):37, February 2019. ISSN 1572-946X. doi:10.1007/s10509-019-3521-4.

W. M. Folkner, R. D. Kahn, R. A. Preston, et al. Mars dynamics from Earth-based tracking of the Mars Pathfinder lander. *Journal of Geophysical Research: Planets*, 102(E2):4057–4064, 1997a. ISSN 2156-2202. doi:10.1029/96JE02125.

W. M. Folkner, C. F. Yoder, D. N. Yuan, E. M. Standish, and R. A. Preston. Interior Structure and Seasonal Mass Redistribution of Mars from Radio Tracking of Mars Pathfinder. *Science*, 278(5344): 1749–1752, December 1997b. ISSN 0036-8075, 1095-9203. doi:10.1126/science.278.5344.1749.

W. M. Folkner, J. G. Williams, D. H. Boggs, R. S. Park, and P. Kuchynka. The Planetary and Lunar Ephemerides DE430 and DE431. *Interplanetary Network Progress Report*, 196:1–81, February 2014.

W. M. Folkner, V. Dehant, S. Le Maistre, et al. The Rotation and Interior Structure Experiment on the InSight Mission to Mars. *Space Science Reviews*, 214(5):100, August 2018. ISSN 1572-9672. doi:10.1007/s11214-018-0530-5.

W. Folkner, P. Charlot, M. Finger, et al. Determination of the extragalactic-planetary frame tie from joint analysis of radio interferometric and lunar laser ranging measurements. *Astronomy and Astrophysics*, 287:279–289, 1994.

F. Forget, F. Hourdin, R. Fournier, et al. Improved general circulation models of the Martian atmosphere from the surface to above 80 km. *Journal of Geophysical Research: Planets*, 104(E10):24155–24175, 1999. ISSN 2156-2202. doi:10.1029/1999JE001025.

A. Genova, S. Goossens, F. G. Lemoine, et al. Long-term variability of CO2 and O in the Mars upper atmosphere from MRO radio science data. *Journal of Geophysical Research: Planets*, 120(5):849–868, 2015. ISSN 2169-9100. doi:10.1002/2014JE004770.

A. Genova, S. Goossens, F. G. Lemoine, et al. Seasonal and static gravity field of Mars from MGS, Mars Odyssey and MRO radio science. *Icarus*, 272:228–245, July 2016. ISSN 0019-1035. doi:10.1016/j.icarus.2016.02.050.

M. L. Gobinddass, P. Willis, O. de Viron, et al. Improving DORIS geocenter time series using an empirical rescaling of solar radiation pressure models. *Advances in Space Research*, 44(11):1279–1287, December 2009. ISSN 0273-1177. doi:10.1016/j.asr.2009.08.004.

R. M. Haberle, M. M. Joshi, J. R. Murphy, et al. General circulation model simulations of the Mars Pathfinder atmospheric structure investigation/meteorology data. *Journal of Geophysical Research: Planets*, 104(E4):8957–8974, 1999. ISSN 2156-2202. doi:10.1029/1998JE900040.

L. Iess, M. Di Benedetto, N. James, et al. Astra: Interdisciplinary study on enhancement of the end-to-end accuracy for spacecraft tracking techniques. *Acta Astronautica*, 94(2):699–707, February 2014. ISSN 0094-5765. doi:10.1016/j.actaastro.2013.06.011.

R. A. Jacobson. The orbits and masses of the Martian satellites and the libration of Phobos. *The Astronomical Journal*, 139(2):668–679, January 2010. ISSN 1538-3881. doi:10.1088/0004-6256/139/2/668.

R. Jacobson, A. Konopliv, R. Park, and W. Folkner. The rotational elements of Mars and its satellites. *Planetary and Space Science*, 152:107–115, March 2018. ISSN 00320633. doi:10.1016/j.pss.2017.12.020.

H. L. J. Justh. Mars-GRAM 2010: Improving the Precision of Mars-GRAM. Paris, France, February 2011.

Ö. Karatekin, J. Duron, P. Rosenblatt, et al. Mars' time-variable gravity and its determination: Simulated geodesy experiments. *Journal of Geophysical Research: Planets*, 110(E6), 2005. ISSN 2156-2202. doi:10.1029/2004JE002378.

Ö. Karatekin, T. V. Hoolst, J. Tastet, O. de Viron, and V. Dehant. The effects of seasonal mass redistribution and interior structure on Length-of-Day variations of Mars. *Advances in Space Research*, 38(4):739–744, January 2006. ISSN 0273-1177. doi:10.1016/j.asr.2005.03.117.

W. M. Kaula. *Theory of satellite geodesy: applications of satellites to geodesy*. Dover Publications, Mineola, N.Y, dover ed edition, 2000. ISBN 978-0-486-41465-2.

A. Khan, C. Liebske, A. Rozel, et al. A Geophysical Perspective on the Bulk Composition of Mars. *Journal of Geophysical Research: Planets*, 123(2):575–611, February 2018. ISSN 2169-9097. doi:10.1002/2017JE005371.

A. S. Konopliv, C. F. Yoder, E. M. Standish, D.-N. Yuan, and W. L. Sjogren. A global solution for the Mars static and seasonal gravity, Mars orientation, Phobos and Deimos masses, and Mars ephemeris. *Icarus*, 182(1):23–50, May 2006. ISSN 00191035. doi:10.1016/j.icarus.2005.12.025.

A. S. Konopliv, S. W. Asmar, W. M. Folkner, et al. Mars high resolution gravity fields from MRO, Mars seasonal gravity, and other dynamical parameters. *Icarus*, 211(1):401–428, January 2011. ISSN 00191035. doi:10.1016/j.icarus.2010.10.004.

A. S. Konopliv, R. S. Park, and W. M. Folkner. An improved JPL Mars gravity field and orientation from Mars orbiter and lander tracking data. *Icarus*, 274:253–260, August 2016. ISSN 00191035. doi:10.1016/j.icarus.2016.02.052.

P. Kuchynka, W. M. Folkner, A. S. Konopliv, et al. New constraints on Mars rotation determined from radiometric tracking of the Opportunity Mars Exploration Rover. *Icarus*, 229:340–347, February 2014. ISSN 0019-1035. doi:10.1016/j.icarus.2013.11.015.

S. M. Kudryavtsev. Accurate Analytical Calculation of Effects of Rorations of the Central Planet on a Staellite's Orbit. *Celestial Mechanics and Dynamical Astronomy*, 67(2):131–144, February 1997. ISSN 1572-9478. doi:10.1023/A:1008213326840.

V. Lainey, V. Dehant, and M. Pätzold. First numerical ephemerides of the Martian moons. *Astronomy & Astrophysics*, 465(3):1075–1084, April 2007. ISSN 0004-6361, 1432-0746. doi:10.1051/0004-6361:20065466.

S. Le Maistre, M.-J. Péters, V. Dehant, and J.-C. Marty. On the impact of the operational and technical characteristics of the lara experiment on the nutation determination. *Planetary and Space Science*, (2), Submitted.

S. Le Maistre. *The rotation of Mars and Phobos from Earth-based radio-tracking observations of a lander*. PhD thesis, Université catholique de Louvain, 2013. Retrieved from http://hdl.handle.net/2078.1/135864.

S. Le Maistre, P. Rosenblatt, A. Rivoldini, et al. Lander radio science experiment with a direct link between Mars and the Earth. *Planetary and Space Science*, 68(1):105–122, August 2012. ISSN 0032-0633. doi:10.1016/j.pss.2011.12.020.

P. Lognonné, W. B. Banerdt, D. Giardini, et al. SEIS: Insight's Seismic Experiment for Internal Structure of Mars. *Space Science Reviews*, 215(1):12, January 2019. ISSN 1572-9672. doi:10.1007/s11214-018-0574-6.

W. Lowrie. *A student's guide to geophysical equations*. Cambridge University Press, Cambridge ; New York, 2011. ISBN 978-1-107-00584-6.

J. A. Marshall and S. B. Luthcke. Modeling radiation forces acting on Topex/Poseidon for precision orbit determination. *Journal of Spacecraft and Rockets*, 31(1):99–105, January 1994. ISSN 0022-4650. doi:10.2514/3.26408.

J. C. Marty, G. Balmino, J. Duron, et al. Martian gravity field model and its time variations from MGS and Odyssey data. *Planetary and Space Science*, 57(3):350–363, March 2009. ISSN 0032-0633. doi:10.1016/j.pss.2009.01.004.

J. C. Marty, S. Loyer, F. Perosanz, et al. GINS: the CNES/GRGS GNSS scientific software. page 4, 2011.

E. Mazarico, M. T. Zuber, F. G. Lemoine, and D. E. Smith. Effects of Self-Shadowing on Nonconservative Force Modeling for Mars-Orbiting Spacecraft. *Journal of Spacecraft and Rockets*, 46(3): 662–669, May 2009. ISSN 0022-4650. doi:10.2514/1.41679.

A. Milani and G. Gronchi. *Theory of Orbit Determination*. Cambridge University Press, 2010. ISBN 978-0-521-87389-5. Google-Books-ID: 5oLK7QtX6j4C.

O. Montenbruck and E. Gill. *Satellite orbits: models, methods, and applications*. Springer, Berlin, 2012. ISBN 978-3-540-67280-7 978-3-642-58351-3. OCLC: 876786620.

T. D. Moyer. *Formulation for observed and computed values of Deep Space Network data types for navigation*. Deep-space communications and navigation series. Wiley-Interscience, Hoboken, N.J, 2003. ISBN 978-0-471-44535-7.

G. Petit and B. Luzum. IERS Conventions (2010). *IERS Technical Note*, 36, 2010.

R. D. Reasenberg and R. W. King. The rotation of Mars. *Journal of Geophysical Research*, 84(B11): 6231, 1979. ISSN 0148-0227. doi:10.1029/JB084iB11p06231.

A. Rivoldini, T. Van Hoolst, O. Verhoeven, A. Mocquet, and V. Dehant. Geodesy constraints on the interior structure and composition of Mars. *Icarus*, 213(2):451–472, June 2011. ISSN 0019-1035. doi:10.1016/j.icarus.2011.03.024.

F. Roosbeek. Analytical developments of rigid Mars nutation and tide generating potential series. *Celestial Mechanics and Dynamical Astronomy*, 75(4):287–300, December 1999. ISSN 1572-9478. doi:10.1023/A:1008310918697.

M. Sahin, P. A. Cross, and P. C. Sellers. Variance component estimation applied to satellite laser ranging. *Bulletin Géodésique*, 66(3):284–295, October 1992. ISSN 0949-7714, 1432-1394. doi:10.1007/BF02033189.

B. V. Sanchez, D. D. Rowlands, R. M. Haberle, and J. Schaeffer. Atmospheric rotational effects on Mars based on the NASA Ames general circulation model. *Journal of Geophysical Research: Planets*, 108 (E5), 2003. ISSN 2156-2202. doi:10.1029/2002JE001984.

B. V. Sanchez, D. D. Rowlands, and R. M. Haberle. Variations of Mars gravitational field based on the NASA/Ames general circulation model. *Journal of Geophysical Research: Planets*, 111(E6), 2006. ISSN 2156-2202. doi:10.1029/2005JE002442.

T. Sasao, S. Okubo, and M. Saito. A Simple Theory on the Dynamical Effects of a Stratified Fluid Core upon Nutational Motion of the Earth. In E. P. Fedorov, M. L. Smith, and P. L. Bender, editors, *Nutation and the Earth's Rotation*, International Astronomical Union / Union Astronomique Internationale, pages 165–183. Springer Netherlands, Dordrecht, 1980. ISBN 978-94-010-9568-6. doi:10.1007/978-94-010-9568-6_27.

D. E. Smith, M. T. Zuber, H. V. Frey, et al. Mars Orbiter Laser Altimeter: Experiment summary after the first year of global mapping of Mars. *Journal of Geophysical Research: Planets*, 106(E10):23689–23722, October 2001. ISSN 01480227. doi:10.1029/2000JE001364.

D. E. Smith, M. T. Zuber, M. H. Torrence, et al. Time variations of Mars' gravitational field and seasonal changes in the masses of the polar ice caps. *Journal of Geophysical Research: Planets*, 114(E5), 2009. ISSN 2156-2202. doi:10.1029/2008JE003267.

F. Sohl and T. Spohn. The interior structure of Mars: Implications from SNC meteorites. *Journal of Geophysical Research: Planets*, 102(E1):1613–1635, 1997. ISSN 2156-2202. doi:10.1029/96JE03419.

A. Spiga, D. Banfield, N. A. Teanby, et al. Atmospheric Science with InSight. *Space Science Reviews*, 214(7):109, October 2018. ISSN 1572-9672. doi:10.1007/s11214-018-0543-0.

B. D. Tapley, B. E. Schutz, and G. H. Born. *Statistical orbit determination*. Elsevier Academic Press, Amsterdam ; Boston, 2004. ISBN 978-0-12-683630-1.

G. J. Taylor. The bulk composition of Mars. *Chemie der Erde - Geochemistry*, 73(4):401–420, December 2013. ISSN 0009-2819. doi:10.1016/j.chemer.2013.09.006.

C. L. Thornton and J. S. Border. *Radiometric Tracking Techniques for Deep Space Navigation: Thornton/Radiometric Tracking Techniques*. John Wiley & Sons, Inc., Hoboken, NJ, USA, January 2003. ISBN 978-0-471-72845-0 978-0-471-44534-0. doi:10.1002/0471728454.

T. Van Hoolst. Rotation of the Terrestrial Planets. In *Treatise on Geophysics*, pages 121–151. Elsevier, 2015. ISBN 978-0-444-53803-1. doi:10.1016/B978-0-444-53802-4.00168-8.

T. Van Hoolst and A. Rivoldini. Chapter 18 - Interior Structure and Evolution of Mars. In T. Spohn, D. Breuer, and T. V. Johnson, editors, *Encyclopedia of the Solar System (Third Edition)*, pages 379–396. Elsevier, Boston, January 2014. ISBN 978-0-12-415845-0. doi:10.1016/B978-0-12-415845-0.00018-9.

T. Van Hoolst, V. Dehant, and P. Defraigne. Chandler wobble and Free Core Nutation for Mars. *Planetary and Space Science*, 48(12-14):1145–1151, October 2000a. ISSN 00320633. doi:10.1016/S0032-0633(00)00099-4.

T. Van Hoolst, V. Dehant, and P. Defraigne. Sensitivity of the Free Core Nutation and the Chandler Wobble to changes in the interior structure of Mars. *Physics of the Earth and Planetary Interiors*, 117 (1-4):397–405, January 2000b. ISSN 00319201. doi:10.1016/S0031-9201(99)00109-0.

K. F. Wakker. Fundamentals of astrodynamics. 2015.

M. A. Wieczorek. Thickness of the Martian crust: Improved constraints from geoid-to-topography ratios. *Journal of Geophysical Research*, 109(E1), 2004. ISSN 0148-0227. doi:10.1029/2003JE002153.

C. F. Yoder and E. M. Standish. Martian precession and rotation from Viking lander range data. *Journal of Geophysical Research: Planets*, 102(E2):4065–4080, February 1997. ISSN 01480227. doi:10.1029/96JE03642.

C. F. Yoder, A. S. Konopliv, D. N. Yuan, E. M. Standish, and W. M. Folkner. Fluid Core Size of Mars from Detection of the Solar Tide. *Science*, 300(5617):299–303, April 2003. ISSN 0036-8075, 1095-9203. doi:10.1126/science.1079645.

M. Zannoni and P. Tortora. Numerical Error in Interplanetary Orbit Determination Software. *Journal of Guidance, Control, and Dynamics*, 36(4):1008–1018, May 2013. ISSN 0731-5090. doi:10.2514/1.59294.

R. Ziese and K. Willner. Mutual event observations of solar system objects by SRC on Mars Express - Analysis and release of observations. *Astronomy & Astrophysics*, 614:A15, June 2018. ISSN 0004-6361, 1432-0746. doi:10.1051/0004-6361/201731644.

M. T. Zuber, F. G. Lemoine, D. E. Smith, et al. Mars Reconnaissance Orbiter Radio Science Gravity Investigation. *Journal of Geophysical Research: Planets*, 112(E5), 2007. ISSN 2156-2202. doi:10.1029/2006JE002833.

Appendix A: Rotation of spherical harmonics coefficients

A.1. Method from Kudryavtsev (1997)

The method described in Kudryavtsev (1997) allows to compute the spherical harmonics coefficients following an elementary rotation around the X, Y, or Z axis of the original frame.

For a rotation around the Z axis of an angle w, indicating with C_{nm} and S_{nm} the (unnormalized) spherical harmonic coefficients in the original frame, and with C^z_{nm} and S^z_{nm} the spherical harmonic coefficients in the rotated frame, the latter coefficients are found as:

$$\begin{aligned} C^z_{nm} &= C_{nm}\cos(mw) + S_{nm}\sin(mw) \\ S^z_{nm} &= S_{nm}\cos(mw) - C_{nm}\sin(mw) \end{aligned} \tag{A.1}$$

For rotations around the other two axes the formulas are more involved:

$$\begin{aligned} C^*_{nm} &= \Re(\Gamma_{nm}) \\ S^*_{nm} &= \Im(\Gamma_{nm}) \end{aligned} \tag{A.2}$$

where the asterisk can be either x or y, depending on the rotation axis, and:

$$\begin{aligned} \Gamma_{nm} = &\frac{\delta_m n!}{(n+m)!} H^*_0 C_{n0} + \sum_{s=1}^{N}\left[\frac{\delta_m\,(n+s)!}{2\,(n+m)!}\left(H^*_s + (-1)^s H^*_{-s}\right)\right] C_{ns} + \\ &+ \sum_{s=1}^{N}\left[i\frac{\delta_m\,(n+s)!}{2\,(n+m)!}\left(H^*_s + (-1)^s H^*_{-s}\right)\right] S_{ns} \end{aligned} \tag{A.3}$$

Here $i = \sqrt{-1}$ is the imaginary unit,

$$\delta_m = \begin{cases} 1, & \text{if } m = 0 \\ 2, & \text{if } m \neq 0 \end{cases}$$

and

$$H^x_s = \sum_k i^{2n-2k-m-s} C^k_{n-m} Cn + m^{n-k-s}\left(\cos\frac{u}{2}\right)^{2k+m+s}\left(\sin\frac{u}{2}\right)^{2n-2k-m-s} \tag{A.4}$$

$$H^y_s = \sum_k (-1)^{n-k-s} C^k_{n-m} Cn + m^{n-k-s}\left(\cos\frac{v}{2}\right)^{2k+m+s}\left(\sin\frac{v}{2}\right)^{2n-2k-m-s} \tag{A.5}$$

The terms C^k_{n-m} and $Cn + m^{n-k-s}$ are binomial coefficients, u and v are the angles of the elementary rotations around the X and the Y axis, respectively, and the limits of the index k are given by:

$$\max(0, -m-s) \leq k \leq \min(n-m, n-s) \tag{A.6}$$

A.2. Method from Dirkx et al. (2019)

Given an input rotation matrix R, it is converted to quaternion rapresentation according to:

$$\begin{aligned} q_0 &= \frac{\sqrt{1 + R_{11} + R_{22} + R_{33}}}{2} \\ q_1 &= \frac{R_{32} - R_{23}}{4q_0} \\ q_2 &= \frac{R_{13} - R_{31}}{4q_0} \\ q_3 &= \frac{R_{21} - R_{12}}{4q_0} \end{aligned} \tag{A.7}$$

If the trace of the rotation matrix is close to -1 the process is stopped, in order to avoid singularities, and the spherical hamronics coefficients are left unchanged.

What follows is then taken entirely from Dirkx et al. (2019) and the references therein. From the quaternions, the Cayley-Klein parameters are computed as:

$$\begin{aligned} a &= q_0 - iq_3 \\ b &= q_2 - iq_1 \end{aligned} \tag{A.8}$$

Then the vector $\boldsymbol{c}$ is defined as:

$$\boldsymbol{c} = [\Re(a), \Im(a), \Re(b), \Im(b)]^T \tag{A.9}$$

The Wigner D-matrices are hence computed by recursion, starting from:

$$D^0_{0,0} = 1 \tag{A.10}$$

$$D^1_{m,k} = \begin{bmatrix} (a^*)^2 & \sqrt{2}a^*b & b^2 \\ -\sqrt{2}a^*b^* & |a|^2 - |b|^2 & \sqrt{2}ab \\ (ab^*)^2 & -\sqrt{2}ab^* & (a^*)^2 \end{bmatrix} \tag{A.11}$$

where a^* and b^* are the complex conjugate of the Cayley-Klein parameters a and b. The values of the subscripts m, k, with $-l \leq m, k \leq l$, determine a specific element of the generic D-matrix, relative to the central elements. Therefore, the central element is indicated by the subscript $0, 0$, while the values of m are positive for the rows below the central one, and values of k are positive for columns to the right of the central one.

Then, for the D-matrices of higher degree and for $m \geq 0$:

$$D^l_{mk} = \sum_{p=-1}^{1} c^{l;p}_{mk} D^1_{1,-p} D^{l-1}_{m-1,k+p} \tag{A.12}$$

with

$$\begin{aligned} c^{l;-1}_{mk} &= \sqrt{\frac{(l+k)(l+k-1)}{(l+m)(l+m-1)}} \\ c^{l;0}_{mk} &= \sqrt{\frac{2(l+k)(l+k)}{(l+m)(l+m-1)}} \\ c^{l;1}_{mk} &= \sqrt{\frac{(l-k)(l-k-1)}{(l+m)(l+m-1)}} \end{aligned} \tag{A.13}$$

For $m < 0$:

$$D^l_{mk} = (-1)^{m-k} \left(D^l_{-m,-l}\right)^* \tag{A.14}$$

Given:

$$\overline{v}_{lmk} = (-1)^{k+m}\sqrt{\frac{2-\delta_{0k}}{2-\delta_{0m}}} \tag{A.15}$$

the matrices $\mathfrak{R}^l_{mk}$ and $\mathfrak{I}^l_{mk}$ are defined as:

$$\begin{aligned}\mathfrak{R}^l_{m,k} &= \mathfrak{R}\left(\overline{v}_{lmk}D^l_{mk}\right)\\ \mathfrak{I}^l_{m,k} &= \mathfrak{I}\left(\overline{v}_{lmk}D^l_{mk}\right)\end{aligned} \tag{A.16}$$

The fully normalized coefficients $\overline{C}^{F_2}_{lm}$ and $\overline{S}^{F_2}_{lm}$ in the rotated frame F_2 are then found from the fully normalized coefficients in the original frame, F_1, according to:

$$\begin{aligned}\overline{C}^{F_2}_{lm} &= (2-\delta_{0m})\left(\mathfrak{R}^l_{m,0}\overline{C}^{F_1}_{l0} + \frac{1}{2}\sum_{k=1}^{l}\left(\left(\mathfrak{R}^l_{m,k}+(-1)^k\mathfrak{R}^l_{m,-k}\right)\overline{C}^{F_1}_{lk} + \left(\mathfrak{I}^l_{m,k}+(-1)^{k+1}\mathfrak{I}^l_{m,-k}\right)\overline{S}^{F_1}_{lk}\right)\right)\\ \overline{S}^{F_2}_{lm} &= -(2-\delta_{0m})\left(\mathfrak{I}^l_{m,0}\overline{C}^{F_1}_{l0} + \frac{1}{2}\sum_{k=1}^{l}\left(\left(\mathfrak{I}^l_{m,k}+(-1)^k\mathfrak{I}^l_{m,-k}\right)\overline{C}^{F_1}_{lk} + \left(-\mathfrak{R}^l_{m,k}+(-1)^k\mathfrak{R}^l_{m,-k}\right)\overline{S}^{F_1}_{lk}\right)\right)\end{aligned} \tag{A.17}$$

B

Appendix B: MOP optimization plots

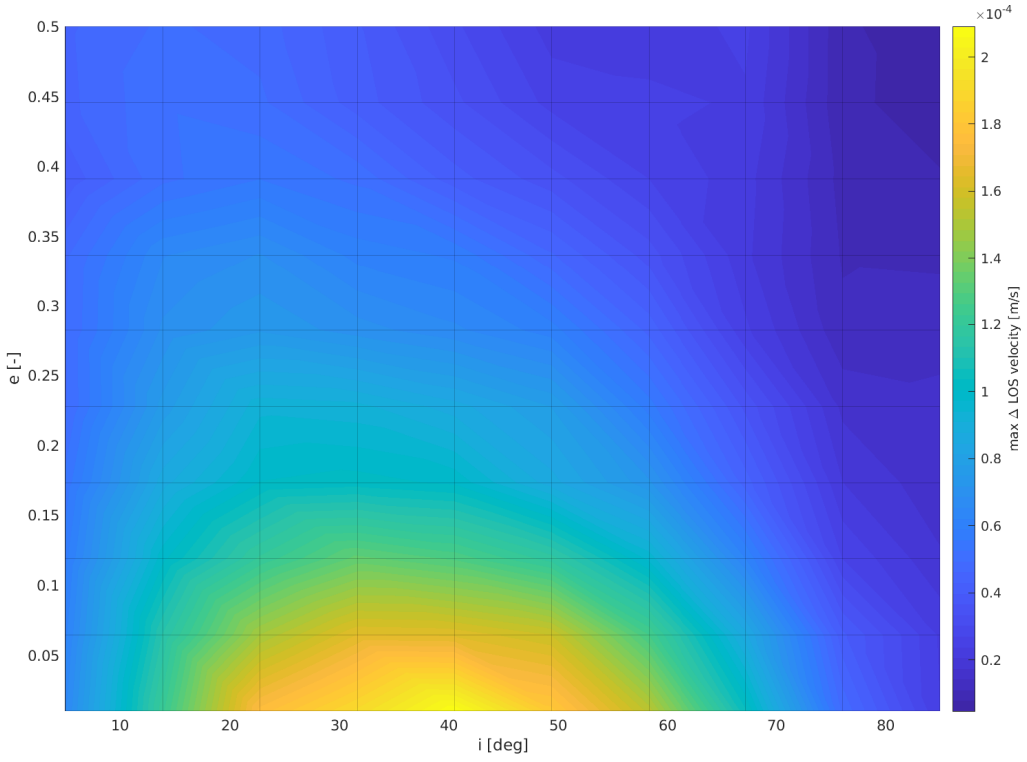

Figure B.1: Maximum signature of PM on the LOS velocity computed over 10 days with ORB, as a function of the orbit eccentricity and inclination, assuming a fixed pericenter altitude of 600 km

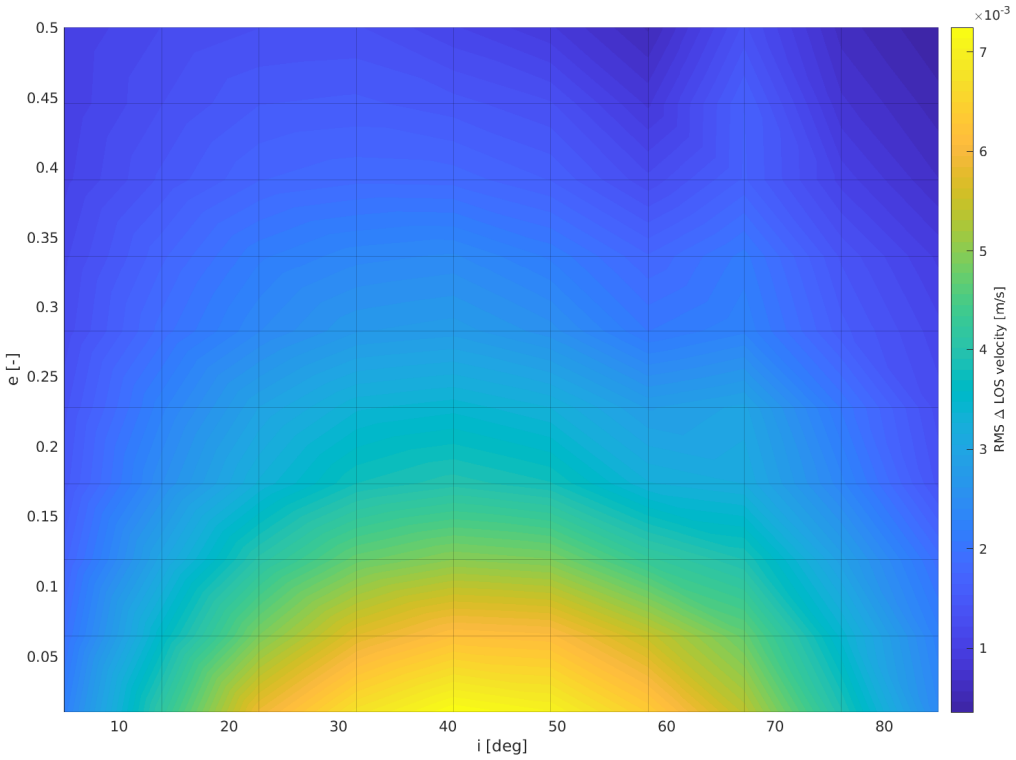

Figure B.2: RMS of the signature of PM on the LOS velocity computed over 700 days with ORB, as a function of the orbit eccentricity and inclination, assuming a fixed pericenter altitude of 400 km

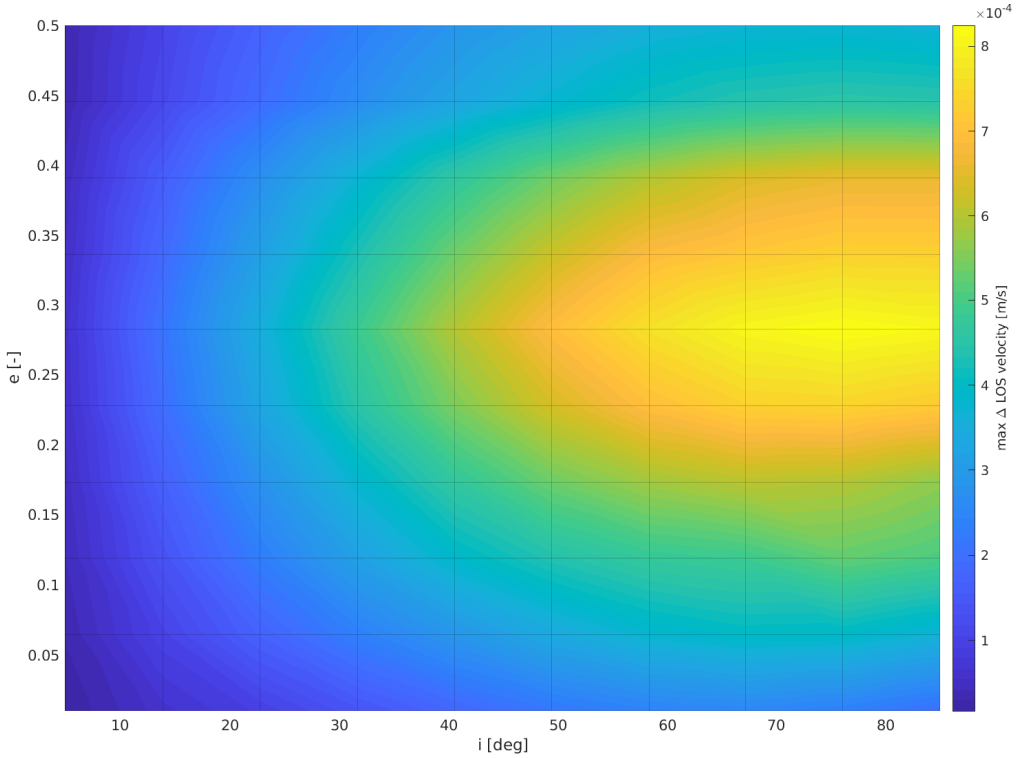

Figure B.3: Maximum signature of PM on the LOS velocity computed over 10 days with ORB, as a function of the orbit eccentricity and inclination, assuming a fixed pericenter altitude of 400 km. The initial values of the ω, Ω, and M angles are here all equal to $45°$